UNIVERSITY OF CALIFORNIA
RIVERSIDE

Evolution of Galaxies in the Cosmic Web

A Dissertation submitted in partial satisfaction
of the requirements for the degree of

Doctor of Philosophy

in

Physics

by

Behnam Darvish Sarvestani

December 2015

Dissertation Committee:
Dr. Bahram Mobasher, Chairperson
Dr. Gabriela Canalizo
Dr. Brian Siana

The Dissertation of Behnam Darvish Sarvestani is approved:

Committee Chairperson

University of California, Riverside

Acknowledgements

I wish to acknowledge everyone who helped me out during my academic career. I would especially like to thank my parents, brothers, and sisters for their continuous support and encouragement. I would also like to thank all my teachers and mentors who contributed greatly to my education and understanding and, more importantly, to be a better human. Without them, I would not have been able to achieve many of my goals.

My special thanks goes to my supervisor, Professor Bahram Mobasher, who was not only a superb mentor, but also a great friend. I learned from him how to be a great human being. I am thankful to him for providing me with a relaxed environment and a tremendous degree of freedom so that I could peacefully do my research.

I am very grateful to my friend Dr. David Sobral who significantly helped me during my studies and had an essential role in making this dissertation possible.

I wish to thank Drs. Gabriela Canalizo and Brian Siana for their tremendous help and guidance. I thank them for agreeing to be members of my dissertation committee and for reading my thesis. I additionally wish to thank Dr. Brian Siana for all his hard work to make our astronomy department a more dynamic and convivial place.

I would like to thank my great friends Hooshang Nayyeri, Shoubaneh Hemmati, Ehsan Norouzifar, Mostafa Khezri, Irene Shivaei, Ali Beyramzadeh, my splendid friends at the FZX house, including Michael Beaumier, Christopher Heidt, Patrick Odenthal, Oleg Martynov, and all my wonderful friends in Riverside with whom I have had joyful moments. I will always have pleasant memories of them, and I am very grateful for their friendship.

A comprehensive list of people who helped me become the person that I am today is not feasible. However, I am really grateful to all of them (You know who you are!).

This work is partly based on research that has been either published in the Astrophysical Journal (2014ApJ...796...51D and 2015ApJ...805..121D) or submitted to (manuscript number: ApJ99672).

To my Parents,
Thanks for your endless love and continuous support

ABSTRACT OF THE DISSERTATION

Evolution of Galaxies in the Cosmic Web

by

Behnam Darvish Sarvestani

Doctor of Philosophy, Graduate Program in Physics
University of California, Riverside, December 2015
Dr. Bahram Mobasher, Chairperson

We study the effects of environment on the evolution of galaxies, with an emphasis on two different approaches towards the definition of environment: (1) environment defined based on the local surface density of galaxies and (2) environment defined based on the major components of the cosmic web; i.e., filaments, clusters and the field. In the first approach, surface density field is estimated using a variety of estimators and tested with simulations. Using the estimated surface densities assigned to galaxies, we observe a strong environmental dependence on the properties of galaxies (e.g., SFR, sSFR and the quiescent fraction) at $z \lesssim 1$. We explore the fractional role of stellar mass and environment in quenching the star-formation. In the second approach, we use the Multi-scale Morphology Filter algorithm to disentangle the density field into its component. We apply this method to a sample of star-forming galaxies for a large-scale structure at $z \sim 0.84$ in the HiZELS-COSMOS field. We show that the observed median SFR, stellar mass, sSFR, the mean SFR−mass relation and its scatter for star-forming galaxies do not strongly depend on the cosmic web. However, the fraction of Hα star-forming galaxies varies with environment and is enhanced in filaments. Furthermore, we study the physical properties of a spectroscopic sample of star-forming galaxies in a large filament in the COSMOS field at $z \sim 0.53$, with spectroscopic data taken with the Keck/DEIMOS spectrograph, and compare them with a control sample of field galaxies. We spectroscopically confirm the presence of a large galaxy filament ($\sim$ 8 Mpc). We show that within the uncertainties, the ionization parameter, EW, EW versus sSFR relation, EW versus stellar mass relation, line-of-sight velocity dispersion, dynamical mass, and stellar-to-dynamical mass ratio are similar for filament and field star-forming galaxies. However, we show that on average, filament star-forming galaxies are more metal-enriched ($\sim$ 0.1$-$0.15 dex) and the electron densities are significantly lower (a factor of $\sim$17) in filament star-forming systems compared to those in the field. Our results highlight the potential role of galaxy filaments and intermediate-density environments on the evolution of galaxies, which has been poorly investigated.

Contents

List of Figures

List of Tables

Chapter 1

Introduction

The standard model of cosmology is based upon the cosmological principle, the concept of a spatially homogeneous and isotropic universe when averaged over scales of $\gtrsim$100 Mpc. On smaller scales, the universe is inhomogeneous. Dark matter, gas and galaxies tend to congregate to form structures in the universe. Galaxies are organized in a complex network known as the cosmic web (Bond et al., 1996). The cosmic web has a broad dynamical range of environments: voids that are deprived of matter, planar walls and sheets, filamentary structures, and dense clusters and groups of galaxies woven together by filaments. This large-scale picture of the universe has been revealed in numerical simulations and observed distribution of galaxies in the local universe (Bond et al., 1996; York et al., 2000; Colless et al., 2001). Galaxies form and evolve in the cosmic web and their evolution is essentially driven by a combination of internal processes and their location in the cosmic web (external processes).

Galaxy clusters and dense regions form at the intersection of filamentary structures and constantly grow their mass through the infall of nearby galaxies and the coalescence of galaxy groups (Frenk et al., 1996). In the local universe, star-formation activity is a strong function of the environment. Galaxy clusters and denser environments are mainly populated by passive, red, quiescent early-type galaxies, whereas active, blue, star-forming late-type systems are preferentially found in low-density environments (Dressler, 1980; Balogh et al., 2004; Kauffmann et al., 2004; Baldry et al., 2006; Bamford et al., 2009; Peng et al., 2010). The correlations between galaxy properties and their host environment still exist out to z ∼1. However, these environmental trends often weaken with increasing redshift (Capak et al., 2007a; Cooper et al., 2007; Peng et al., 2010; Sobral et al., 2011; Muzzin et al., 2012; Scoville et al., 2013). Comparison between low- and high-z studies has already revealed a strong galaxy evolution as a function of the environment over the past ∼8 billion years. For example, the fraction of blue, star-forming galaxies increases with redshift, a relation known as the Butcher-Oemler effect (Butcher and Oemler, 1978; Couch and Sharples, 1987; Aragon-Salamanca et al., 1993; Dressler et al., 1994), and the ratio of giant-to-dwarf red-sequence cluster galaxies increases with redshift (De Lucia et al., 2007; Stott et al., 2007; Gilbank and Balogh, 2008; Capozzi et al., 2010). These studies indicate that a large population of star-forming galaxies has truncated the star-formation activity due to the environmental effects since z ∼1, and has migrated to the quiescent population.

Similar trends are observed with stellar mass of galaxies, that is, on average, more massive galaxies are redder, less star-forming, and more likely present early-type morphologies (Baldry et al., 2006; Bamford et al., 2009; Peng et al., 2010). Because stellar mass and environmental densities are shown to be correlated (Kauffmann et al., 2004; Baldry et al., 2006), this adds more complexities to the interpretation of the observations. Nevertheless, recent studies have investigated the fractional role of the environment and stellar mass on quenching the star-formation activity in galaxies, emphasizing that both are relevant for truncation of star-formation (Peng et al., 2010; Sobral et al., 2011). Moreover, "environmental quenching" and "mass quenching" seem to independently lead to the cessation of the star-formation in galaxies. That is, more massive galaxies are more likely to be quenched, independent of their environment (mass quenching) and galaxies in denser environments are more likely to be quenched, independent of their stellar mass (Peng et al., 2010).

Finding the exact physical mechanisms of galaxy quenching is still one of the unsolved problems in galaxy evolution. Many internal (e.g., stellar and AGN feedbacks that are linked to the mass quenching process) and external (e.g., due to galaxy environment) physical drivers are thought to attribute to the quenching process. Several environmental physical processes that are able to quench galaxies have been proposed. These include ram pressure stripping (Gunn and Gott, 1972; Abadi et al., 1999), strangulation (Larson et al., 1980; Balogh et al., 2000; Peng et al., 2015), galaxy−galaxy interactions and harassment (Mihos et al., 1992; Mihos and Hernquist, 1996; Moore et al., 1998), tidal interaction between the potential well of the environment and the galaxy (Merritt, 1984; Fujita, 1998), thermal evaporation (Cowie and Songaila, 1977), and halo quenching (Birnboim and Dekel, 2003; Dekel and Birnboim, 2006) (also see Boselli and Gavazzi, 2006 for a review). The strength and quenching timescale of each physical process varies depending on many parameters such as the properties of the quenching environment (e.g., density, temperature, velocity dispersion, and dynamical state) and those of the galaxy being quenched (e.g., stellar mass, satellite versus central dichotomy). However, the ultimate consequence of each effect is to quickly or gradually remove the gas content/gas reservoir of galaxies and/or heat up the cold gas so that no further star-formation activity is possible.

Despite the well-established relation between the galaxy environment and its star-formation activity (presented by e.g., the star-formation rate (SFR), the fraction of star-forming galaxies, galaxy color, and the SFR−stellar mass relation) in the local universe and low-z, there is no general consensus at $z \sim 1$ and higher redshifts. Several studies have retrieved the local universe trends (Patel et al., 2009; Muzzin et al., 2012), whereas others have observed a flattening of the relation (Grützbauch et al., 2011; Scoville et al., 2013), and even the reversal of the SF−density relation (higher star-formation activity in higher density environments, Elbaz et al., 2007; Cooper et al., 2008a). Nonetheless, much of the discrepancy seems to originate from the way the environment is defined (e.g., galaxy clusters versus the field, local number density of galaxies as a proxy of their environment) and the scale at which the environmental studies has been performed (e.g., rich clusters,galaxy groups and intermediate-density environments, Sobral et al., 2011).

There is substantial evidence for the truncation of the atomic and molecular gas content of cluster galaxies (especially in the outer part of the disk), possibly due to ram pressure stripping (Cayatte et al., 1990; Gavazzi et al., 2005; Boselli et al., 2008; Fumagalli et al., 2009; also see Boselli and Gavazzi, 2014 for a review). If we assume that dust content of galaxies traces the atomic and molecular gas, in principle, the dust distribution in galaxies should depend on their host environment, most likely truncated outside-in as galaxies fall into deeper potential well of denser clusters. There seems to be evidence for this picture. For example, as part of the Herschel Virgo Cluster Survey, Cortese et al. (2010) showed that atomic-gas-deficient spiral galaxies in the Virgo cluster also demonstrate signs of deficiency in their dust content. Similarly, Cortese et al. (2012) found that the total dust content of atomic-gas-deficient spiral galaxies in Virgo is lower compared to normal field galaxies.

Taken at face value, one might naively expect a continuous decline in the star-formation and dust content of galaxies from the field to dense core of clusters. However, before galaxies undergo a full quenching process in dense regions, they may experience a temporary enhancement in star-formation activity and gas content. For example, ram pressure stripping can initially compress the gas/dust which is favorable for star-formation and likely increasing the column density of the gas and dust (Gallazzi et al., 2009). Tidal galaxy−galaxy interactions can lead to the compression and inflow of the gas in the periphery of galaxies into the central part, feeding and rejuvenating the nuclear activity which results in a temporary enhancement in star-formation activity (Mihos et al., 1992; Mihos and Hernquist, 1996; Kewley et al., 2006; Ellison et al., 2008; Sol Alonso et al., 2010; Rupke et al., 2010; Perez et al., 2011; Ellison et al., 2013) and likely dusty star-formation. Galaxy−galaxy encounters are more likely to happen when the interacting systems have lower velocities (in low-velocity-dispersion environments) and closer to each other (denser regions). Intermediate-density environments such as galaxy groups, infalling regions of clusters, cluster outskirts, substructures of unvirialized, merging clusters and galaxy filaments provide the ideal conditions for such interactions (Moss, 2006; Perez et al., 2009; Tonnesen and Cen, 2012). Therefore, one might expect a temporary enhancement in star-formation activity and dusty star-formation in intermediate-density environments before the galaxies becomes fully dead/quenched. This has been found in several previous studies, referring to the intermediate-density environments as sites of enhanced star-formation rate, star-forming fraction and obscured star-formation activity (Smail et al., 1999; Best, 2004; Wolf et al., 2005; Fadda et al., 2008; Porter et al., 2008; Koyama et al., 2008; Gallazzi et al., 2009; Koyama et al., 2010, 2011; Biviano et al., 2011; Coppin et al., 2012; Pintos-Castro et al., 2013; Darvish et al., 2014). There is also substantial evidence for the association of the intermediate-density environments with the most active systems such as AGN and starburst galaxies (Cappelluti et al., 2005; Gilmour et al., 2007; Kocevski et al., 2009). All these studies highlight that in order to have a full grasp of the evolution of galaxies with environment, we should not limit our studies to only galaxy clusters versus field-like environments. Thus, it is of great importance to probe a larger-scale environment of galaxies that covers the intermediate-density environments, such as galaxy filaments as well.

In chapter 2, we define the environment of galaxies, with an emphasis on developing the tools used to quantify both the small-scale (using the local number density of galaxies) and large-scale (components of the cosmic web, such as filaments) environment of galaxies. In chapter 3, we use the local number density of galaxies as a proxy for their environment, and study its relation and evolution with other galaxy properties, such as stellar mass, SFR, color, galaxy type, and the fraction of different types of galaxies. We concentrate on the relation between the cosmic web and star-formation activity in galaxies at $z \sim 1$ in chapter 4. Chapter 5 focuses on a detailed spectroscopic study of galaxies in filaments at $z \sim 0.5$. Finally, chapter 6 summarizes the most important results.

Chapter 2

Density Field Estimation and Cosmic Web of Galaxies

Abstract

It is well-known that galaxy's environment has a fundamental effect in shaping its properties. In this chapter, we discuss the methods developed for describing the local, as well as the large-scale environment of galaxies with an emphasis on two different approaches towards the definition of environment: (1) environment defined as the local number density of galaxies and (2) environment defined based on the major components of the cosmic web; i.e., filaments, clusters and the field. In the first approach, the density field is estimated with different methods (weighted adaptive kernel smoothing, 10th and 5th nearest neighbors, Voronoi tessellation and Delaunay triangulation). The performance of each estimator is evaluated with extensive simulations. We show that overall, there is a good agreement between the estimated density fields using different methods over $\sim$2 dex in overdensity values. However, our simulations show that adaptive kernel and Voronoi tessellation outperform other methods. In the second approach, we develop the 2D version of the Multi-scale Morphology Filter (MMF) algorithm to disentangle the density field into its major components such as filaments and clusters. This algorithm describes the local

geometry of each point in the density field based on the signs and the ratio of eigenvalues of the Hessian matrix (second order derivative of the density field). Results from this chapter will be used in the following chapters to study observed properties of galaxies in different environments.

2.1 Introduction

It is known that the environment where galaxies reside plays a fundamental role in their evolution. In the local universe, denser environments are dominated by red, passive, early-type galaxies whereas less dense regions are preferentially populated by blue, star-forming, late-type systems (Dressler, 1980; Balogh et al., 2004; Kauffmann et al., 2004; Baldry et al., 2006; Bamford et al., 2009; Peng et al., 2010). These environmental trends still hold at higher redshifts (Capak et al., 2007a; Cooper et al., 2007; Peng et al., 2010; Sobral et al., 2011; Muzzin et al., 2012; Scoville et al., 2013), although they usually tend to weaken with increasing redshift. While it is evident that almost any observable property of a galaxy demonstrates some association with the environment, there is still a question that needs to be addressed first. What do we really mean by "environment"?

Recent advances in numerical simulations (Millennium, Springel et al., 2005; Illustris, Vogelsberger et al., 2014) combined with extensive spectroscopic observations of local galaxies (SDSS, York et al., 2000; 2dFGRS, Colless et al., 2001; GAMA, Driver et al., 2011) have revealed that the universe has a web-like pattern (i.e., the "cosmic web"; Bond et al., 1996), containing dark matter, gas, and luminous galaxies. Galaxies in the cosmic web are organized in a network containing dense clusters, sparsely populated voids, planar walls, and thread-like filamentary structures linking overdense regions. Therefore, the most natural approach in defining the environment of a galaxy is to locate it within the cosmic web. However, the complexity and lack of a fully objective method in identifying the major components of the cosmic web often limit the environmental studies of galaxies within the comic web to numerical simulations or large spectroscopic surveys in the local universe.

The conventional method of defining the environment as two extreme regions in the density distribution of galaxies (i.e., galaxy cluster and the general field) does not usually account for the full dynamical range of the density field. For example, there are intermediate environments such as galaxy groups, outskirts of clusters, and filaments that are equally important (Fadda et al., 2008; Porter et al., 2008; Tran et al., 2009; Geach et al., 2011; Coppin et al., 2012; Mahajan et al., 2012; Pintos-Castro et al., 2013; Darvish et al., 2014). Moreover, the selection of whether galaxies belong to the cluster environment or the general field is somewhat subjective.

The detection of galaxy clusters through their diffuse X-ray emission (Gioia et al., 1990; Ebeling et al., 1998, 2001; Böhringer et al., 2000, 2004; Mehrtens et al., 2012), the red sequence and its variants (Gladders and Yee, 2000; Goto et al., 2002; Gladders and Yee, 2005; Miller et al., 2005; Koester et al., 2007; Hao et al., 2010; Muzzin et al., 2013b), weak gravitational lensing (Dietrich et al., 2007; Gavazzi and Soucail, 2007; Miyazaki et al., 2007) and the Sunyaev-Zel'dovich effect (Marriage et al., 2011; Planck Collaboration et al., 2011; Williamson et al., 2011; Reichardt et al., 2013) adds more assumptions and limitations in the environmental studies. For example, weak lensing, hot X-ray emission, and the Sunyaev-Zel'dovich effects are more sensitive to virialized, massive galaxy clusters. The red-sequence technique, which relies on observations in only two filters, is very successful and economically efficient in detecting a large sample of galaxy clusters that have a tight red sequence of quiescent galaxies. However, this technique assumes the existence of a tight red sequence for clusters, requires modeling the red-sequence, and uses only the quiescent systems as a proxy of their host cluster environment. Moreover, the quiescent galaxies become less abundant at higher redshifts, which makes the cluster detection techniques based on the red sequence (or galaxy color) challenging at high redshift. All these methods may produce biased environments, which may lead to misinterpretation of the evolutionary history of galaxies as a function of their host environment.

Another approach in defining the environment is to use the local number density (usually surface density) of galaxies as a proxy to their host region. Among the most common density estimators used in the literature are the nearest neighbor (usually fifth or tenth NN) and count-in-cell (CC) methods. However, although simple to implement and computationally fast, the performance of these methods strongly depends on the depth of the data, the number of neighbors considered in the analysis (in NN method), and the size of the cell (in CC method). A small value of N (a small cell size for CC method) results in a spiky density field that makes it vulnerable to unrealistic density values due to Poisson noise and random clustering of spatially uncorrelated galaxies. A large value of N (a large cell size for CC method) is prone to underestimation of the surface density and oversmoothing the details of galaxy distribution. In addition, for the NN method, the sum of the area (volume) assigned to each galaxy is not equal to the total area (volume) of any survey and it has also been shown that its integral over all area (volume) diverges.

More importantly, it is still not clear whether the environmental effects depend on the physical scales at which the environment is estimated. For example, Kauffmann et al. (2004), Blanton et al. (2006), and Cucciati et al. (2010) find that the effect of the environment on the star-formation history of galaxies is only effective at the small scales ($\lesssim$1 Mpc), whereas Balogh et al. (2004) find that the equivalent width of Hα (a measure of the specific star-formation rate (sSFR) in galaxies) is a function of the environment measured on scales of $\sim$1 and $\sim$5 Mpc, independent of each other. Scale-dependent density estimators, such as the NN and CC algorithms, are not able to directly address this issue.

In this chapter, we perform a comprehensive analysis of the (surface) density field using the weighted versions of the fifth NN, tenth NN, adaptive kernel smoothing, Voronoi tessellation, and Delaunay triangulation methods. This is done using a K_s-band selected sample of galaxies in the COSMOS field (Scoville et al., 2007b). The large size of the COSMOS ($\sim$2 deg^2), together with the high accuracy of the photometric redshifts in this field, enable us to delineate the Large Scale Structure with great accuracy out to $z \sim$3. In this analysis, we use the full photo-z probability distribution function (PDF) of individual galaxies to significantly reduce the projection effect. The performance of each method is checked with extensive realistic and Monte-Carlo simulations. We then use the estimated density field as an input for the 2D version of the Multi-Scale Morphology Filter (MMF) algorithm (Aragón-Calvo et al., 2007). We describe the MMF algorithm in details that will be used to extract the cosmic web of galaxies. The methods discussed in this chapter are extensively used in the following chapters to investigate the role of the local (based on the local number density of galaxies) and the large (based on the components of the cosmic web) scale environment of galaxies on their evolution.

The format of this chapter is as follows. In Section 2, we briefly review the data used to estimate the density field. Section 3 outlines the algorithm used to determine the density field, followed by the surface density estimation methods in Section 4. Section 5 deals with the simulations used to check the performance of different density estimators. Comparisons between different methods are given in Section 6. In Section 7, we describe the cosmic web extraction using the MMF algorithm and provide some examples of the delineated cosmic web in the COSMOS field. We give a summary of this chapter in Section 8.

Throughout this chapter, we assume a flat concordance ΛCDM cosmology with H_0=70 kms^{-1} Mpc^{-1}, Ω_m=0.3 and Ω_Λ=0.7. All magnitudes are expressed in the AB system and stellar masses are given assuming a Chabrier initial mass function (IMF).

2.2 Data and Sample Selection

In order to examine different density estimation techniques, we select an area of ∼1.8 deg^2 in the COSMOS field (Capak et al., 2007b; Scoville et al., 2007b). Here, we use the COSMOS UltraVISTA K$_s$-band selected photometric redshift (photo-z) catalog (McCracken et al., 2012; Ilbert et al., 2013). The K$_s$-band selection is equivalent to a stellar mass-selected sample and enables us to reliably detect galaxies (especially quiescent systems) at intermediate to high redshifts. This catalog consists of ground- and space-based photometric data in 30 bands, spanning the range UV to mid-IR. Using this extensive data set, accurate photometric redshifts are measured for galaxies out to z ∼3. Stars, active galactic nuclei (AGN), and X-ray sources were identified and removed from the sample. The final selection criteria used to define the sample are:

1. An area of $149.3 < \alpha_{2000} < 150.8$ and $1.6 < \delta_{2000} < 2.8$ corresponding to $\sim$1.8 deg^2. The area is selected to be large enough for the effect of the LSS to be discernible.

2. Redshift within the range $0.05 < z < 3.2$ to allow photometric redshifts with a high degree of accuracy.

3. Galaxies brighter than $K_s < 24$, because the photo-z uncertainties increase significantly at $K_s \gtrsim 24$.

The total sample contains 191,151 galaxies.

2.3 Determination of the Large Scale Distribution of Galaxies

In any study of the LSS of galaxies, we need the angular position (α,δ) of the galaxies and a measure of their radial distance (using spectroscopic or photometric redshifts) to estimate the density field. Here, we use the full photo-z PDF of each individual galaxy to significantly reduce the projection effect. In summary, the density field estimation involves the following steps:

1. First, we construct a series of overlapping redshift slices (z-slices) in redshift space. The widths of these slices are obtained by the photo-z accuracy of the underlying sample of galaxies at each redshift.

2. For each z-slice, we select a *subset* of galaxies belonging to that slice. The galaxies in the subset are selected in such a way that the median of their photo-z PDF is located within that z-slice. For a given subset, we associate a weight to each galaxy. This weight shows the likelihood of each galaxy belonging to the z-slice of our interest. The weight is determined by the photo-z PDF of each galaxy and the boundaries of the z-slice.

3. At each z-slice and for its subset of galaxies, we then compute the weighted surface density field using one of the estimation methods described in Section 2.4.

In the following, we give a detailed description of points 1 and 2. Using this information, we then apply different density estimators to the data in Section 2.4.

2.3.1 Redshift Slicing

In order to construct the density field of galaxies, one needs a large, homogeneous, and unbiased sample of galaxies with very accurate redshifts. However, there are serious complications in constructing such samples. First, building a homogeneous sample is difficult. Second, relying on a purely spectroscopic sample would bias the study because it would only concentrate on bright objects and mostly those with emission lines (i.e., star-forming galaxies, which are often less clustered compared to quiescent systems). Spectroscopic samples also do not usually target enough number of galaxies in dense regions. Thirdly, finding accurate photometric redshifts requires a homogeneous set of multi-waveband photometric data. Thanks to the wealth of the photometric data available in the COSMOS field, we have been able to obtain highly accurate photometric redshifts for a large population of galaxies in this field (Mobasher et al., 2007; Ilbert et al., 2009, 2013). Figure 2.1 shows the median of photo-z uncertainty (Δz_{med}) as a function of (photometric) redshift for the sample of galaxies used in this study. Δz for each galaxy is calculated as the (lower and higher) 68% confidence interval of its photo-z PDF. The median of the photo-z uncertainty is $\Delta z_{med} \lesssim 0.01$ out to $z \sim 1$, reaching $\Delta z_{med} \sim 0.1$ at $z \sim 2$. Studying the 3D density estimations solely based on the photo-z of galaxies, without taking their photo-z uncertainties into account, may result in an erroneous evaluation of the density field. This is mainly due to the fact that the physical lengths corresponding to even the smallest photo-z uncertainties are larger than the typical sizes of most physical structures, such as galaxy clusters and groups (e.g., at $z \sim 1$, the photo-z uncertainty of $\Delta z \sim 0.01$ is equivalent to the comoving radial length of ~ 24 Mpc). Here, we limit our analysis to the 2D surface density estimations by constructing a series of narrow slices in the redshift space. This is done by defining a

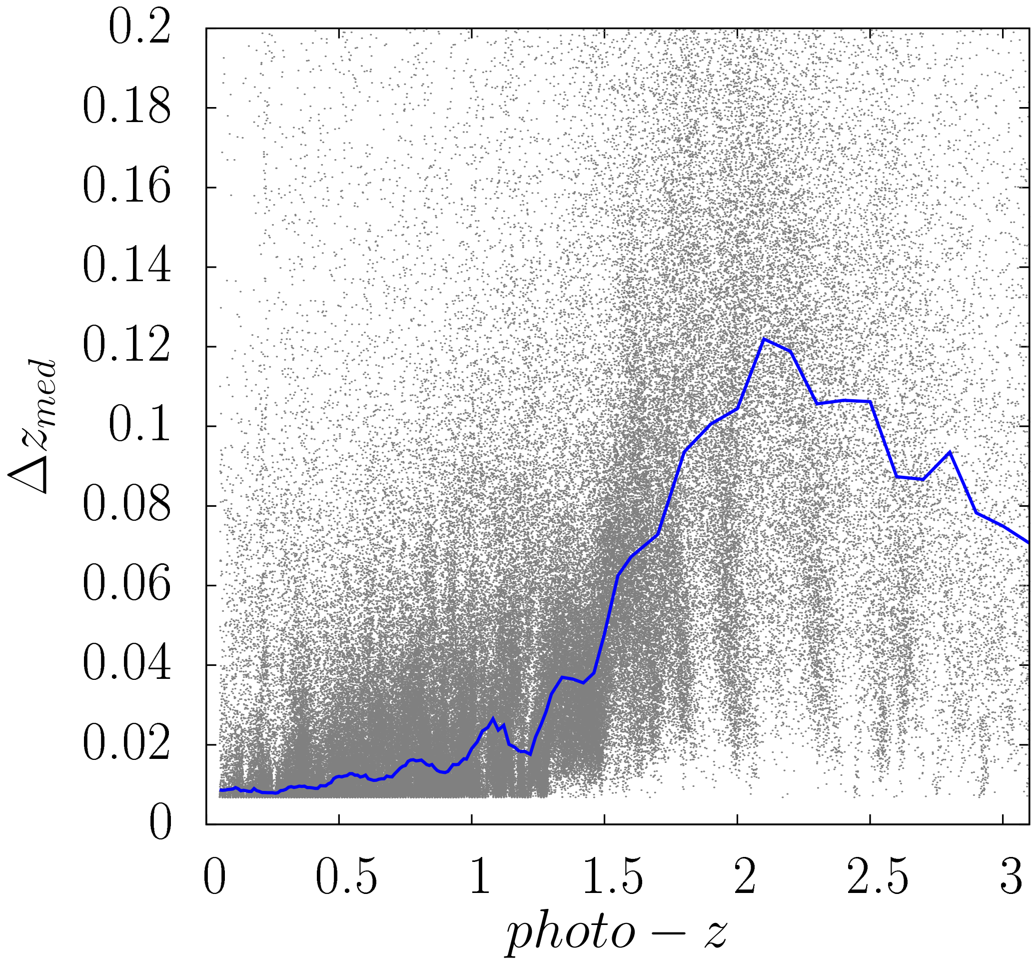

Figure 2.1: Photo-z uncertainty of galaxies used in this study. The blue solid line shows the median of the photo-z uncertainty (Δz_{med}) at each redshift. Δz for each galaxy is calculated as the (lower and higher) 68% confidence interval of its photo-z PDF. Note the accuracy of photo-z values. The median of the photo-z uncertainty is $\Delta z_{med} \lesssim 0.01$ out to $z \sim 1$, reaching $\Delta z_{med} \sim 0.1$ at $z \sim 2$.

series of overlapping redshift slices (z-slices). The width of each slice is set by the photometric redshift accuracy of the data at any given redshift. The slices overlap to allow proper contribution from galaxies that reside close to the boundaries of each slice. In practice, we make sure that approximately half of each z-slice is trespassed into its adjacent z-slices. The width of each z-slice (δz) at redshift z is defined as twice the median of the photo-z uncertainty (Δz_{med}) at that redshift:

$$\delta z = 2\Delta z_{med} \tag{2.1}$$

Figure 2.1 shows how Δz_{med} changes with redshift. In this study, a total number of 133 overlapping z-slices were used over the redshift range $0.1 < z < 3.2$.

Choosing a much narrower z-slice results in smaller number statistics and decreased completeness of the underlying sample of galaxies. This subsequently leads to an underestimation of the surface density field. On the other side, broadening the z-slice increases the risk of contamination from foreground and background galaxies, as well as a possible overestimation of the density field. Thus, our choice is a compromise between both limits.

2.3.2 Photo-z Probability Weights

To estimate the surface density field, we use the full information of the photo-z PDF for individual galaxies. First, for each z-slice, we select a subset of galaxies. Galaxies in each subset are selected in such a way that their median photo-z PDF is located within the boundaries of that z-slice. We assign a weight (w_i) to each galaxy in this subset based upon its photo-z PDF. This probability weight is calculated by measuring what percentage of the photo-z PDF of each galaxy is contained within the boundaries of the considered z-slice. This weight represents the likelihood that the galaxy in question resides within that z-slice. In practice, it is done by intersecting the z-slice of our interest with the photo-z PDF of each galaxy in the subset. In order to enhance the computational performance, we assume a Gaussian photo-z PDF for galaxies, except for those that have a second photo-z

peak with P >5% in their PDF. For the latter, the full photo-z PDF is used in estimating the weights. Eventually, at each redshift and for each z-slice, we have a subset of galaxies with associated weights that will later be used as the input for the weighted surface density estimation methods. Figure 2.2 (a) shows the distribution of galaxies for a z-slice centered at z=0.92 in the COSMOS. For demonstration, the size of each point is selected to be proportional to the galaxy weight. This subset of galaxies, and their associated weights, is used to estimate the weighted surface density field at z=0.92.

We note that the weight introduced in this section can be generalized to other galaxy properties, such as stellar mass, luminosity, and color, depending on the astrophysics of our problem.

2.4 Surface Density Estimation: The Methods

Using the information obtained in Section 2.3, we now construct the density field for galaxies in the COSMOS, using weighted versions of four independent methods: adaptive kernel, NN, Voronoi tessellation, and Delaunay triangulation (Sections 2.4.1 to 2.4.4). We then evaluate their performance with simulations in Section 2.5 and compare them with each other in Section 2.6.

2.4.1 Weighted Adaptive Kernel Estimator

In this method, we use an iterative procedure to compute the surface density field (Darvish et al., 2014). First, we estimate the surface density associated with the ith galaxy in a given z-slice, $\hat{\Sigma}_i$, by summing over all the weighted fixed kernels placed on the positions of galaxies, j, where $i \neq j$:

$$\hat{\Sigma}_i = \frac{1}{\sum_{\substack{j=1 \\ j\neq i}}^{N} w_j} \sum_{\substack{j=1 \\ j\neq i}}^{N} w_j K(\mathbf{r}_{\mathrm{i}}, \mathbf{r}_{\mathrm{j}}, \mathrm{h}) \tag{2.2}$$

where N is the number of galaxies in the subset, $K(\mathbf{r}_{\mathrm{i}}, \mathbf{r}_{\mathrm{j}}, \mathrm{h})$ is the fixed kernel, $\mathbf{r}_{\mathrm{i}}$ is the position of the galaxy for which the initial estimate of surface density is measured, and

(a)

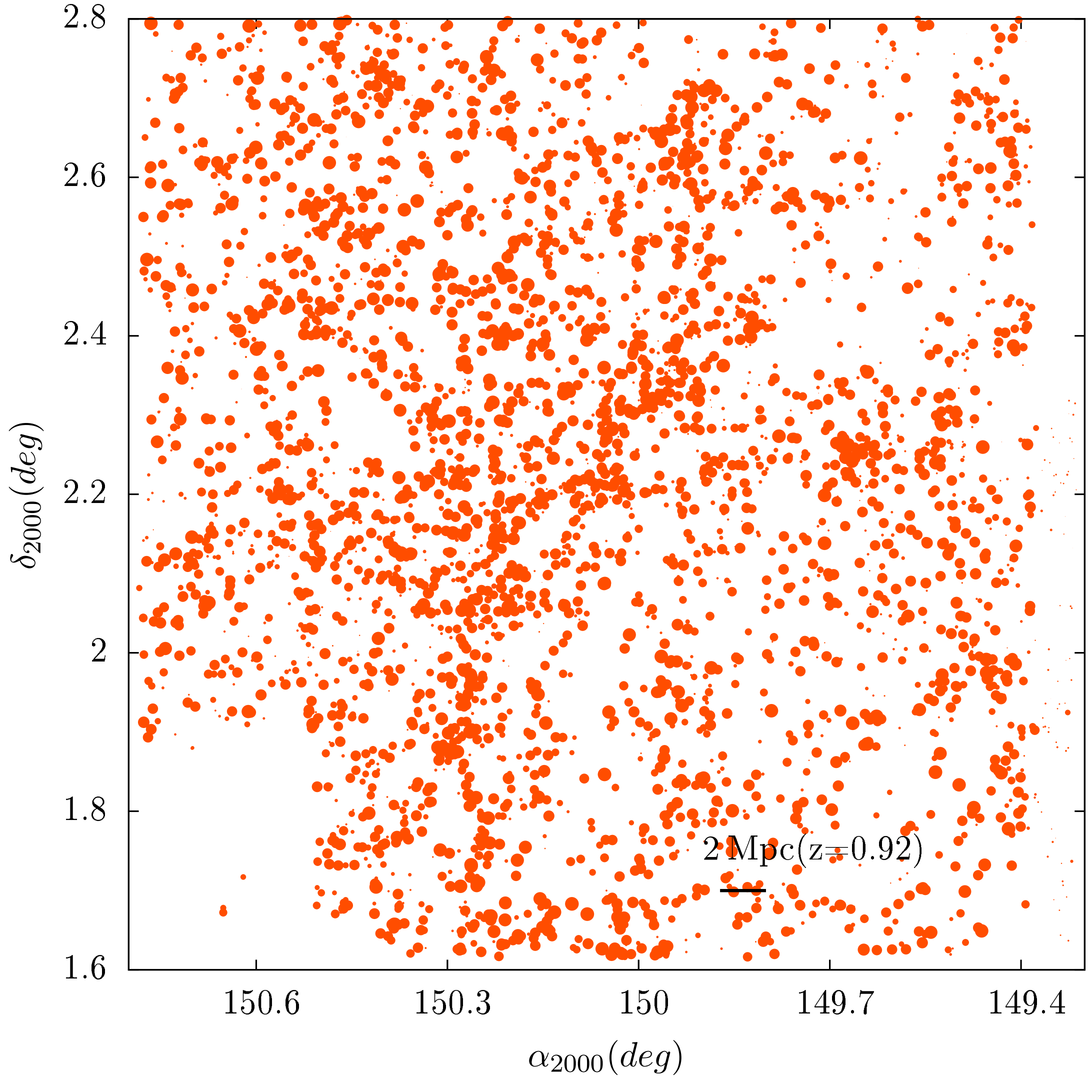

Figure 2.2: Comparison of surface density fields in the COSMOS at z=0.92, estimated with different methods. (a) Distribution of galaxies for a z-slice located at z=0.92. The size of each point is proportional to the galaxy weight. (b) Surface density field estimated using the weighted adaptive kernel smoothing method for the distribution of galaxies at z=0.92. (c) Surface density field estimated using the weighted tenth NN method, (d) fifth NN, (e) Voronoi tessellation, and (f) Delaunay triangulation methods.

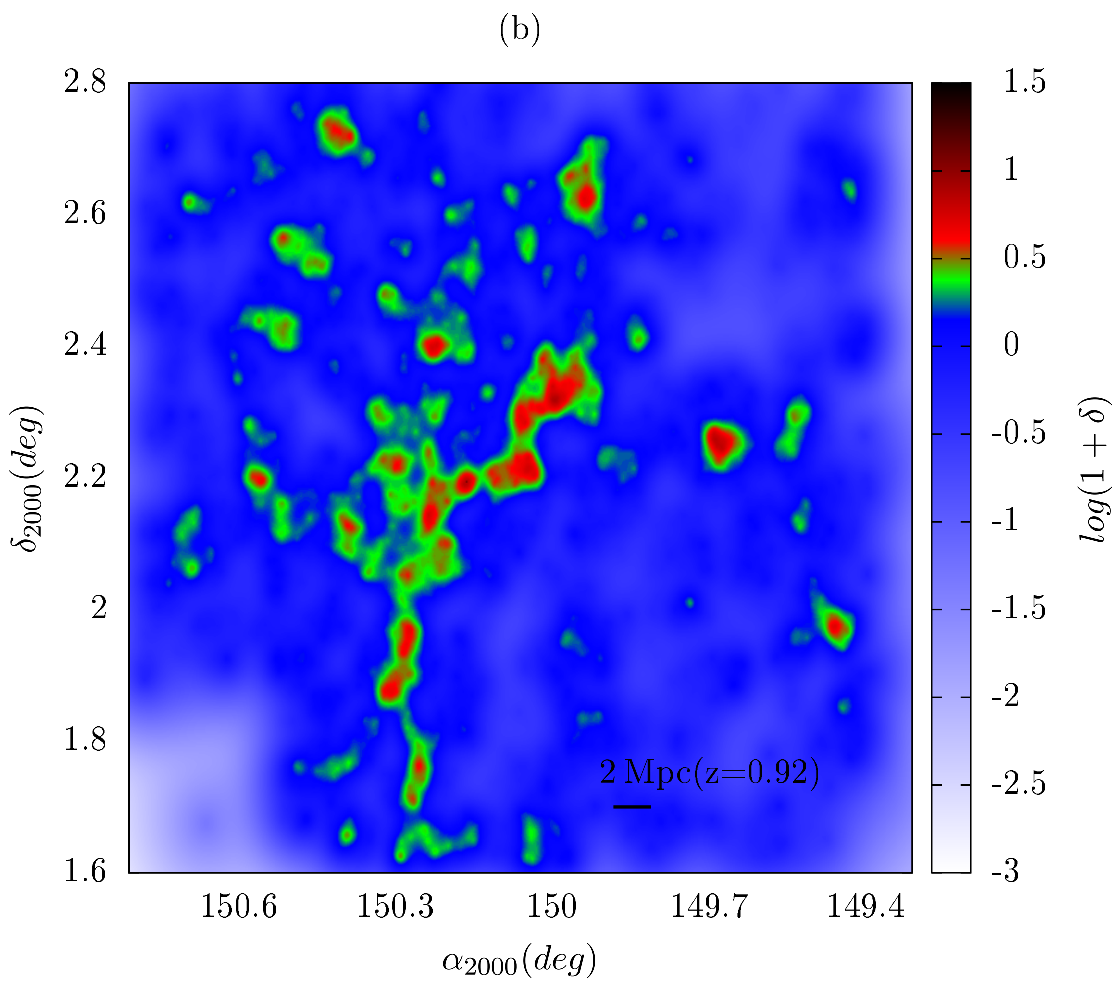

Figure 2.2: cont. (b)

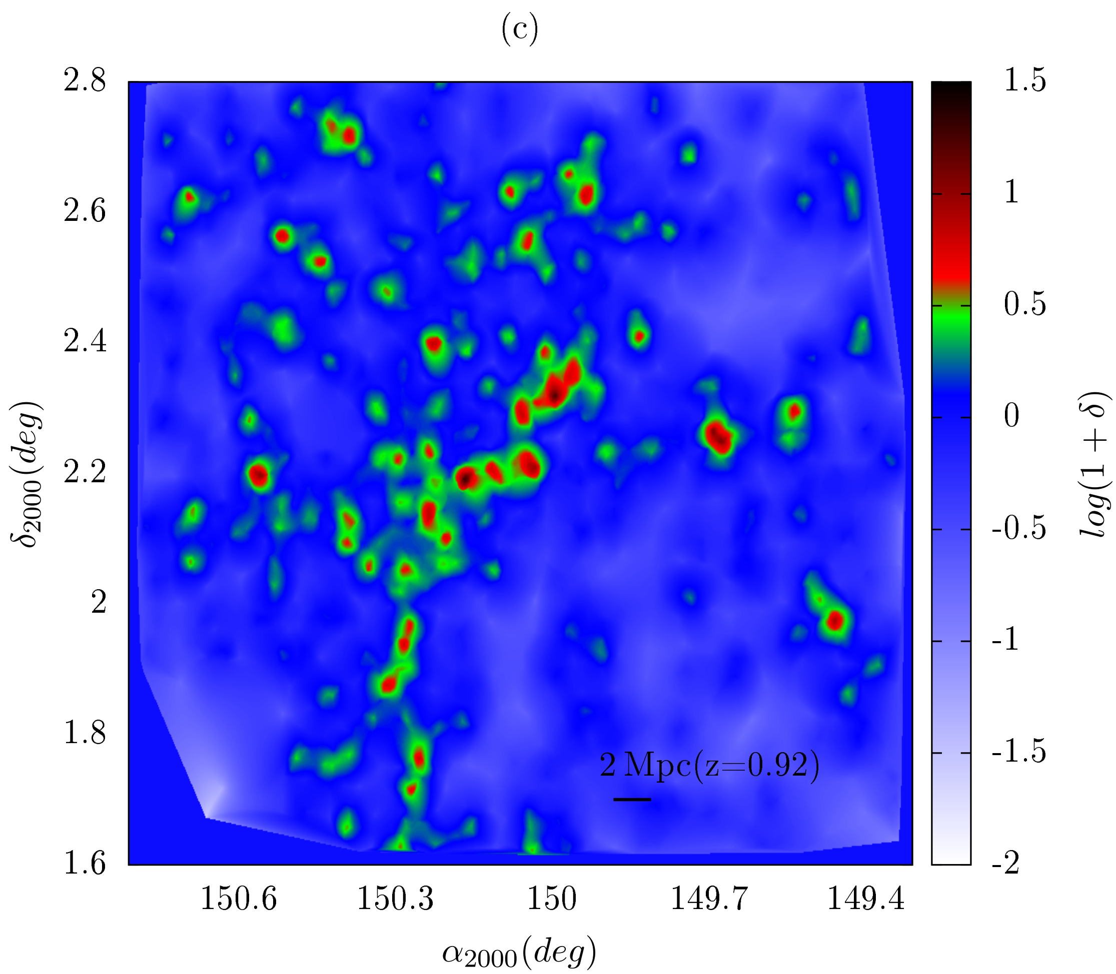

Figure 2.2: cont. (c)

(d)

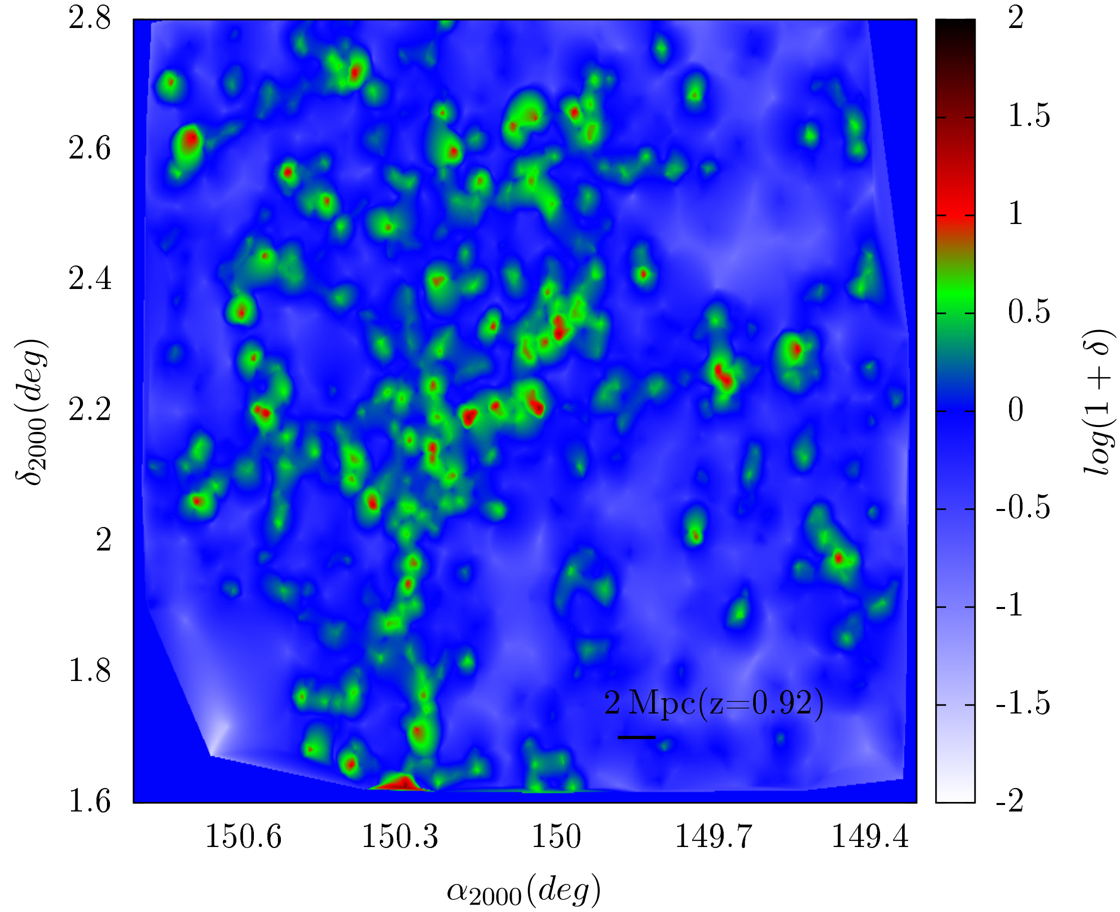

Figure 2.2: cont. (d)

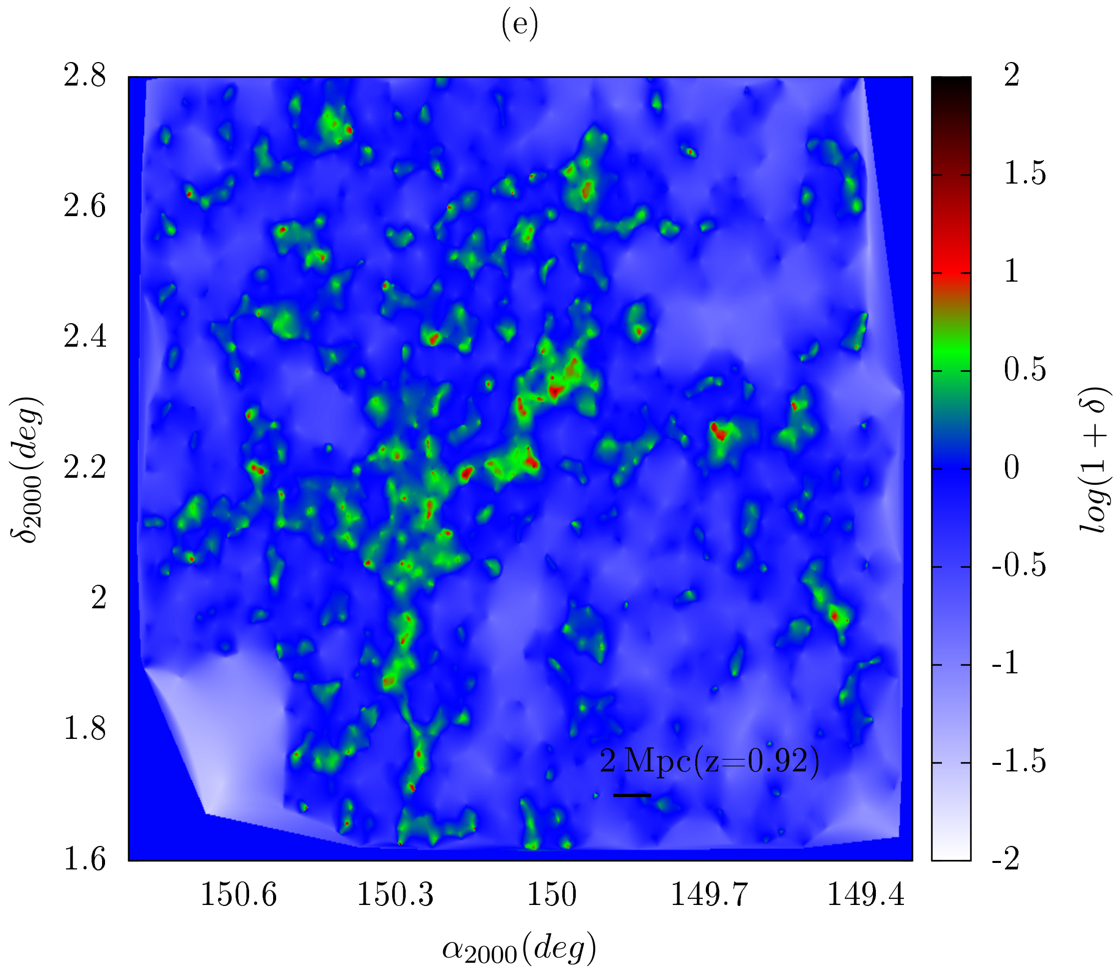

Figure 2.2: cont. (e)

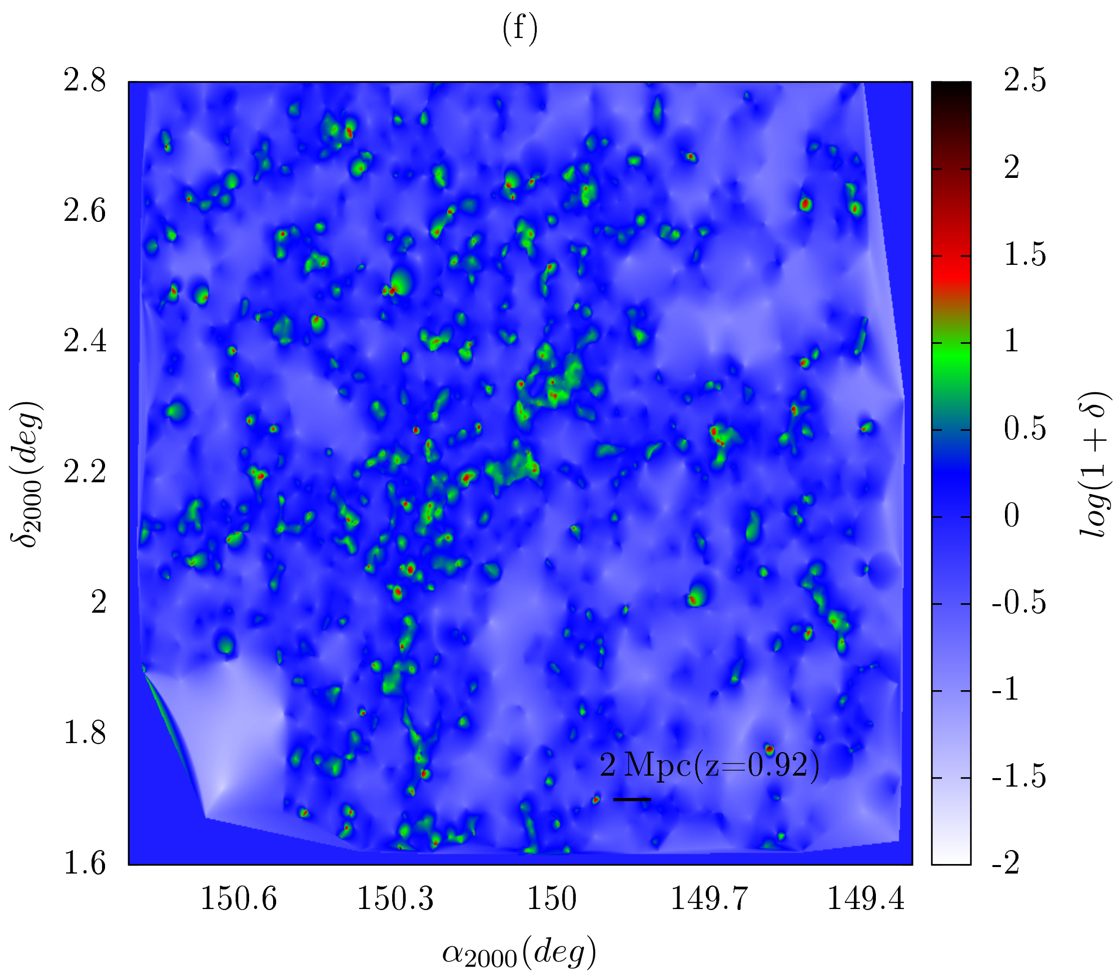

Figure 2.2: cont. (f)

$\mathbf{r}_\mathrm{j}$ is the position of the rest of the galaxies. The width of the kernel is expressed by the parameter, h, which is a proxy for the degree of smoothing. For the first estimate of the density, this is taken to be fixed. For the kernel smoothing function, we use a 2D symmetric Gaussian defined as:

$$K(\mathbf{r}_\mathrm{i}, \mathbf{r}_\mathrm{j}, \mathrm{h}) = \frac{1}{2\pi \mathrm{h}^2} \mathrm{e}^{-\frac{|\mathbf{r}_\mathrm{i} - \mathbf{r}_\mathrm{j}|^2}{2\mathrm{h}^2}} \tag{2.3}$$

A large kernel width (h) results in oversmoothing of the density field which tends to wash out real features, whereas a small value tends to break up regions into smaller uncorrelated substructures. Here, we use a fixed physical length of h=0.5 Mpc which corresponds to the typical value of R_{200} for X-ray clusters and groups in the COSMOS field (Finoguenov et al., 2007; George et al., 2011). However, a constant value of h for the whole field has the problem that it underestimates the surface density in crowded regions while overestimating in sparsely populated areas. To overcome this problem, we introduce the adaptive smoothing width, h_i, which is a measure of the local surface density associated with each galaxy, $\hat{\Sigma}_i$. This is defined as h_i=$h \times \lambda_i$, where λ_i is a parameter that is inversely proportional to the square root of the surface density associated with the ith galaxy, at the position of that galaxy (Silverman, 1986):

$$\lambda_i = (G/\hat{\Sigma}(\mathbf{r}_\mathrm{i}))^{0.5} \tag{2.4}$$

where G is the geometric mean of all the $\hat{\Sigma}(\mathbf{r}_\mathrm{i})$ values. Having the adaptive kernel, we now calculate the surface density field, $\Sigma(\mathbf{r})$, at each location on a fine 2D grid, $\mathbf{r}$=(x,y) as:

$$\Sigma(\mathbf{r}) = \frac{1}{\sum_{i=1}^{\mathrm{N}} \mathrm{w}_\mathrm{i}} \sum_{i=1}^{\mathrm{N}} \mathrm{w}_\mathrm{i} \mathrm{K}(\mathbf{r}, \mathbf{r}_\mathrm{i}, \mathrm{h}_\mathrm{i}) \tag{2.5}$$

The surface density field is evaluated on a fine grid with a grid size (resolution) of 50 kpc at each redshift. We note that the surface density field estimated through this method is almost independent of the type of the kernel function. We examined several other standard kernels, including exponentially decaying, Epanechnikov ($K(r) \propto (1 - r^2)$) and cosine arch ($K(r) \propto cos(\frac{\pi}{2} r)$) and did not find any significant difference in the final results. Throughout this work, we define overdensity as:

$$1 + \delta = \frac{\Sigma}{\Sigma_{median}} \tag{2.6}$$

where Σ_{median} is the median of the surface density field at each redshift. Figure 2.2 (b) shows an example of the surface density field for a z-slice in the COSMOS field centered at z=0.92, using the weighted adaptive kernel density estimator. Note the wide range of overdensities and the variety of environments, including dense regions linked together through thread-like filamentary structures.

2.4.2 Weighted k-Nearest Neighbors (k-NN) estimator

In a regular (non-weighted) k-NN method, the inverse of the area containing the kth nearest neighbors to each galaxy is used as a proxy for local surface density at the position of that galaxy. Because the galaxies in our sample are weighted, we incorporate the role of weights in the density estimation. The surface density at the position of the ith galaxy, $\Sigma(\mathbf{r}_\mathrm{i})$, is estimated as:

$$\Sigma(\mathbf{r}_\mathrm{i}) = \frac{\sum_{\mathrm{j=1}}^{\mathrm{k}} \mathrm{j w_{ij}}}{\pi \sum_{\mathrm{j=1}}^{\mathrm{k}} \mathrm{w_{ij} d_{ij}^2}} \tag{2.7}$$

where $\mathbf{r}_\mathrm{i}$ is the position of ith galaxy, w_{ij} is the photo-z probability weight (Section 2.3.2) associated with the jth nearest neighbor to the galaxy located at $\mathbf{r}_\mathrm{i}$, and d_{ij} is the distance between them (the distance between the galaxy positioned at $\mathbf{r}_\mathrm{i}$ and its jth neighbor). Using the distance to the fifth (k=5) or tenth (k=10) nearest neighbor is very common in the literature (see for example, Cooper et al. (2005); Sobral et al. (2011)). In this work, we use the weighted versions of both the fifth (NN_5) and tenth (NN_{10}) nearest neighbor estimators. Figures 2.2 (c) and (d) show examples of the surface density field at z=0.92, estimated using NN_{10} and NN_5, respectively. The NN_5 method gives a larger density value in very dense regions compared to NN_{10}, as expected. The overall traces of NN_5 are seen in the NN_5 plot. However, the NN_5-based density field looks spikier and clumpier due to the smaller physical lengths that the NN_5 method spans.

2.4.3 Weighted Voronoi Tessellation Estimator

In a simple Voronoi tessellation method, we divide the 2D z-slice plane into a number of regions (Voronoi cells) assigned to each galaxy located at $\mathbf{r}_\mathrm{i}$. The Voronoi cell of each galaxy is defined as all points in the z-slice plane that are closer to that galaxy than to any other galaxy. It is acquired from the intersection of half-planes. Based on this definition, in more crowded, denser regions the Voronoi cells of galaxies incline toward smaller values. Therefore, we can use the inverse of the area of the Voronoi cell of each galaxy as a measure of the local density at the position of that galaxy (Ebeling and Wiedenmann, 1993; Bernardeau and van de Weygaert, 1996). This is given by:

$$\Sigma(\mathbf{r}_\mathrm{i}) = \frac{1}{\mathrm{A}_\mathrm{i}} \tag{2.8}$$

Where $\Sigma(\mathbf{r}_\mathrm{i})$ is the surface density at the position of the ith galaxy and A_i is the area of its Voronoi cell.

In order to assimilate the role of galaxy weights, we tried two different approaches. In the first approach, we modified the metric used for the definition of distance between the points in the z-slice plane and galaxies. This was done by dividing the Euclidean metric by the weight of each galaxy. Implementing this approach to the data was not successful and resulted in unrealistically high-density values for the majority of galaxies (with small weights) located in sparsely populated regions. Thus, we alternatively use a Monte-Carlo acceptance−rejection process in order to take the role of weights into consideration. The steps are as follows:

1. For each galaxy with its corresponding weight w_i, we generate a random number R_i between the minimum and maximum weight values in each z-slice.

2. If $w_i > R_i$, we accept the galaxy (with its associated weight w_i) in the density estimation procedure.

3. We estimate the surface density for the accepted galaxies using a simple Voronoi tessellation method. This surface density is evaluated at the position of accepted galaxies only.

4. We interpolate[1] the estimated densities into the points of a grid ($\mathbf{r}$) (the grid resolution is 50 kpc at each redshift) constructed on the z-slice plane. This gives us a Monte-Carlo estimated surface density field $\tilde{\Sigma}(\mathbf{r})$.

5. We repeat this procedure N times and take the mean of all the Monte-Carlo density fields as the actual density field $\Sigma(\mathbf{r})$:

$$\Sigma(\mathbf{r}) = \frac{1}{\mathrm{N}} \sum_{\mathrm{m}=1}^{\mathrm{N}} \tilde{\Sigma}_{\mathrm{m}}(\mathbf{r}) \tag{2.9}$$

Finally, the local surface density of each galaxy is then estimated as that of its closest point in the grid constructed over the z-slice plane. To save computational time, we use N=10 in step 5. Figure 2.2 (e) shows an example of the surface density field at z=0.92, estimated with the weighted Voronoi tessellation algorithm. Note the large dynamical range of overdensities. Unlike the nearest neighbor, Voronoi tessellation is scale-independent and is able to span a wide range of physical lengths. In addition, it does not make any assumptions about the geometry and morphology of the structures in the density field. This characteristic makes it superior to adaptive kernel and NN methods.

2.4.4 Weighted Delaunay Triangulation Estimator

This method relies on segmenting the z-slice plane into triangles whose vertices are defined by the position of galaxies in the z-slice plane. For each triangle, these three vertices (position of galaxies) are selected such that their circumcircle does not encompass any other galaxy. In this method, each galaxy is eventually surrounded by a series of neighboring triangles whose overall area tend to be smaller in denser regions (Schaap and van de Weygaert, 2000; Platen et al., 2011). For the ith galaxy surrounded by m neighboring triangles,

[1] We use the natural neighbor interpolation developed by Sibson.

the estimated surface density is expressed as the inverse of the sum of the areas of its neighboring triangles:

$$\Sigma(\mathbf{r}_\mathrm{i}) = \frac{1}{\sum_{\mathrm{n}=1}^{\mathrm{m}} \mathrm{a}_\mathrm{n}} \tag{2.10}$$

where $\Sigma(\mathbf{r}_\mathrm{i})$ is the surface density at the position of the ith galaxy and a_n is the area of the nth triangle neighboring the ith galaxy.

In order to take the weight of galaxies into account, we utilize a Monte-Carlo acceptance-rejection approach explained in Section 2.4.3. Figure 2.2 (f) shows an example of the surface density field at z=0.92, estimated with the weighted Delaunay method. When compared with other estimation methods, this method overestimates the densities in very dense regions and the resulting density field is clumpier and contains much more substructures.

2.5 Simulations

In order to evaluate the performance of each surface density estimation method, we run two sets of simulations. The details are given in the following subsections.

2.5.1 Simulation 1

In the first set of simulations, we apply the surface density estimators to a sample of galaxies that was randomly drawn from some previously known surface density profiles (Scoville et al., 2007a). Since the simulated surface density values are known, we can directly compare them with the estimated surface densities that are predicted by each of our density estimators. Here, we make 30 different simulated structures. These structures are placed on an area similar to that of the COSMOS field.

The simulated structures and the field contain 5000 galaxies at z=1, similar to the total number of observed galaxies at that redshift in the COSMOS field. For simplicity, we assume that all have the same weight (w=1). 2222 of these galaxies are randomly distributed on an area covering 1.5×1.2 deg^2. The rest of them are drawn randomly from a series of Gaussian profiles. These Gaussian structures have a variety of sizes (0.1-2 Mpc)

(a)

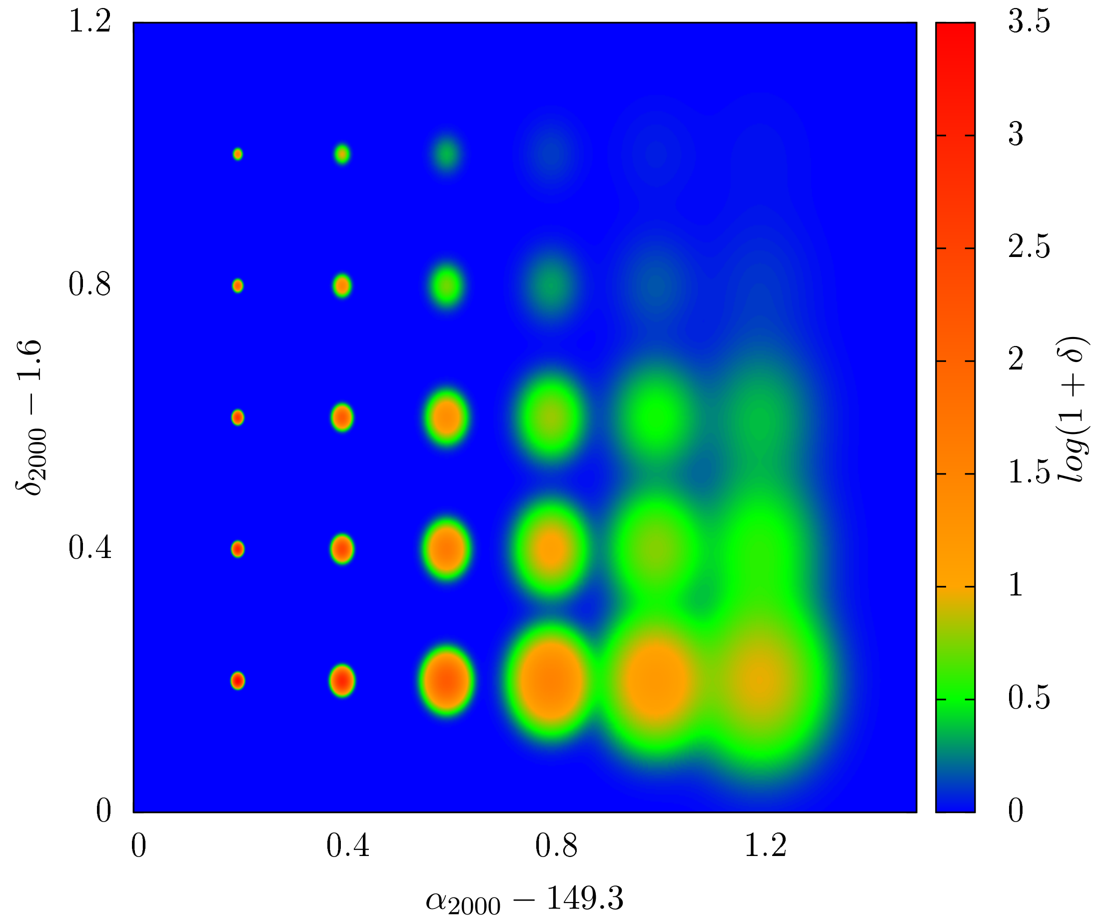

Figure 2.3: (a) Overdensity map for simulated structures. Here, we make 30 different simulated structures placed on a constant background. They are assumed to be located at z=1 and cover an area similar to that of the COSMOS field. The structures have Gaussian profiles with a variety of sizes (0.1-2 Mpc) and the number of galaxies in these structures ranges from 3 to 300. (b) Distribution of galaxies randomly drawn from the structures. The simulated structures and the field contain 5000 galaxies. Almost half of them (2778) belong to the structures while the rest are randomly distributed on an area covering 1.5×1.2 deg^2, which serve like the field. (c) Predicted overdensity maps using the adaptive kernel, (d) tenth NN, (e) fifth NN, (f) Voronoi tessellation and, (g) Delaunay triangulation. All these methods perform relatively well when compared to the expected density field, with the adaptive kernel and Voronoi tessellation performing relatively better than other estimators.

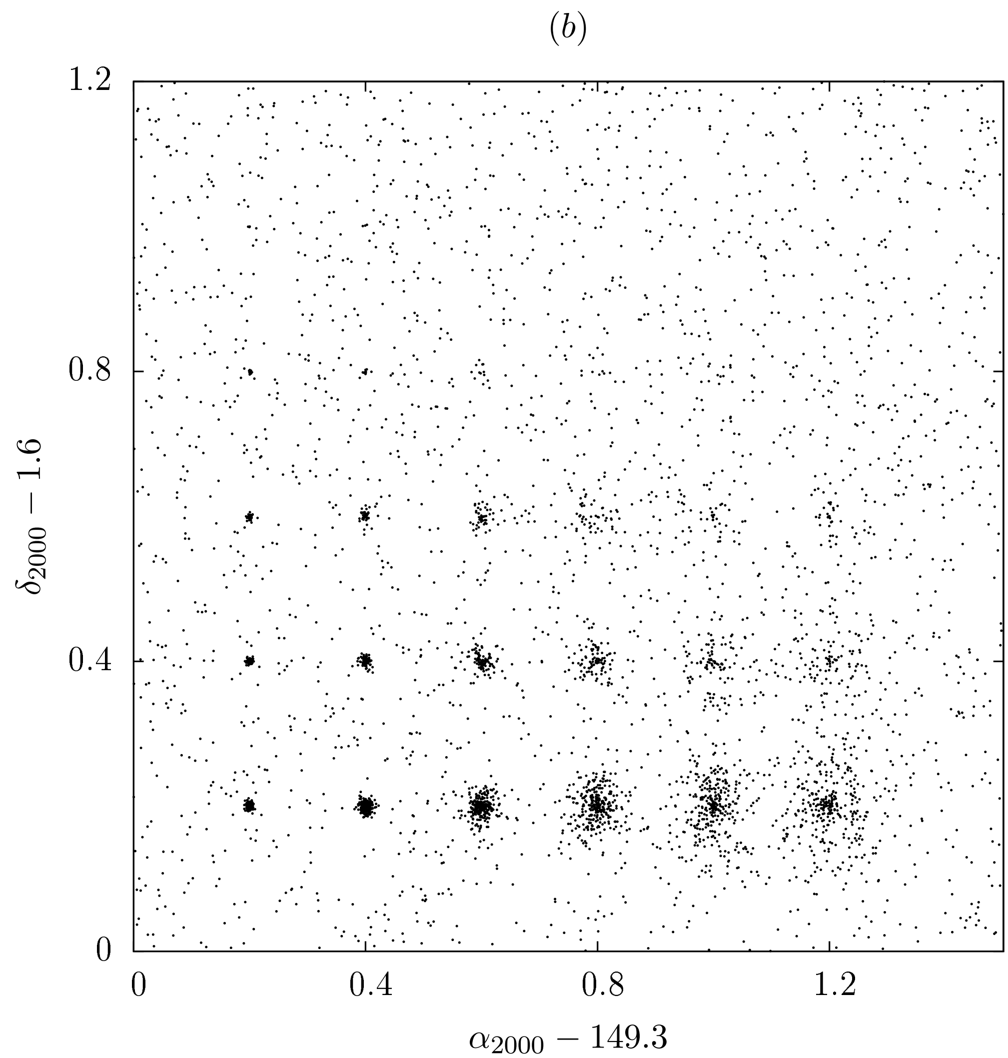

Figure 2.3: cont. (b)

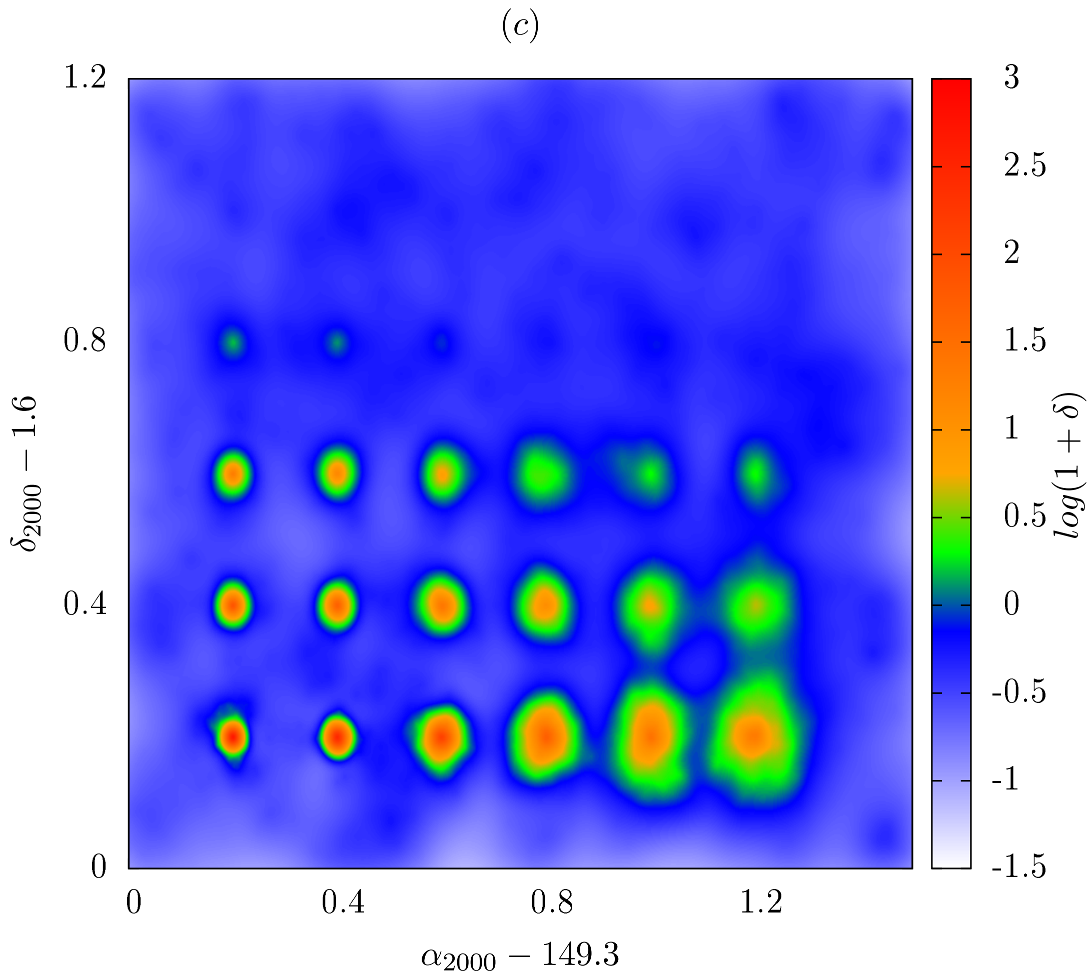

Figure 2.3: cont. (c)

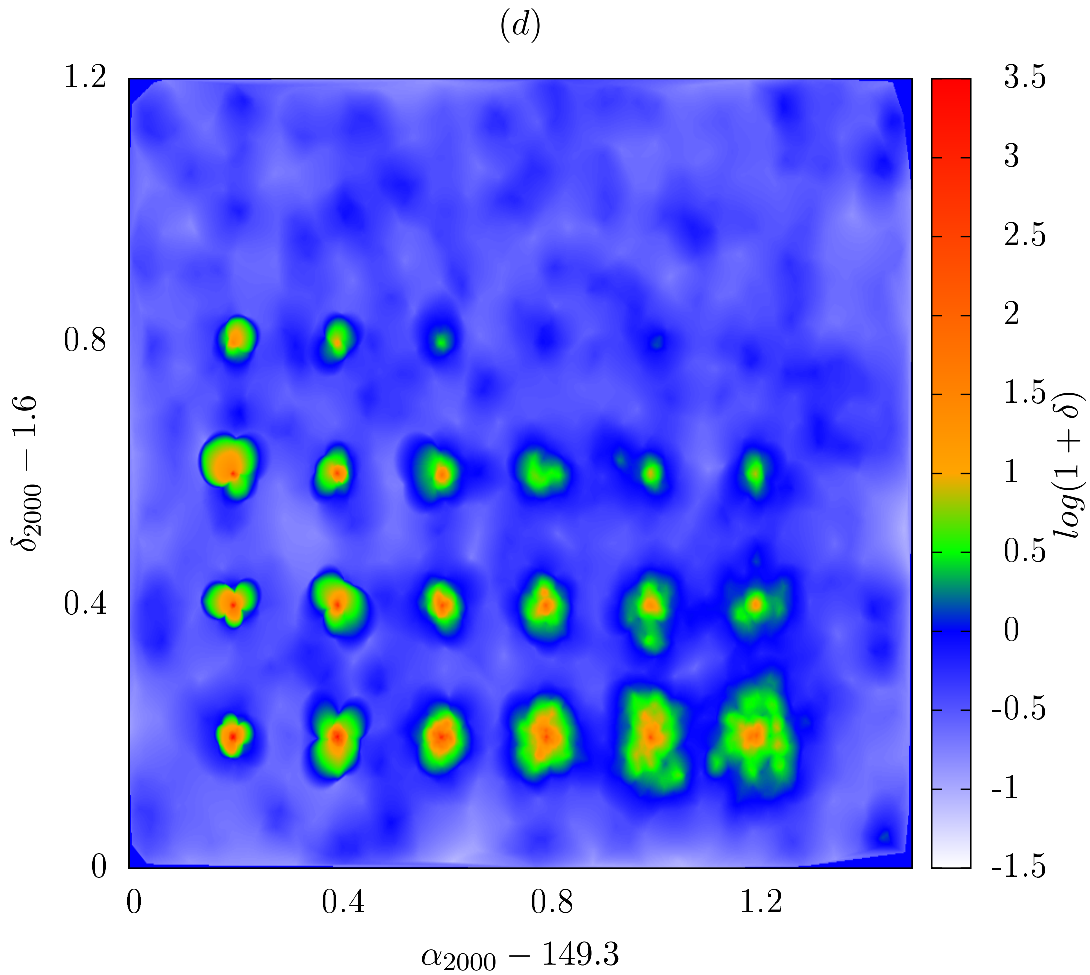

Figure 2.3: cont. (d)

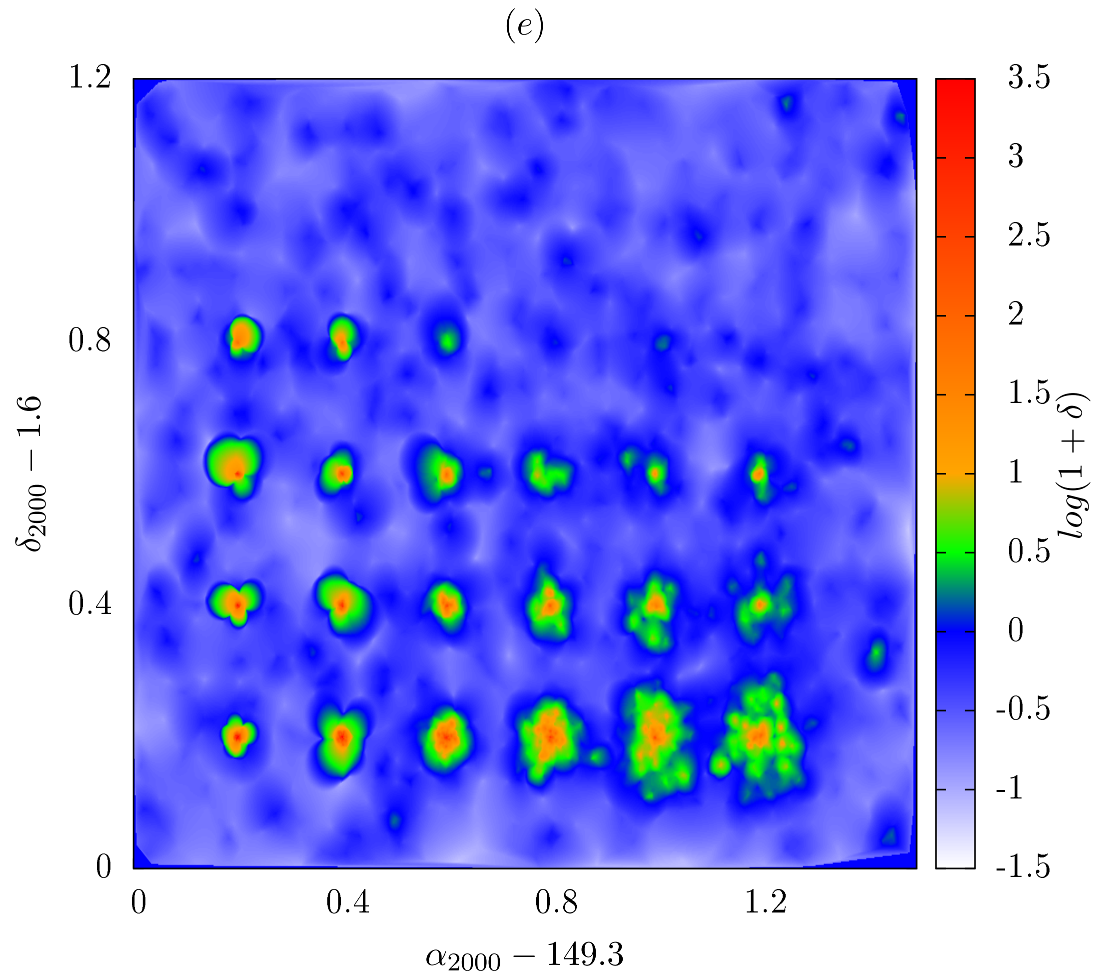

Figure 2.3: cont. (e)

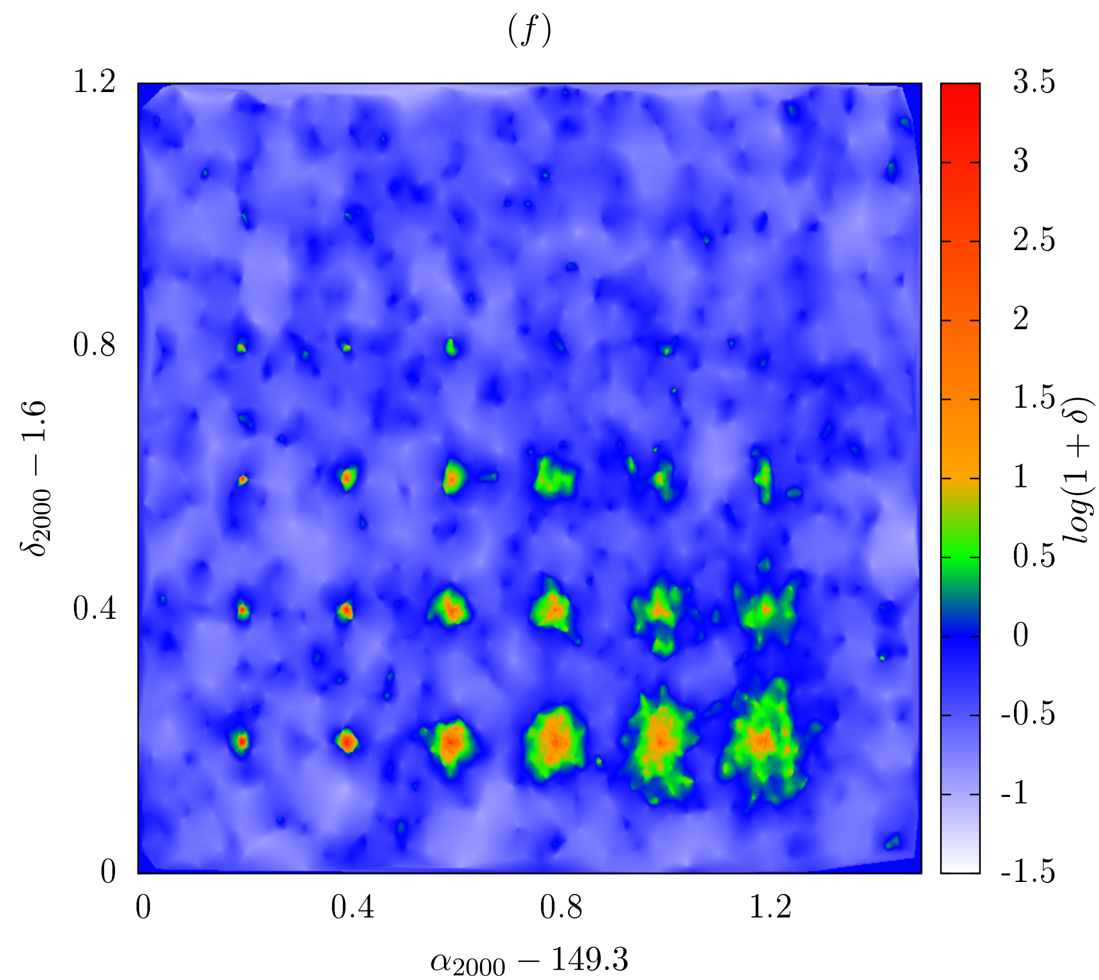

Figure 2.3: cont. (f)

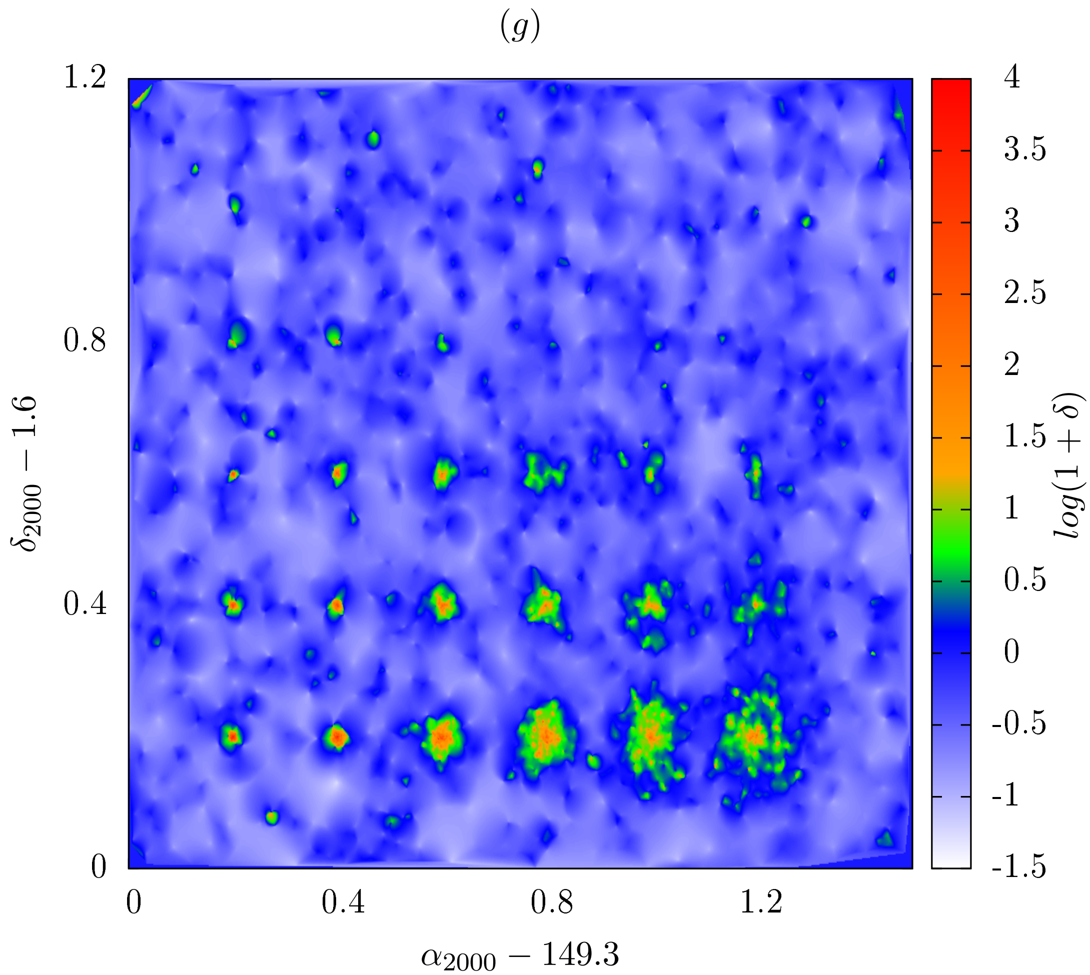

Figure 2.3: cont. (g)

and the number of galaxies in these structures ranges from 3 to 300. The properties of these structures are shown in Table 2.1. We apply the density field estimation methods explained in Section 2.4 to the simulated galaxies to explore how well they can predict the input density field. Figure 2.3 shows the density field of the simulated structures, the distribution of galaxies randomly drawn from the structures, and the predicted density fields using different estimation methods. All these methods perform relatively well when compared to the expected density field. We stress that some of the difference between the expected and predicted density fields is caused by the shot noise, which becomes specifically important when the number of galaxies in simulated structures is small and the width of the profile is large. In order to quantify the performance of different density estimation methods, we define the mean squared error (MSE) as:

$$MSE = \frac{1}{N}\sum_{i=1}^{N}(\Delta_i^{sim} - \Delta_i)^2 \tag{2.11}$$

where N is the total number of generated galaxies, Δ_i^{sim}=log(1+δ_i^{sim}) is the logarithm of the overdensity of the ith galaxy in the simulation, and Δ_i is a similar quantity, predicted by one of the density estimator methods. A smaller value of MSE shows a higher similarity between the simulation and predicted density fields, and is a measure of the performance of the estimation methods in predicting the true value of the density field. The MSE values are tabulated in Table 2.2. It is clear that the adaptive kernel, Voronoi tessellation, and NN_{10} methods outperform the NN_5 and Delaunay triangulation algorithms.

We note that due to the catastrophic failure in estimating the photometric redshifts, the actual discrepancy between the simulated and predicted density fields can be higher.However, the catastrophic failure fraction (defined as the fraction of galaxies that satisfy $|z_{phot} - z_{spec}|/(1+z_{spec})>0.15$) for K_s <24 galaxies in the COSMOS field) is relatively small and estimated to be $< 1\%$ for bright sources, reaching $\lesssim$10% for fainter galaxies (Ilbert et al., 2013). We redo the simulation taking into account the catastrophic failure and estimate the new MSE statistics. We assume that 10% of the simulated galaxies are affected by the catastrophic failure (i.e., they do not actually belong to the simulated z-slice) and they are randomly distributed over the area containing the simulated structures (random distribution is a fair assumption because the catastrophic failure mostly affects fainter galaxies, which tend to be less clustered). This means that the actual background for the overdensity map of the simulated structures should have a smaller value. With the new simulation, all density field estimators perform almost equally worse with catastrophic failure (as predicted). The MSE statistics are increased by $\sim$0.01$-$0.02 ($\sim$3%$-$6%) for all density estimators. In this work, we do not correct for the catastrophic failure, but we highlight that it has a small effect and that the trends are not affected much by it.

2.5.2 Simulation 2

In the previous simulations, although the "true" density values are known (which makes the comparison with the predicted densities feasible), the complex geometry of the real astronomical density fields and their diverse dynamical range are not fully considered; i.e, the simulated density profiles have simple mathematical shapes, whereas the real astronomical data consist of an irregular web of filaments, voids, walls, and clusters with a variety of physical scales and geometries. Furthermore, the previous simulation greatly suffers from the shot noise, especially when the number of randomly drawn galaxies is small and/or the known density profiles have broad, close-to-the-field shapes. In order to consider the complexity of the cosmic web in the analysis, one can use the numerical simulations that produce mock galaxy distributions, which resemble the real density maps. Since the "true" density field is unknown in these quasi-real simulations, we should rely on an estimator to have an initial guess of the density field. In the second set of simulations, we make a sample of galaxies that resemble the true distribution of galaxies in the COSMOS. This is performed using a Monte-Carlo acceptance$-$rejection approach, which is a method similar to the one explained in Section 2.4.4, taking the following steps:

1. For each z-slice, we estimate the surface density field for the real data using one of the density estimators explained in Section 2.4. For simplicity, we assume that all

Table 2.1: Properties of Simulated Structures

Structure	α_{2000} Right Ascension(deg)	δ_{2000} Declination(deg)	σ Mpc	N
1	149.5	1.8	0.1	300
2	149.7	1.8	0.2	300
3	149.9	1.8	0.5	300
4	150.1	1.8	1.0	300
5	150.3	1.8	1.5	300
6	150.5	1.8	2.0	300
7	149.5	2.0	0.1	100
8	149.7	2.0	0.2	100
9	149.9	2.0	0.5	100
10	150.1	2.0	1.0	100
11	150.3	2.0	1.5	100
12	150.5	2.0	2.0	100
13	149.5	2.2	0.1	50
14	149.7	2.2	0.2	50
15	149.9	2.2	0.5	50
16	150.1	2.2	1.0	50
17	150.3	2.2	1.5	50
18	150.5	2.2	2.0	50
19	149.5	2.4	0.1	10
20	149.7	2.4	0.2	10
21	149.9	2.4	0.5	10
22	150.1	2.4	1.0	10
23	150.3	2.4	1.5	10
24	150.5	2.4	2.0	10
25	149.5	2.6	0.1	3
26	149.7	2.6	0.2	3
27	149.9	2.6	0.5	3
28	150.1	2.6	1.0	3
29	150.3	2.6	1.5	3
30	150.5	2.6	2.0	3

The simulated structures have a Gaussian profile with a variety of sizes and number of galaxies. α_{2000} is the right ascension of the center of structure, δ_{2000} is the declination of the center of structure, σ is the sigma of the Gaussian profile, and N is the number of galaxies randomly drawn from the Gaussian profile.

Table 2.2: Comparison Between the Simulation (Simulation 1) and Prediction

	Kernel	NN_{10}	NN_5	Voronoi	Delaunay
MSE	0.26	0.28	0.30	0.27	0.34

We use the MSE measure defined in Section 2.5.1 to compare the simulated density field (simulation 1) with the one predicted by different estimators. A smaller value of MSE indicates a better performance.

Table 2.3: Comparison Between the Simulation (Simulation 2) and Prediction

	Kernel	NN_{10}	NN_5	Voronoi	Delaunay
MSE	0.003	0.035	0.062	0.025	0.158

We use the MSE measure defined in Section 2.5.1 to compare the simulated density field (simulation 2) with the one predicted by different estimators. A smaller value of MSE indicates a better performance.

galaxies in the z-slice have the same weight (w=1). The estimated density field gives us a first order approximation of the shape of the true density field.

2. For each z-slice, we randomly select a position, $(x,y)_{random}$, in the area covering the data and assign a random number, Σ_{random}, between the minimum and the maximum density values in that z-slice to the point $(x,y)_{random}$. We also report the density value at this random position from step 1 and call it $\hat{\Sigma}$.

3. If $\hat{\Sigma} > \Sigma_{random}$, we accept the point $(x,y)_{random}$ as one of the points in the simulated data set and consider $\hat{\Sigma}$ as its true density.

4. For each z-slice, we repeat steps 1-3 until we have a simulated data set with the same number of galaxies as the actual data set.

Given the above steps, for each z-slice, we now have a sample of simulated galaxies with *known* surface densities. The distribution of these galaxies resembles the actual data in the COSMOS. We apply our surface density estimation methods to the simulated data with known densities and compare their expected and predicted densities. Although we now consider the complexity of the real galaxy distribution, these simulations rely on an initial estimator to determine the rough shape of the density field (i.e., step 1). We therefore use the adaptive kernel density estimator in order to perform the first step of the simulation. [2] Table 2.3 shows the performance of different surface density estimators when compared with the new set of simulations. Here, we use the MSE measure introduced in Section 2.5.1 to compare the results. According to the new simulations and the results of the MSE statistics, the adaptive kernel, Voronoi tessellation, and NN_{10} methods perform better in estimating the simulated density field. In both sets of simulations, the NN_5 and (especially) the Delaunay tessellation algorithms seem to fall behind compared to other estimators.

2.6 Comparison

Using two sets of simulations, we showed that all density estimation methods perform relatively well in estimating the density field. However, the adaptive kernel, Voronoi tessellation, and NN_{10} are found to outperformed the others. In this section, we compare different estimation methods regardless of their performance. Due to the edge effect, the surface density of the galaxies located near the edge of the survey and masked areas are unrealistically underestimated. In order to take this into account, we limit the comparison to galaxies that are more than 1 Mpc (physical) away from the edge of survey and large masked areas. Figure 2.4 shows a comparison between different estimation methods using 176,893 galaxies at $0.1< z <3.2$. There is a relatively good agreement between different estimation methods over $\sim$2 orders of magnitude in overdensity values. However, when we compare the Delaunay triangulation method with the rest, it overestimates the density values in dense regions while underestimating the density in sparsely populated regions (field) when compared with adaptive kernel and NN_{10} methods.

Each surface density estimator method has its own advantages and disadvantages, as explored below:

[2] This results in a bias in favor of the performance of the adaptive kernel density estimator when we compare it with the simulations. However, we used other estimators as well to initiate the simulation and found that the adaptive kernel estimator has an overall relatively good performance in all these simulations.

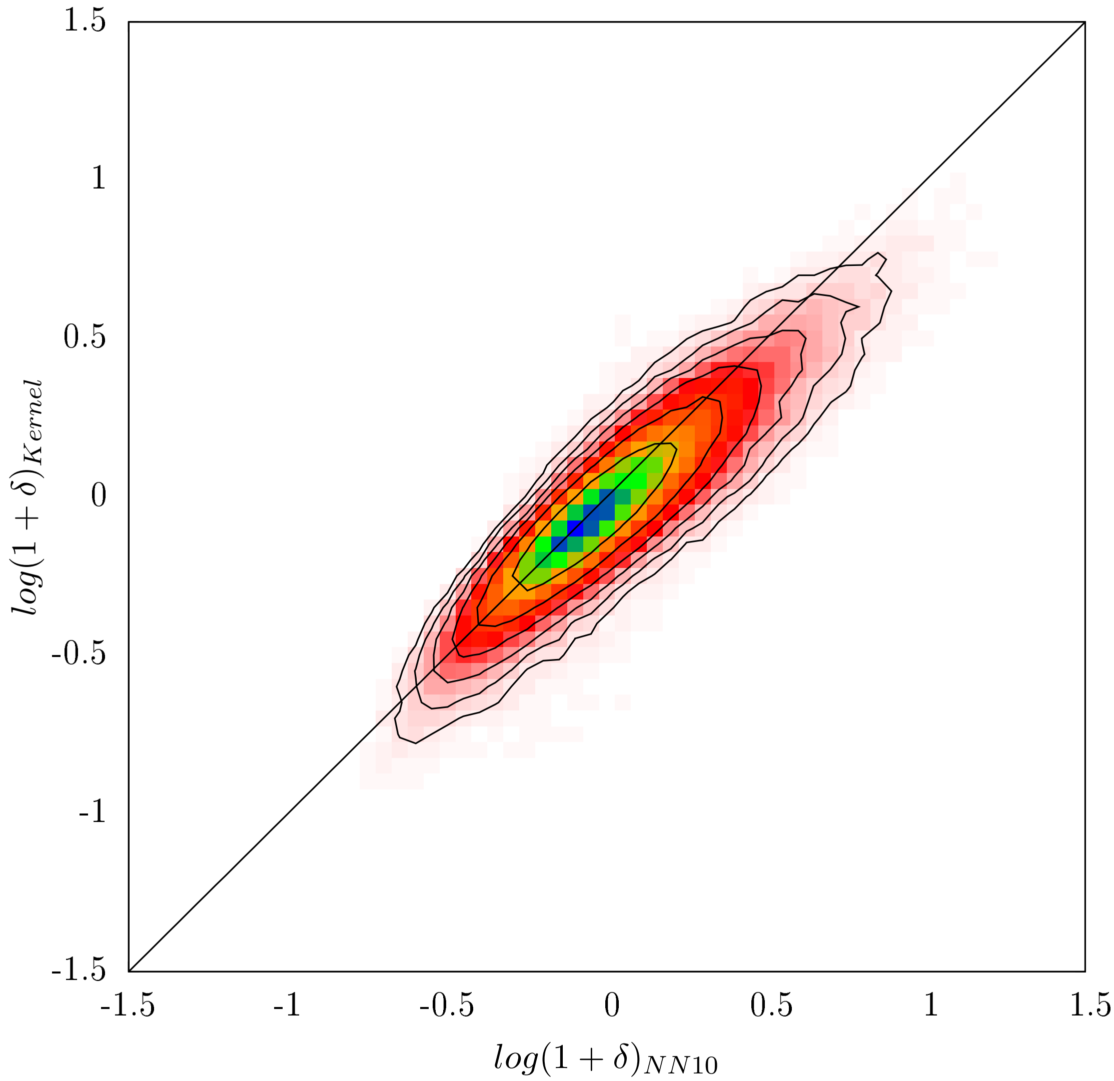

Figure 2.4: Comparison between different estimation methods using 176,893 galaxies at 0.1$<z<$3.2. In order to minimize the edge effect, we limit the comparison to galaxies that are 1 Mpc away from the edge of the field and large masked regions. There is a good agreement between different estimation methods over ∼2 orders of magnitude in overdensity values. However, when we compare the Delaunay triangulation method with the rest, it overestimates the density values in dense regions while underestimating the density in sparsely populated areas.

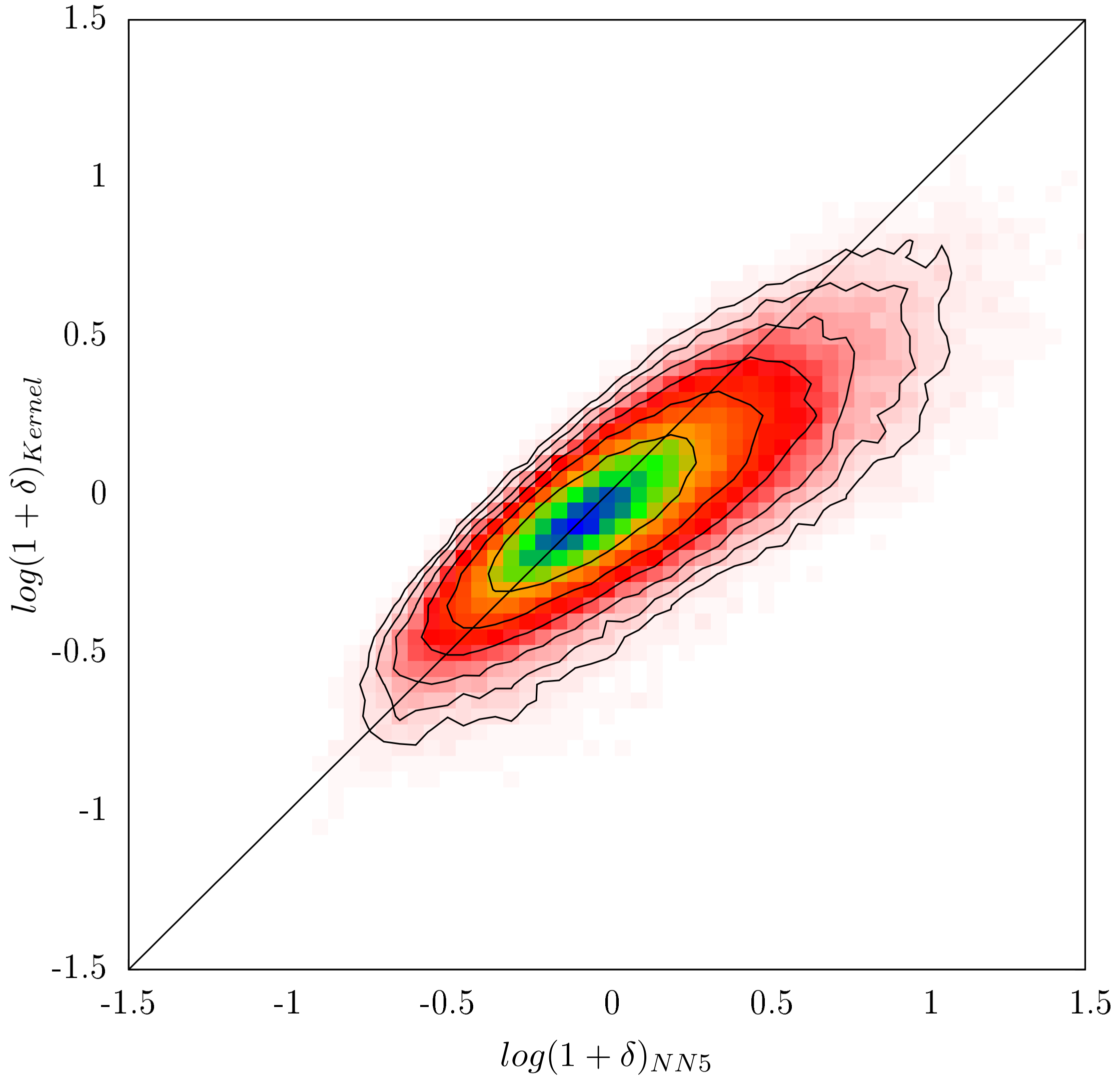

Figure 2.4: cont. (Kernel-NN_5)

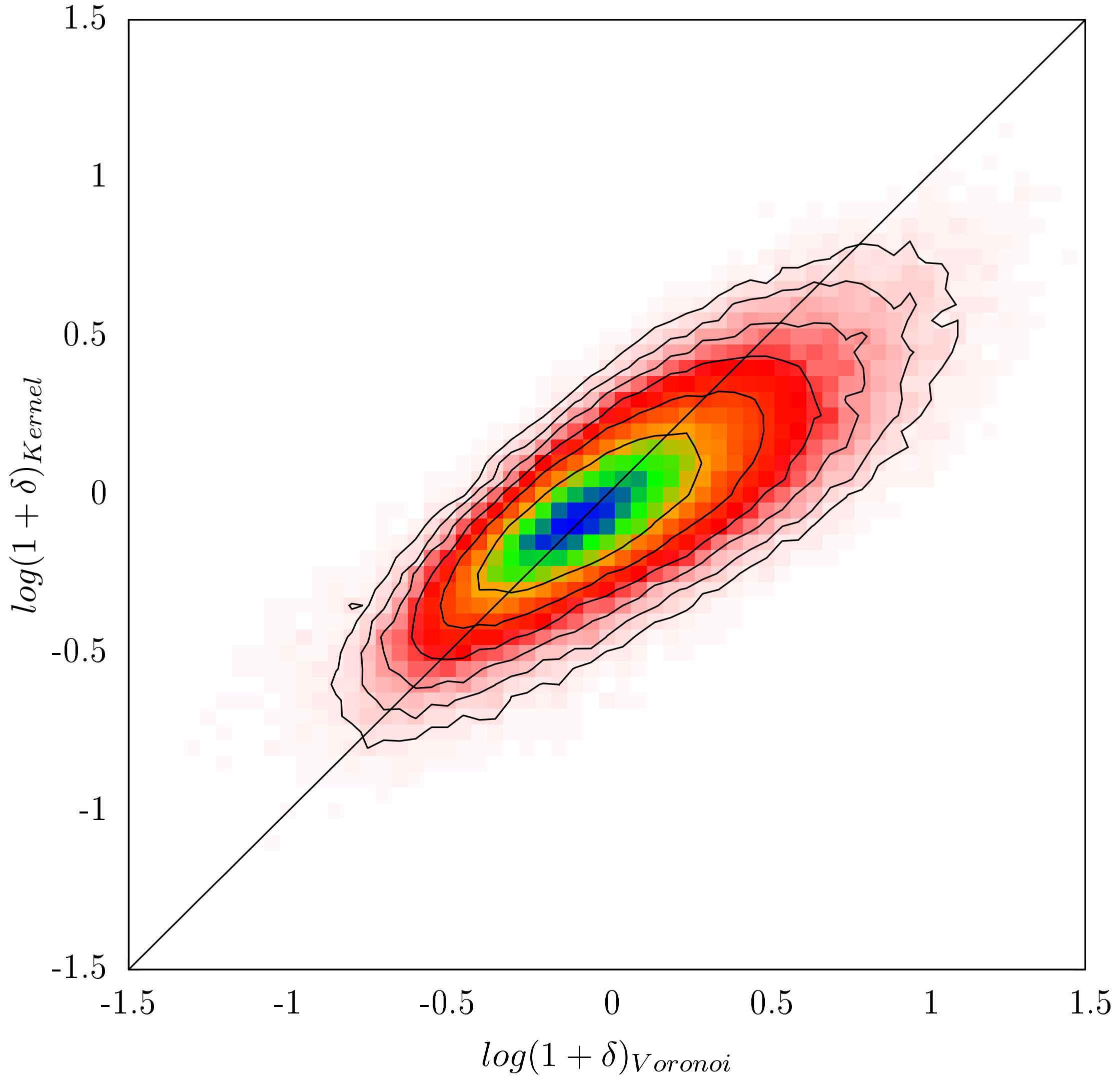

Figure 2.4: cont. (Kernel-Voronoi)

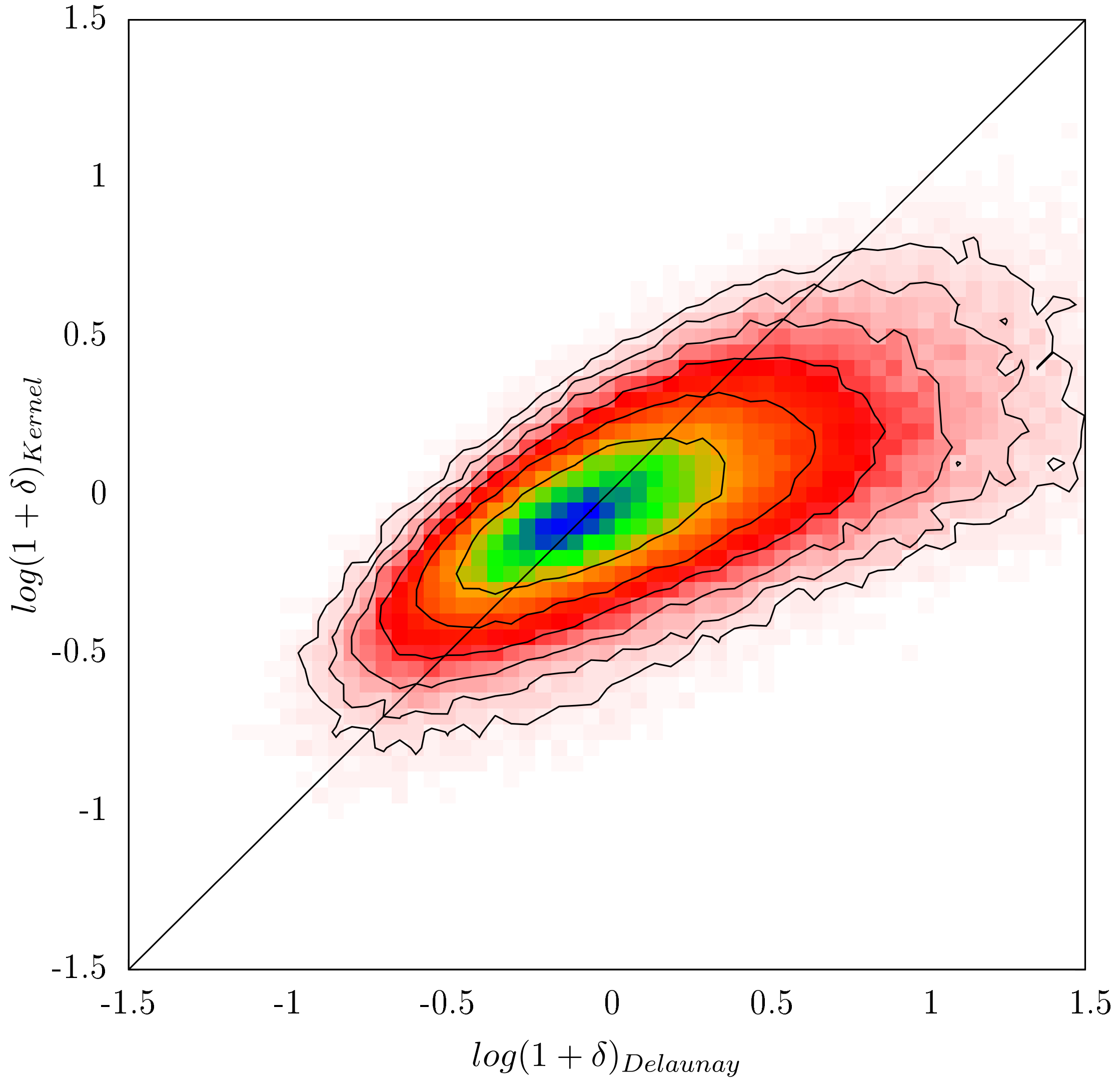

Figure 2.4: cont. (Kernel-Delaunay)

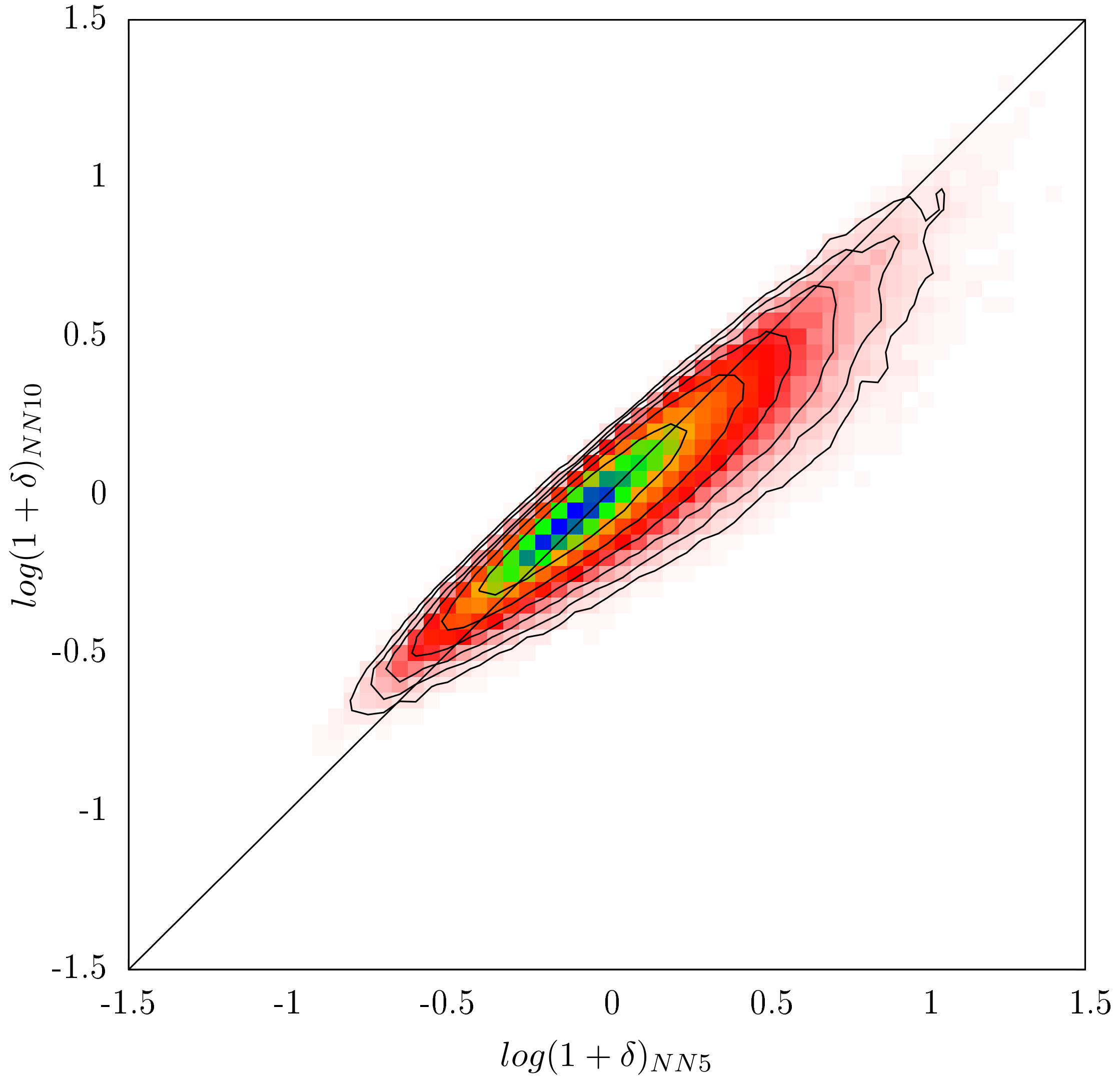

Figure 2.4: cont. (NN_{10}-NN_5)

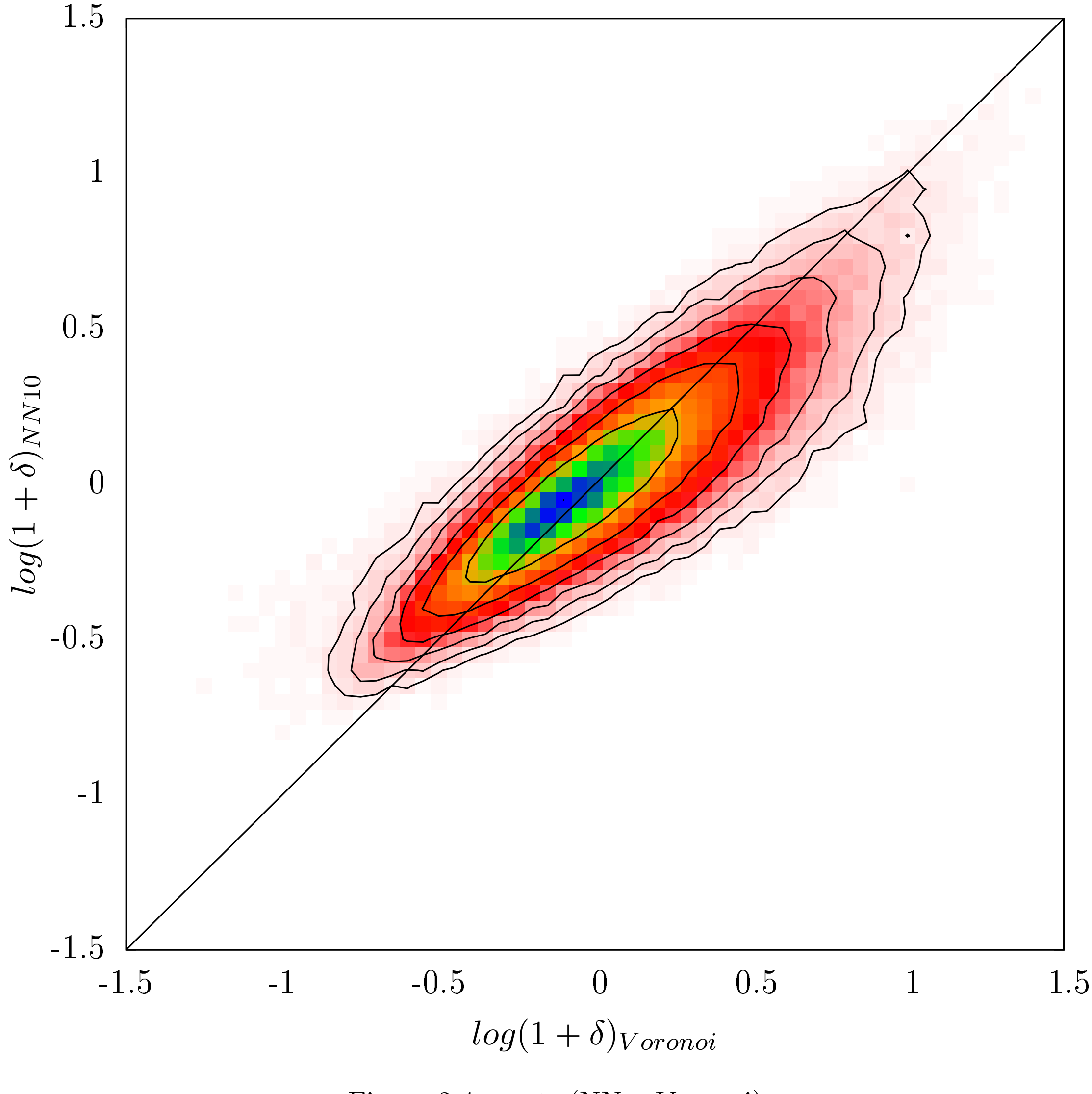

Figure 2.4: cont. (NN_{10}-Voronoi)

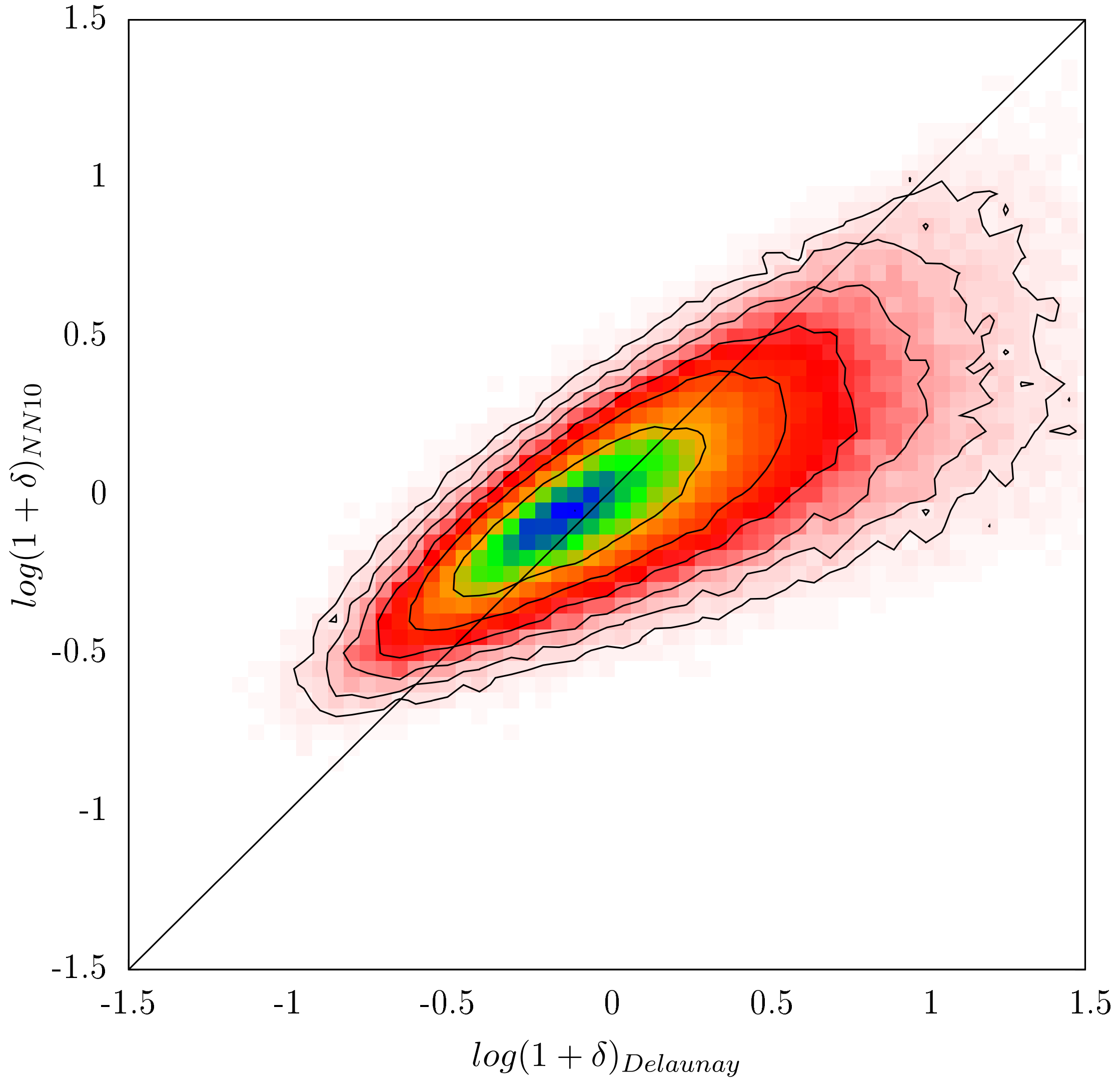

Figure 2.4: cont. (NN_{10}-Delaunay)

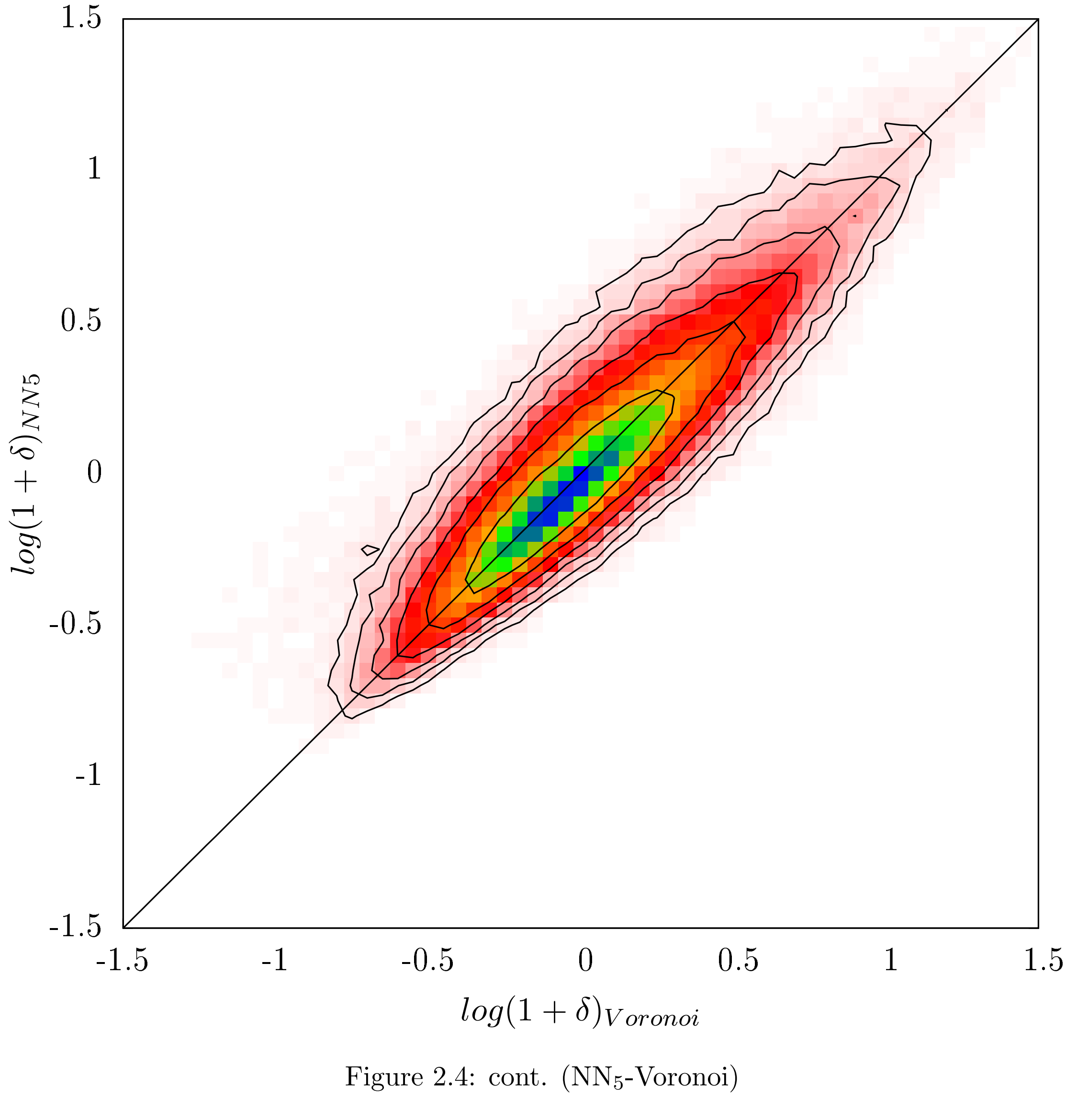

Figure 2.4: cont. (NN_5-Voronoi)

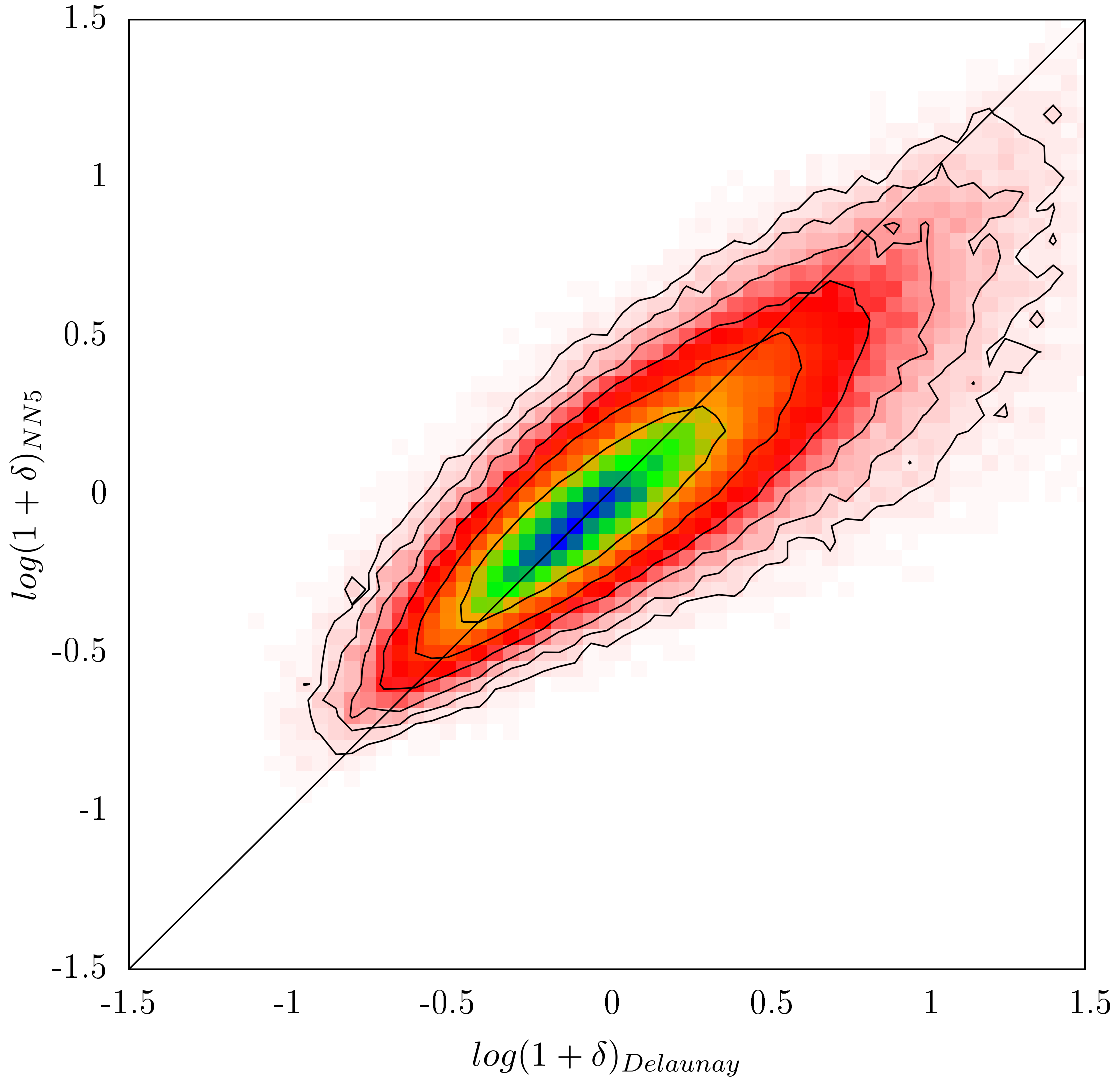

Figure 2.4: cont. (NN_5-Delaunay)

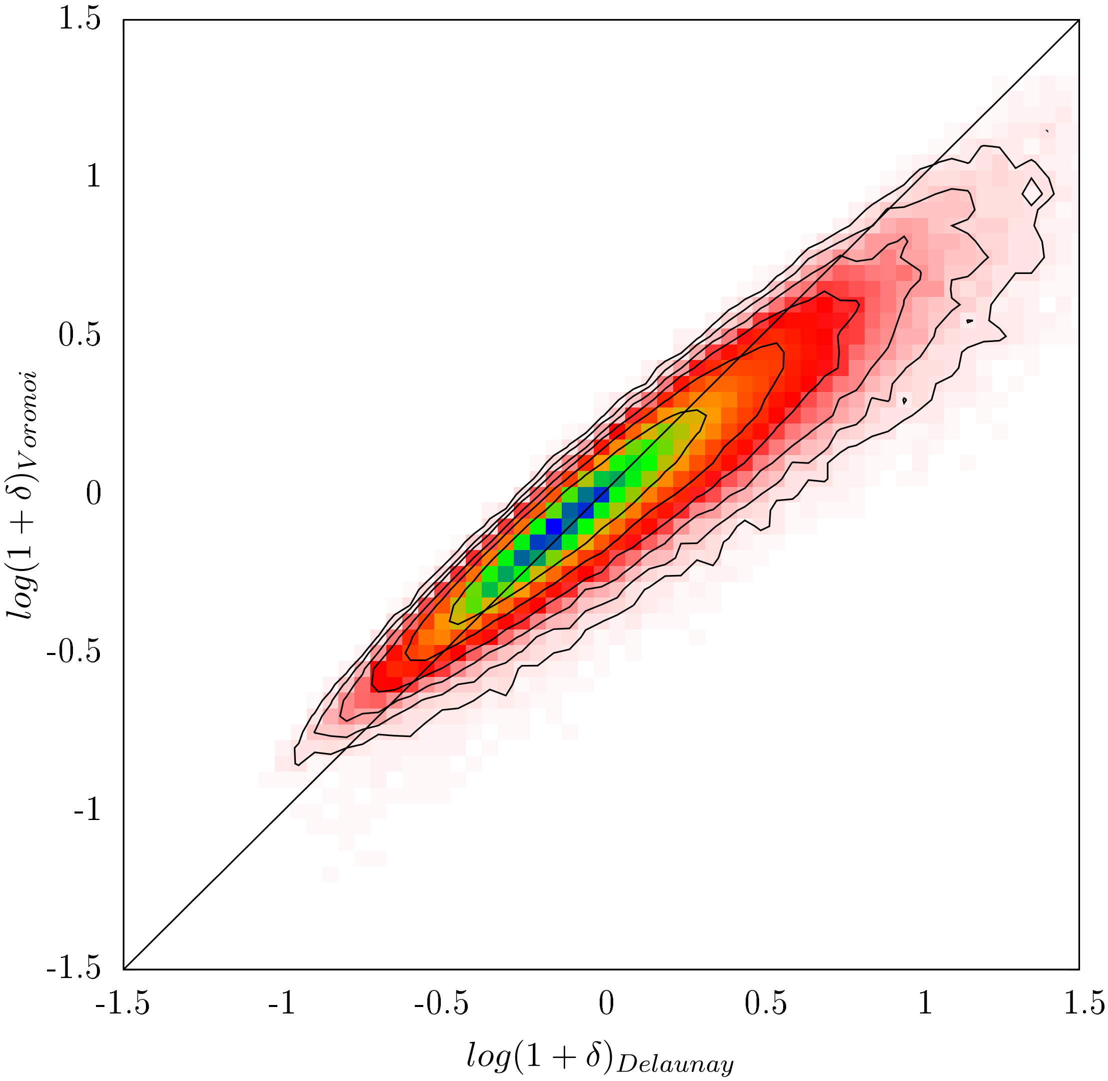

Figure 2.4: cont. (Voronoi-Delaunay)

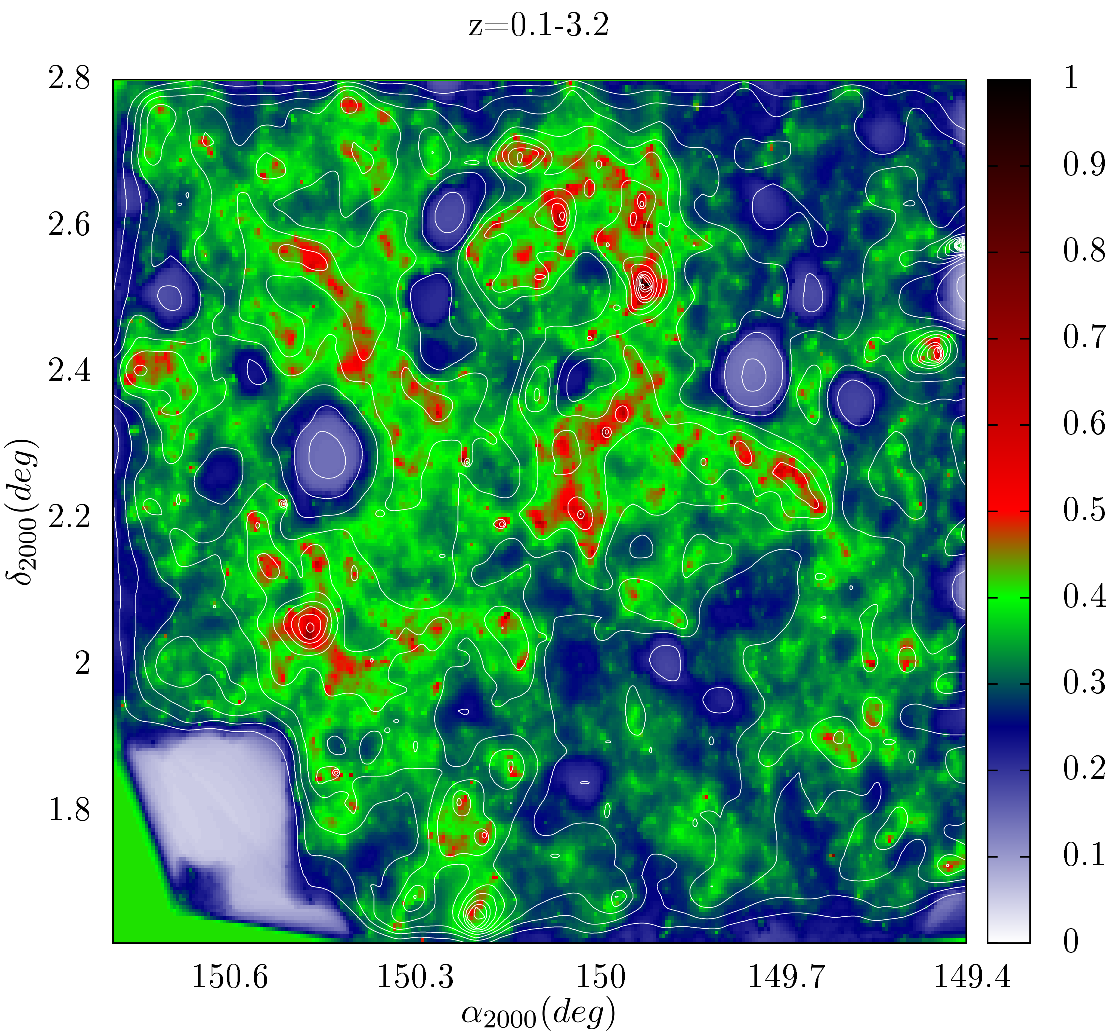

Figure 2.5: Projected overdensity map in the whole COSMOS field at $0.1 < z < 3.2$, using the weighted Voronoi tessellation method. In constructing this, the overdensity maps from all the z-slices between z=0.1 and z=3.2 are stacked and normalized to the peak. We compare it with the stacked overdensity map from Voronoi-based algorithm of Scoville et al. (2013). The contours used to demonstrate the map from Scoville et al. (2013) are at levels 0.2−1 with 0.05 spacing between them. There is a very good agreement between Scoville et al. (2013) and our work. We also find a relatively good agreement between the denser regions in our work and the position of X-ray clusters/groups (Finoguenov et al., 2007; George et al., 2011), as well as the projected mass map form the weak lensing analysis of Massey et al. (2007) in the COSMOS.

1. Adaptive Kernel: we smooth the density field with a suitable kernel function, so this method is less affected by the shot noise and possible random clustering of foreground and background sources. Calculation of the global kernel width (h) is motivated based on some physical scales (e.g., the typical size of galaxy clusters and groups), which makes it suitable for practical observational situations. We can easily add weights to the estimator by multiplying the kernel function with a proper weight. This method conserves the total number of galaxies (i.e, the integral of the surface density field over the whole area yields the total number of galaxies). However, the selection of the appropriate kernel size is a serious problem, because a small kernel size tends to overestimate the sparsely populated regions in the density field whereas a large kernel size washes out real features. This is partly overcome by adaptively changing the kernel width, but at the expense of increasing the computational time by adding an extra step to initially estimate the density field at the position of galaxies. Because we estimate the surface density at the positions of a grid, an intermediate interpolation is required to assign the density values from the grid points to the position of the galaxies. It is also computationally expensive in its adaptive format as it requires extra steps to determine the local adaptive kernel width.

2. k-NN: it is by far the easiest method to implement and the fastest to perform computationally. It estimates the surface density directly at the position of galaxies, which does not require any interpolation. Adding weights to this method is readily done. However, its performance strongly depends on the number of neighbors considered in the analysis (k). A small value of k results in a spiky density field that makes it vulnerable to unrealistic density values due to Poisson noise and random clustering of spatially uncorrelated galaxies. A large value of k is prone to underestimation of the surface density and oversmoothing the details of galaxy distribution. The sum of the area assigned to each galaxy is not equal to the total area of survey. It has also been shown that its integral over all areas diverges.

3. Voronoi Tessellation: this method covers a wide dynamical range in densities and is able to estimate densities in a broad range, from the dense core of clusters to sparse regions devoid of galaxies. It is a non-parametric and scale-independent method that makes no prior assumption about the shape of the density field. We directly evaluate the surface density at the position of the galaxies. However, we cannot assign closed Voronoi areas to galaxies near the edge of the field. Adding weights to this method is not straightforward. Here, we used a Monte-Carlo method to take the role of weights into consideration. However, this comes at the expense of a computationally expensive process, by making several Monte-Carlo samples. Apart from the computational time, it is a robust estimator.

4. Delaunay Triangulation: in terms of advantages and disadvantages, it is very similar to the Voronoi tessellation method. However, we can assign a delaunay area to all galaxies in the sample, even those that are located at the edge of the field. Also in this method, the total area assigned to galaxies surpasses the area of the survey. Despite its similarity to the Voronoi tessellation, this method does not perform well compared to other estimation methods (at least for the COSMOS field).

Due to the good performance of the Voronoi tessellation method, its large dynamical range, scale independence, and no prior assumption it makes about the morphology of the structures, we use it to construct the density field in the COSMOS and compare the estimated density field with previous studies. Figure 2.5 shows the projected overdensity map in the whole COSMOS field at $0.1< z <3.2$, using the weighted Voronoi tessellation method. In constructing this, we stack the overdensity maps from all the z-slices between z=0.1 and z=3.2 and, normalize it to the peak of stacked overdensities. We compare it with the stacked overdensity map from Voronoi-based algorithm of Scoville et al. (2013). The contours used to demonstrate the map from Scoville et al. (2013) are at levels $0.2-1$ with 0.05 spacing between them. We see a very good agreement between Scoville et al. (2013) and our work. We also find a relatively good agreement between the denser regions in our work and the position of the X-ray clusters and groups (Finoguenov et al., 2007; George et al., 2011). When compared with the projected mass map form the weak lensing analysis of Massey et al. (2007) in the COSMOS field, our projected map agrees with that of Massey et al. (2007). We are able to recover all the massive structures in the weak lensing map. Our estimated density field is also consistent quantitatively with the density field of Kovač et al. (2010), who used zCOSMOS spectroscopic data out to $z \sim 1$, the optical galaxy groups of (Knobel et al., 2009, 2012) using the zCOSMOS data set, and the protocluster candidates of Chiang et al. (2014) at $1.6 < z < 3.1$ in the COSMOS field.

2.7 Cosmic Web Extraction

To identify and extract spatial structures such as filaments and clusters in the underlying galaxy distribution, we utilize the 2D version of the MMF algorithm developed by Aragón-Calvo et al. (2007). This algorithm is able to assign a filament and a cluster signal to each point in the surface density field based on the local geometry of the point in question. If the local geometry of a point in the density field has a greater resemblance to a thread-like structure (filament) than a circular-like feature (cluster), its filamentary signal surpasses its cluster signal. The local geometry of each point is calculated based on the signs and ratio of eigenvalues of the Hessian matrix $H(\mathbf{r})$ which is the second-order derivative of the surface density field:

$$H(\mathbf{r}) = \begin{bmatrix} \nabla_{xx}\Sigma(\mathbf{r}) & \nabla_{xy}\Sigma(\mathbf{r}) \\ \nabla_{yx}\Sigma(\mathbf{r}) & \nabla_{yy}\Sigma(\mathbf{r}) \end{bmatrix} \tag{2.12}$$

where ∇_{ij}s denote the second derivatives in the i and j directions. Since structures have a variety of physical sizes, this algorithm builds a scale-independent structure map by smoothing the surface density field over a range of physical scales and eventually selecting the greatest cluster and filament signal among all the various signal values at different physical scales. Here, we use a circularly symmetric Gaussian smoothing function with various physical scales in the range $\sim$0.125$-$1.5 Mpc. Ultimately, each point in the density

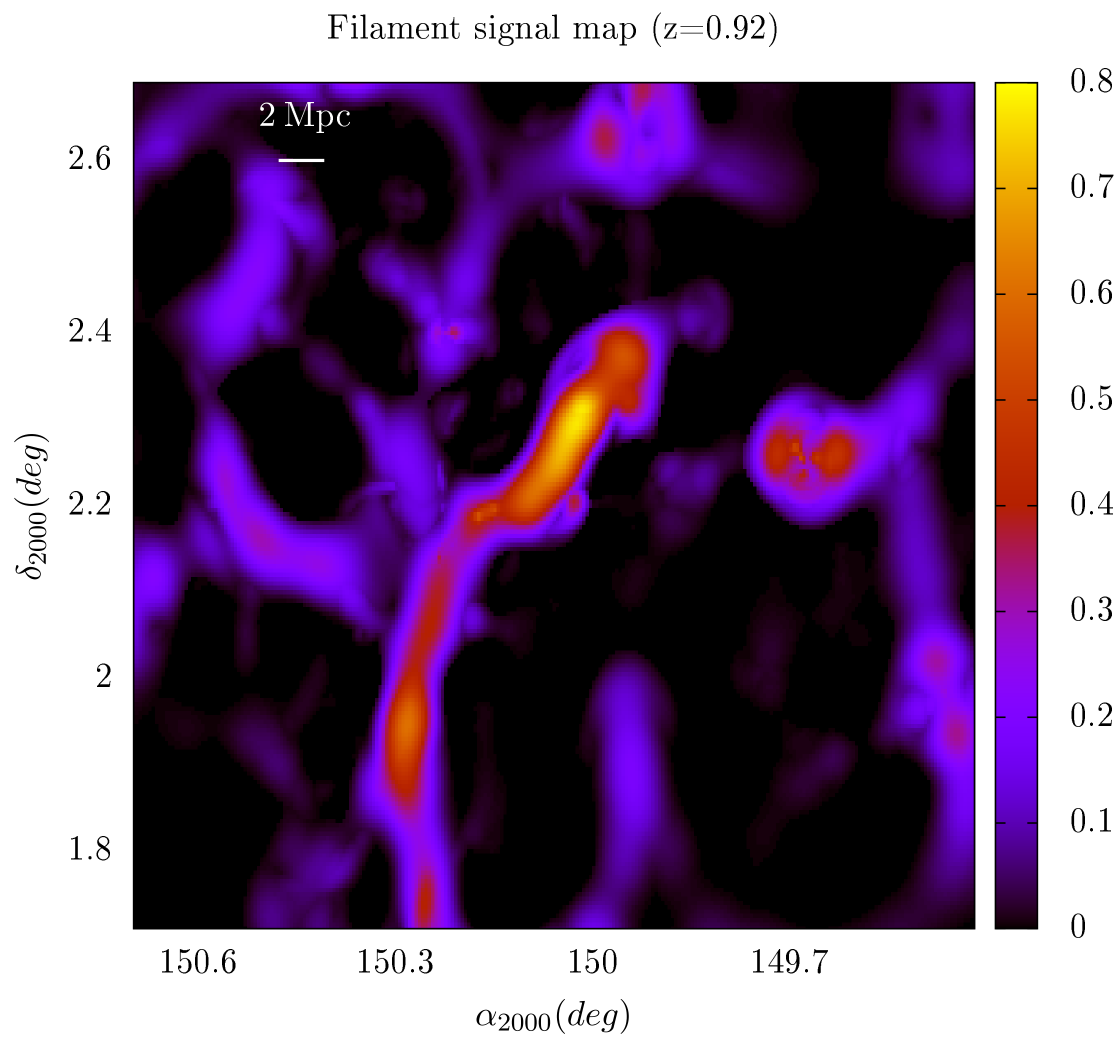

Figure 2.6: Filament signal map (top panel) and cluster signal map (bottom panel) for a z-slice located at z=0.92 in the COSMOS field. The signal maps are constructed using the 2D version of the MMF algorithm (Aragón-Calvo et al., 2007). Note the complex network of filaments and clusters.

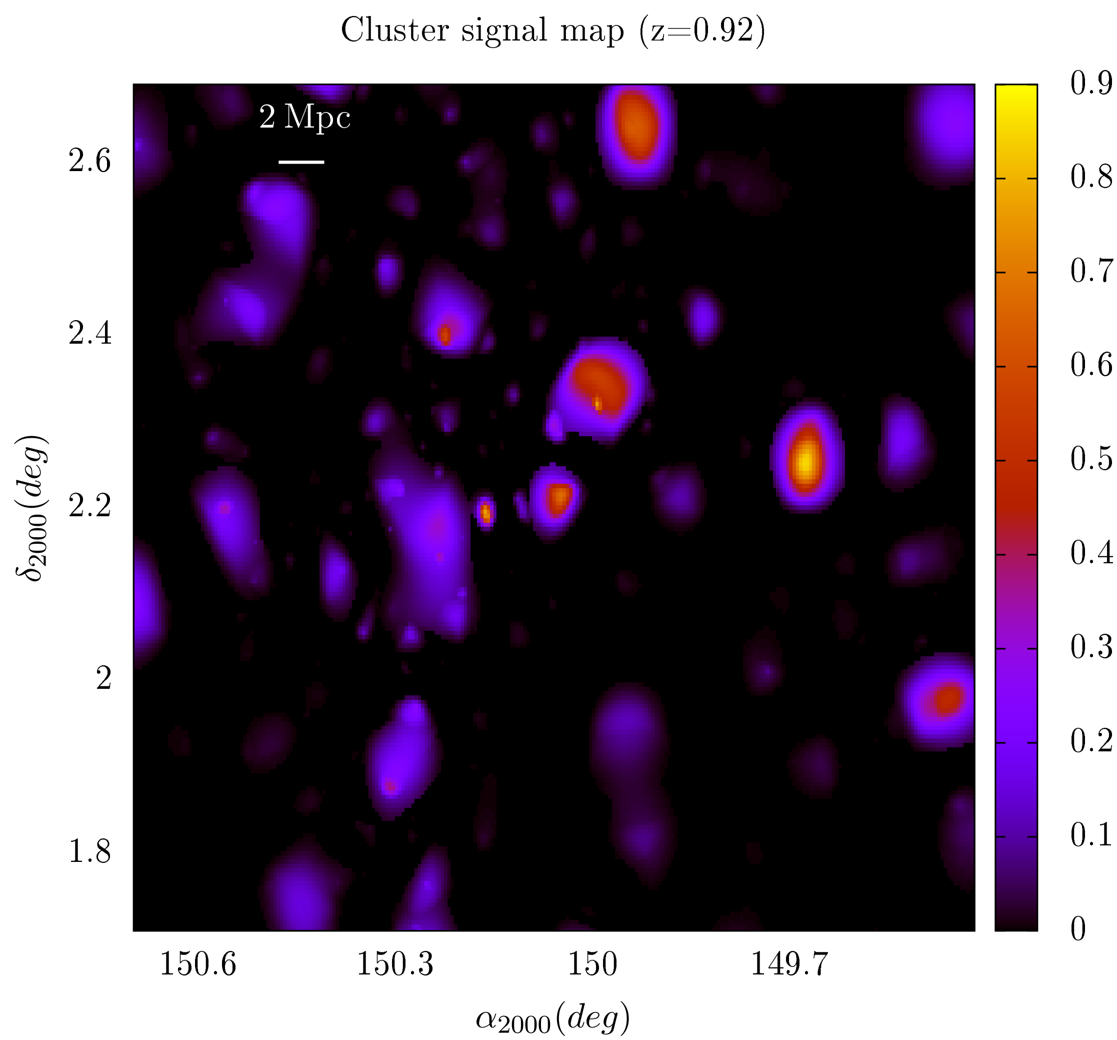

Figure 2.6: cont. (bottom)

field has an associated filament-like value between 0 and 1 (filament signal, S_f) as well as a cluster-like value between 0 and 1 (cluster signal, S_c) that are interpolated into the positions of galaxies. S_f and S_c indicate the degree of resemblance of the local environment of any given point to a filament or cluster, respectively. Figure 2.6 shows the filament signal map (top panel), along with the cluster signal map (bottom panel) for a z-slice in the COSMOS field centered at z=0.92. Note the complex network of filamentary structures and clusters. In Chapters 4 and 5, we will use this algorithm to delineate the cosmic web for some large-scale structures in the COSMOS field.

2.8 Summary and Conclusion

In this chapter, we used a K_s-band selected sample of galaxies with accurate photometric redshifts in COSMOS at z=0.1−3.1 in order to estimate the density field. The density field was determined with the weighted versions of the adaptive kernel smoothing, tenth and fifth NN, Voronoi tessellation and Delaunay triangulation methods. We evaluated the performance of each density estimator using extensive realistic and Monte-Carlo simulations. We found an overall good agreement between the density field estimated with different methods over ∼2 orders of magnitude. We performed extensive simulations to show that the adaptive kernel smoothing and Voronoi tessellation outperform other methods in estimating the density field of galaxies. We recommend using these estimators as a more reliable and robust substitute for the widely-used NN or count in aperture methods. We introduced the robust MMF algorithm which was able to disentangle the cosmic web into its components. The algorithms developed in this chapter will be extensively used in the following chapters that deal mostly with the effects of environment and cosmic web on properties of galaxies.

Chapter 3

New Insights into the Evolution of Galaxies with Environment

Abstract

We study the effects of environment on properties of galaxies using a mass complete sample of quiescent and star-forming systems in the COSMOS field out to $z \sim 3$. Galaxy environment is defined based on the local surface density of galaxies estimated with the Voronoi tessellation method. We show that at $z \lesssim 1$, the median star-formation rate (SFR) and specific SFR (sSFR) of all galaxies (quiescent and star-forming) strongly depend on the environment, and almost independent of it at higher redshifts ($z \gtrsim 1$). However, we find that for the star-forming galaxies, the median SFR and sSFR does not significantly change with environment, regardless of the redshift. We show that the fraction of quiescent galaxies depends on the environment at $z \lesssim 1$, and it depends on stellar mass at all the redshifts considered in this study ($0.1 < z < 3.1$). Moreover, the quiescent fraction at a fixed environment depends on stellar mass at all the redshifts ($0.1 < z < 3.1$), whereas at a fixed stellar mass, it depends on the environment only at $z \lesssim 1$. In addition, we show that the quiescent fraction growth rate does not change much with environment at look-back time $\gtrsim 8$ Gyr. However, at look-back time $\lesssim 8$ Gyr, it is higher in denser environments. We show that at a fixed

stellar mass, the median color of quiescent galaxies does not depend on their host environment out to $z \sim 3$. We find that the comoving number and stellar mass density of massive ($>10^{11}M_\odot$) star-forming galaxies have not significantly changed since $z \sim 3$, regardless of their environment. However, for massive quiescent systems at lower redshifts ($z \lesssim 1.3$), we find a significant evolution in the number and stellar mass densities in denser environments compared to lower density regions. Our results suggest that environment plays a significant role in quenching star-formation activity in galaxies at $z \lesssim 1$, while stellar mass is the dominant quenching mechanism at $z \gtrsim 1$.

3.1 Introduction

Galaxy distribution is divided into two relatively distinct populations: (1) a population of massive, red, passive galaxies with little to no on-going star-formation activity, mostly occupying what is known as the red sequence, and (2) a population of less-massive, blue, star-forming galaxies that lie on the blue cloud. In the local universe, passive galaxies predominantly inhabit denser environments of galaxy clusters, whereas star-forming systems are mostly found in the field. It has been shown that: (1) the fraction of blue, star-forming galaxies is higher in higher redshift clusters than those in the low-z and local clusters, an observation known as the Butcher-Oemler effect (e.g., Butcher and Oemler, 1978; Aragon-Salamanca et al., 1993), (2) the ratio of more massive (giant) to less massive (dwarf) red sequence cluster galaxies decreases with cosmic time (e.g., De Lucia et al., 2007; Stott et al., 2007), (3) there is a significant fraction of post-starburst galaxies (whose star-formation activity has quickly shut down in the past $\sim$Gyr prior to the observation) in clusters, and a higher fraction of them in clusters than the field at intermediate redshifts (e.g., Dressler and Gunn, 1983; Poggianti et al., 2009), and (4) the fraction of S0 galaxies is significantly lower at higher redshift clusters (e.g., Dressler et al., 1999; Postman et al., 2005). All these observations suggest that over the past $\sim$8 Gyr, a large fraction of blue star-forming galaxies have truncated their star-formation, and have migrated to the quiescent population that dominates denser environments at lower redshifts, possibly due to the environmental effects.

However, any galaxy property that depends on the environment also shows some degree of association with stellar mass. For example, on average, more massive galaxies are redder, less-star forming and more likely to have early-type morphologies (e.g., Kauffmann et al., 2004; Baldry et al., 2006; Peng et al., 2010). Therefore, two major (and possibly distinct) quenching mechanisms are proposed, that are generally known as "environment quenching" and "mass quenching" (e.g., Peng et al., 2010). These processes seem to suppress the star-formation activity independent of each other. In other words, more massive galaxies are more likely to become quiescent independent of their host environment, and galaxies in denser regions are more likely to become quenched independent of their stellar mass. Moreover, environment quenching has been attributed to satellites, whereas mass quenching is primarily linked to central galaxies (e.g., Peng et al., 2012). Physically, it has been proposed that both environment and mass quenching can be explained by the "halo quenching" process (Gabor and Davé, 2015), a physical mechanism which states that the gas in halos more massive than $10^{12}M_{\odot}$ is hindered from cooling as it becomes shock-heated (Birnboim and Dekel, 2003; Dekel and Birnboim, 2006). Despite all the progress, it is still not completely clear how these quenching mechanisms affect properties of galaxies at different redshifts, and their fractional role in suppressing the star-formation as a function of look-back time and galaxy properties.

In this chapter, we apply the Voronoi tessellation algorithm to a mass complete sample of galaxies in the COSMOS field (Scoville et al., 2007b) to investigate the role of density-based definition of environment on the rest-frame color, SFR, sSFR, quiescent fraction, and comoving number and mass density of galaxies out to z$\sim$3. We also study the dependence of environmental effects on stellar mass and galaxy type and the redshift evolution of the trends.

The format of this chapter is as follows. In Section 2, we briefly review the data, along with the selection of quiescent and star-forming galaxies. In Section 3, we present the main results. A summary of this work is given in Section 4.

Throughout this chapter, we assume a flat concordance ΛCDM cosmology with H_0=70 kms^{-1} Mpc^{-1}, Ω_m=0.3 and Ω_Λ=0.7. All magnitudes are expressed in the AB system and stellar masses are given assuming a Chabrier IMF.

3.2 Data and Sample Selection

The data used in this study is similar to those introduced in Chapter 2. However, the magnitude cut K_s <24 used in Section 2.2 of Chapter 2 leads to a magnitude-limited sample whose stellar mass varies with redshift. Therefore, we need to first define a mass complete sample of galaxies at different redshifts. In the following subsections, we select the mass complete sample of galaxies and then explain the selection of quiescent and star-forming galaxies.

Stellar Mass Complete Samples

The magnitude cut K_s <24 introduced in Chapter 2 results in a magnitude-limited sample whose mass completeness is a function of redshift and stellar mass-to-light ratio M/L. In order to estimate the mass completeness of our sample, we use the method explained in Pozzetti et al. (2010) and Ilbert et al. (2013). First, for each galaxy, we calculate the limiting stellar mass (M_{lim}), that is, the mass it would have at its redshift, if its apparent magnitude were equal to the magnitude limit of the sample (K_s=24). This is given by $\log(M_{lim}/M_\odot)=\log(M/M_\odot)+0.4(K_s\text{-}24)$, where M is the estimated stellar mass of the galaxy with apparent magnitude K_s. At each redshift, the stellar mass completeness limit (M_{comp}) corresponds to the mass with 95% of the galaxies having their M_{lim} below the stellar mass completeness limit.

This guarantees that only less than 5% of galaxies could be missed in the lower mass regime of the stellar mass distribution of galaxies. The mass completeness limit also depends on the stellar M/L ratio and is higher for quiescent galaxies. Therefore, in constructing the mass complete samples at each redshift, we make sure that we rely on the quiescent galaxies

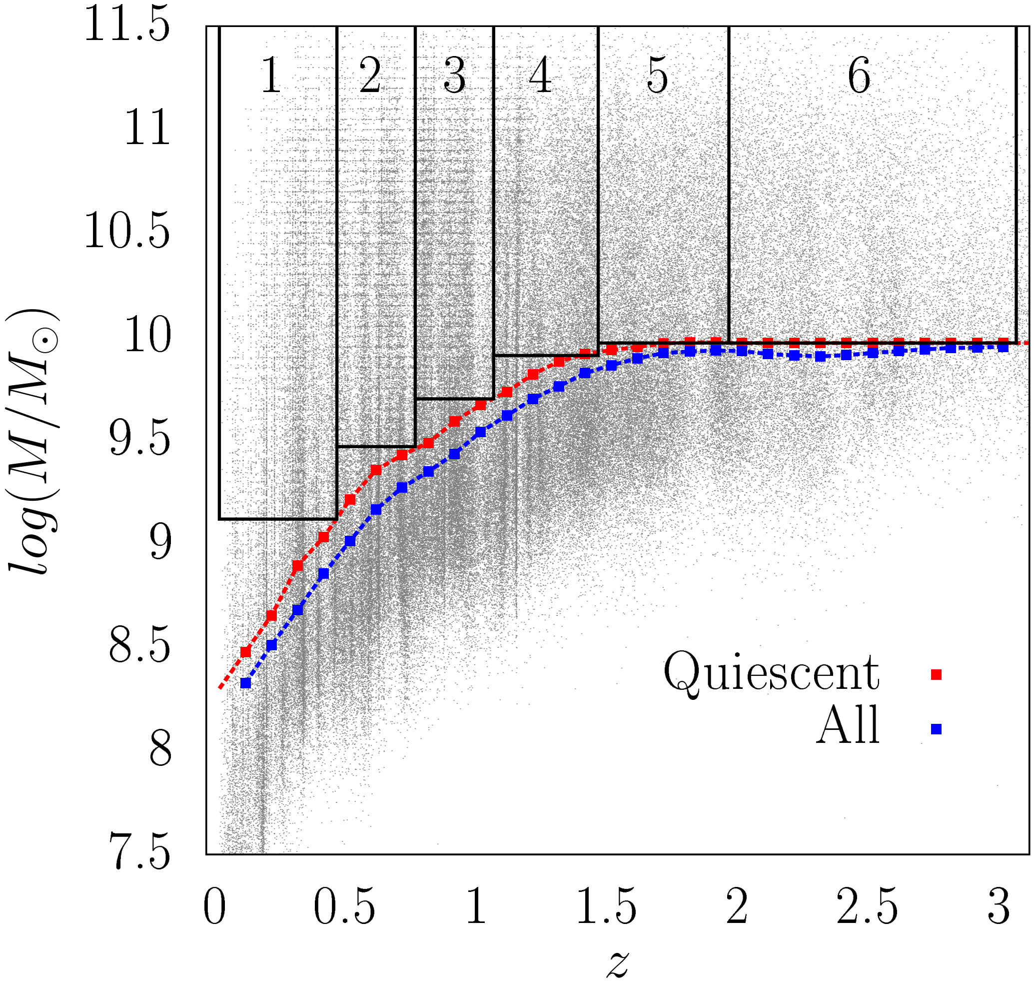

Figure 3.1: Mass completeness limit for all the galaxies, along with that of the quiescent systems as a function of redshift. The mass completeness limit is defined in such a way that only less than 5% of the galaxies could be missed in the lower mass distribution of the galaxies. Using the mass completeness limits for the quiescent systems, we define six mass complete samples at different redshifts, as shown here with labels 1−6.

Table 3.1: Properties of Mass Complete Samples

Sample Number	Redshift Range	Mass Completeness Limit $\log(M_{\odot})$	Number of Galaxies
1	$0.1 \leq z < 0.5$	9.14	9338
2	$0.5 \leq z < 0.8$	9.47	11760
3	$0.8 \leq z < 1.1$	9.70	13885
4	$1.1 \leq z < 1.5$	9.93	13640
5	$1.5 \leq z < 2.0$	9.97	12217
6	$2.0 \leq z < 3.1$	9.97	12641

to estimate the stellar completeness limit. This minimizes the loss of low-mass quiescent galaxies, especially at higher redshifts. The selection of quiescent/star-forming galaxies is explained in Section 3.2. Figure 3.1 shows the stellar mass of galaxies as a function of redshift for the magnitude-limited sample (K_s <24) defined in Section 2.2. The mass completeness limits for all the galaxies (quiescent and star-forming) and quiescent systems are shown in Figure 3.1. As mentioned, only less than 5% of galaxies could be missed in the lower mass population of galaxies. The mass completeness limit is higher for quiescent systems. Here, we define six mass complete samples out to $z \sim 3$, as shown in Figure 3.1. The properties of these mass complete samples are given in Table 3.1.

Selection of Quiescent/Star-forming Systems

The selection of quiescent and star-forming systems can be performed using a single rest-frame color through the Color−Magnitude Diagram (CMD). However, the single color selection is problematic for several reasons. The existence of dusty, star-forming galaxies that mimic the color of quiescent systems can significantly contaminate the quiescent population and tends to unrealistically increase the quiescent fraction and their comoving number densities (Brammer et al., 2009). The larger scatter in the rest-frame color at higher redshifts (mostly due to photo-z uncertainties) can wash out the red sequence and the disappearance of the rest-frame color bimodality at $z \gtrsim 1.5$ (Williams et al., 2009). Here, we use rest-frame two-color NUV−r^+ versus r^+−J plane in order to select quiescent and star-forming pop-

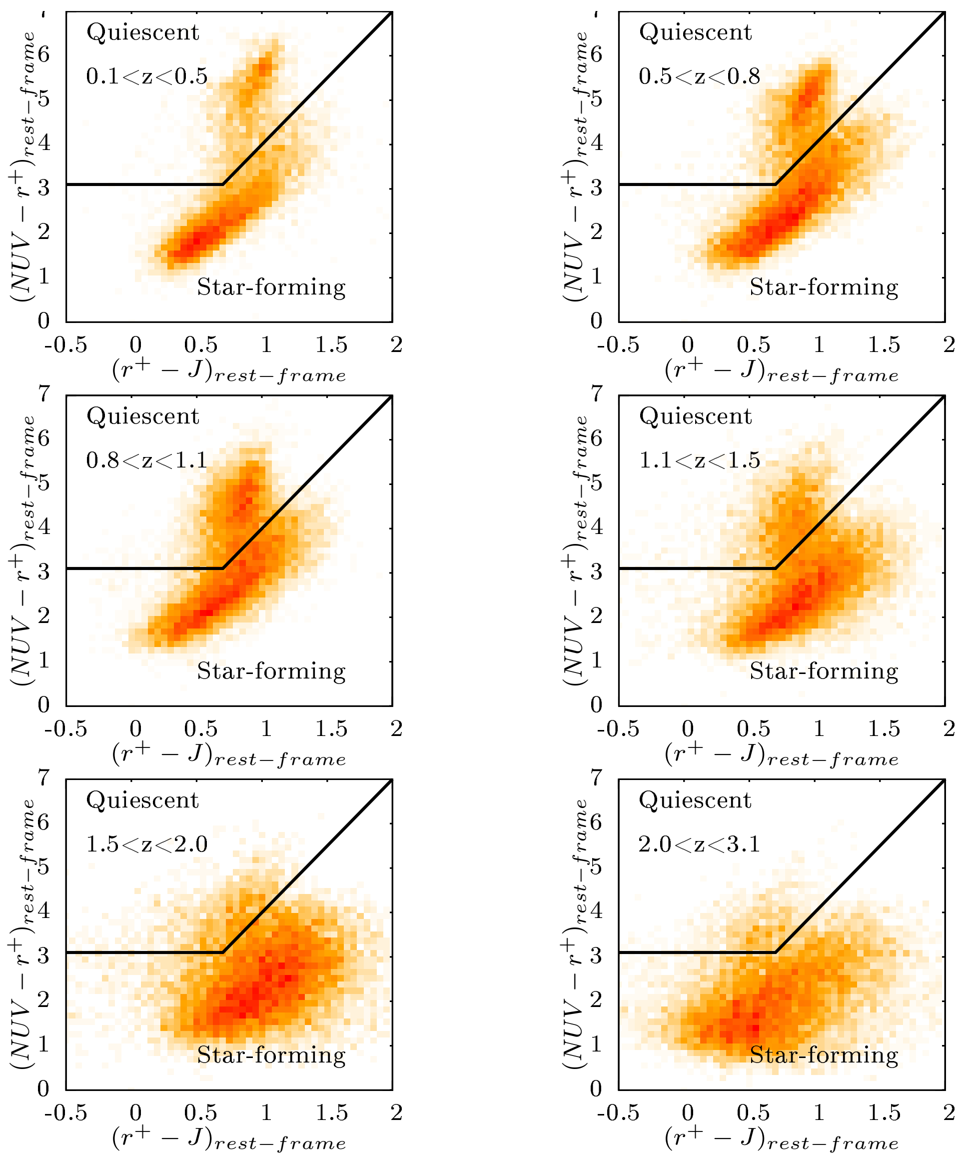

Figure 3.2: NUV$-r^+$ versus r^+-J color$-$color plots used to select quiescent and star-forming populations in our mass complete samples at z=0.1$-$3.1. Galaxies with their rest-frame color NUV$-r^+ > 3.1$ and NUV$-r^+ > 3(r^+-\text{J})+1$ are selected as quiescent systems (Ilbert et al., 2013).

ulations in our mass complete samples. It has been shown that the rest-frame NUV$-r^+$ color is a better indicator of the recent star-formation activity (Martin et al., 2007) and has a wider dynamical range compared to the more commonly used rest-frame U$-$V color (Ilbert et al., 2013). Here, galaxies with a rest-frame color NUV$-r^+ > 3.1$ and NUV$-r^+$ $> 3(r^+-\mathrm{J})+1$ are selected as quiescent systems (Ilbert et al., 2013). Figure 3.2 shows the rest-frame NUV$-r^+$ versus r^+-J distribution of galaxies in the mass complete samples and the color cuts used to separate quiescent and star-forming systems. Two distinct populations of galaxies are clearly seen out to $z \sim 3$. We stress that in our two-color selection technique, adding dust to the star-forming galaxies causes them to move diagonally from the bottom left to the top right of Figure 3.2, making them separable from the quiescent systems (Williams et al., 2009; Ilbert et al., 2013).

3.3 Results

Using the surface density field constructed in the COSMOS field with the Voronoi tessellation method, we now study the dependence of the observable parameters of galaxies, such as SFR and quiescent fraction on their local overdensity. We also investigate the redshift evolution and the dependence of the environmental trends on stellar mass and galaxy type.

3.3.1 SFR and sSFR Evolution with Environment and Galaxy Type

We now investigate the relation between the SFR (and sSFR) and overdensity and how this relation evolves with redshift. The SFR is based on the SED template-fitting and was extracted by (Ilbert et al., 2013). Figure 3.3 (top left) shows the median SFR of galaxies (star-forming and quiescent) as a function of overdensity for our mass complete samples at different redshifts. The errorbars incorporate Poisson errors and the cosmic variance uncertainties. The cosmic variance contribution is estimated using (Moster et al., 2011). Regardless of the environment, we find that at a fixed overdensity, the median SFR is higher for higher-z samples compared to those at lower redshifts. This is consistent with the continuous decline in the global star formation density of the universe since $z \sim 2-3$ that has been seen in many previous studies (see Madau and Dickinson, 2014 for a review). However, we clearly see that the amount of decline depends on the environment. At $z \lesssim 1$, the median SFR strongly depends on the overdensity and decreases with increasing overdensity, especially for the overdensity values $\log(1+\delta) \gtrsim 0.5$. For example, for the $0.1 < z < 0.5$ sample, the median SFR decreases by ~ 2 orders of magnitude as the overdensity increases by almost the same factor. We note again that the decrement in the median SFR starts to be practically observable at $\log(1+\delta) \gtrsim 0.5$. However, at higher redshifts ($z \gtrsim 1$), we do not find a significant relation between the median SFR and overdensity, and the median SFR becomes almost independent of the environment (overdensity).

Although we find a strong SFR$-$overdensity anti-correlation for the $z \lesssim 1$ samples, however, this correlation depends on the galaxy type. Figure 3.3 (top right) shows the median SFR of only the star-forming galaxies as a function of overdensity for the mass complete samples at different redshifts. When we only consider the star-forming galaxies, the median SFR becomes independent of the environment (overdensity) at all the redshifts considered for this study ($0.1 < z < 3.1$). In other words, when a galaxies becomes star-forming, on average, its star-formation activity becomes independent of the environment that it occupies (Figure 3.3 (top right)). Therefore, the SFR$-$overdensity trends for the $z \lesssim 1$ samples seen in Figure 3.3 (top left) is because of the existence of the quiescent galaxies that populate denser environments. Denser environments increase the likelihood of a galaxy to become quiescent. However, if it is star-forming, on average, its SFR becomes almost intact by the environment in which it resides.

We find similar results for the relation between sSFR, overdensity, redshift, and galaxy type (Figure 3.3 (bottom left and right panels)). At $z \lesssim 1$, there is a tight anti-correlation between the median sSFR and the overdensity for all the galaxies, especially for $\log(1+\delta) \gtrsim 0.5$. However, for the $z \gtrsim 1$ samples, we find that the sSFR becomes independent of the overdensity values. We also find no relation between the sSFR and the environment (overdensity) for the star-forming galaxies at the redshifts of this study.

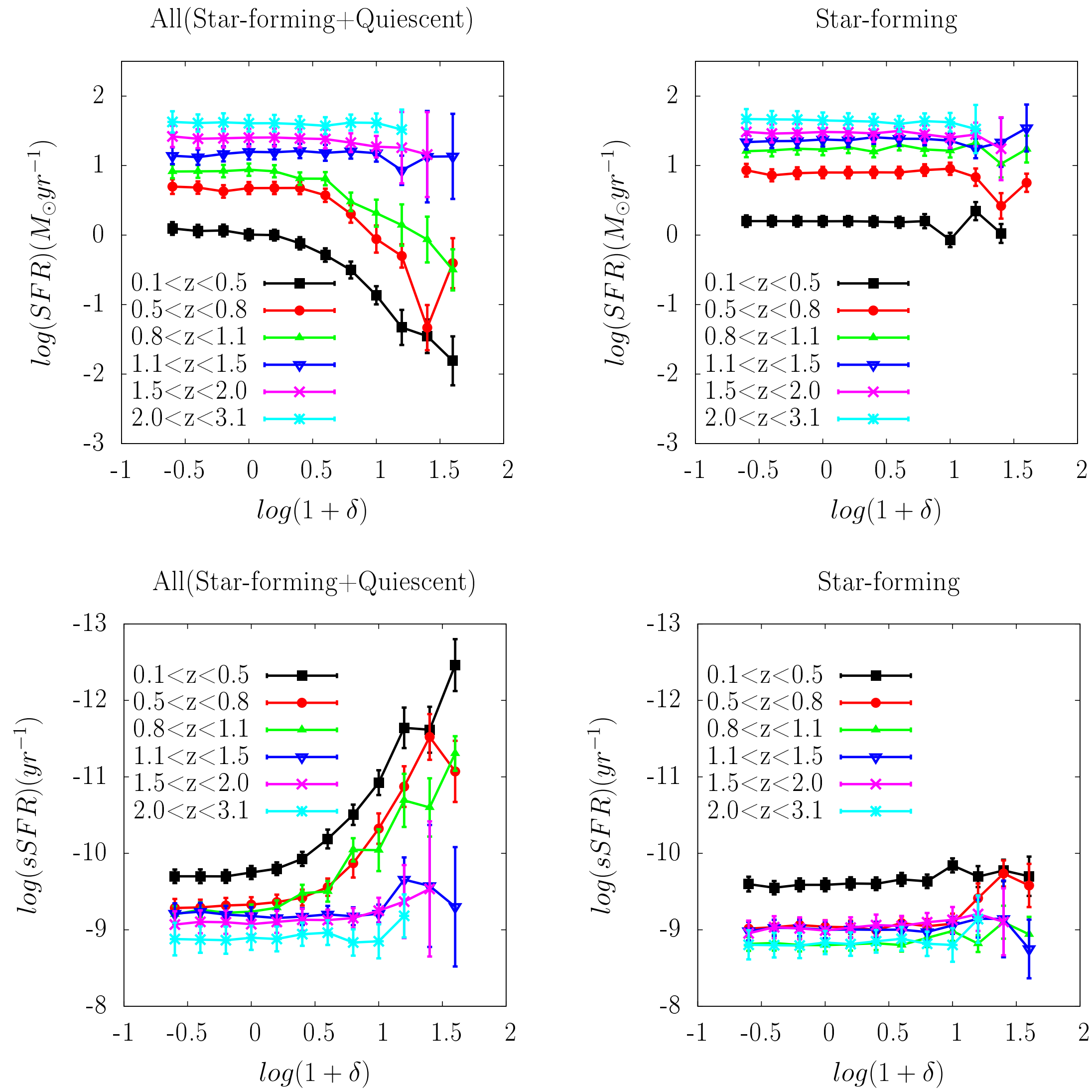

Figure 3.3: Median SFR (top) and sSFR (bottom) as a function of overdensity at different redshifts for all the galaxies (left) and only the star-forming systems (right). The errorbars incorporate Poisson errors and cosmic variance uncertainties. At $z\lesssim1$, the median SFR and sSFR strongly depend on the overdensity and they decrease with increasing overdensity. However, at higher redshifts ($z\gtrsim1$), the median SFR and sSFR become almost independent of the environment (overdensity). When we only consider the star-forming galaxies, the median SFR and sSFR become independent of the environment (overdensity) at all the redshifts considered for this study (0.1< z <3.1).

Using a large sample of galaxies in the COSMOS field at $z \lesssim 3$, Scoville et al. (2013) found a strong anti-correlation between the median SFR and environmental density percentile for their low redshift samples. However, at $z \gtrsim 1.2$, Scoville et al. (2013) did not find a strong relation between environment and the median SFR of the observed galaxies, as shown in their Figures 15 and 16. They found similar trends between the SF timescale (inverse of the sSFR) and environmental density percentile, in a sense that at $z \lesssim 1.2$, the SF timescale is larger at higher density percentile levels. These results are fully consistent with what we found in this section, and our results confirm the similar previous studies in the COSMOS field.

At low-z ($z \lesssim 0.2$), there are many studies that show a lower SFR or sSFR in denser regions compared to less-dense, field-like environments (see e.g., Balogh et al., 2004; Kauffmann et al., 2004; Baldry et al., 2006), which are in agreement with our result in this section for our low-z samples. However, at intermediate redshifts ($z \sim 1$), current studies of the environmental dependence of the SFR in galaxies have led to conflicting results. Some agree with the relations observed in the local universe (e.g., Patel et al., 2009; Muzzin et al., 2012), some report no/weak dependence on the environment (e.g., Grützbauch et al., 2011; Scoville et al., 2013), and there are even claims for a reversal of the SF−density relation(higher star-formation in denser regions,e.g., Elbaz et al., 2007; Cooper et al., 2008a). We clearly see no reversal of the SF−density relation for our z∼1 sample, and our results follow the local universe trends, completely consistent with e.g., Patel et al. (2009) and Muzzin et al. (2012). As already noted by Scoville et al. (2013), the claim of the SF−density reversal by Cooper et al. (2008a) is hard to judge according to their Figure 19(b). We argue that the reversal seen in Elbaz et al. (2007) is probably due to the cosmic variance and the small dynamical range of the environments considered in their study as they only used the GOODS fields. Furthermore, later studies in the GOODS fields by Popesso et al. (2011) attributed this reversal to the AGN contamination, and Ziparo et al. (2014) found no evidence for the reversal of the star-formation activity at $z \sim 1$ using a similar data set. Sobral et al. (2011) also showed that at $z \sim 1$, there is an increase of SF activity for star-forming galaxies at intermediate densities, likely associated with galaxy groups. This is followed by a decline for the richest clusters, and that this is probably the reason for discrepancies: some studies only reach up to poor group environments, while others only probe rich clusters. Sobral et al. (2011) showed that once the full range of environments is probed and correctly labeled, all the apparently contradictory results can be reconciled.

Similar to what we found in this section for the star-forming galaxies, several studies in a broad range of redshifts have shown that, on average, many properties of the star-forming galaxies that are directly or indirectly linked to star-formation activity (e.g., SFR, sSFR, emission line EW, main-sequence of star-forming galaxies) are invariant to their environment (e.g., Peng et al., 2010; Wijesinghe et al., 2012; Muzzin et al., 2012; Koyama et al., 2013b, 2014; Hayashi et al., 2014; Lin et al., 2014; Darvish et al., 2014, also see chapter 5). Therefore, the main role of environment is argued to set the fraction of quiescent/star-forming galaxies (e.g., Peng et al., 2010; Sobral et al., 2011; Muzzin et al., 2012; Darvish et al., 2014). In other word, denser environments increase the likelihood of galaxies to become quenched. However, as they form stars, on average, their star formation activity remains largely independent of the environment they occupy. In chapter 5, we discuss the difference in the SFHs as a possibility for the difference in the fraction of star-forming galaxies in different environments. Nevertheless, recent studies show that not all characteristics of the star-forming galaxies are independent of environment. For example, metallicities and electron densities have shown to be a function of the environment (e.g., Shimakawa et al., 2015; Kacprzak et al., 2015; Sobral et al., 2015b, also see chapter 5). In the following section, we focus on the fraction of quiescent/star-forming galaxies as a function of overdensity, stellar mass, and redshift and try to disentangle the partial role of the environment and stellar mass on the star-formation quenching in galaxies.

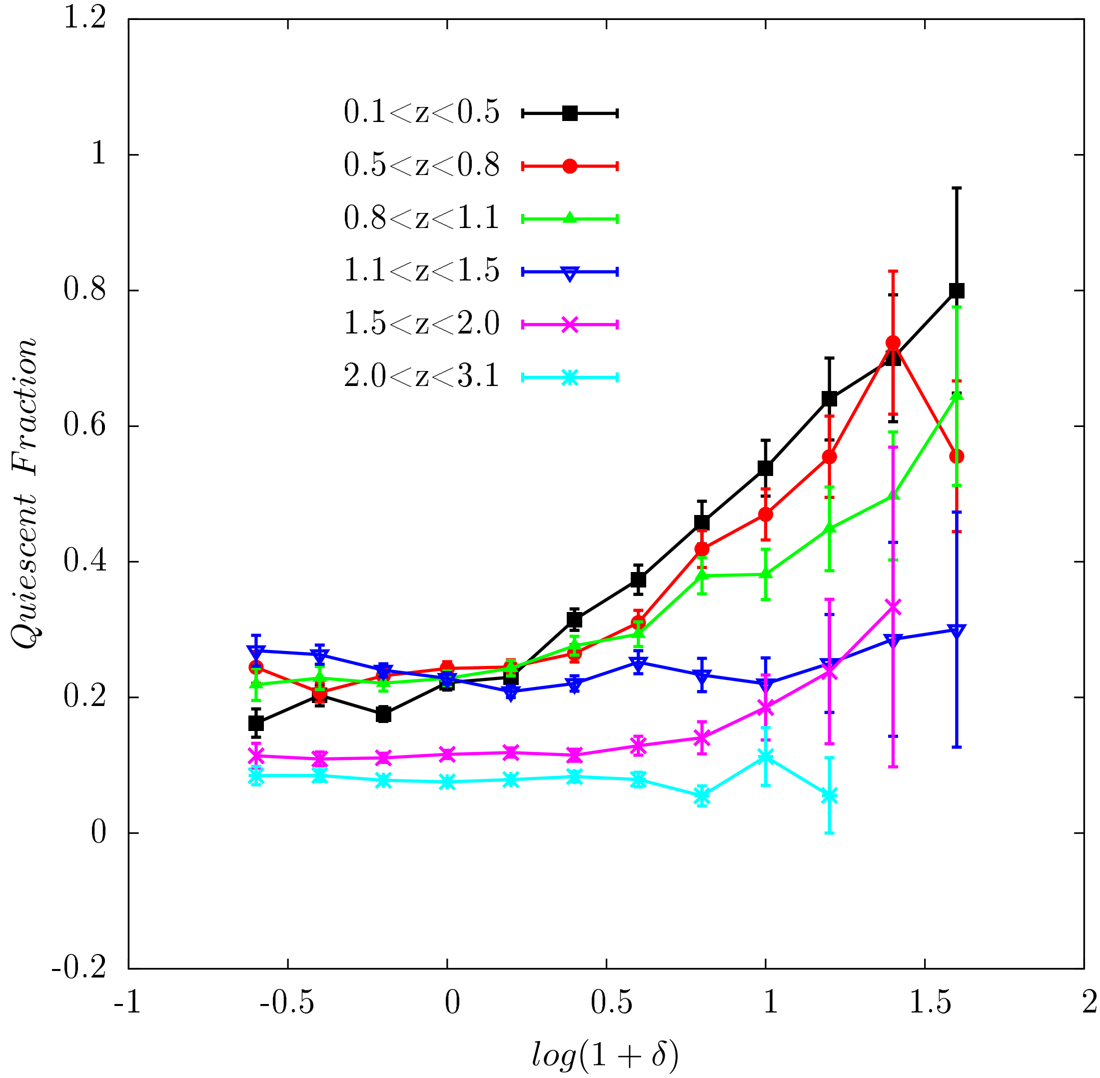

Figure 3.4: Fraction of quiescent galaxies as a function of overdensity (top) and stellar mass (bottom) and at different redshifts. At $z\lesssim1$, we find that the fraction of quiescent galaxies strongly depends on the overdensity. This increases with overdensity from $\sim$20% at $\log(1+\delta)\lesssim0.5$ to $\sim$60%$-$80% at $\log(1+\delta)\sim1.6$. However, at higher redshifts ($z\gtrsim1$), the fraction of quiescent galaxies does not significantly change with environment (overdensity). In addition, we find that at a fixed overdensity, the fraction of quiescent galaxies is higher at lower redshifts, which is a manifestation of the Butcher-Oemler effect. The fraction of quiescent galaxies (located at different environments) strongly depends on stellar mass as well. At all redshifts (for both $z<1$ and $z>1$ samples), the fraction of quiescent galaxies monotonically increases with stellar mass. However, at a fixed stellar mass, this fraction is higher at lower redshifts compared to higher-z samples. This is an indication of the galaxy mass-downsizing.

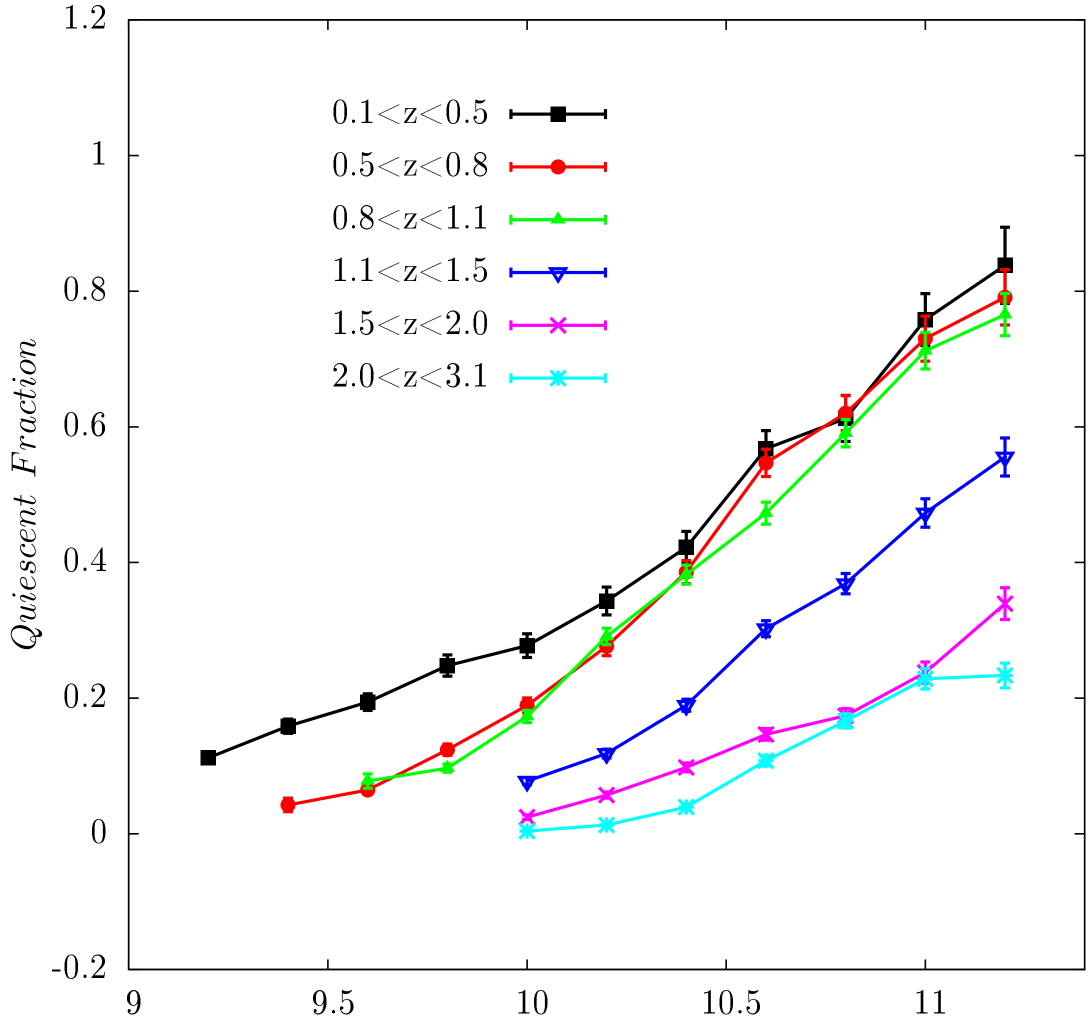

Figure 3.4: cont. (bottom)

3.3.2 Evolution of the Quiescent Fraction with Environment and Stellar Mass

In the previous section, we argued that the main role of environment is to set the fraction of quiescent/star forming galaxies. We now investigate this by studying the fraction of quiescent galaxies as a function of overdensity, stellar mass, and redshift. Figure 3.4 (top panel) shows the fraction of quiescent galaxies (with different stellar masses) as a function of overdensity and for our mass complete samples at different redshifts. The errorbars are estimated following Poisson statistics and the uncertainties due to the cosmic variance. At $z \lesssim 1$, we find that the fraction of quiescent galaxies depends on the overdensity. This increases with overdensity from $\sim$20% at $\log(1+\delta) \lesssim 0.5$ to $\sim$60%$-$80% at $\log(1+\delta) \sim 1.6$. The increase is specifically sharp at $\log(1+\delta) \gtrsim 0.5$. However, the fraction of quiescent galaxies does not significantly change with environment (overdensity) at $z \gtrsim 1$ (except for the $1.5 < z < 2.0$ sample at the densest regions, although those have large errorbars). For example, at $2.0 < z < 3.1$, the fraction of quiescent galaxies as a function of overdensity remains at $\sim$10% at all overdensity levels. Additionally, we find that at a fixed overdensity, the fraction of quiescent galaxies is higher at lower redshifts. This is a clear manifestation of the Butcher-Oemler effect (Butcher and Oemler, 1978), stating that the fraction of blue star-forming galaxies is higher for higher-z galaxy clusters compared to their local counterparts (see e.g., Butcher and Oemler, 1978; Couch and Sharples, 1987; Aragon-Salamanca et al., 1993; Dressler et al., 1994).

Figure 3.5 (top panel) shows the quiescent fraction as a function of look-back time for some fixed overdensity values. We see that at look-back times $\gtrsim$8 Gyr, the quiescent fraction increases with cosmic time almost independent of the environment. However, we find that at $z \lesssim 1$ (look-back time $\lesssim$ 8 Gyr) the enhancement in the fraction of quiescent galaxies with cosmic time is larger for galaxies located in denser environments. We quantify the quiescent fraction growth with cosmic time assuming a linear growth in the quiescent fraction at a given overdensity. Figure 3.5 (bottom panel) shows the quiescent fraction growth rate as a function of overdensity for galaxies located at $z \lesssim 1.3$ and $z \gtrsim 1.3$. At $z \gtrsim 1.3$, the quiescent fraction growth rate is almost independent of the environment. However, at $z \lesssim 1.3$ and at a given overdensity, the quiescent fraction grows constantly with cosmic time, but the growth rate increases with density. Galaxies are transferred from the star-forming population to the quiescent system more rapidly in denser environment compared to less-dense regions.Our result regarding the growth of the quiescent fraction agrees quantitatively with e.g., Capak et al. (2007a).

It has been shown that the fraction of quiescent galaxies is also a function of stellar mass (e.g., Baldry et al., 2006). We investigate the relation between stellar mass and overdesnity, as shown in Figure 3.4 (bottom panel). According to Figure 3.4 (bottom panel), the fraction of quiescent galaxies (located at different environments) strongly depends on stellar mass. At all redshifts (for both z <1 and z >1 samples), the fraction of quiescent galaxies monotonically increases with increasing stellar mass. However, at a fixed stellar mass, this fraction is higher at lower redshifts compared to higher-z samples. For example, at 2.0< z <3.1, the fraction of quiescent galaxies varies from ∼0% for log(M/M$_\odot$)∼10 systems to ∼20% for log(M/M$_\odot$)∼11 galaxies. Whereas, at 0.1< z <0.5, log(M/M$_\odot$)∼10 galaxies comprise ∼30% of quiescent population and this fraction increases to ∼80% for log(M/M$_\odot$)∼11 galaxies. In fact, this is another form of galaxy mass-downsizing (Cowie et al., 1996; Bundy et al., 2006, e.g.,), indicating that higher mass galaxies form and quench their star-formation activity earlier than less massive systems. According to Figure 3.4 (bottom panel), by 2.0< z <3.1, ∼20% of log(M/M$_\odot$)∼11 have already assembled and quenched their star-formation activity, whereas for log(M/M$_\odot$)∼10, this fraction (∼20%) is observed at much later times (at 0.8< z <1.1). Using this, we derive the typical time delay between the quenching of less massive (log(M/M$_\odot$)∼10) and more massive (log(M/M$_\odot$)∼11) galaxies and estimate it to be Δt ∼3.4±0.9 Gyr.

One major difference that is clearly seen in the top and bottom panels of Figure 3.4 is that at all redshifts (0.1< z <3.1), the fraction of quiescent galaxies depends on stellar mass, but this fraction depends on overdensity (environment) only at z ∼1 and not significantly at higher redshifts. This leads us to the conclusion that environmental quenching is only

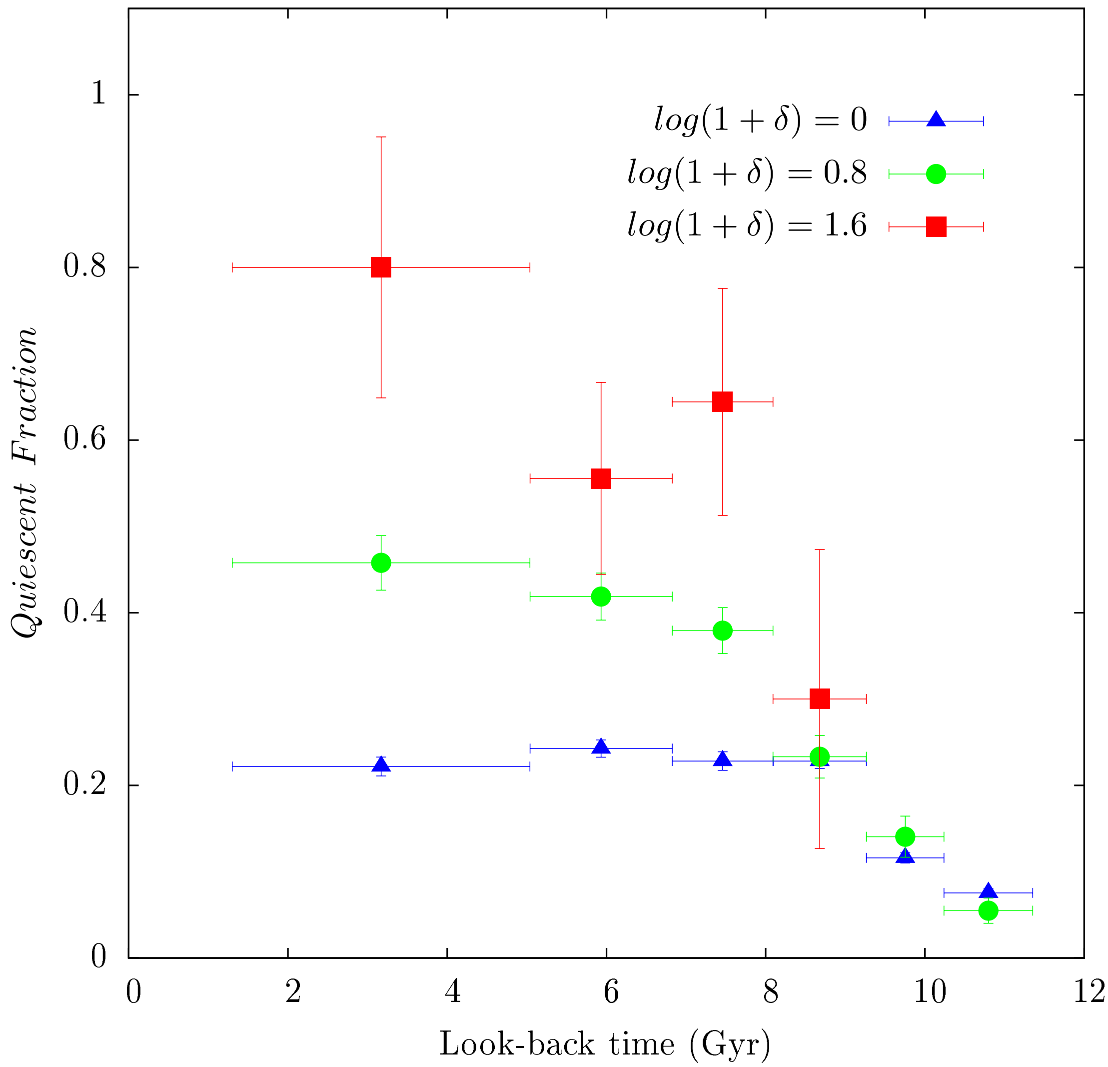

Figure 3.5: (top panel) Fraction of quiescent galaxies as a function of look-back time for some fixed overdensity values. At look-back times $\gtrsim$8 Gyr, the quiescent fraction increases with cosmic time almost independent of the environment. However, at $z\lesssim1$ (look-back time $\lesssim$ 8 Gyr), the growth in the fraction of quiescent galaxies with cosmic time is larger for galaxies located in denser environments. (bottom panel) Quiescent fraction growth rate (per Gyr) as a function of overdensity for galaxies located at $z\lesssim1.3$ and $z\gtrsim1.3$ samples. At $z\gtrsim1.3$, the quiescent fraction growth rate is almost independent of the environment. However, at $z\lesssim1.3$, the growth rate increases with overdensity.

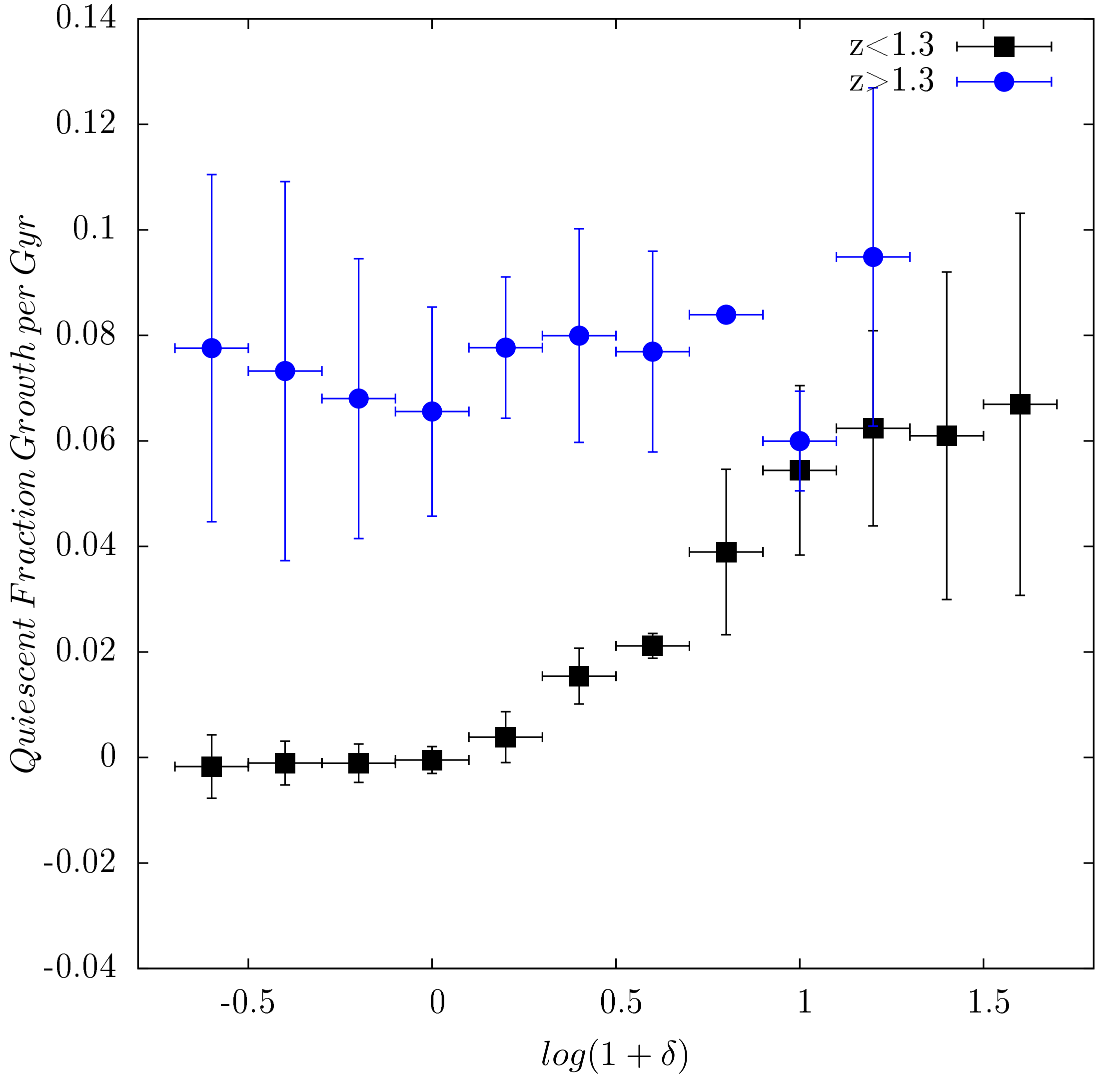

Figure 3.5: cont. (bottom)

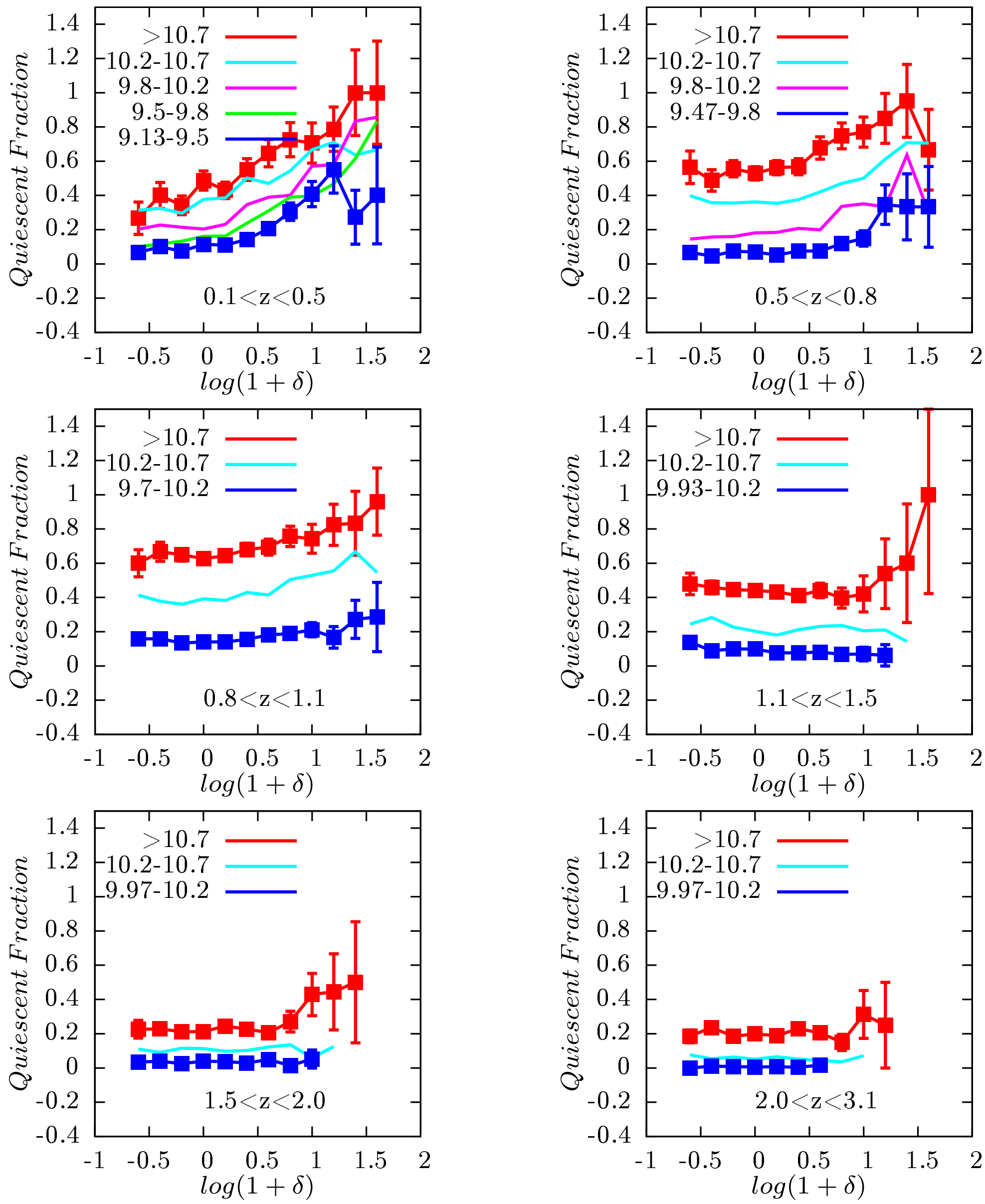

Figure 3.6: Fraction of quiescent galaxies as a function of overdensity for different stellar mass bins and at different redshifts. Different colors correspond to different stellar mass bins. At all the redshifts considered in this study (0.1< z <3.1), the fraction of quiescent galaxies at a fixed environment strongly depends on stellar mass, i.e., the fraction of quiescent galaxies at all fixed density levels is always higher for more massive galaxies compared to less massive systems out to z∼3.

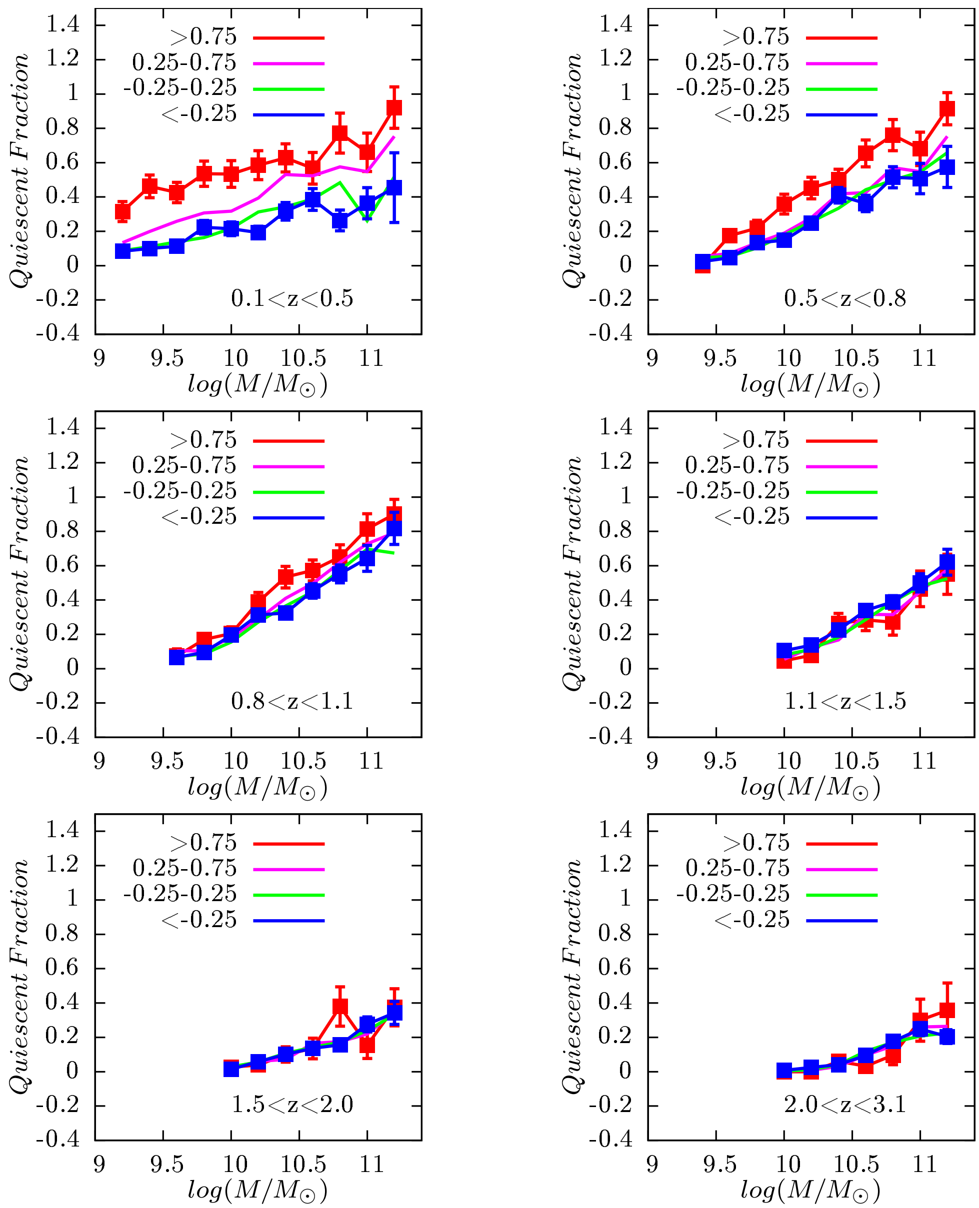

Figure 3.7: Fraction of quiescent galaxies as a function of stellar mass for different overdensity bins and at different redshifts. Different colors correspond to different overdensity bins. At a fixed stellar mass, quiescent fraction depends on environment (overdensity) only at $z \lesssim 1$ and not significantly at higher redshifts. At a fixed stellar mass and at $z \lesssim 1$, this fraction is higher in denser regions.

effective at z$\lesssim$1, whereas mass quenching is the dominant quenching mechanism at z$\gtrsim$1. We further investigate this by studying the fraction of quiescent galaxies as a function of overdensity and redshift for fixed stellar mass bins (Figure 3.6) and the fraction of quiescent galaxies as a function of stellar mass and redshift for fixed overdensity bins (Figure 3.7). Figure 3.6 shows the fraction of quiescent galaxies as a function of overdensity for different stellar mass bins and at different redshifts. Different colors correspond to different stellar mass bins. According to this figure, at all the redshifts considered (0.1< z <3.1), the fraction of quiescent galaxies at a fixed environment strongly depends on stellar mass, i.e., the fraction of quiescent galaxies at all fixed density levels is always higher for more massive galaxies compared to less massive systems out to z$\sim$3. However, as shown in Figure 3.7, the fraction of quiescent galaxies at a fixed stellar mass depends on environment (overdensity) (shown with different colors) only at $z\lesssim$1 and not significantly at higher redshifts. At a fixed stellar mass and at z$\lesssim$1, this fraction is higher in denser regions.

When we combine the results shown in Figures 3.4, 3.6 and 3.7, we conclude that the quenching of galaxies due to environmental effects (external processes) is practically effective at lower redshifts ($z\lesssim$1), while stellar mass of galaxies (internal processes) is the dominant quenching mechanism at higher redshifts ($z\gtrsim$1). Our results in this section are in agreement with e.g., Peng et al. (2010), Sobral et al. (2011), and Muzzin et al. (2012). Muzzin et al. (2012) studied the effects of stellar mass and environment on properties of a spectroscopic sample of galaxies at 0.85< z <1.20. They showed that the sSFR of star-forming galaxies at fixed environment depends on stellar mass; but at fixed stellar mass, it is independent of environment. Peng et al. (2010) studied a sample of galaxies in the SDSS and zCOSMOS (z$\sim$0.7) and showed that for massive galaxies, mass quenching is the primary quenching mechanism for all environments and at all redshifts, while environmental quenching become predominantly important at lower redshifts, especially for less massive galaxies. Sobral et al. (2011) showed that stellar mass is the main predictor of star-formation activity in galaxies at z $\sim$1, but the environment is responsible for star-formation quenching in all galaxies in dense environments. All these results signify the importance of galaxy environment in suppressing the star-formation activity at lower redshifts, and they are qualitatively in agreement with our results in this section.

3.3.3 Evolution of Rest-frame Color with Environment and Stellar Mass For Quiescent Galaxies

We now investigate the effect of the environment on the rest-frame $u^*{-}B_J$ color of quiescent systems with different stellar masses and its evolution with redshift. Here, we define two environments: the high-density environment (galaxy group and cluster scales) is defined as regions with overdensity values $\log(1+\delta)\geq0.5$ and the low-density environment (field-like environment) is defined as those with $\log(1+\delta)<0.5$. The selection of the cut between low- and high-density environments is somewhat arbitrary. However, it is shown in Sections 3.3.1 and 3.3.2 that the environmental effects (e.g., the increase in the fraction of quiescent galaxies with overdensity) start to effectively rise at $\log(1+\delta)\gtrsim0.5$ in the COSMOS field. Therefore, we use this cut to separate the density field into low- and high-density environments. Based on this definition, we study the redshift evolution of the rest-frame u^*-B_J color as a function of the environment and stellar mass for quiescent galaxies. Figure 3.8 shows the redshift evolution of the median rest-frame $u^*{-}B_J$ color for quiescent galaxies with different stellar masses located in high- and low-density environments. For clarity, the evolution is shown for only a few stellar mass bins (ΔM=$\pm$0.1 dex around the selected masses). We choose the center of the redshift bins (Table 3.1) to be the redshift of the given points. The median color at each given environment, stellar mass and redshift is estimated using all the quiescent systems in that environment, with their redshift located in the redshift range of the mass complete samples and with stellar masses within ΔM$\pm$0.1 dex of the given stellar mass. The color uncertainties are estimated using 10,000 bootstrap resamples added in quadrature to the median observational uncertainties in color. We assume that the evolution of the rest-frame $u^*{-}B_J$ color for quiescent systems is linear with redshift,

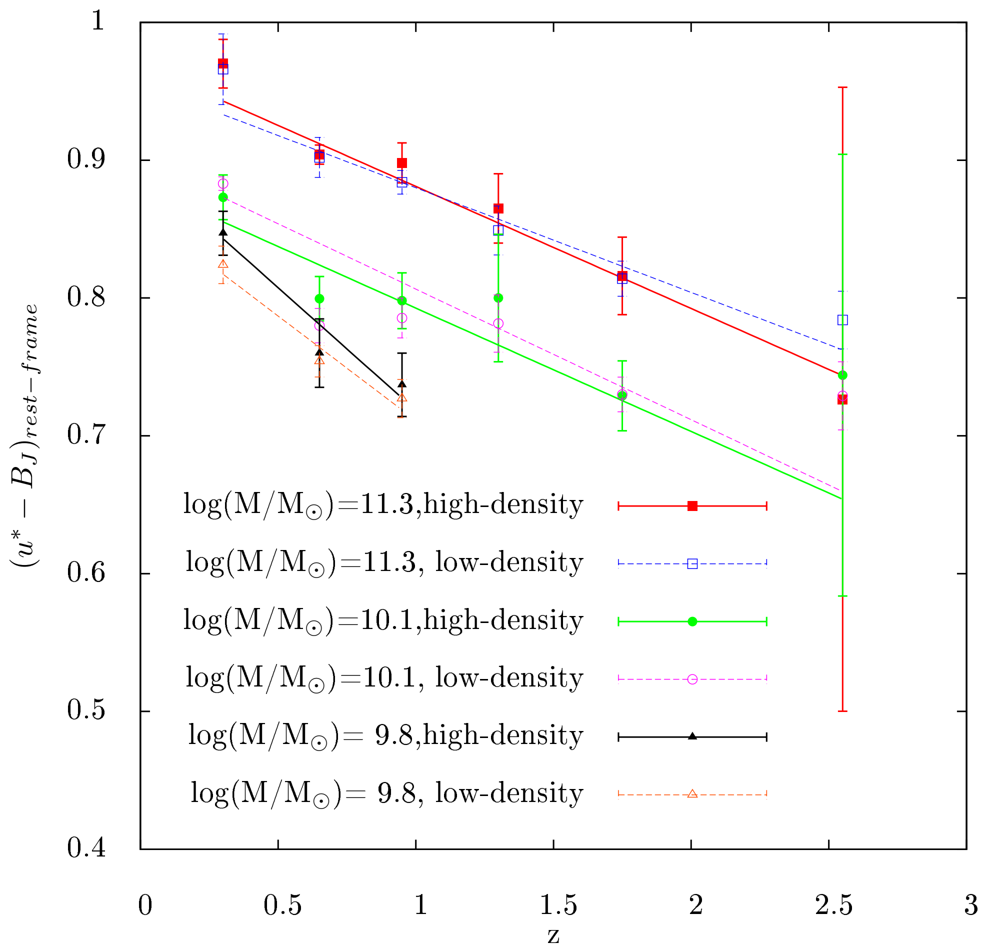

Figure 3.8: Redshift evolution of the median rest-frame u^*-B_J color for quiescent galaxies with different stellar masses located in high- and low-density environments. For clarity, the evolution is shown for only a few stellar masses. The color uncertainties are estimated using 10,000 bootstrap resamples added in quadrature to the median observational uncertainties in color. We assume that the evolution of the rest-frame u^*-B_J color for quiescent systems is linear with redshift, and fit a straight line to the median colors at any given mass and environment. At a fixed redshift and stellar mass, the color of quiescent galaxies is independent of environment. However, at a fixed redshift and environment, the color of quiescent galaxies depends on stellar mass. Quiescent galaxies become redder with cosmic time and their evolution is independent of the environment in which they reside. Quiescent galaxies more massive than $\log(M/M_\odot)\gtrsim10$ become $\sim$0.2 mag redder in rest-frame u^*-B_J color since $z\sim2.5$. Since $z\sim1$, less massive systems ($\log(M/M_\odot)\sim9.5-10$) redden by $\sim$0.1 mag, regardless of their environment. We also find that more massive quiescent galaxies ($\log(M/M_\odot)\sim11$) are $\sim$0.1 mag redder in the rest-frame u^*-B_J color compared to less massive ($\log(M/M_\odot)\sim10$) systems, and this color difference is almost independent of the environment and redshift.

and fit a straight line to the median colors at any given mass and environment:

$$(u^* - B_J)_{rest}(z) = \alpha z + (u^* - B_J)_{rest}(z = 0) \tag{3.1}$$

The result of the fit to the median colors for different environments and stellar masses is given in Table 3.2. According to Figure 3.8 and Table 3.2, quiescent galaxies become redder with cosmic time and their evolution is independent of the environment in which they reside. We particularly find that irrespective of environment, quiescent galaxies that are more massive than $\log(M/M_\odot)\gtrsim10$ become $\sim$0.2 mag redder since $z\sim2.5$. This is in agreement with Kriek et al. (2008) who showed a reddening of $\sim$0.25 mag in the rest-frame U$-$B color for massive (2×10^{11} $M_\odot$) red galaxies in the field since $z\sim2.3$. This reddening is also seen in less massive quiescent systems ($\log(M/M_\odot)$=10$-$11) and is independent of environment since $z\sim3$. Due to the incompleteness in stellar mass, we can not study the color evolution of less massive galaxies ($\log(M/M_\odot)\lesssim10$) at $z\gtrsim1$. However, at $z\lesssim1$, these systems ($\log(M/M_\odot)\sim$9.5$-$10) redden by $\sim$0.1 mag, regardless of their environment. We also see that at any given redshift out to $z\sim3$, more massive quiescent systems are redder compared with less massive systems, regardless of their environment. Particularly, we find that more massive quiescent galaxies ($\log(M/M_\odot)\sim11$) are $\sim$0.1 mag redder in the rest-frame u^*-B_J color compared with less massive ($\log(M/M_\odot)\sim10$) systems and this color difference is independent of the environment. The fact that more massive quiescent systems are redder than the less massive ones is a manifestation of the Color$-$Magnitude Relation (CMR), because the stellar mass is proportional to the luminosity (magnitude) of galaxies. The CMR is seen in both the field (less dense) and cluster (dense) quiescent galaxies, and in the local universe out to higher redshifts (see, e.g., (Bower et al., 1992; Blakeslee et al., 2003; Bell et al., 2004; Brammer et al., 2009; Mei et al., 2009; Wilson et al., 2009; Papovich et al., 2010)).

For quiescent galaxies, we find that the rest-frame color at a fixed environment depends on stellar mass, but at a fixed mass it is independent of environment. At first glance this

Table 3.2: Parameters of the Linear Fit

M	α		$(u^*\text{-}B_J)_{rest}(z{=}0)$	
$\log(M_\odot)$	High-density	Low-density	High-density	Low-density
11.3	-0.089 ± 0.020	-0.076 ± 0.010	0.969 ± 0.016	0.956 ± 0.012
10.8	-0.082 ± 0.032	-0.076 ± 0.011	0.917 ± 0.026	0.920 ± 0.016
10.5	-0.082 ± 0.023	-0.065 ± 0.016	0.916 ± 0.024	0.882 ± 0.019
10.1	-0.089 ± 0.020	-0.095 ± 0.022	0.882 ± 0.018	0.901 ± 0.018
9.8	-0.178 ± 0.041	-0.151 ± 0.035	0.896 ± 0.025	0.863 ± 0.024
9.6	-0.176	-0.157	0.885	0.853

Parameters of the linear fit ($(u^*{-}B_J)_{rest}(z){=}\alpha z{+}(u^*\text{-}B_J)_{rest}(z{=}0)$) of the rest-frame $u^*{-}B_J$ color evolution for quiescent galaxies with different stellar masses, presented in Figure 3.8.

seems to contradict the studies showing a tight correlation between color and the local density of galaxies (e.g., Balogh et al., 2004). However, the stellar mass also depends strongly on density and color−density relation is actually a manifestation of a more fundamental color−mass relation. When controlled for the stellar mass (or luminosity), the color−density relation becomes independent of the environment (overdensity).

The environmental independence of the color−mass relation is consistent with several previous studies. In the local universe, for example, Balogh et al. (2004) showed that at a fixed luminosity (equivalent to a fixed stellar mass), the mean rest-frame color of red galaxies in the SDSS at z <0.08 is nearly independent of their environment. Independently, Baldry et al. (2006) showed that at z <0.1, the color−mass distribution of galaxies (red and blue) does not significantly change with environment. The same result is also seen in Hogg et al. (2004), who found the independence of red bulge-dominated galaxy colors on the environment in the SDSS at z <0.12. Using the SDSS data, Park et al. (2007) showed that when morphology and luminosity (equivalent to stellar mass in our study) are fixed, other physical properties of galaxies, including color, are nearly independent of the local density of the galaxies. They also showed that more luminous galaxies are redder than less luminous systems, and this was independent of the environment. This is consistent with our results. The environmental invariance of color for bright galaxies in the SDSS is also seen in Tanaka et al. (2004).

Several studies at higher redshifts are also consistent with our results. For example, Cassata et al. (2007) showed that at $z \sim 0.7$ in the COSMOS field, the observed CMD for red and early-type galaxies is independent of the local density of galaxies. Scodeggio et al. (2009) found that for a sample of galaxies in the VVDS survey at $0.2 < z < 1.4$, color is independent of the local density of galaxies at a fixed stellar mass. Using the zCOSMOS data out to $z \sim 1$, Moresco et al. (2010) found that the rest-frame color of red galaxies at a fixed stellar mass is almost independent of environment, but depends on stellar mass at a fixed environment. They also found that the average colors of massive red galaxies ($\log(M/M_\odot)=10.8$) are redder than low-mass galaxies (($\log(M/M_\odot)=10$) throughout their entire redshift range. This is entirely consistent with our results in this section. By extending this study to higher redshifts, we demonstrate that the results hold to $z \sim 3$. Cucciati et al. (2010) showed that for red massive galaxies (($\log(M/M_\odot) \gtrsim 10.7$) in the zCOSMOS 10k-sample, the color−density relation is globally flat up to $z \sim 1$, which is consistent with our results. Recently, Bassett et al. (2013) compared the rest-frame U−B color of the galaxies in a cluster with those in the field at $z=1.6$ in the CANDELS-UDS field, and found no difference between the color of the quiescent galaxies in these two environments. This agrees well with our results at $z > 1$.

3.3.4 Effect of the Environment on the Comoving Number and Mass density of Massive Galaxies

In this section, we investigate the evolution of comoving number (n) and mass (ρ) density for massive ($>10^{11}$ $M_\odot$) galaxies (quiescent and star-forming) in different environments since $z \sim 3$. We start our analysis by studying the evolution of n and ρ for massive ($> 10^{11}$ $M_\odot$) quiescent/star-forming systems regardless of the environment. This allows us to compare n and ρ with previous studies that often do not consider the role of environment in the analysis. Later, we discuss the role of environment.

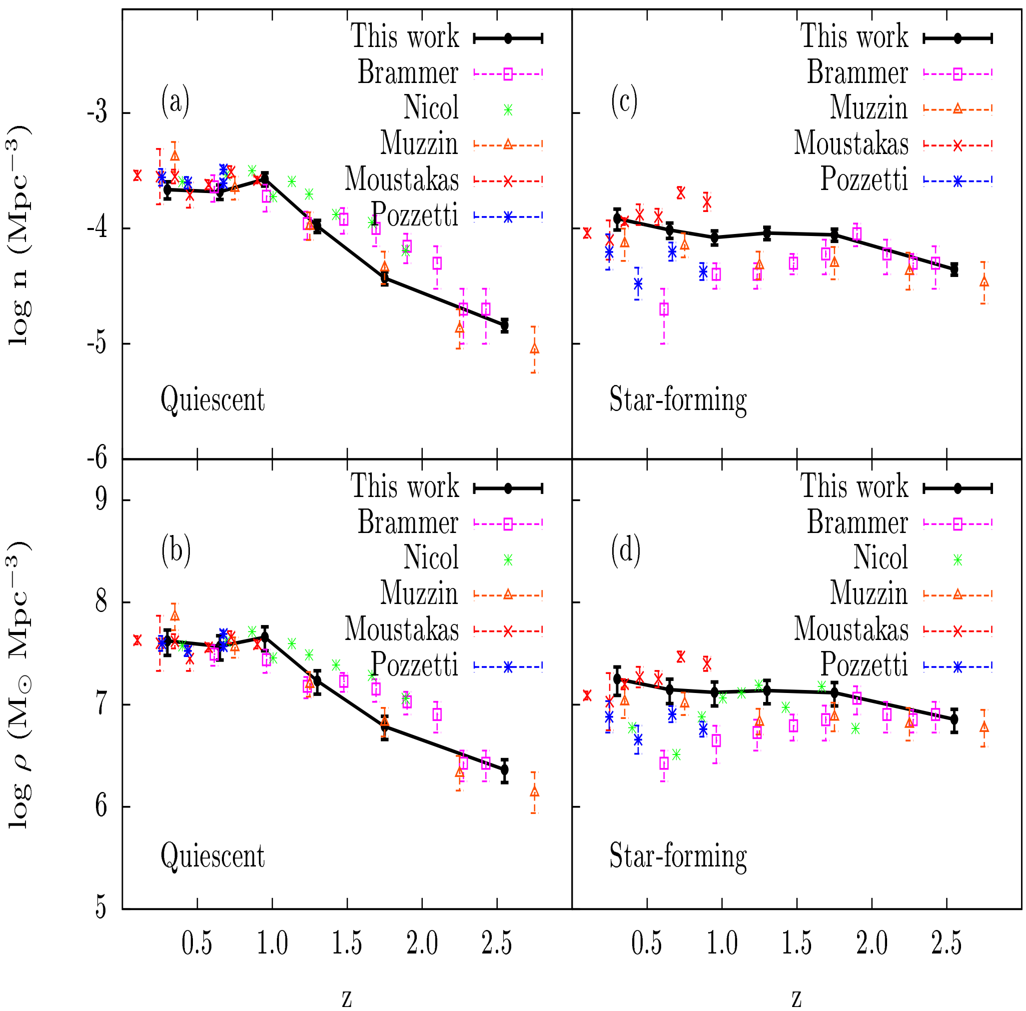

Figure 3.9: Evolution of comoving number (n) and mass (ρ) density for massive (>10^{11} $M_\odot$) galaxies (quiescent and star-forming) since z ∼3, along with a comparison with some previous studies. Error bars for number densities incorporate both Poisson error and uncertainties due to the cosmic variance. Uncertainty in mass density is estimated using 10,000 bootstrap resamples, added in quadrature to the observational uncertainties and those due to the cosmic variance. The comoving number and mass density of massive quiescent systems rapidly increase from z ∼3 to z ∼1. However, from z ∼1 to the present time, they remain almost unchanged within the uncertainties. We find almost no evolution in the comoving number and mass density of massive star-forming galaxies since z ∼2. The number and mass density of the massive star-forming galaxies are slightly increased from z=2.0−3.1 to z=1.5−2.0 (a factor of ∼2) and remain almost unaltered since then.

Table 3.3: Comoving Number Density, n (in Units of 10^{-4} Mpc^{-3}) and Mass Density, ρ (in Units of 10^{7} M$_{\odot}$ Mpc^{-3}) of Massive ($> 10^{11}$ M$_{\odot}$) Quiescent and Star-forming Galaxies in Different Redshift Bins

Property	Redshift					
	$0.1\leq z<0.5$	$0.5\leq z<0.8$	$0.8\leq z<1.1$	$1.1\leq z<1.5$	$1.5\leq z<2.0$	$2.0\leq z<3.1$
n_Q	2.17±0.37	2.08±0.30	2.68±0.35	1.05±0.13	0.37±0.05	0.15±0.02
n_{SF}	1.22±0.25	0.97±0.15	0.84±0.12	0.91±0.11	0.88±0.11	0.44±0.05
ρ_Q	4.20±1.17	3.73±1.00	4.57±1.20	1.71±0.44	0.61±0.16	0.23±0.06
ρ_{SF}	1.78±0.55	1.40±0.37	1.32±0.35	1.37±0.35	1.31±0.34	0.72±0.18

Figure 3.9 shows the evolution of the comoving number and mass density of massive ($> 10^{11}$ M$_{\odot}$) quiescent and star-forming galaxies since $z\sim3$, along with a comparison with some previous studies. Some of these studies use Kroupa IMF to estimate stellar masses. For those, we modify the mass densities based on the Chabrier IMF (M$_{Chab}\sim0.89$ M$_{Kroupa}$). The redshift of our data points is selected as the center of the redshift bins introduced for mass complete samples (Table 3.1). Error bars for number densities incorporate both Poisson error and uncertainties due to the cosmic variance. Uncertainty in mass density is estimated using 10,000 bootstrap resamples, added in quadrature to the observational uncertainties and those due to the cosmic variance. For observational uncertainties, we use the median of the stellar mass uncertainties of the galaxies in each subsample. We use the cosmic variance calculator of Moster et al. (2011) to estimate the cosmic variance uncertainties. For the $11<\log(M/M_{\odot})<11.5$ galaxies, the fractional uncertainties due to the cosmic variance change between ∼15%−10% at $\sim z$=0.1−3 in the COSMOS.

Massive Quiescent Galaxies

Figure 3.9 (a) and (b) show a rapid increase in the comoving number and mass density of massive quiescent systems from $z\sim3$ to $z\sim1$. However, we observe a change of pattern at $z\sim1$. From $z\sim1$ to the present time, the number and mass density of massive quiescent galaxies remain almost unchanged within uncertainties. From z=2−3.1 to z=1.5−2.0, the number and mass density of massive quiescent galaxies increase by a factor of ∼2.5. From

z=1.5−2.0 to z=0.8−1.1, the rise in the number and mass density of massive quiescent galaxies is steeper and they are increased by a factor of ∼6−8.

The lack of evolution (or insignificant evolution) since $z \sim 1$ in the comoving number and mass density of massive quiescent systems is consistent with several studies. In terms of sample selection, the closest works to our study are those of Ilbert et al. (2013) and Muzzin et al. (2013a). Ilbert et al. (2013) did not find any significant evolution in the number and mass density of high-mass end quiescent galaxies at $z < 1$, which is consistent with our results. As seen in Figure 3.9 (a) and (b), Muzzin et al. (2013a) data points follow our observed trends for n and ρ relatively well, within the uncertainties. As seen in Figure 3.9 (a) and (b), for quiescent galaxies at $z < 1$, our result is also in a good agreement with $>10^{11} M_{\odot}$ red-sequence galaxies in the COMBO17+4 Survey from Nicol et al. (2011), massive U−V−J selected quiescent galaxies in the NMBS survey from Brammer et al. (2011), $\log(M/M_{\odot})$=11−11.5 red galaxies in zCOSMOS from Pozzetti et al. (2010), quiescent systems in the PRIMUS survey from Moustakas et al. (2013), and $>10^{11} M_{\odot}$ rest-frame (U−V) selected red galaxies in VIPERS from Davidzon et al. (2013). Several luminosity function studies at $z < 1$, such as Scarlata et al. (2007b) and Cool et al. (2008), saw almost no evolution in the number density of very luminous (L∼2.5−3 L^{*}) red or early-type galaxies since $z \sim 1$, which is also in agreement with our results.

The sharp rise in the comoving number and mass density of massive quiescent systems from z=3-1 is also in agreement with some previous studies. For example, Ilbert et al. (2013) found that the comoving number and mass density of 10^{11} $M_{\odot}$ quiescent galaxies increase by factors of 25 and 13, respectively, between $2.5 < z < 3$ and $0.8 < z < 1.1$. This is similar to our result, which showed an increase of ∼15−20 in n and ρ from $z \sim 3$ to $z \sim 1$ for massive quiescent systems. Our results also agree qualitatively and quantitatively with Brammer et al. (2011), Domínguez Sánchez et al. (2011), Nicol et al. (2011), and Muzzin et al. (2013a).

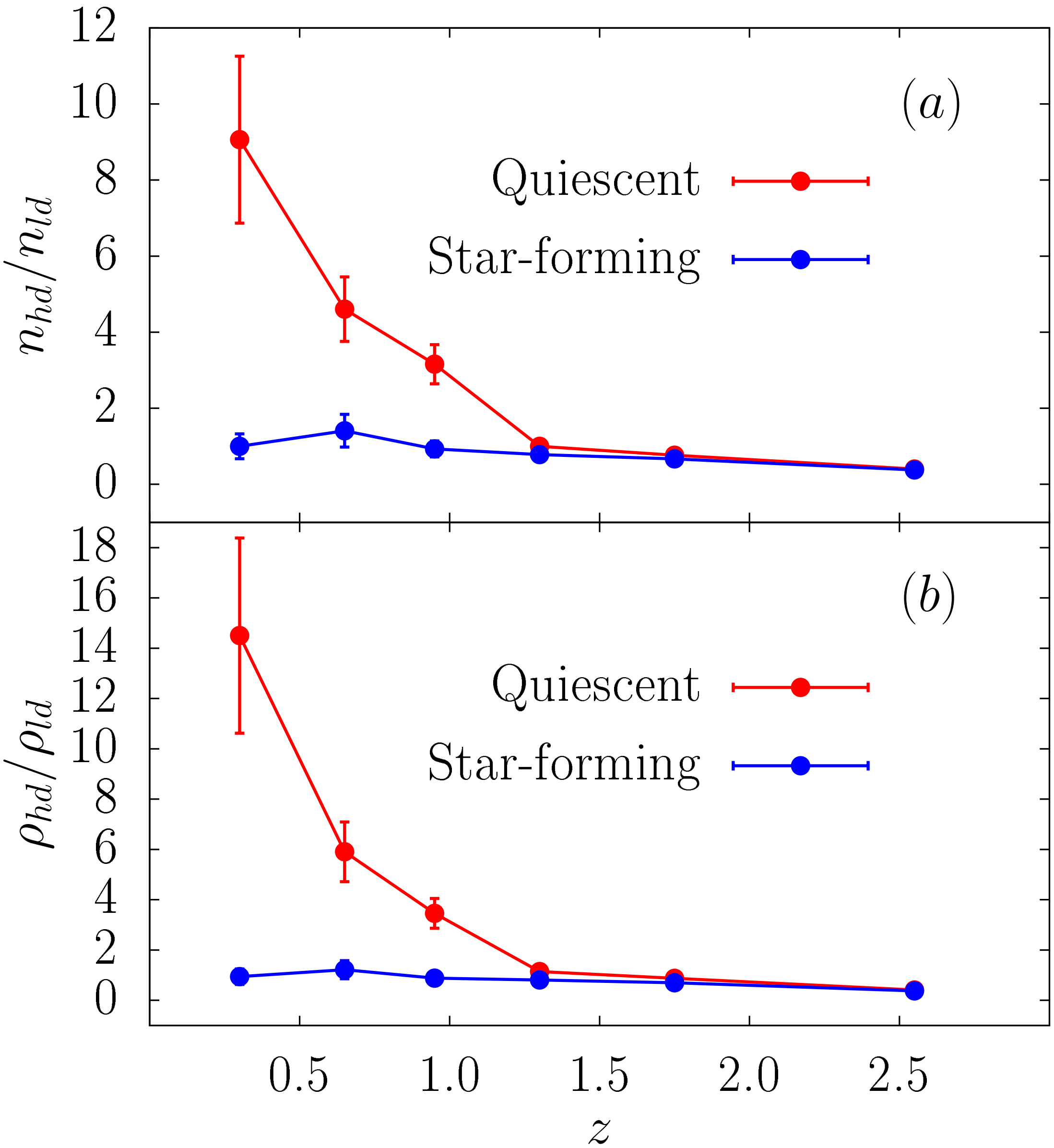

Figure 3.10: (a) The ratio of the comoving number density in high-density environments to low-density environments (n_{hd}/n_{ld}) for massive ($> 10^{11}$ $M_{\odot}$) quiescent and star-forming galaxies as a function of redshift. (b) The ratio of the stellar mass density in high-density environments to low-density environments (ρ_{hd}/ρ_{ld}) for massive ($> 10^{11}$ $M_{\odot}$) quiescent and star-forming galaxies as a function of redshift. Both number and mass density ratios do not significantly change with redshift for massive star-forming galaxies. For massive quiescent systems, these ratios significantly change at lower redshifts, indicating the prevalence of massive quiescent galaxies in denser environments at lower redshifts.

Massive Star-forming Galaxies

The situation is different for massive ($>10^{11}$ $M_\odot$) star-forming systems. According to Figure 3.9 (c) and (d), we find almost no evolution in the comoving number and mass density of star-forming galaxies since z ∼2. The number and mass density of massive star-forming galaxies are slightly increased from z=2.0−3.1 to z=1.5−2.0 (a factor of ∼2) and remain almost unaltered since then. This slight (insignificant) increase is seen in Brammer et al. (2011) from z ∼2.5−2.0, followed by a decline since z ∼2. In our study we do not find any sign of decline in the comoving number and mass density of the massive star-forming systems since z ∼2.[3]. Our result also agrees well with Pozzetti et al. (2010), Davidzon et al. (2013), Ilbert et al. (2013), Muzzin et al. (2013a), and Sobral et al. (2014). However, Moustakas et al. (2013) found that the number (and mass) density of massive star-forming galaxies are decreased slightly by a factor of ∼2 since z ∼1 (Figure 3.9 (c) and (d)). Within the uncertainties, we do not find a significant disagreement between our result and that of Moustakas et al. (2013), although we detect no evolution in n and ρ for massive star-forming galaxies. We argue that even in the presence of a real evolution in number and mass density of massive star-forming systems since z ∼1, we would not be able to observe it due to the larger error bars in our study compared with Moustakas et al. (2013).

The comoving number and mass density values for massive ($> 10^{11}$ $M_\odot$) quiescent and star-forming populations are given in Table 3.3.

Massive Quiescent/Star-forming Systems in Different Environments

Now, we investigate the role of the environment in shaping the number and mass density of massive quiescent and star-forming galaxies. In order to estimate comoving number and mass densities in different environments, one needs to determine what fraction of the density field is occupied by massive galaxies in different environments. Practically, this is not straightforward because the definition of environment and the selection of low- and

[3] Brammer et al. (2011) state in their paper that the comoving number density evolution of $>10^{11}$ $M_\odot$ star-forming galaxies is nearly flat out to z=2.0

high-density regions are arbitrary. We highlight that we only wish to *relatively* compare the number and mass densities in different environments, rather than determine the exact values in these regions. If there are any systematic errors in determining the number and mass densities in different environments, they would likely be cancelled out because we take the ratio of these in low- and high-density regions. We define the ratio of the comoving number density of massive ($> 10^{11}$ M$_\odot$) galaxies in high-density (n_{hd}) to low-density (n_{ld}) environments as:

$$\frac{n_{hd}}{n_{ld}} = \frac{\sum_i 1/V_i^{hd}}{\sum_j 1/V_j^{ld}} \tag{3.2}$$

where V_i^{hd} and V_j^{ld} are the volumes associated with the ith and jth massive galaxy in high- and low-density environments, respectively. The volume assigned to each galaxy is estimated using its Voronoi area (A) and the radial comoving length (Δl) that corresponds to its z-slice; i.e. V_i=$A_i \Delta l_i$. Similarly, we define the ratio of the mass density of massive ($> 10^{11}$ M$_\odot$) galaxies in high-density (ρ_{hd}) to low-density (ρ_{ld}) environments as:

$$\frac{\rho_{hd}}{\rho_{ld}} = \frac{\sum_i M_i^{hd}/V_i^{hd}}{\sum_j M_j^{ld}/V_j^{ld}} \tag{3.3}$$

where M_i^{hd} and M_j^{ld} are the stellar masses associated with the ith and jth massive galaxy in high- and low-density environments, respectively.

Figure 3.10 shows the redshift evolution of n_{hd}/n_{ld} and ρ_{hd}/ρ_{ld} for massive quiescent and star-forming galaxies. Uncertainties in number density ratios incorporate both Poisson error and the cosmic variance. The error bars for mass density ratios are estimated using 10,000 bootstrap resamples added in quadrature to the observational uncertainties in stellar mass and those due to the cosmic variance. For massive ($> 10^{11}$ M$_\odot$) star-forming systems, the number and mass densities in different environments remain almost the same, and we find almost no evolution in the comoving number and mass density ratios in different environments with cosmic time. Massive star-forming galaxies populate dense and less-dense regions almost equally, regardless of their redshift. The situation is different for massive quiescent galaxies. At $z \gtrsim 1.3$, there is no significant evolution in the comoving number and mass density ratios in different environments. At these redshifts, the number and mass density ratios for massive quiescent galaxies are almost equal to those of massive star-forming systems. However, at lower redshifts ($z \lesssim 1.3$), we find a significant evolution in the comoving number and mass density ratios for massive quiescent systems in different environments. These ratios for massive quiescent galaxies monotonically increase with cosmic time at $z \lesssim 1.3$. At $z \lesssim 0.5$, the number and mass density of massive quiescent galaxies are ∼1 dex higher in denser regions compared with less-dense environments. Dense environments at low redshifts are populated by massive quiescent galaxies.

It is challenging to make a direct, quantitative comparison between our results in this section and similar studies in the literature, due to the differences in sample selections, the definition of environment, and the classification of low- and high-density regions. However, we *qualitatively* compare our results in this section with some similar studies. Using zCOSMOS data at $z <1$, Bolzonella et al. (2010) studied the galaxy stellar mass function (SMF) as a function of galaxy type and environment. They found that massive galaxies are preferentially located in high-density environments, which are characterised on average by a higher M^* and that the spectral-type selected early-type galaxies dominate the high-mass ($\log(M/M_{\odot}) \gtrsim 10.7$) end of the SMF. In other words, massive red galaxies are preferentially reside in high-density regions at z$\lesssim$1, which is in agreement with our results for massive quiescent galaxies in dense environments. Recently, Mortlock et al. (2015) studied the SMF of galaxies in the UKIDSS/UDS and CANDELS fields, and found that at higher redshifts ($z >1$), the SMF parameters for galaxies in low and high densities are almost the same. However, at $z <1$, they found evidence that (1) the high-mass end of the galaxy SMF is more dominated by galaxies in dense environments, (2) The high-mass end of the Sérsic index > 2.5 SMF is dominated by quiescent galaxies, and (3) on average, ϕ^* and M^* values of the SMF are larger for red galaxies in denser regions compared with those in less-dense environments (At $z \sim 0.5$, ϕ^* is ∼1 dex larger for red galaxies in denser regions, which is similar to our result in this section). Combining these results, we conclude that at lower redshifts, high-density environments cause the build-up of high-mass, quiescent galaxies.

This is completely consistent with our results in this section regarding the higher number and mass densities in denser regions for massive, quiescent systems at lower redshifts, as well as the lack of any significant differences at higher redshifts.

We stress that our results here rely on the density field estimation based on the flux-limited sample (K_s <24) introduced in Section 2.2. However, as we already discussed in Section 3.2, this magnitude cut results in a sample with varying stellar mass as a function of redshift. In other words, the "typical" galaxies defining the environment change with redshift, with less massive galaxies defining the low-z and more massive systems defining the high-z environments. Because there is some degree of correlation between the galaxy stellar mass and environment (Kauffmann et al., 2004; Baldry et al., 2006), our results in this section may be affected by the selection of galaxies used to estimate the density field (environment). However, in the appendix, we investigate the role of different samples used for density estimation on the results, and will show that the results do not change (they even become stronger) and we recover the same trends discussed in this section.

We conclude that the comoving number and mass density of massive, star-forming systems do not evolve much with redshift, regardless of their environment. This scenario is also true for massive, quiescent galaxies at higher redshifts ($z \gtrsim 1.3$). However, at lower redshifts, the comoving number and mass density of massive, quiescent galaxies are greater in high-density environments compared with less-dense regions. This highlights the significant role of the environment in quenching the star-formation activity in galaxies at lower redshifts.

We stress that the lack of environmental effects on the properties of galaxies at higher redshifts ($z \gtrsim 1$) may be partly due to the growth of the large-scale structure with cosmic time and the cosmic variance. As time progresses, less-dense environments eventually coalesce to assemble more massive, denser regions. Therefore the absence of the environmental effects does not necessarily mean that the environment at higher redshifts is not able to quench the star-formation activity in galaxies as effectively as it does at lower redshifts. The likelihood of finding massive halos that are able to suppress the star-formation activity at higher redshifts is low, given the small size of the COSMOS field and the rarity of massive halos at higher redshifts. If we could numerously find such dense massive halos at higher redshifts in our survey, we might be able to see similar environmental trends to those we observe in lower redshifts and the local universe.

3.4 Summary and Conclusions

In this chapter, we studied the effects of the environment on a mass complete sample of quiescent and star-forming galaxies out to z$\sim$3 in the COSMOS field. The rest-frame NUV$-r^+-$J color-color plots were used to separate the galaxy population into quiescent and star-forming systems. We investigated the median SFR, sSFR, quiescent fraction, rest-frame color, and the comoving number and mass density of galaxies as a function of their environment (overdensity), stellar mass, galaxy type, and redshift. Our main results are:

1. The median SFR and sSFR of galaxies are strong functions of environment at $z\lesssim1$, in a sense that they both decrease with increasing overdensity at $z\lesssim1$. However, at $z\gtrsim1$, they are almost independent of the environment.

2. When we only consider the star-forming galaxies, their median SFR and sSFR do not significantly change with environment out to $z\sim3$. In other words, if a galaxy is star-forming, on average, its SFR and sSFR are unaltered by its host environment. However, denser environments increase the chance of a galaxy to become quiescent. Hence, the role of environment seems to control the fraction of star-forming and quiescent galaxies.

3. At a given overdensity, the median SFR and sSFR of galaxies (quiescent and star-forming) are higher at higher redshifts compared to lower-z samples, indicating an overall decline in the global star-formation activity in galaxies since $z\sim$2-3.

4. The fraction of quiescent galaxies significantly changes with environment (overdensity) at $z\lesssim1$, and it is higher in denser regions. However, at $z\gtrsim1$, it is almost independent

of the environment. At a given overdensity, the fraction of quiescent galaxies is always higher at lower redshifts. This is an indication of the Butcher-Oemler effect.

5. The quiescent fraction growth rate is almost independent of environment at look-back time $\gtrsim$8 Gyr. However, at lower redshifts (look-back time $\lesssim$8 Gyr), it increases with increasing overdensity. Galaxies become quenched more rapidly in denser environments compared to less-dense regions.

6. The fraction of quiescent galaxies depends on stellar mass at all the redshifts considered in this study (0.1< z <3.1), and it is higher for more massive systems. At a given stellar mass, the fraction of quiescent galaxies is higher at lower redshifts. This is another manifestation of the galaxy mass-downsizing. We estimate the typical time delay between the quenching of less massive (log(M/$M_{\odot}$)$\sim$10) and more massive (log(M/$M_{\odot}$)$\sim$11) galaxies to be Δt $\sim$3.4$\pm$0.9 Gyr.

7. At all the redshifts considered in this study (0.1< z <3.1), the fraction of quiescent galaxies at a fixed environment strongly depends on stellar mass, i.e., the fraction of quiescent galaxies at all fixed density levels is always higher for more massive galaxies compared to less massive systems out to z$\sim$3. However, at a fixed stellar mass, quiescent fraction depends on environment (overdensity) only at $z\lesssim$1 and not significantly at higher redshifts. At a fixed stellar mass and at z$\lesssim$1, this fraction is higher in denser regions. All these results suggest that environmental quenching is practically important at $z\lesssim$1, whereas mass quenching is the major factor of star-formation truncation in galaxies at $z\gtrsim$1.

8. At a given stellar mass, the median rest-frame u^*-B_J color of quiescent galaxies is independent of the environment in which they reside. Quiescent galaxies become redder with cosmic time and their color evolution is independent of their environment. Since z $\sim$3, more massive quiescent galaxies (log(M/$M_{\odot}$)$\gtrsim$10) have become $\sim$0.2 mag redder in rest-frame u^*-B_J, whereas less massive quiescent systems have reddened by $\sim$0.1 mag since z $\sim$1.

9. On average, more massive quiescent galaxies are redder compared to less massive ones at any given redshift, regardless of their environment. The lack of a correlation between color and environment at fixed stellar mass for quiescent galaxies suggests that the relation between stellar mass and the local density of the galaxies is more fundamental than the color−density relation.

10. The average comoving number and mass density of massive ($\log(M/M_{\odot})>11$) star-forming galaxies have not evolved much since $z\sim3$. However, for massive quiescent galaxies, number and mass densities rise sharply from $z\sim3$ to $z\sim1$ and remain almost unchanged since then.

11. The evolution of the comoving number and mass density of massive star-forming galaxies do not depend on their environment. They remain almost unchanged since $z\sim3$, regardless of their host environment. The situation is different for massive quiescent galaxies. The comoving number and mass density of massive quiescent galaxies do not change much with environment and redshift from $z\sim3$ to $z\sim1.3$, which is similar to those of star-forming galaxies. However, at lower redshifts ($z\lesssim1.3$), we find a significant evolution in the number and mass density of massive quiescent galaxies in denser environments compared with less-dense regions. Dense environments at lower redshifts are populated with massive quiescent galaxies, which signifies the role of the environment in quenching the star-formation activity in galaxies at lower redshifts.

Chapter 4

Cosmic Web and Star Formation Activity in Galaxies

Abstract

In this chapter, we investigate the role of the delineated cosmic web/filaments on star-formation activity by exploring a sample of 425 narrow-band selected Hα emitters, as well as 2846 color$-$color selected underlying star-forming galaxies for a large-scale structure at z=0.84 in the COSMOS field from the HiZELS survey. Using the scale-independent Multi-scale Morphology Filter algorithm, we are able to quantitatively describe the density field and disentangle it into its major components: fields, filaments, and clusters. We show that the observed median star-formation rate (SFR), stellar mass, specific star-formation rate (sSFR), the mean SFR$-$mass relation, and its scatter for both Hα emitters and underlying star-forming galaxies do not strongly depend on different classes of environment, in agreement with previous studies. However, the fraction of Hα emitters varies with environment and is enhanced in filamentary structures at $z\sim$1. We propose mild galaxy$-$galaxy interactions as the possible physical agent for the elevation of the fraction of Hα star-forming galaxies in filaments. Our results show that filaments are the likely physical environments that are often classed as the "intermediate" densities, and that the cosmic web likely plays

a major role in galaxy formation and evolution which has so far been poorly investigated.

4.1 Introduction

It is well known that the properties of galaxies are directly affected by their host environment. In the local universe, red, passive, early-type galaxies reign over-densities and galaxy clusters while blue, star-forming, late-type galaxies are preferentially found in less-dense, field environments (e.g., Dressler, 1980; Kauffmann et al., 2004; Balogh et al., 2004). The same trends are seen with stellar mass; i.e., on average, more massive galaxies are redder (e.g., Baldry et al., 2006), less star-forming (e.g., Peng et al., 2010) and more likely have early-type morphologies (e.g., Bamford et al., 2009). Since both environment and stellar mass influence the observable properties of galaxies, it is important to consider the effects of both and their fractional role on the evolution of galaxies.

For example, a tight relation has been recently found between the SFR and stellar mass of star-forming galaxies (i.e., the "main sequence"), showing that more massive star-forming galaxies are more actively forming stars (Brinchmann et al., 2004; Daddi et al., 2007; Elbaz et al., 2007; Noeske et al., 2007b; Karim et al., 2011; Reddy et al., 2012 see also Speagle et al., 2014 for a full list of references). The role of the environment on this SFR−mass relation, along with its slope, intercept and intrinsic scatter, and the evolution of all these parameters with look-back time can impose strong constraints on scenarios of formation and evolution of galaxies (Noeske et al., 2007a; Daddi et al., 2007; Whitaker et al., 2012). As a result, an increasing number of studies are now focused on the role of environment on the SFR−mass relation, with rather controversial results especially at $z \gtrsim 1$ (e.g. Koyama et al., 2013b; Zeimann et al., 2013).

Current studies of the environmental dependence of the SFR in galaxies at $z \gtrsim 1$ have led to conflicting results. Some agree with the relations observed in the local universe (Patel et al., 2009), some report no/weak dependence on the environment (Grützbauch et al., 2011; Scoville et al., 2013), and there are even claims for a reversal of the SF−density relation (higher star-formation in denser regions Elbaz et al., 2007; Cooper et al., 2008a; Tran et al., 2010). Sobral et al. (2011) also showed that at $z \sim 1$, there is an increase of SF activity for star-forming galaxies at intermediate densities, likely associated with galaxy groups, followed by a decline for the richest clusters and that this is the reason for discrepancies: some studies only reach up to poor group environments, while others only probe rich clusters. Sobral et al. (2011) showed that once the full range of environments is probed and correctly labeled, all the apparently contradictory results can be fully reconciled.

Studies of the effect of large-scale structure on properties of galaxies have so far been mostly confined to field versus cluster environments. However, there are intermediate environments such as galaxy groups, outskirts of clusters, and filaments which are equally important (e.g., see Kodama et al., 2001). Thus, a rising number of studies now highlight the importance of intermediate environments, revealing an enhancement of mean SFR (Porter and Raychaudhury, 2007; Porter et al., 2008; Sobral et al., 2011; Coppin et al., 2012) or the fraction of star-forming galaxies (see Section 4.4.1 for more references) in medium environments. However, the environment in these studies is often loosely defined as the excess number of galaxies or visual inspection of overdensities. Indeed, a density-based definition of environment cannot differentiate between regions with intermediate densities such as filaments, groups, and periphery of clusters. These could have the same local number density but host different physical processes (e.g., Aragón-Calvo et al., 2010 showed that a pure density-based structural identification does not provide an accurate description of reality given the overlap among different parts of the LSS and that environment defined only in terms of density fails to incorporate the intrinsic dynamics of the LSS).

The explicit role of the geometry and dynamics of the "cosmic web" (Bond et al., 1996)—a web-like structure containing dense clusters, sparsely populated voids, planar walls, and thread-like filamentary structures linking overdense regions—in the formation and evolution of galaxies is relatively unexplored. The geometry and dynamics of the cosmic web, as revealed by numerical simulations such as the Millennium simulation (Springel et al., 2005; Boylan-Kolchin et al., 2009) and large spectroscopic surveys in the local universe such as 2dFGRS (Colless et al., 2001) and SDSS (York et al., 2000), can be approximated by collapse of a primordial gas cloud along its three main axes through successive stages, first leading to the formation of a wall, subsequently a filament, and finally a cluster (Zel'dovich, 1970; Shandarin and Zeldovich, 1989). The difficulty of this natural approach toward the definition of environment lies in the limitation to numerical simulations (Colberg et al., 2005; Stoica et al., 2005; Aragón-Calvo et al., 2007) or spectroscopic surveys in the local universe (Tempel et al., 2014).

In this chapter, we study the star-formation activity in a super-structure ($\sim$10$\times$15 Mpc) at z $\sim$0.8$-$0.9 in the Cosmic Evolution Survey (COSMOS) field (Scoville et al., 2007b) by identifying a striking filamentary structure linking clusters and groups, which is also traced by the distribution of narrow-band selected star-forming galaxies at this redshift (Sobral et al., 2011, 2013a). Here, the cosmic web is robustly described by the Multi-scale Morphology Filter (MMF) algorithm (Chapter 1) in a consistent and homogeneous manner. The Hα emission line is used as diagnostic of SF activity. The multi-waveband capabilities, as well as the wealth of ancillary information in the COSMOS field including accurate photometric redshifts (photo-z) (Δz $\sim$0.01 out to z $\sim$1) and stellar masses (ΔM$\sim$0.1 dex) also equip us with a reliable distribution of the underlying control sample of galaxies at z $\sim$0.85.

The format of this chapter is as follows. In Section 2, we briefly review the data, explain stellar mass and star-formation rate measurements, and discuss completeness and contamination in the data. Section 3 presents the methods used to identify the LSS. The main results of this work, along with comparison with other studies are given in Section 4 and discussed in Section 5. We give a summary of this chapter in Section 6.

Throughout this chapter, we assume a flat concordance ΛCDM cosmology with H_0=70 kms^{-1} Mpc^{-1}, Ω_m=0.3 and Ω_Λ=0.7. All magnitudes are expressed in the AB system and stellar masses and star-formation rates are given assuming a Chabrier initial mass function (IMF).

4.2 The Data

For this study, we use a sample of narrow-band selected star-forming galaxies and an underlying control sample (star-forming and quiescent) selected to the same magnitude and mass limits and with the same areal coverage. The star-forming sample is based on Hα emission line which directly originates from HII regions in star-forming galaxies and is an excellent tracer of the SFR. The star-forming sample is mainly used as a robust indicator of star-formation activity for which environmental effects will be studied. The control sample here is primarily used to identify the LSS (Section 4.3) and to determine the fraction of Hα star-forming galaxies associated with the LSS (Section 4.4.1). The star-forming galaxies in the control sample are also used to double-check the validity of results based on the Hα selected star-forming sample and to investigate the role of different SFR estimators on the results. In the following subsections, we describe each of these samples in more detail, along with their stellar mass and SFR estimations and their corresponding completeness and contamination.

4.2.1 The Star-forming Sample

This consists of a complete sample of Hα emitting star-forming galaxies at z=0.845, selected through narrow-band near-infrared (J filter) observations, performed as a part of the High-z Emission Line Survey (HiZELS) (Geach et al., 2008; Sobral et al., 2009, 2012, 2013a), covering an area of $\sim$0.8 deg^2 in the COSMOS field (Scoville et al., 2007b). The sample includes a total of 425 galaxies with K<23 and log(M/M$_\odot$)$\geq$9, located in a narrow redshift slice of Δz=0.03 centered at z=0.845 (0.83$\leq z \leq$0.86). This sample is flux limited ($\sim 8 \times 10^{-17}$ ergs^{-1}cm^{-2} which is equivalent to the SFR limit of $\sim$ 1.5 M$_\odot$yr^{-1} at z $\sim$0.84) and is selected homogeneously down to the rest-frame Hα+[NII] equivalent width limit of $\sim$ 25 Å. For more properties of this sample, see, e.g., Sobral et al. (2011) and Sobral et al. (2014).

4.2.2 The Control Sample

The control sample is based on the COSMOS UltraVISTA K_s-band selected photometric redshift catalog (Ilbert et al., 2013; McCracken et al., 2012). The K_s-band selected catalog consists of ground- and space-based imaging data in 30 bands. Due to the large number of filters covering a broad wavelength range, the photometric redshifts are very secure. It has been shown that at z <1.5, the photo-z accuracy is better than 1% with less than 1% of catastrophic failure (Ilbert et al., 2013). At the redshift of this study, the median redshift uncertainty is $\Delta z \sim$0.01. Galaxies in the control sample have the same magnitude, mass, and areal coverage as the Hα sample and have more than 10% probability of belonging (P_{limit}=0.1) to the redshift slice of Hα emitters (0.83$\leq z \leq$0.86). This probability weight is calculated by measuring what percentage of the photo-z probability distribution function (PDF) for each galaxy lies within the redshift slice defined by the narrow-band Hα sample. This results in a K_s-band selected sample containing 3920 galaxies. Increasing the P_{limit} results in a control sample less contaminated by foreground and background sources. However, this also has an increasing risk of losing sources; i.e., a less complete sample at $z \sim$0.84 (see Section 4.2.4). Here, we use a 10% cut as a trade-off between contamination and completeness. Nevertheless, we scrutinized a variety of probability limits (0.05, 0.2, 0.3, 0.4, and 0.5) and were able to retrieve the same results.

The underlying galaxies were later divided into quiescent and star-forming systems based on their rest-frame two-color NUV$-r^+$ versus r^+-J plot. Previous studies show that the rest-frame NUV$-r^+$ color is a better indicator of the recent star-formation activity (Martin et al., 2007) and has a wider dynamical range compared to the rest-frame U$-$V color (Ilbert et al., 2013). Here, galaxies with rest-frame color NUV$-r^+ >$ 3.1 and NUV$-r^+ >$ 3(r^+-J)+1 are selected as quiescent systems. Figure 4.1 shows the rest-frame NUV$-r^+$ versus r^+-J distribution of galaxies in the control sample and the color cuts used to separate quiescent and star-forming systems. We clearly see two populations of galaxies. We stress that adding dust to the star-forming galaxies causes them to move diagonally from the bottom left to the top right of Figure 4.1, making them separable from the quiescent systems

(Ilbert et al., 2013). The star-forming galaxies in the control sample will later be used, along with the Hα sample, to study the effects of different SFR estimators on the results.

4.2.3 Mass and SFR Estimation

Mass and SFR for the Star-forming Sample

For the Hα sample, the stellar masses were estimated by SED template fitting using rest-frame UV, optical, near-, and mid-IR data available in 18 bands as explained in Sobral et al. (2011) and Sobral et al. (2014). The synthetic templates were generated using Bruzual (2007) models, assuming a Chabrier IMF, five different metallicities, an exponentially declining SFH with different e-folding time scales (τ=0.1$-$10 Gyr), and Calzetti et al. (2000) dust extinction. Stellar masses here are based on the median of the stellar mass PDF, marginalized over all other parameters. The Hα sample is complete to log(M/M$_\odot$)$\sim$9$-$9.5 at z=0.84 and the stellar mass has a typical observational uncertainty of ΔM$\sim$0.1 dex.

Hα fluxes are obtained by computing the emission line flux within the narrow-band J filter, after removing the contribution from the [NII] line. The [NII] contribution is estimated using the relation between [NII]/Hα line ratio and the rest-frame Hα+[NII] equivalent width from SDSS (Villar et al., 2008). This relation seems to hold true at the redshift of our study (Stott et al., 2013). Hα luminosities are based on 2$''$ diameter aperture photometry ($\sim$16 kpc physical diameter at z $\sim$0.84). Since we miss $\sim$23% of the total flux in the 2$''$ aperture (Sobral et al., 2014), a correction factor of 1.3 is applied to the measured luminosities. Dust-corrected Hα star-formation rates were obtained using aperture corrected Hα luminosities and the relation from Kennicutt (1998), modified for a Chabrier IMF: SFR(M$_\odot$yr^{-1})=4.4$\times$10^{-42}L$_{H\alpha}$(ergs^{-1}). Dust correction was performed based on the empirical relation between median stellar mass and median dust extinction presented in Garn and Best (2010). This relation is shown to be applicable to star-forming galaxies at least up to z $\sim$1.5 without evolution (Sobral et al., 2012; later confirmed by Ibar et al., 2013, Domínguez et al., 2013, and Price et al., 2014). The typical observational uncertainty in the SFR is dominated by the uncertainty in the dust correction (ΔSFR$\sim$0.2 dex).

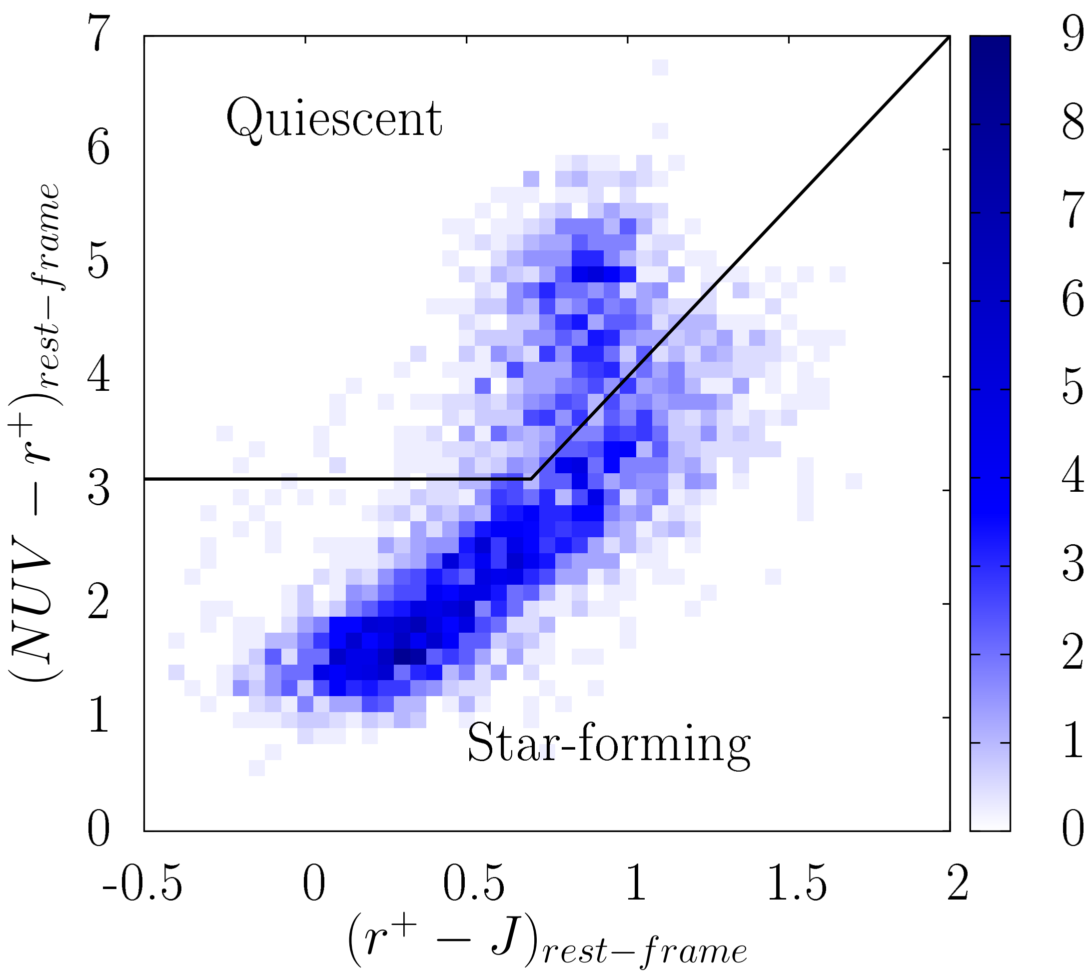

Figure 4.1: Rest-frame NUV$-r^+$ versus r^+-J color distribution of galaxies in the control sample. Two populations of galaxies are seen here. The black solid line shows the cut we used to separate the quiescent galaxies from the star-forming systems.

Mass and SFR for the Control Sample

Stellar masses for galaxies in the control sample were derived as explained in Ilbert et al. (2013). This was performed by generating a library of synthetic spectra using BC03 (Bruzual and Charlot, 2003) with a Chabrier IMF, three different metallicities, an exponentially declining SFH with different e-folding time scales (τ=0.1−30 Gyr), and a Calzetti et al. (2000) extinction law. Contributions from nebular emission lines were included. These synthetic spectra were fitted to the rest-frame multi-color photometry from UV to mid-IR using the "Le Phare" code (Arnouts et al., 2002; Ilbert et al., 2006). The stellar mass for the control sample corresponds to the median of the stellar mass PDF, marginalized over all other parameters. At $z \sim 1$, we detect galaxies with masses as low as $\log(M/M_{\odot}) \sim 8.9$ given a sample selected at $K_s < 23$. We estimate the mass completeness limit following the procedure explained in Ilbert et al. (2013) and Pozzetti et al. (2010). The typical observational uncertainty of stellar mass for the control sample is $\Delta M \sim 0.1$ dex. These stellar masses are also available for the majority of Hα emitters.

Dust-corrected star-formation rates are derived from the rest-frame NUV continuum (NUV corresponds to the *GALEX* filter centered on 0.23 μm) and the *Spitzer* 24 μm flux (for galaxies with 24 μm detections). Rest-frame observed and extinction-corrected NUV flux were calculated in Ilbert et al. (2013). *GALEX* NUV flux values were estimated from the BC03 best-fit photo-z SED templates using the NUV magnitudes computed by Zamojski et al. (2007). The *Spitzer* 24 μm flux is extracted from the available catalogs as part of the S-COSMOS survey (Sanders et al., 2007). MIPS 24 μm total flux was computed by Aussel and Le Floc'h (Le Floc'h et al., 2009) assuming a 10,000 K blackbody as the underlying spectrum. The SFRs are estimated in one of the two ways explained below:

1. For galaxies with no 24 μm detection, we use the equation given in Kennicutt (1998), modified for the Chabrier IMF, in order to estimate SFR based on the dust-corrected NUV continuum flux (L_{NUV}^{corr}): $\mathrm{SFR}(M_{\odot}\mathrm{yr}^{-1})=0.786\times10^{-28}L_{NUV}^{corr}(\mathrm{ergs}^{-1}\mathrm{Hz}^{-1})$.

2. For galaxies with available 24 μm flux, the SFR is estimated based on the observed 24

μm flux density using the relation given in Rieke et al. (2009): log(SFR($M_{\odot}yr^{-1}$))= $A(z)$+$B(z)$(log(4π $D_L^2 f_{obs}$)-53), where $A(z)$ and $B(z)$ are redshift- and wavelength-dependent constants, D_L is the luminosity distance in cm, and f_{obs} is the observed 24 μm flux density in Jy. Here, we use $A_{24}(z{=}0.8)$=0.445 and $B_{24}(z{=}0.8)$=1.381 (Rieke et al., 2009).

The typical uncertainty in the SFR for the control sample is ΔSFR$\sim$0.1 dex.

4.2.4 Completeness and Contamination

In order to estimate the completeness and contamination in both the Hα and the underlying control samples, we use the VLT-VIMOS zCOSMOS spectroscopic survey (Lilly et al., 2007) selected as i^+ <22.5. Here, only the highly reliable spectroscopic redshifts are considered (Classes 3 and 4 with spectroscopic reliability > 99.5%). Using the spectroscopic data, we estimate the completeness as the ratio of the number of underlying galaxies in the control sample that have spectroscopic redshifts within the Hα redshift slice (0.83$\leq$ z $\leq$0.86) to the total number of galaxies with spectroscopic redshifts in the same slice. Contamination is computed as the fraction of galaxies in the underlying control sample with spectroscopic redshifts located outside the Hα redshift slice. Previous studies show the Hα sample to be < 4% contaminated and > 96% complete (see Sobral et al., 2010 and Sobral et al., 2013a). For the control sample, we estimate the contamination and completeness to be 64% and 74%, respectively (Figure 4.2). As explained in Section 4.2.3, a probability limit of 10% (P_{limit}=0.1) was used to select galaxies in the control sample; i.e., galaxies have a likelihood of > 10% belonging to the redshift slice 0.83$\leq$ z $\leq$0.86 set by the Hα sample. A higher probability limit results in a more reliable and less contaminated control sample. However, this also leads to a less complete and statistically smaller sample. Figure 4.2 shows completeness and contamination fractions in the control sample as a function of the probability limit (P_{limit}) used to define it. Completeness declines with increasing probability limit faster than contamination decreases.

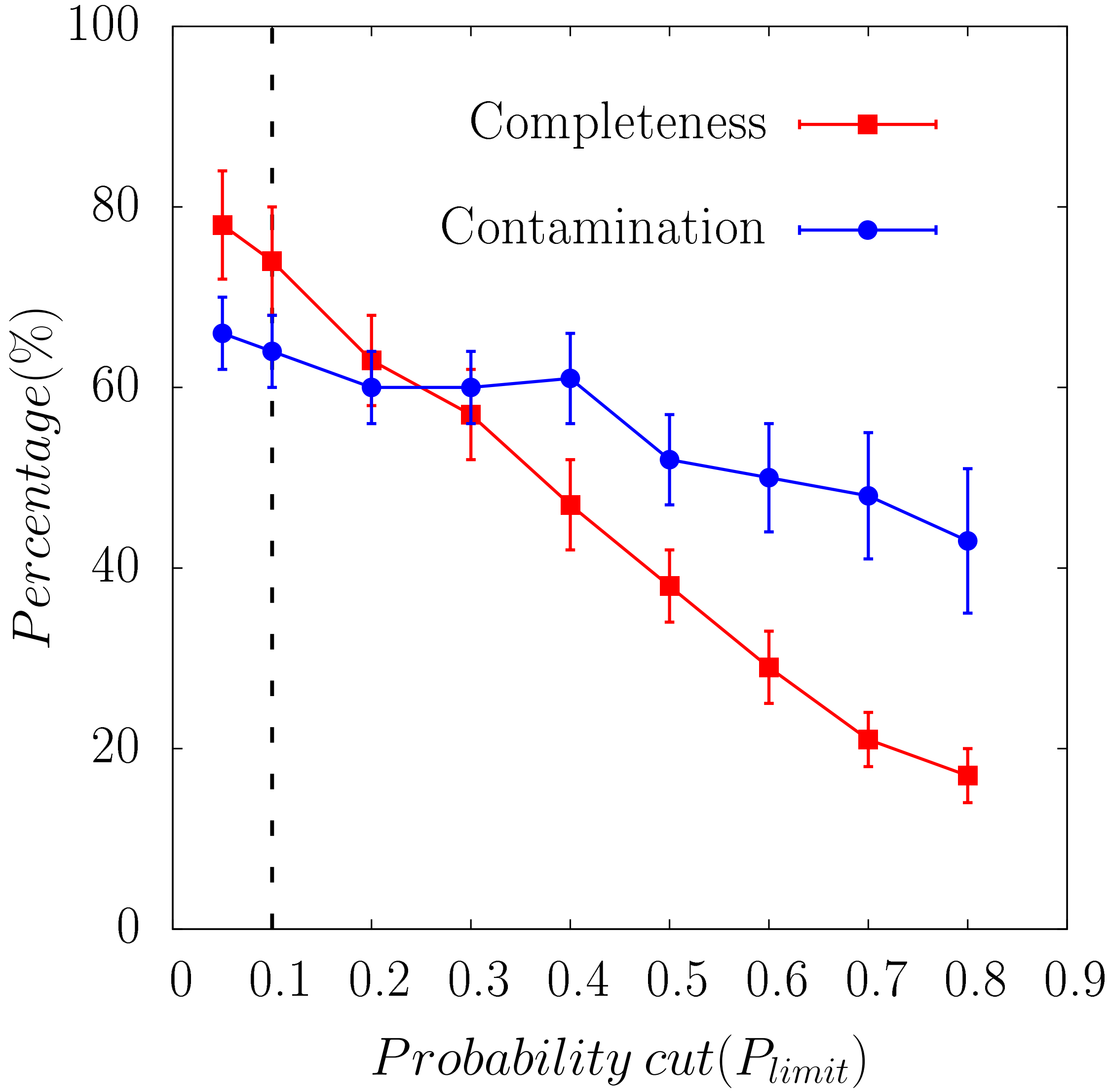

Figure 4.2: Completeness and contamination functions for the control sample as a function of the probability limit, P_{limit}. The probability limit is defined as the minimum probability of galaxies in the control sample to belong to the redshift slice defined by the Hα narrow-band selected sample (0.83$\leq z \leq$0.86). Error bars are estimated assuming Poisson statistics. We estimate the completeness by counting the number of underlying galaxies in the control sample that have spectroscopic redshifts within the Hα redshift slice, compared to the total number of galaxies with spectroscopic redshifts in the same slice. Contamination is defined as the fraction of galaxies in the underlying sample with spectroscopic redshifts located outside the Hα redshift slice. Choosing a larger P_{limit} results in a less contaminated but simultaneously less complete and statistically smaller control sample. The control sample here is selected to have a probability limit P_{limit}=0.1, demonstrated by the dashed line in the figure.

In estimating the contamination and completeness for the control sample, we assume that they are independent of the apparent magnitude and we can extrapolate the results from bright (i^{+} <22.5) to faint galaxies. This is a valid assumption given that (1) at i^{+} <24, a comparison between the photometric and spectroscopic data shows that the photo-z accuracy is ∼0.01 (Ilbert et al., 2009), smaller than the redshift slice defined by the Hα sample (∼0.03) and (2) the majority of galaxies in the control sample (∼93%) are brighter than i^{+} <24.

We also stress that since massive red galaxies which dominate denser environments will have sharply peaked photo-z PDFs compared to less massive blue systems, they will be more complete and less contaminated. As a result, the completeness/contamination might be a function of the environment. We investigate the environmental dependence of completeness/contamination and find that although the completeness and contamination functions vary with the environment (highest completeness/lowest contamination in clusters), the correction factor (used in Sections 4.3.1 and 4.4.1) is almost independent of the environment (the higher completeness is accompanied by a lower contamination which leaves the correction factor almost intact) and this will not affect our results.

4.3 Large Scale Structure Identification

In this section, we use the underlying distribution of galaxies in the control sample to estimate the local surface density field of galaxies from which the cosmic web (filaments and clusters) is extracted.

4.3.1 Local Surface Density

In order to identify and extract the LSS (filaments and clusters) in the underlying galaxy distribution, first we need to estimate the surface density field within the redshift slice defined by our narrow-band Hα survey (0.83≤ z ≤0.86). The surface density field is evaluated using the weighted adaptive kernel density estimator described in detail in Chapter 1.

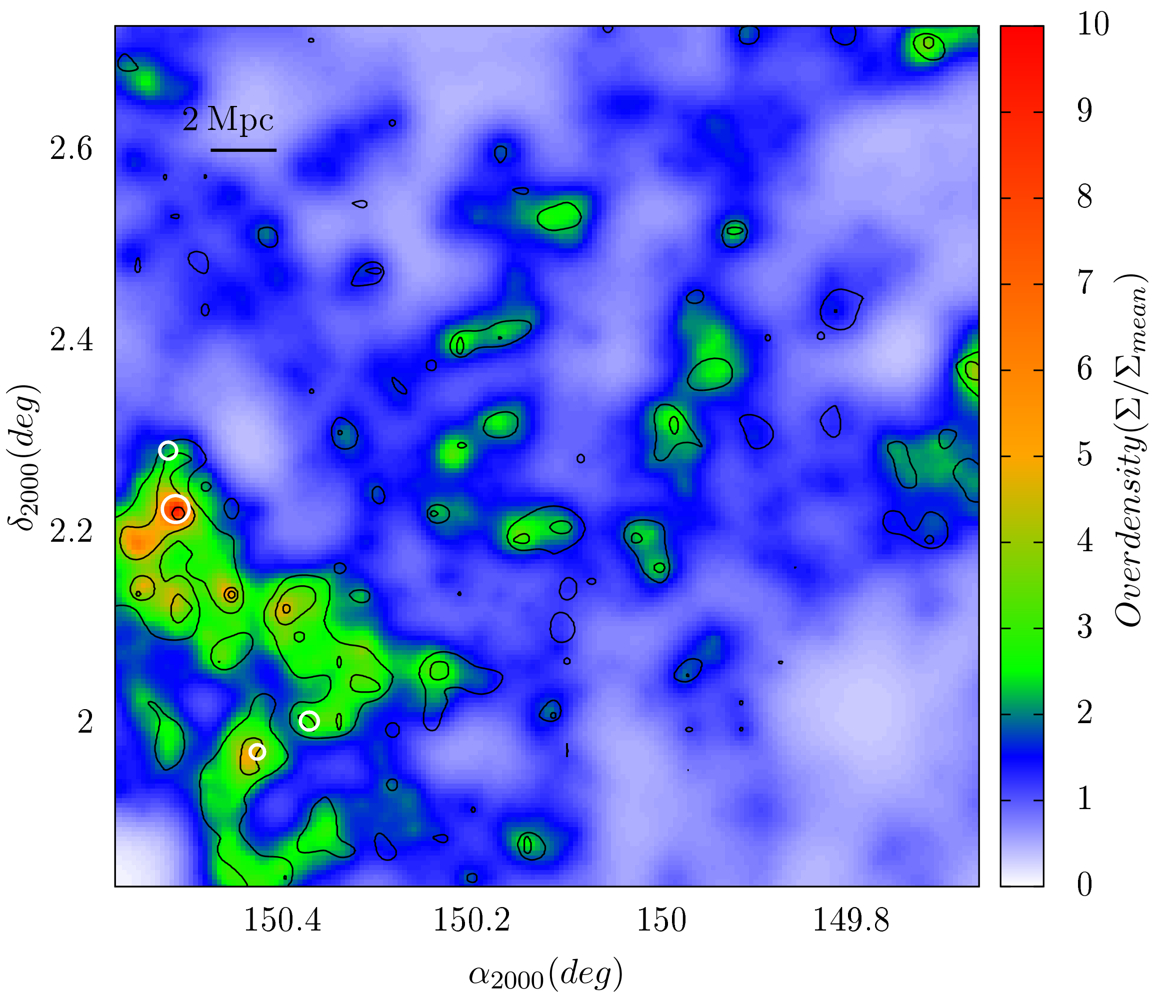

Figure 4.3: Overdensity map constructed from the K_s-band selected control sample, using the weighted adaptive kernel density estimator for the redshift slice $0.83 \leq z \leq 0.86$ in the HiZELS area of the COSMOS field. Overdensity is defined as the surface density normalized to the mean surface density at that redshift. Black contours are extracted from Scoville et al. (2013) Voronoi tessellation density estimator for the redshift slice $0.83 \lesssim z \lesssim 0.85$. For clarity, only three contour levels are demonstrated and these are at 1/2, 1/4, and 1/8 of the overdensity peak. White circles also show the R_{200} region of the X-ray clusters/groups in the redshift range $0.82 \leq z \leq 0.87$ over the same area. There is a very good consistency between our density estimation and that of Scoville et al. (2013). Note the super-structure in the lower left side of the map.

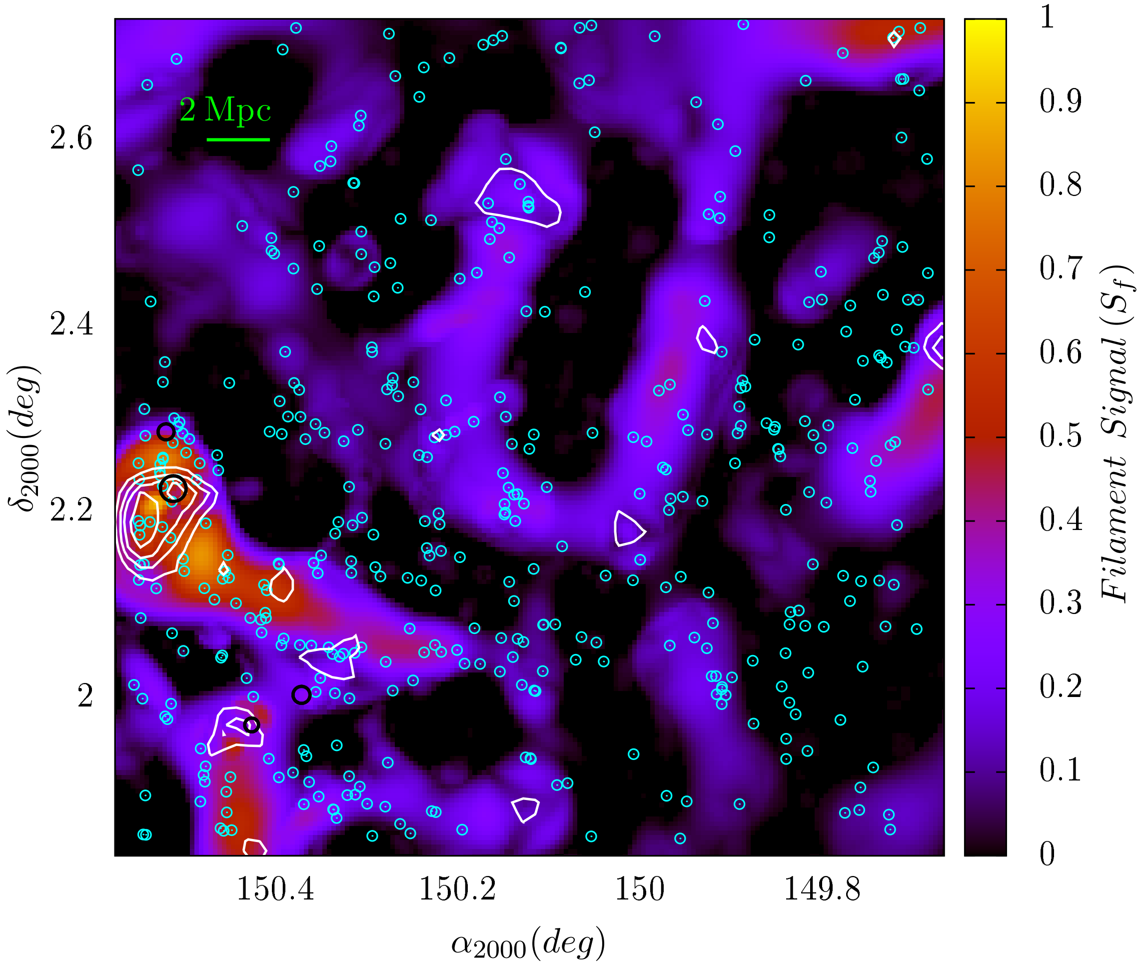

Figure 4.4: Filament signal map constructed from the K_s-band selected underlying distribution of galaxies using the MMF algorithm for the redshift slice 0.83≤ z ≤0.86 in the HiZELS area of the COSMOS field. The white contours are extracted from the cluster signal map for the same underlying galaxies as explained in the text. Black circles show the R_{200} region of the X-ray clusters/groups in the redshift range 0.82≤ z ≤0.87 over the same area. Blue circles show the distribution of Hα emitters overlaid on the filament signal map. Note the filamentary structure with a great filamentary signal value connecting the overdensities and clusters in the lower left side of this map and its corresponding thread-like distribution of Hα emitters tracing the same region.

Here, for the global kernel width, we use a physical length of h=0.5 Mpc which corresponds to the typical value of R_{200} for X-ray clusters and groups in the COSMOS field (Finoguenov et al., 2007; George et al., 2011). The surface density field is evaluated on a 300×240 grid with a grid size (resolution) of 0.005 deg (corresponding to ∼0.125 Mpc physical size at z ∼0.85). The estimated surface density field needs to be corrected for incompleteness and contamination in the control sample since the incompleteness tends to underestimate the density values whereas the contamination has a tendency to overestimate them. Thus, we introduce a correction factor, η, simply defined as:

$$\eta = \frac{(1 - contamination)}{completeness} \tag{4.1}$$

The surface density field corrected for completeness and contamination, $\Sigma_c(\mathbf{r})$, becomes:

$$\Sigma_c(\mathbf{r}) = \eta \mathbf{\Sigma}(\mathbf{r}) \tag{4.2}$$

The density field corresponding to the underlying galaxies near the edge of the field covering Hα emitters is biased toward the smaller values, affecting the surface densities near the edge of the field. To minimize this edge effect, we make use of a larger underlying galaxy sample distributed well beyond the Hα coverage to estimate densities. Later, we limit our analysis to the area of Hα emitters.

We stress that since we use galaxy weights, w_is, to estimate the surface density field (Chapter 1), our method is immune to spurious structures due to possible random clustering of foreground and background galaxies. These contaminating galaxies would have smaller weights (because only the tail of their photo-z PDF would overlap the redshift slice associated with the Hα sample) and therefore, they contribute only marginally to the estimated density field.

We confirm the robustness of the estimated density field in this section by comparing it with the X-ray clusters/groups (Finoguenov et al., 2007; George et al., 2011) and Voronoi tessellation-based density field of Scoville et al. (2013). This is presented in Figure 4.3

where we find a very good agreement between our weighted adaptive kernel estimator and the independent estimation based on voronoi tessellation (Scoville et al., 2013). There is also a good consistency between the overdense regions and the position of the X-ray clusters/groups.

4.3.2 Filament, Cluster and Field Selection

To identify and extract spatial structures such as filaments and clusters in the underlying galaxy distribution, we utilize the 2D version of the MMF algorithm introduced in Chapter 1. In this chapter, three environments are defined: clusters as regions with a cluster signal greater than 0.5 and also greater than or equal to that of a filament (S_c >0.5 and $S_c \geq S_f$), filaments as regions with filament signals greater than 0.5 and greater than that of a cluster (S_f >0.5 and $S_f > S_c$), and the remaining regions with both cluster and filament signals less than or equal to 0.5 ($S_c \leq$0.5 and $S_f \leq$0.5) as part of the general field. The structures identified over the area covered by the Hα narrow-band survey are shown in Figure 4.4. We demonstrate the filament signal values as a heat map whereas the cluster signal values are shown as contours. We have confirmed the resulting structures in Figure 4.4 by comparing them with the structures depicted from X-ray observations. The X-ray groups and clusters in the redshift range 0.82$\leq z \leq$0.87 (Finoguenov et al., 2007; George et al., 2011) are overlaid on our predicted structures in Figure 4.4 and show close agreement.

Using the defined environments, we estimate the average number density of Hα emitters to be $\delta_{H\alpha}$=1.53±0.29, 0.45±0.09, and 0.13±0.01 arcmin^{-2} in clusters, filaments, and the field, respectively. The errors are estimated assuming Poisson statistics. $\delta_{H\alpha}$ values clearly show that dense, intermediate, and sparse environments are respectively occupied by clusters, filaments, and the field. A better representation of the density in different classes of environment is seen in Figure 4.5. A normalized distribution of overdensity values of the surface density field (estimated in Section 4.3.1) within regions defined as clusters, filaments, and the field is shown in Figure 4.5. Although they inhabit relatively distinct values of overdensity, there is a substantial degree of overlap which means that a pure density-based definition of environment is not fully adequate to identify different structures. Intermediate densities do correspond mostly to filaments (even though only our analysis actually disentangles them from clusters and the field). Throughout this work, we use the environment defined based on the MMF algorithm as a robust indicator of the cosmic web.

We also note that ideally, one wishes to select clusters and filaments with the highest signal value but practically, this leads to a statistically smaller sample size (especially for Hα emitters). The selection cut here (0.5) is due to a trade-off between the sample size and the reality (significance) of clusters and filaments. Nevertheless, we fine-tuned around the selection cut and examined some other values (0.3, 0.4, and 0.6) and found no significant change in the results.

4.4 Results and Comparison with Other Studies

4.4.1 Fraction of Star-forming Galaxies in the Cosmic Web

Using the structures identified in Section 4.3.2, we now study the fraction of star-forming Hα emitters (the ratio of the number of Hα emitters to the total number of underlying galaxies in the control sample) in filaments, clusters, and the field. This fraction is corrected for contamination and incompleteness. In order to examine the effect of photometric selection on our result, we perform this on both our original K_s-band and i^+-band selected control samples in the COSMOS (the i^+-band selected catalog is from Capak et al., 2007b). The correction factor, η, is 0.49 and 0.47 for the K_s and i^+-band samples, respectively. An increase in the fraction of Hα emitters is seen in the filaments relative to both the cluster and the field environments (Figure 4.6). This trend is not influenced by the photometric selection wavelength (i^+-band versus K_s-band) in the underlying galaxy population. The error bars in Figure 4.6 are evaluated assuming Poisson statistics. As noted by Ilbert et al. (2013), the longer wavelength selection (K_s-band here) can more reliably detect galaxies at intermediate to high redshifts and we mention that the results based on the K_s-band are likely more robust.

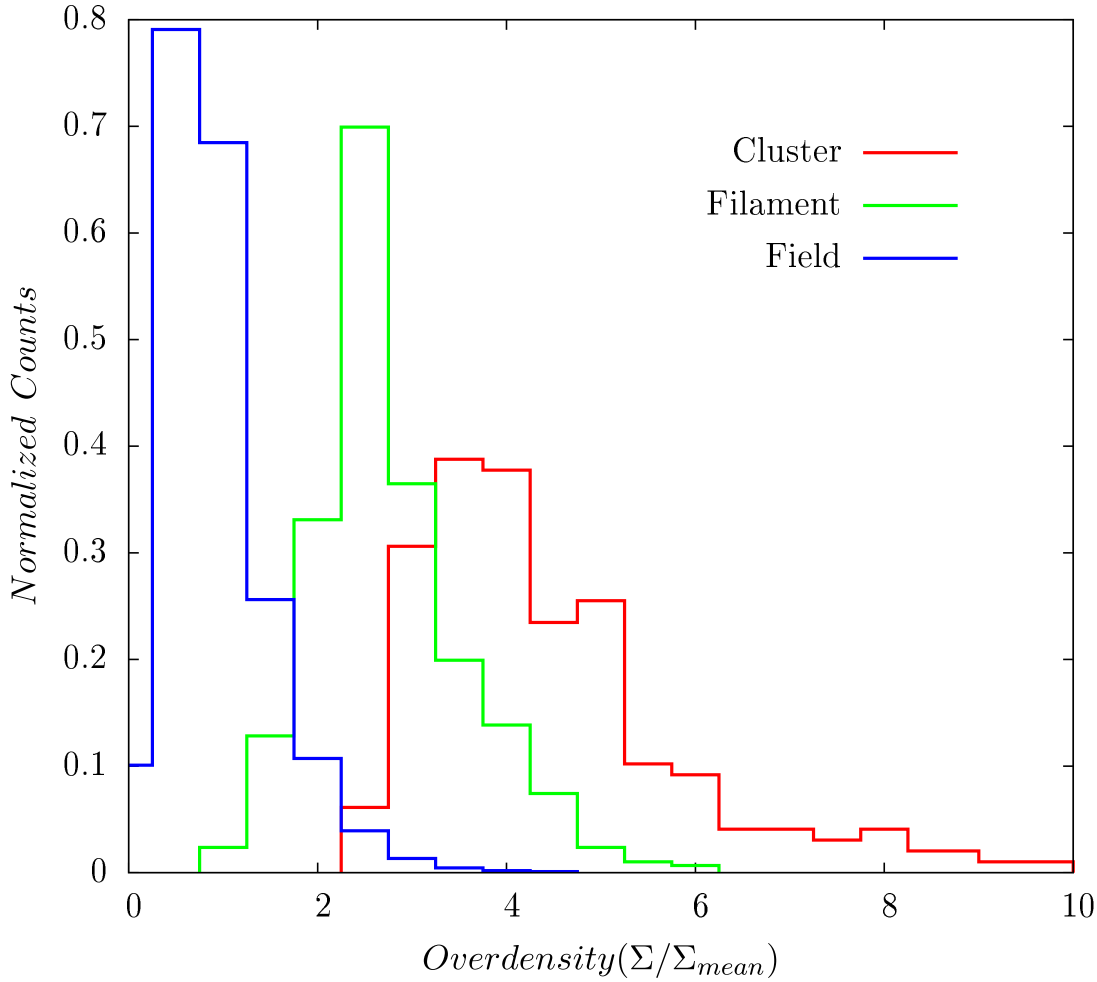

Figure 4.5: Normalized distribution of overdensity values within regions defined as clusters, filaments, and the field. While these structures occupy roughly a distinct range of overdensity values, there is significant overlap. We find that intermediate densities correspond mostly to filaments (even though only our analysis actually disentangles them from clusters, and the field).

The enhancement in the fraction of Hα emitters in filaments (i.e., intermediate densities) is consistent with previous studies, depicting the importance of intermediate environments,i.e., galaxy groups, the outskirts of galaxy clusters, and filaments, in the evolution of galaxies. These results hold at low-z ($z\lesssim$0.5, Fadda et al., 2008; Tran et al., 2009; Biviano et al., 2011; Geach et al., 2011; Koyama et al., 2011; Mahajan et al., 2012), intermediate-z ($z\sim$1, Koyama et al., 2008, 2010; Sobral et al., 2011; Pintos-Castro et al., 2013), and high-z ($z\gtrsim$1.5, Koyama et al., 2014; Santos et al., 2014).

At $z\sim$1, the closest work to our study in terms of sample selection is that of Sobral et al. (2011) who showed that at $z\sim$0.85, the fraction of Hα emitters from both COSMOS- and UDS-HiZELS surveys, when compared to the underlying population of galaxies at the same redshift, peaks at intermediate environments, in agreement with our result. Pintos-Castro et al. (2013) performed a thorough IR study of a super-structure at $z\sim$0.85 and showed that although the average star-formation does not show any clear environmental dependence (cf. Section 4.4.2), the fraction of star-forming galaxies indicates that intermediate densities are preferred. They showed that the enhancement in the fraction of star-forming far-IR emitters in medium densities is seen for both optically red and blue far-IR emitters and also in different mass-binned samples. This is also consistent with our results here regarding the enhancement in the fraction of Hα emitters in filaments, although they used far-IR emitters as indicators of star-forming galaxies and number density of galaxies as a measure of environment. A combined narrow-band Hα and *AKARI* mid-IR imaging survey of a z=0.81 super-structure by Koyama et al. (2010) revealed that the red Hα emitters and mid-IR galaxies are more commonly found in medium density environments such as cluster outskirts, groups, and filaments. This reinforced the results of a similar study of the same structure by Koyama et al. (2008), which showed that the fraction of both red and blue 15 μm selected galaxies is highest in medium density environments. Both of these studies by Koyama et al. (2008) and Koyama et al. (2010) at $z\sim$0.8 agree with our results in this section but we note that we are explicitly identifying filamentary structures as the drivers of such enhancement.

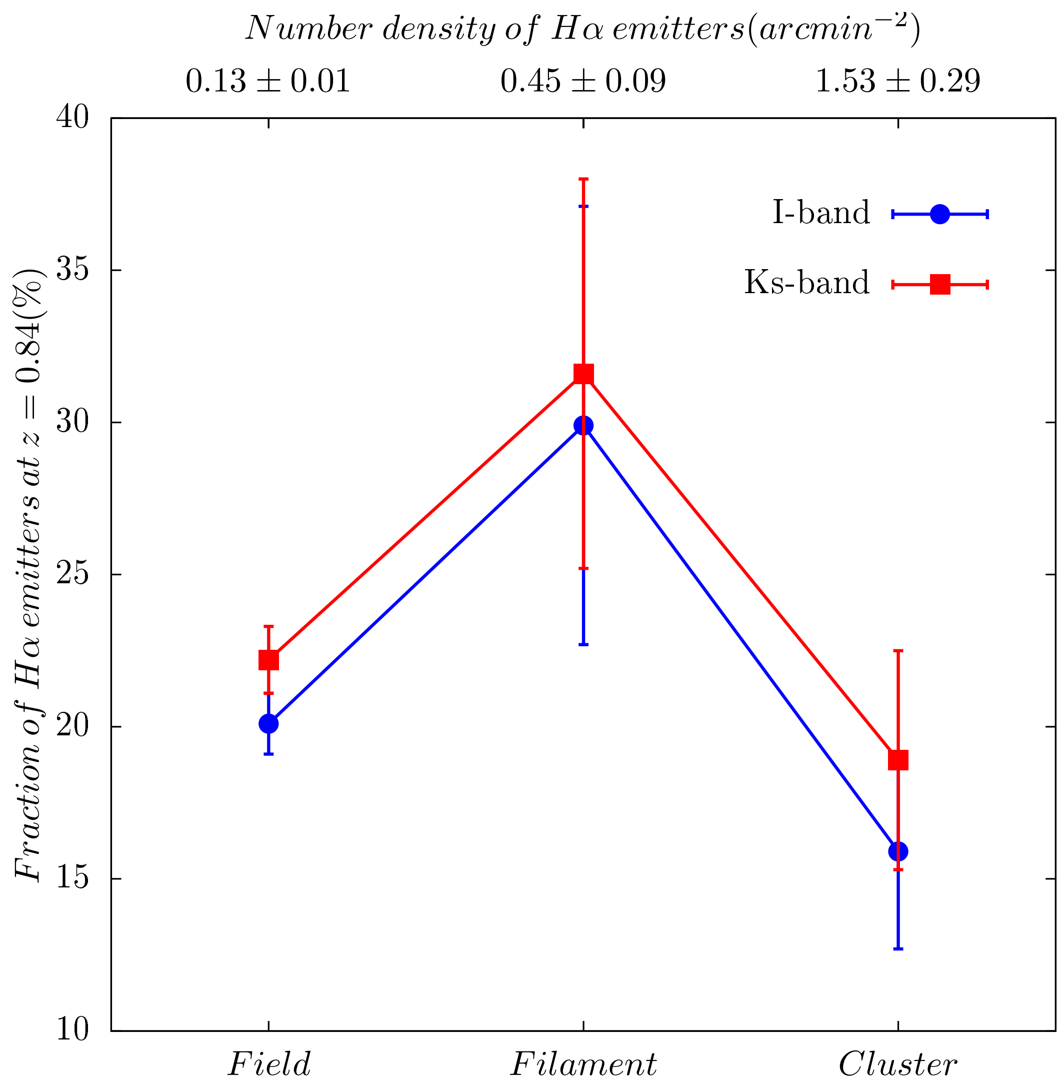

Figure 4.6: Fraction of Hα emitters (the ratio of the number of Hα emitters to the total number of underlying galaxies in the control sample) corrected for completeness and contamination in the number of underlying galaxies over different cosmic environments and for both the K_s-band and the i^+-band selected control samples. The error bars are evaluated assuming Poisson statistics. Note an elevation in the fraction of Hα emitters in filaments relative to clusters and the field. This trend is not much affected by photometric selection of the control sample. We also show the average number density of Hα emitters (in units of arcmin^{-2}) in clusters, filaments, and the field on top of the figure.

At lower redshift ($z \lesssim 0.5$), there are several studies consistent with our results. For example, Geach et al. (2011) analyzed a super-structure at z=0.55, comprising several dense regions connected by a filamentary structure, using *GALEX* NUV and *Spitzer* MIPS 24 μm data and showed that although on average, there is no significant difference between the SFRs of star-forming galaxies in the super-structure and the randomly selected field (Compare with Section 4.4.2), there are intermediate-scale regions within the super-structure where the probability of a galaxy undergoing star-formation is enhanced. This increased probability is analogous to our results here regarding the elevation in the fraction of star-forming galaxies in filaments. At $z \sim 0.2$, Fadda et al. (2008) discovered two galaxy filaments associated with a cluster (Abell 1763) and found that starburst galaxies preferentially inhabit the two filaments compared to the cluster core and the outer regions excluding filaments. A more recent study of the same supercluster by Biviano et al. (2011) confirmed the previous results, showing that the filament contains the highest fraction of IR-emitting galaxies. These agree with our results although they used a different prescription to identify filaments and a redshift different from our sample. Studies on galaxy group scales at $z \sim 0.4$ by Tran et al. (2009) and Koyama et al. (2011) also show an overall good agreement with our results in filaments. Recently, Stroe et al. (2014) found that the LF of Hα galaxies around the shock-induced radio relics of a cluster at $z \sim 0.2$ is significantly boosted compared to the field. We argue that such enhancement could be driven by collapsing filamentary structures when two very massive clusters merge.

The enhancement in the fraction of star-forming galaxies at intermediate environments is also seen at higher redshifts. For example, Koyama et al. (2014) showed that for a rich cluster at $z \sim 1.5$, Hα-emitting galaxies are preferentially located in the cluster outskirts and Santos et al. (2014) found a huge excess of star-forming fraction relative to the corresponding passive fraction in a $1-3$ Mpc distance from the center of a massive cluster compared to the cluster core and the field. Smail et al. (2014) also found no significant variation in mean SFR with environment for a structure at $z \sim 1.6$—consistent with our results in Section 4.4.2— and that the highest density regions of this structure are devoid of the most actively star-forming galaxies (far-IR, submillimeter, MIPS, and radio sources), which instead are preferentially found in intermediate density environments.

In our study, we used a robust quantitative technique to identify structures with a special emphasis on filaments as locations with intermediate environments. Although the techniques used to identify the structures are different, our results are in close qualitative agreement with previous studies at different redshifts that were discussed above. We conclude that star-forming galaxies are more commonly found in intermediate density regimes at least out to $z\sim1.5$, regardless of how they are selected (Hα, IR, etc.) or how their environments are defined. For this study, it seems that filaments are likely responsible for this enhancement.

The boost in the star-formation activity at intermediate environments is not confined to only an elevation in the star-forming fraction. For example, some studies have shown that the rise in the star-formation activity at medium environments is a result of an increase in the mean SFR of galaxies (e.g., Coppin et al., 2012; Porter and Raychaudhury, 2007; Porter et al., 2008) or due to an enhancement in both the SFR of galaxies and their fraction at intermediate density regimes (e.g., Fadda et al., 2008; Sobral et al., 2011). Here, we showed that filaments lead to an observed enhancement in the star-formation fraction. In the following section, we will investigate whether this enhancement is a consequence of an increase in the SFR of many galaxies in filaments or merely due to some galaxies having their star-formation switched on by filaments.

4.4.2 The SFR and Stellar Mass in the Cosmic Web

We now investigate the *observed* distribution of SFR, stellar mass, and sSFR in different environments. For the star-forming galaxies in the Hα sample, the median SFR, stellar mass, and sSFR are independent of the environment (Table 4.1). The same is true for the underlying star-forming galaxies in the control sample (Table 4.2). The uncertainties in the median values are estimated from 10,000 bootstrap trials.

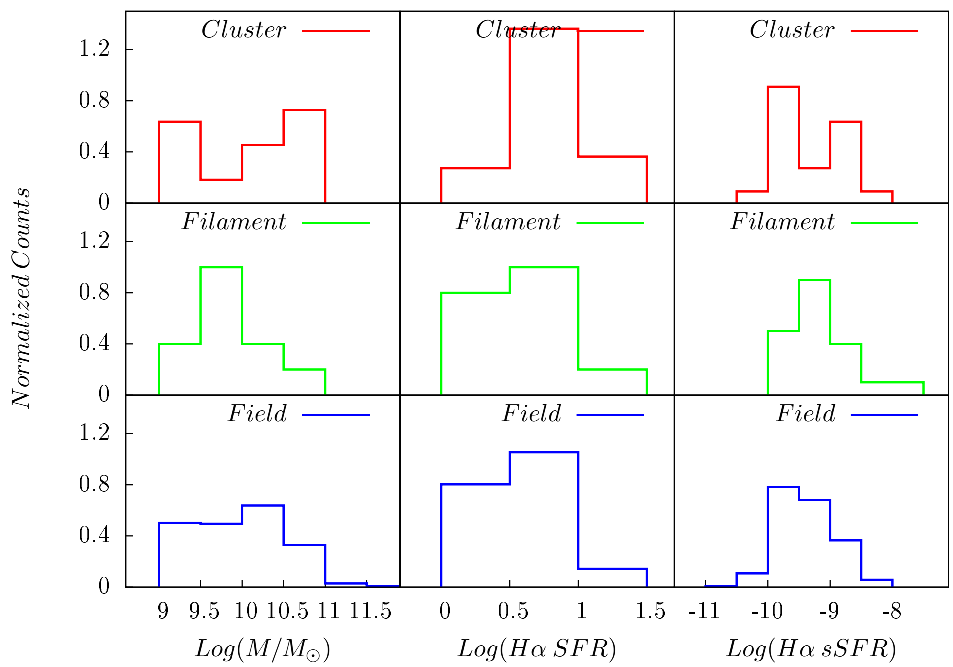

Figure 4.7: Normalized stellar mass, SFR, and sSFR distribution of Hα emitters in clusters, filaments, and the field at $z \sim 0.8-0.9$. These observed distributions are similar in different environments. Using the K-S test we show that it is statistically unlikely that the above-mentioned distributions are drawn from different parent populations. The K-S test p-value is > 0.01 in all cases.

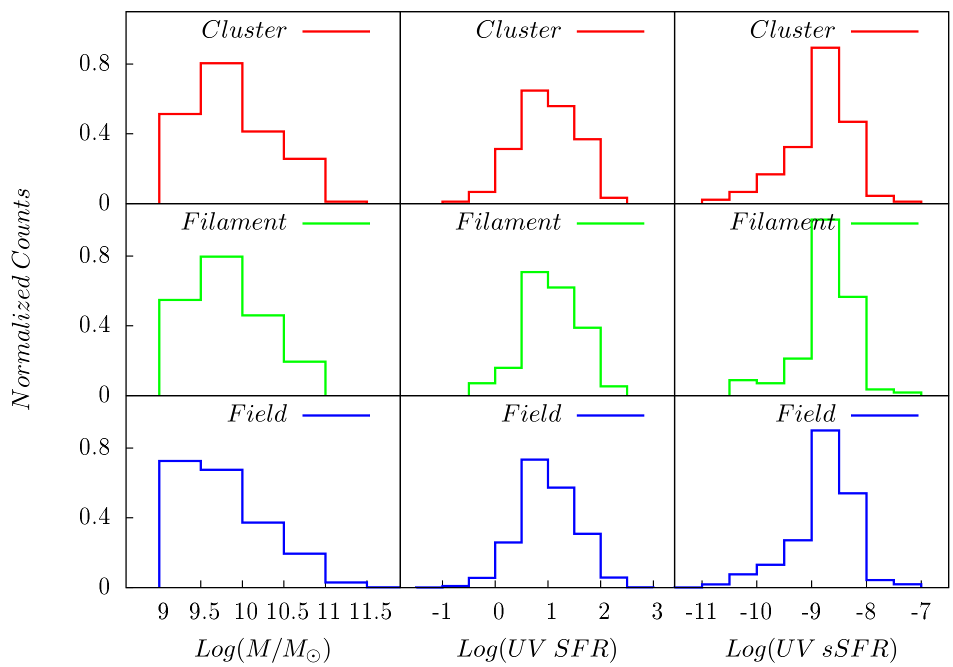

Figure 4.8: Same as Figure 4.7 but for star-forming galaxies in the control sample.

Table 4.1: Median SFR (Based on Hα Line), Stellar Mass and sSFR in the Cosmic Web at $z \sim 0.8-0.9$ for the Hα Sample

Cosmic Structure	SFR $M_\odot yr^{-1}$	Stellar Mass $\log(M_\odot)$	sSFR $\log(yr^{-1})$
Cluster	4.47±1.15	10.20±0.24	−9.45±0.22
Filament	4.50±0.73	9.85±0.10	−9.32±0.13
Field	3.58±0.14	10.01±0.06	−9.43±0.04

The errors are estimated by bootstrap resampling from 10,000 trials.

Table 4.2: Median SFR (form UV Flux), Stellar Mass and sSFR in the Cosmic Web at $z \sim 0.8-0.9$ for the Star-forming Control Sample

Cosmic Structure	SFR $M_\odot yr^{-1}$	Stellar Mass $\log(M_\odot)$	sSFR $\log(yr^{-1})$
Cluster	9.57±1.41	9.76±0.04	−8.81±0.05
Filament	11.13±1.62	9.79±0.06	−8.64±0.05
Field	8.97±0.30	9.68±0.01	−8.67±0.02

The errors are estimated by bootstrap resampling from 10,000 trials.

A comparison between the observed distribution of Hα-based SFRs in different environments reveals similarities (Figure 4.7), showing that the environment does not significantly affect the SFR of selected star-forming galaxies. The observed distribution of the stellar mass and the sSFR is also found to be independent of the environment for the Hα sample (Figure 4.7). These results also hold true for the selected star-forming galaxies in the control sample (Figure 4.8).

Table 4.3: Results of the K-S Test for Distributions of Hα SFR, Stellar Mass, and sSFR from the Hα Sample in Different Cosmic Structures

Cosmic Structures	p-value (log(SFR) distributions)	p-value (log(Mass) distributions)	p-value (log(sSFR) distributions)
Cluster and Filament	0.22	0.05	0.22
Cluster and Field	0.02	0.08	0.44
Filament and Field	0.14	0.24	0.18

The p-values are the probabilities that the two distributions are drawn from the same parent population.

Table 4.4: Results of the K-S Test for Distributions of UV SFR, Stellar Mass, and sSFR from the Star-forming Galaxies in the Control Sample in Different Cosmic Structures

Cosmic Structures	p-value (log(SFR) distributions)	p-value (log(Mass) distributions)	p-value (logs(SFR) distributions)
Cluster and Filament	0.62	0.46	0.09
Cluster and Field	0.66	0.02	0.03
Filament and Field	0.19	0.12	0.44

The p-values are the probabilities that the two distributions are drawn from the same parent population.

We perform K-S tests to compare distribution of SFRs, stellar Masses, and sSFRs in different environments and the results are tabulated in Tables 4.3 and 4.4 for both the Hα emitters and the star-forming galaxies in the control sample. Here, the p-value is the probability that the two considered distributions are drawn from the same underlying parent population. It is unlikely that the observed distributions of SFRs, stellar masses, and sSFRs in different environments are extracted from different parent populations, with an evaluated p-value > 0.01 in all cases.

The results in this section are consistent with other independent studies at different redshifts (Peng et al., 2010; Geach et al., 2011; Wijesinghe et al., 2012; Koyama et al., 2010, 2013b,a, 2014; Feruglio et al., 2010; Ideue et al., 2012; Muzzin et al., 2012; Pintos-Castro et al., 2013; Bouché and Lowenthal, 2005; Grützbauch et al., 2011; Brodwin et al., 2013; Hayashi et al., 2014; Santos et al., 2014; Smail et al., 2014). Here, we found no significant evidence that the cosmic web affects the stellar mass, SFR, and sSFR of the *observed* star-forming galaxies at $z \sim 1$; a result that might be partially explained by selection biases.

To further investigate this, we study the environmental (filament, cluster, and field) dependence of the SFR$-$mass relation—often known as the "main-sequence" of star-forming galaxies—for the Hα emitting galaxies and the star-forming galaxies in the control sample. The mean SFR$-$mass relation for the Hα sample appears to be independent of the environment (Figure 4.9). Using the nonlinear least-squares Marquardt$-$Levenberg algorithm, we perform a linear fit (log(SFR)=$a$log(Mass)+b) to the log(SFR)$-$log(Mass) relation for Hα emitters in filaments, clusters, and the field, separately. For clusters and filaments, the slope of the linear fit is fixed to the slope of the best-fitting line for the field Hα sample. The slope of the best-fitting line is a=0.27±0.02 with the intercept being b=−1.99±0.04, −2.04±0.05, and −2.13±0.17 for cluster, filament, and the field Hα emitters, respectively. The intercepts are consistent within the uncertainties. We also evaluate the observed scatter around the mean SFR−mass relation in different environments. The observed scatter for the Hα sample is found to be $\lesssim$0.2 dex, independent of the environment. It is worth mentioning that the typical observational uncertainty in the Hα SFR (Section 4.2.3) is greater than the observed scatter around the mean SFR−mass relation. It is noteworthy that a slight increase in the median Hα SFR is seen in clusters compared to the field. However, this enhancement is not significant and is within the uncertainties.

In another attempt to quantify the environmental dependence of the SFR−mass relation, we use the generalized two-dimensional K-S test (Fasano and Franceschini, 1987) to determine the probability that the populations of cluster, filament, and field Hα emitters on the log(SFR)−log(Mass) plane are drawn from the same parent distribution. The derived p-value is 0.09 (cluster versus filament), 0.06 (cluster versus field), and 0.12 (filament versus field), implying that they are unlikely to be drawn from different parent populations on the log(SFR)−log(Mass) plane (The p-value is > 0.01 in all cases).

The environmental independence of the median SFR and the mean SFR−mass relation for the Hα star-forming galaxies might be effected by the selection biases in the data. In other words, the median SFR of star-forming galaxies might be intrinsically different in different environments but due to selection effects, this difference does not mirror itself into the observed median SFR and/or the mean SFR−mass relation.

Since the Hα selected sample is flux limited (i.e., SFR limited), the SFR−mass relation could be entirely driven by the fixed Hα SFR limit, the shape of the Hα luminosity function, and the mass-dependent dust correction we use in this work. Due to the shape of the luminosity function and the SFR limit of the Hα sample (~ 1.5 $M_\odot yr^{-1}$), the majority of galaxies tend to crowd near the selection limit which defines a relatively narrow horizontal strip in the SFR−mass plane. A mass-dependent dust correction to the Hα sample then introduces a slope in the relation. Since these selection biases apply equally to all environments, this leads all environments to give the same results.

In order to check this, we perform a simulation. We select a mock sample of galaxies with the stellar mass randomly drawn from $9<\log(M/M_{\odot})<11$ and their SFR randomly drawn from the Hα luminosity function based on the HiZELS survey (L^{*}=42.25 ergs^{-1}, α=$-$1.56). We emphasize that in randomly selecting these galaxies, no assumption about an intrinsic correlation between SFR and stellar mass is made. We dust-redden the sample using the mass-dependent dust correction equation used in this work (Section 4.2.3) and apply the HiZELS Hα SFR limit (1.5 M$_{\odot}$yr^{-1}) to mimic the observational selection of the HiZELS survey. We later undo the dust extinction on the galaxies that passed the SFR selection limit. Figure 4.10 (blue symbols) shows the SFR$-$mass relation for these simulated galaxies considering the selection effects. This resembles what we observe in Figure 4.9, despite the fact that we initially introduced no intrinsic relation between SFR and stellar mass *a priori*. The slope of the SFR$-$mass relation for these simulated galaxies is a=0.22$\pm$0.02, similar to that of Figure 4.9, within errors.

To further investigate the selection effects on the results, we double the intrinsic SFR of every galaxy and assume that they happen to be located in filaments. This means that more galaxies will pass the Hα selection limit due to the shape of the luminosity function. The fraction of galaxies that now pass the selection limit is increased by a factor of $\sim$2.2 (cf. Figure 4.6). However, the median SFR and the mean SFR$-$mass relation do not change significantly. Figure 4.10 (red symbols) shows the SFR$-$mass relation for the new simulated galaxies (in filaments) with twice the intrinsic SFR. This SFR$-$mass relation looks similar to that of blue symbols although the intrinsic SFR of each individual galaxy is doubled. The median SFR for detected galaxies is only slightly increased from 5.30$\pm$0.22 M$_{\odot}$yr^{-1} to 5.91$\pm$0.19 M$_{\odot}$yr^{-1}. The slope and intercept values are now a=0.22$\pm$0.02 and b=$-$1.38$\pm$0.17, respectively, and remain almost the same within the uncertainties (these values are a=0.22$\pm$0.02 and b=$-$1.36$\pm$0.20 for blue symbols).

We conclude that the environmental invariance of the median SFR and the mean SFR-

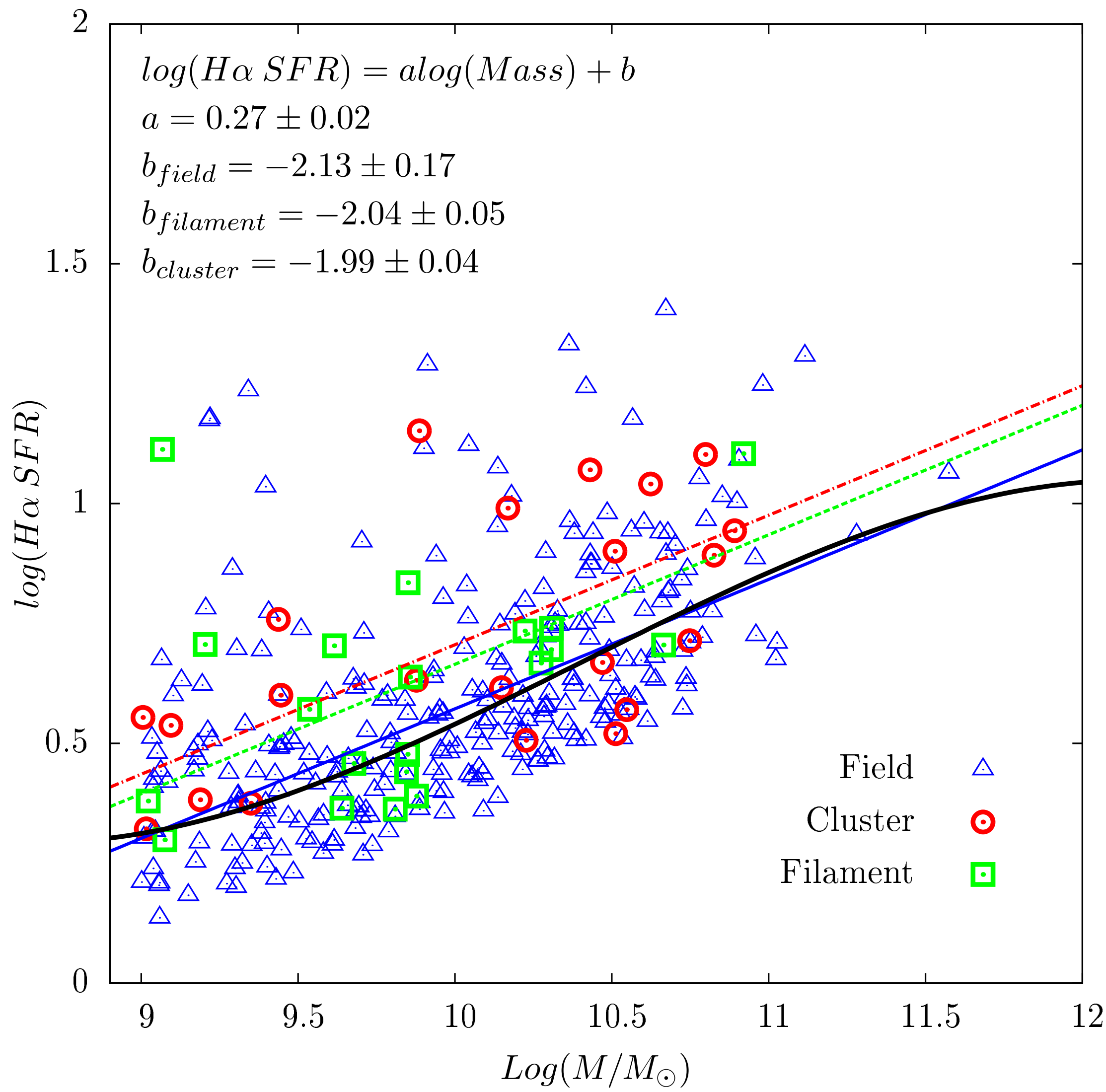

Figure 4.9: SFR−mass relation for Hα emitters in clusters, filaments, and the field. The best-fit lines for clusters, filaments, and the field data are displayed with dot-dash (red), dashed (green), and solid (blue) lines, respectively. The results of the best-fit parameters are given on the top left corner of the figure. The observed SFR−mass relation does not depend on the environment. A careful 2D K-S test also shows that it is statistically unlikely that the 2D log(SFR)−log(Mass) distributions in clusters, filaments, and the field are drawn from different parent populations (p-value > 0.01). The black solid line also shows the Hα selection limit. Note the large envelope of galaxies near the selection limit.

mass relation for the Hα star-forming galaxies is partly due to selection biases. In other words, the intrinsic SFR of star-forming galaxies might be a function of the environment but is not completely seen in the observed SFR−mass relation or the median SFR due to selection effects. The intrinsic enhancement of SFR of Hα emitters in filaments, together with the selection biases, has the same effect of elevating the observed fraction of Hα star-forming galaxies in filaments (results in Section 4.4.1), while leaving the observed median SFR and the mean SFR−mass relation almost intact. Therefore, from the Hα sample alone, the selection biases are sufficiently strong that we cannot conclude whether it is the average SFR of all galaxies that increases in filaments, or whether some galaxies have their star-formation switched on by filaments that lead to an enhancement in the star-forming fraction.

We find similar results for the SFR−mass relation based on the rest-frame NUV$-r^+$ versus r^+−J selected star-forming galaxies in the control sample (Figure 4.11); i.e., the mean SFR−mass relation for selected star-forming galaxies in the control sample is found to be independent of the environment. As explained in Section 4.2.3, the SFR of the control sample is based on the UV continuum and IR flux (where available). A linear fit to the log(SFR)−Log(Mass) data results in a slope of a=0.46±0.02 and intercepts b=−3.52±0.04, −3.45±0.04, and −3.50±0.18 for cluster, filament, and field star-forming galaxies in the control sample, respectively (the slope is fixed to that for the field sample). We evaluate the intrinsic scatter around the mean SFR−mass relation in different environments after subtracting in quadrature the typical observational uncertainty in SFR (Section 4.2.3) from the observed scatter. The intrinsic scatter for the star-forming galaxies in the control sample is ∼0.4 dex, regardless of the environment. Also, similar to the results from the Hα sample, the 2D K-S test exhibits that the environmental discrepancies are insignificant, with p=0.43, 0.05, and 0.11 for cluster and filament, cluster and field, and filament and field, respectively.

We stress that the estimated SFRs for the Hα emitters and the underlying star-forming galaxies have different origins, calculated based on different recipes, and are based on different diagnostics. We apply the K-S test to the distribution of log(Hα SFR/UV SFR)

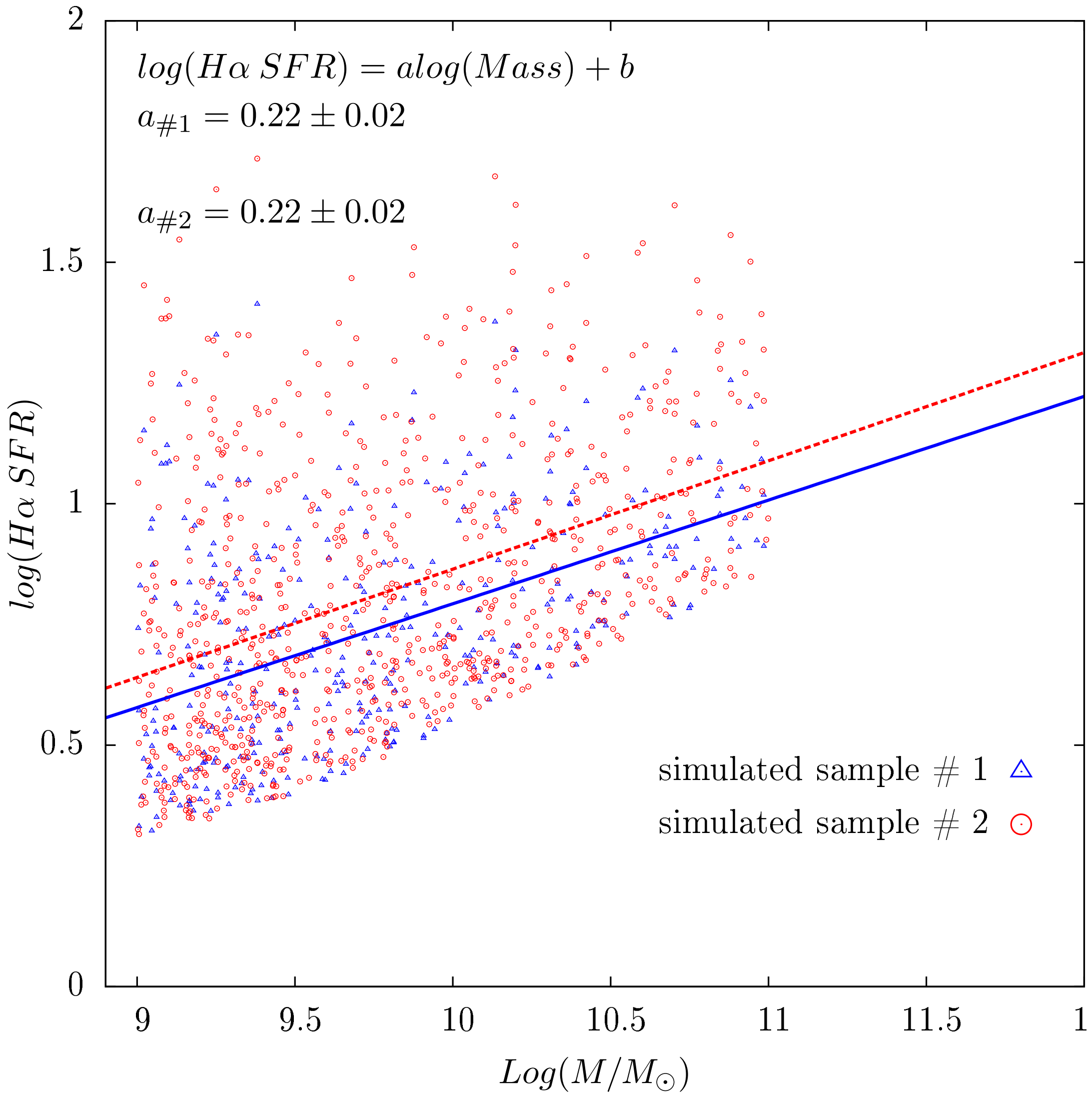

Figure 4.10: Hα SFR−mass relation for two sets of simulations. These simulations are subjected to the observational selection biases of the Hα star-forming sample. The intrinsic SFR of galaxies for simulation # 2 (red symbols) is twice that of simulation # 1 (blue symbols). Despite the intrinsic difference between the SFRs of galaxies in these simulations, their SFR−mass relation is almost the same within the statistical uncertainties.

for the Hα emitters with available UV SFR in three different environments. The K-S test p-value is p=0.59, 0.12, and 0.53 for cluster and filament, cluster and field, and filament and field, respectively, indicating that the result is insensitive to the SFR estimators used in this analysis. We emphasize that our main purpose here was to investigate whether the environment affects the SF activity in star-forming galaxies and not to compare different SFR diagnostics.

Similar to the Hα selected sample, the results based on the star-forming galaxies in the control sample are not completely free from selection biases. It is more difficult to model the effect of the selection bias for the star-forming galaxies in the control sample. However, they might be affected by similar potential biases. The selection of these star-forming galaxies is based on some color−color cuts and if their SFRs were to increase, then some galaxies that did not initially pass the color selection criteria would now do so, probably leading to the same bias.

The environmental independence of the SFR−mass relation for the Hα sample, as well as the star-forming galaxies in the control sample, is in agreement with previous studies at low-z ($z\lesssim$0.5, Peng et al., 2010; Biviano et al., 2011; Wijesinghe et al., 2012; Koyama et al., 2013b; Lin et al., 2014), intermediate-z ($z\sim$1, Koyama et al., 2010; Peng et al., 2010; Ideue et al., 2012; Muzzin et al., 2012; Koyama et al., 2013b; Lin et al., 2014), and high-z ($z\gtrsim$1.5, Hayashi et al., 2011; Grützbauch et al., 2011; Koyama et al., 2013b, 2014).

These studies cover a wide redshift range ($0.05\lesssim z\lesssim 3$) with their galaxy samples selected differently from a variety of surveys (SDSS, COSMOS, zCOSMOS, GAMA, GCLASS, Pan-STARRS1, GOODS-NICMOS, and some specifically targeted structures). They have used different proxies for the definition of environment (the majority of them are based on the local number density of galaxies) and the SFR was estimated with different indicators. This includes dust-corrected Hα-based SFR (Peng et al., 2010; Koyama et al., 2010, 2013b, 2014), [OII]λ3727 (Hayashi et al., 2011; Ideue et al., 2012; Muzzin et al., 2012), total IR luminosity (Biviano et al., 2011), extinction-corrected Hα EW (Wijesinghe et al., 2012), SED template-fitting (Peng et al., 2010), rest-frame UV flux (Grützbauch et al., 2011), and

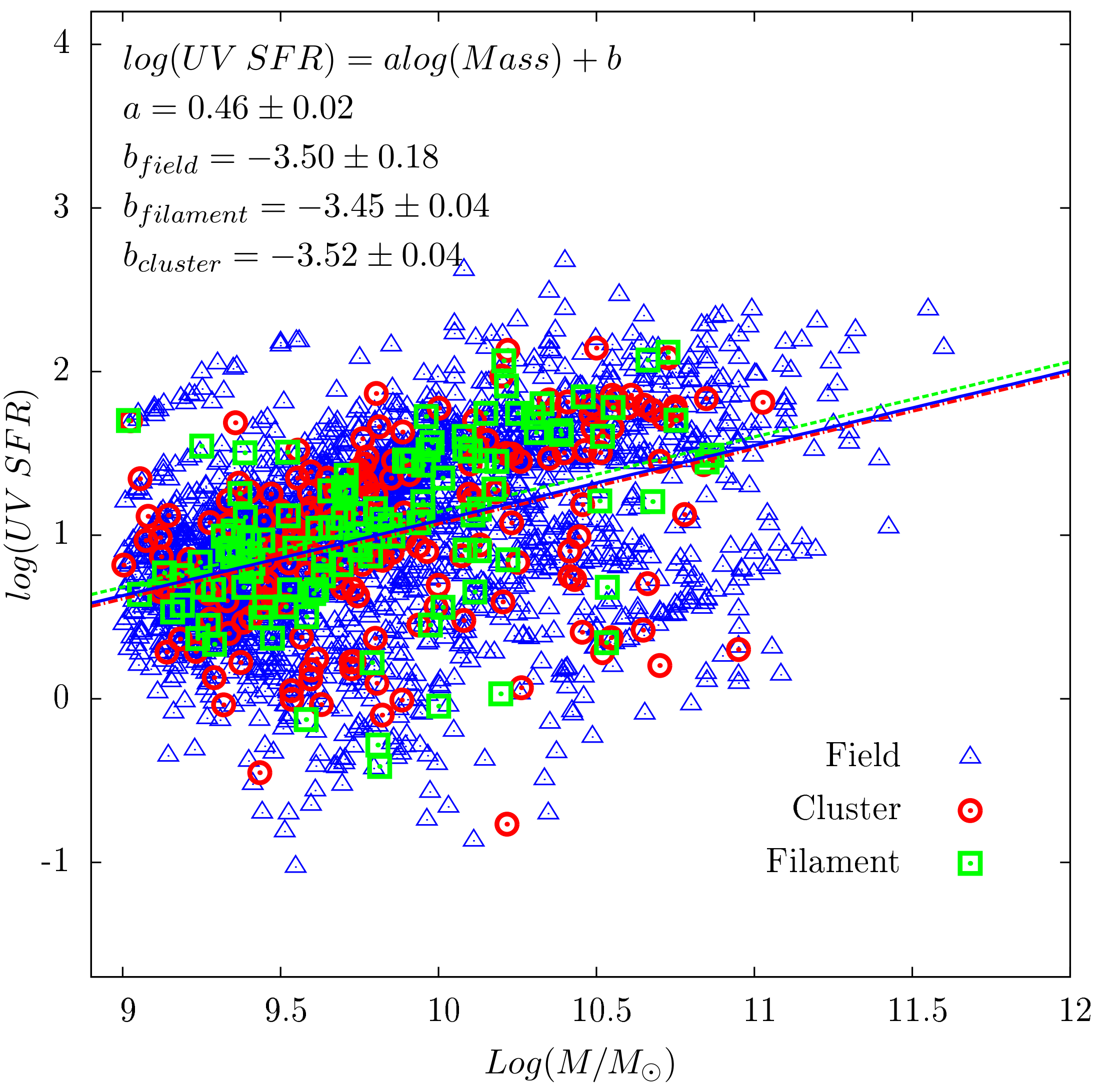

Figure 4.11: Same as Figure 4.9 but for star-forming galaxies in the control sample.

rest-frame U and B magnitudes (Lin et al., 2014). They all have shown that for star-forming galaxies, the SFR−mass or sSFR−mass relation is almost independent of the environment, consistent with our results.

We found that the SFR−mass relation for star-forming galaxies does not depend on the environment, regardless of the methods used to define environment or to estimate SFR. However, it is important to note that the environmental independence of the SFR−mass relation, as seen in this work and some similar studies, might be partially due to selection effects.

4.5 Discussion

We have shown that the fraction of star-forming galaxies varies with environment and is enhanced in filamentary structures. We have also shown that the *observed* properties of the star-forming galaxies (such as their SFR−mass relation) are independent of the cosmic web. However, due to selection biases in the current data, we are unable to discriminate between two scenarios: (1) the observed enhancement in the fraction of star-forming galaxies in filaments is the result of an elevation in the SFR of star-forming galaxies and (2) there is a real intrinsic enhancement of star-forming galaxies in filaments with respect to clusters and the field.

It is possible to disentangle these two scenarios with a significantly deeper (and/or wider) Hα sample. This would equip us with a mass-dependent luminosity function and a significantly broader range of intrinsic SFRs in different environments. Indeed, a deeper/wider sample would introduce less selection biases in the results.

The enhancement of star-formation activity in filaments compared to denser regions like clusters could be attributed to a milder galaxy−galaxy harassment and interaction (Lavery and Henry, 1988; Moore et al., 1996; see also Coppin et al., 2012) in the former. The environment of filaments is not hot compared to clusters (the typical temperature of filaments is $\sim10^5$−10^7 K; e.g., see Cen and Ostriker, 2006; Werner et al., 2008; Zappacosta et al., 2002; Nicastro et al., 2005b). Therefore, galaxies in filaments can still hold their gas content to form stars. Ram-pressure stripping (Gunn and Gott, 1972; Abadi et al., 1999) is practically not effective in suppressing the star-formation in filaments compared to clusters, given the fact that (1) the IGM within filaments is less dense, (2) galaxies in filaments, on average, have a smaller velocity dispersion with respect to the background gaseous medium, and (3) the timescale of SF events in galaxies is shorter than the effective timescale for ram-pressure stripping ($\sim$Gyr). Notice, however, that this argument depends on the galaxy mass. In dwarf galaxies, their shallow potential wells can provide a relatively small restoring force from the ram-pressure force of the IGM in filaments, with the end result of significant gas stripping in low mass galaxies due to the cosmic web at typical gas densities and velocities (e.g., Benítez-Llambay et al., 2013). Instead, for galaxies in the mass range studied here, the restoring force of the dark matter halo + baryons can be more than three orders of magnitude larger than the inner regions of dwarfs, making ram-pressure stripping from filaments largely inefficient.

Another possibility for the enhancement in the fraction of star-forming galaxies in filaments might be due to a more efficient gas accretion rate in filamentary structures. A more efficient gas accretion rate in filaments is able to increase the availability of cold gas for galaxies which, in turn, enhances the intrinsic SFR of galaxies in filaments and would affect their SFR$-$mass relation. However, if the selection biases turned out to be a minor issue and the SFR$-$mass relation was indeed independent of the environment, the gas accretion rate, as the main driver of the SFR$-$mass relation (Dutton et al., 2010), would become independent of the environment and could not possibly account for the increased fraction of star-forming galaxies in filaments.

As galaxies move along filaments toward the central region of galaxy clusters, it is likely that a fraction of them survive their passage through the cluster core and are flung back out into less dense filamentary structures. It is unlikely that these backsplash galaxies (Gill et al., 2005; Pimbblet, 2011) significantly influence our results. Since these systems have already entered the cluster environment, their star-formation was likely truncated due to ram pressure stripping and the gravitational tidal field of the cluster well before they return to filaments. Moreover, backsplash galaxies become important within $\sim 1-2$ virial radii of clusters (Pimbblet, 2011; Mamon et al., 2004), a region that does not cover a significant portion of the filaments in this study.

Here, we argue that the higher number density of galaxies in filaments compared to the field and their lower velocity dispersion compared to those in clusters, increase the chance of gravitational interaction between galaxies, which, in turn, results in a higher chance of star-forming galaxies to be found in filaments (and/or a higher SF activity in filaments). Our results are consistent with a physical process that might be related to mild galaxy−galaxy interactions, as numerical simulations have shown that interactions can trigger star-formation due to tides and compression of the gas (e.g., Barnes, 1991; Springel, 2000; Cox et al., 2008). The scenario proposed here could induce several other observational signatures, such as a larger fraction of irregular morphologies, close galaxy pairs, and AGN (interaction-induced) associated with filaments than in clusters/field.

To further support this idea, we investigated the morphology of the Hα sample using the available ZEST catalog (Scarlata et al., 2007a). Interestingly, we find that the fraction of irregular morphologies is higher in filaments compared to that of clusters and the field. The fraction of irregular Hα emitters is 32%±12%, 8%±5%, and 19%±2% in filaments, clusters, and the field, respectively (see also Sobral et al., 2009 for an overall number of irregulars). However, we mention that the uncertainties in the fraction of irregular Hα emitters is relatively large and we need larger number statistics to robustly constrain it. Another piece of evidence arises from the fraction of galaxy pairs in different environments. We find that the fraction of close galaxy pairs (projected distance $<$ 20 kpc) in the control sample is 7.7%±2.2%, 5.4%±1.4%, and 2.7%±0.3% in filaments, clusters, and the field, respectively, higher in filaments and clusters compared to the field. We also inspected the fraction of AGN in different environments but due to very small number statistics, we cannot make any conclusions with the AGN. We mention that all of the above-mentioned observational signatures can be constrained vigorously with a larger sample, a possibility that we would like to explore in the near future.

4.6 Conclusions

1. Our results improve previous studies based on intermediate environments and agree quantitatively and qualitatively with them, but show that what are often called "intermediate" densities and/or "group" environments are likely to be filaments.

2. Our results show that the observed fraction of star-forming galaxies is enhanced in filaments, relative to the field and cluster environments at $z \sim 0.8-0.9$. This enhancement in the fraction of star-forming galaxies in filaments is either intrinsic and/or due to a boost in the SFR of star-forming galaxies in filaments when combined with the selection biases. A possible physical interpretation for this trend is mild galaxy−galaxy interactions.

3. We also find that —in agreement with other studies— the observed SFR−mass relation and its intrinsic scatter, median SFR, stellar mass, and sSFR is mostly independent of environment for selected Hα emitters and underlying star-forming galaxies at $z \sim 0.8-0.9$. However, we mention that the environmental independence of the median SFR and the SFR−mass relation for star-forming galaxies is affected by the selection biases, i.e., the intrinsic SFR of star-forming galaxies might vary with environment without being observed in the median values or the SFR−mass relation, as a result of selection effects. Indeed, if the environmental invariance of SFR−mass relation turns out to be real (and not much affected by the selection biases), this means that the environment is most relevant to set the star-forming fraction, or to determine if a galaxy is actively forming stars or not (but when it forms stars, on average, it lies on the same relation across environments). This implies that the physical processes involved in triggering/quenching star-formation should act on a relatively short timescale (assuming the SFR−mass relation is actually independent of environment and not much affected by selection biases).

4. Since our analysis is limited to a narrow redshift slice (Δz=0.03, equivalent to a comoving radial length of ∼80 Mpc at z ∼0.84), we discriminate against filaments oriented radially and we miss possible sub-structures along the line of sight. However, this is a limitation to all other similar photo-z-based studies. A better understanding of the geometry of structures can be achieved by 3D reconstruction of them using a large spectroscopic sample.

Chapter 5

Spectroscopic Study of Star-forming Galaxies in Filaments and the Field

Abstract

We study the physical properties of a spectroscopic sample of 28 star-forming galaxies in a large filamentary structure in the COSMOS field at $z \sim 0.53$, with spectroscopic data taken with the Keck/DEIMOS spectrograph, and compare them with a control sample of 30 field galaxies. We spectroscopically confirm the presence of a large galaxy filament ($\sim$ 8 Mpc), along which five confirmed X-ray groups exist. We show that within the uncertainties, the ionization parameter, equivalent width (EW), EW versus specific star-formation rate (sSFR) relation, EW versus stellar mass relation, line-of-sight velocity dispersion, dynamical mass, and stellar-to-dynamical mass ratio are similar for filament and field star-forming galaxies. However, we show that on average, filament star-forming galaxies are more metal-enriched ($\sim 0.1-0.15$ dex), possibly due to the inflow of the already enriched intrafilamentary gas into filament galaxies. Moreover, we show that electron densities are significantly lower (a factor of $\sim$17) in filament star-forming systems compared to those in the field, possibly because of

a longer star-formation timescale for filament star-forming galaxies. Our results highlight the potential pre-processing role of galaxy filaments and intermediate-density environments on the evolution of galaxies, which has been highly underestimated.

5.1 Introduction

Metal enrichment in galaxies is one of the most important aspects of galaxy evolution as it incorporates the fundamental quantities affecting their evolution such as inflows of cold gas, feedback processes and outflows (stellar winds, supernovae and AGN activity), stellar mass, gas fraction, star-formation rate (SFR), and environment. A relatively tight correlation between metallicity and stellar mass (the mass-metallicity relation) has been investigated, with a redshift evolution reflecting the metal enrichment of galaxies over cosmic time (Tremonti et al., 2004; Erb et al., 2006; Maiolino et al., 2008; Xia et al., 2012; Foster et al., 2012; Sánchez et al., 2013; Henry et al., 2013; Zahid et al., 2013; Yabe et al., 2014; Steidel et al., 2014; Masters et al., 2014; Sanders et al., 2015; Maier et al., 2015). It has been shown that this mass-metallicity relation originates from a more fundamental mass, metallicity, SFR relation (the fundamental metallicity relation), forming a tight surface in this 3D space (Mannucci et al., 2010; Lara-López et al., 2013a; Stott et al., 2013; Bothwell et al., 2013; Maier et al., 2014; Nakajima and Ouchi, 2014; de los Reyes et al., 2015). The mass-metallicity evolution is therefore attributed mostly to the selection of galaxies with higher SFRs at higher redshifts (Mannucci et al., 2010). Simulations and physical models suggest that the metal content of galaxies is the result of a balance between inflows and outflows set by the mass outflow rate, whereas the gas content is regulated by the gas inflow rate and the gas consumption timescale within the galaxy, governed by the star-formation law (Davé et al., 2011; Lilly et al., 2013).

Several studies have scrutinized the potential role of environment in the evolution of the mass-metallicity relation, showing that environment has a second-order, insignificant effect in the mass-metallicity relation, with the majority of studies indicating a slight metallicity enhancement in denser environments (Mouhcine et al., 2007; Cooper et al., 2008b; Ellison et al., 2009; Hughes et al., 2013; Sobral et al., 2013b; Kulas et al., 2013; Shimakawa et al., 2015; Kacprzak et al., 2015; Sobral et al., 2015b; Valentino et al., 2015). However, these studies focus mostly on the cluster versus field as two extreme regions in the distribution of galaxies or rely on the local number density of galaxies as a proxy for their environment. The distribution of galaxies is not just limited to clusters and the field as they naturally belong to the complex network of the cosmic web, comprising clusters, groups, filaments, walls, and voids. Using local number density of galaxies as a probe of their environment has its own drawbacks as well. For example, regions with similar local densities such as galaxy groups, the outskirts of clusters, and galaxy filaments might host different physical processes. As an example of complexities that may arise by focusing only on clusters or local densities, Ellison et al. (2009) have shown that cluster galaxies are on average more metal enriched than the field, but this enhancement is primarily driven by local overdensity of galaxies and not merely cluster membership. Therefore, a better understanding of the evolution of galaxies can be achieved by considering a broader range of environments, e.g., by including galaxy filaments in studies.

Filamentary structures are among the most interesting objects in astronomy. On galactic and circumgalactic scales, galaxies are primarily cold-gas fed through narrow filamentary streams as shown in simulations (Dekel et al., 2009a). Recent observations are starting to reveal the existence of such feeding filaments (Cantalupo et al., 2014; Martin et al., 2014b,a), with sizes up to a few hundred kpc. The smooth versus clumpy nature of these filamentary streams has a significant effect on the formation and evolution of disk- and bulge-dominated galaxies (Dekel et al., 2009a,b). Optical emission line filaments with typical sizes of a few tens of kpc are observed in many cooling flow galaxy clusters, often extending from the central brightest cluster galaxy that is accreting the cooling gas (Ford and Butcher, 1979; Cowie et al., 1983; Hu et al., 1985; Heckman et al., 1989; Crawford et al., 1999; McDonald and Veilleux, 2009; McDonald et al., 2010, 2011). On larger scales (a few to several Mpc), filaments make the backbone of the cosmic web of galaxies (Bond et al., 1996), linking clusters, groups, and denser regions in the density field. Although they are expected to occupy $\lesssim 10\%$ of the volume of the cosmic web, simulations have shown that galaxy filaments contain most of the mass in the universe ($\sim 40\%$, Aragón-Calvo et al., 2010) and host a significant fraction of baryons in the form of a warm-hot intergalactic medium gas in the temperature range 10^5-10^7 K (Cen and Ostriker, 1999; Davé et al., 2001; Cen and Ostriker, 2006; Davé et al., 2010; Klar and Mücket, 2012). Filaments are seen in the optical wavelengths as the large-scale thread-like concentration of galaxies (e.g., Pimbblet et al., 2004; Scoville et al., 2007a; Kovač et al., 2010; Guzzo and The Vipers Team, 2013; Scoville et al., 2013; Alpaslan et al., 2014; Tempel et al., 2014; Darvish et al., 2014, 2015), in X-ray as a warm-hot gas in emission and absorption (e.g., Scharf et al., 2000; Zappacosta et al., 2002; Kaastra et al., 2003; Finoguenov et al., 2003; Nicastro et al., 2005b,a; Werner et al., 2008; Danforth et al., 2010; Zappacosta et al., 2010; Nicastro et al., 2010), in the infrared as possible sites of enhanced star-formation activity, linking clusters (e.g., Koyama et al., 2008; Biviano et al., 2011; Coppin et al., 2012; Pintos-Castro et al., 2013), and in the weak-lensing studies as a bridging distribution of dark matter, connecting galaxy clusters (e.g., Jauzac et al., 2012; Dietrich et al., 2012; Higuchi et al., 2015).

Despite the significant importance of filaments, their observational aspect is still poorly investigated or often ignored (see e.g., Kodama et al., 2001; Ebeling et al., 2004 for some earlier studies on filaments). Nevertheless, the limited number of studies in this field has already highlighted the importance of filaments as regions with an enhanced fraction of star forming galaxies and/or star-formation activity (Porter and Raychaudhury, 2007; Porter et al., 2008; Koyama et al., 2008; Fadda et al., 2008; Biviano et al., 2011; Coppin et al., 2012; Pintos-Castro et al., 2013; Darvish et al., 2014). There are also some systematic surveys/works trying to expand galaxy evolution studies beyond the cluster realm by probing the much larger scale structures (of the order of ~ 10 Mpc and beyond) around massive galaxy cluster candidates (see e.g., Kodama et al., 2005; Kartaltepe et al., 2008; Lubin et al., 2009; Sobral et al., 2011). In an attempt to study the role of filaments in galaxy evolution, Darvish et al. (2014) investigated the star-formation activity in a large-scale structure (LSS,

$\sim$10 $\times$ 15 Mpc) at z $\sim$0.84 in the COSMOS field (Scoville et al., 2007b) by identifying a prominent filamentary structure, traced by the distribution of narrow-band selected Hα star-forming galaxies (Sobral et al., 2011). They showed that although, on average, the SFR, SFR$-$mass relation, and specific star-formation rate for star-forming galaxies show similar trends in different environments, the fraction of Hα emitting galaxies is enhanced in filaments compared to clusters and the field, possibly due to mild galaxy$-$galaxy interactions. However, a thorough grasp of the role of filaments in galaxy evolution can only be obtained through a detailed spectroscopic study of galaxies in different environments including filaments.

In this chapter, we focus on the spectroscopic study of galaxies in a significantly large filament ($\sim$ 8 Mpc) at z $\sim$0.53 in the COSMOS field and compare it with a control sample of field galaxies at the same redshift. We will investigate the physical properties of galaxies such as electron density, metallicity, ionization parameter, equivalent width (EW), velocity dispersion, and dynamical mass in these two environments and investigate possible differences.

The format of this chapter is as follows. In Section 2, we briefly describe the methods used to extract the LSS and the filament. Section 3 deals with the spectroscopic observations. Section 4 presents the star-forming emission-line galaxies selected for the spectroscopic analysis. Our results are given in Section 5 and discussed in Section 6. We provide a summary of the results in Section 7.

Throughout this chapter, we assume a flat ΛCDM cosmology with H_0=70 kms^{-1} Mpc^{-1}, Ω_m=0.3 and Ω_Λ=0.7. All magnitudes are expressed in the AB system and stellar masses and star-formation rates are given assuming a Chabrier initial mass function (IMF) (Chabrier, 2003).

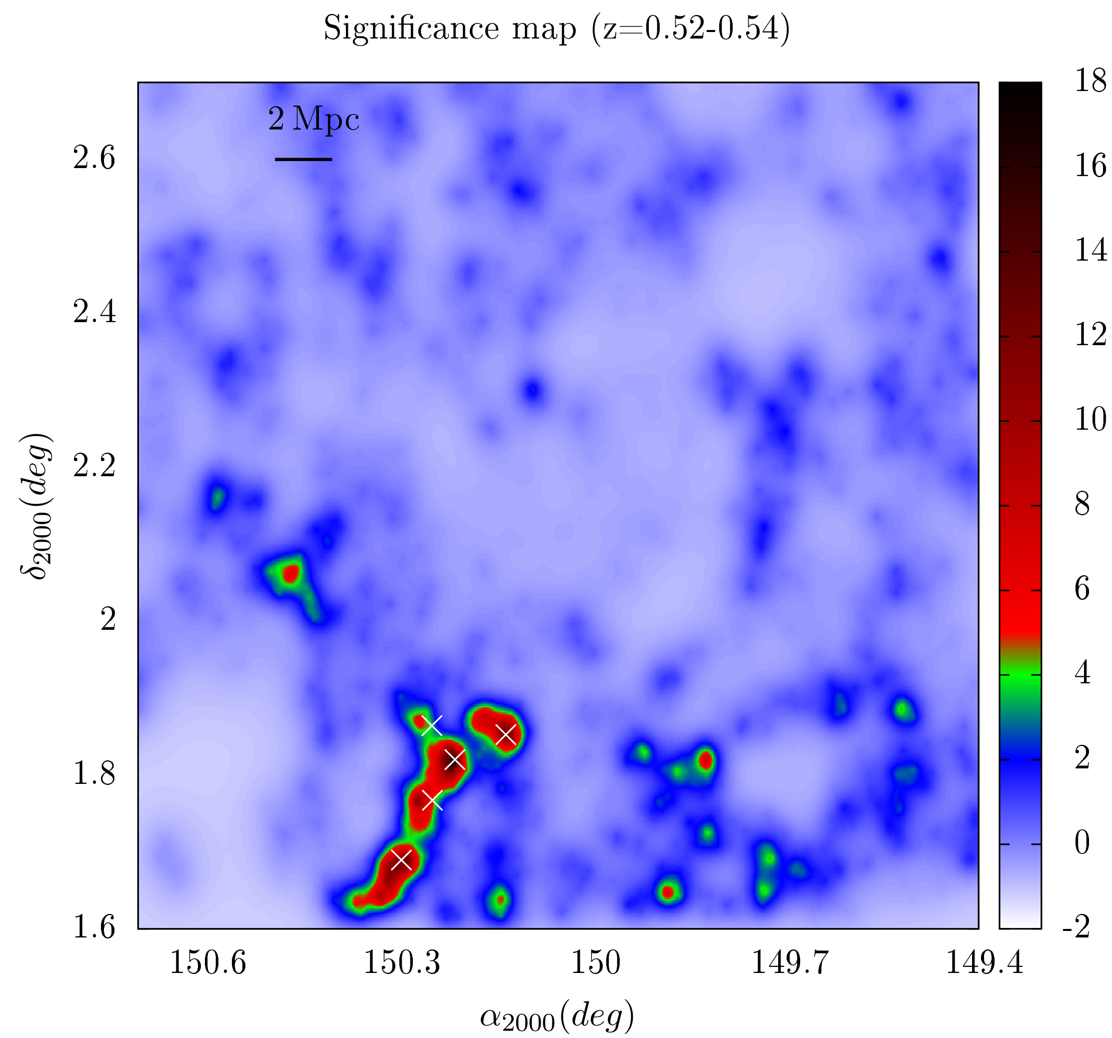

Figure 5.1: Top: Significance map of the density field in the COSMOS at z=0.52-0.54, estimated via the weighted adaptive kernel density estimator of Darvish et al. (2015). A large-scale structure ($\sim$ 8 Mpc) with a filament-like morphology is clearly seen in the lower left. There are at least five confirmed X-ray groups (Finoguenov et al., 2007; George et al., 2011) lying along, or in the vicinity of this filamentary structure (white crosses). Bottom: Filamentary signal map, constructed using the MMF algorithm (Aragón-Calvo et al., 2007; Darvish et al., 2014) at z=0.52-0.54, reveals a large filamentary signal values ($>$ 0.5) in the region covering the LSS, further supporting the reality of the filament.

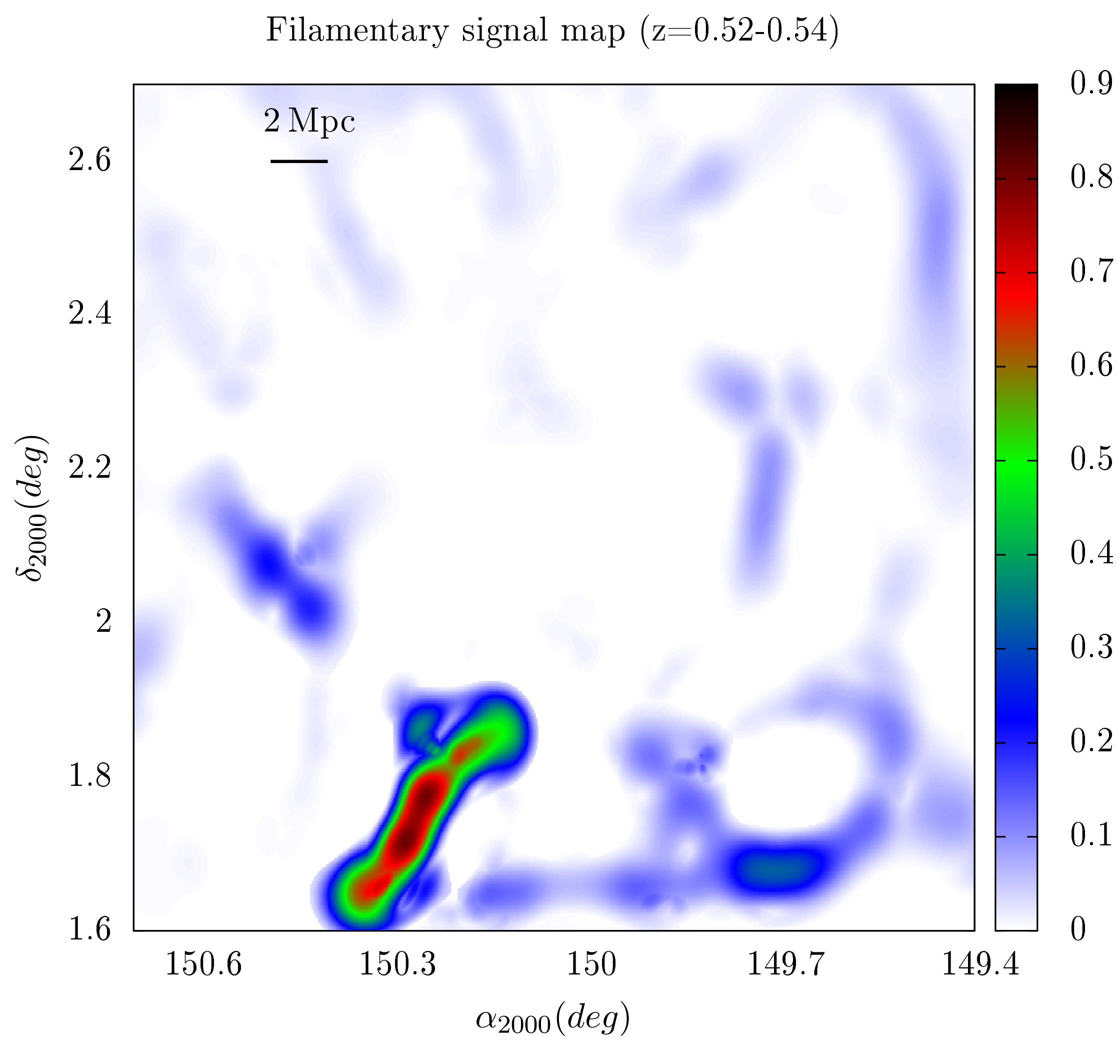

Figure 5.1: cont. (bottom)

5.2 Motivation and the LSS Extraction

We use the estimated density field in the COSMOS field introduced in Chapter 2 to search for large overdensities of galaxies that have a filamentary morphology. The surface density field was estimated in narrow z-slices, using a $K_s < 24$ (McCracken et al., 2012) sample of galaxies with accurate photometric redshifts (photo-z uncertainty $\Delta z \lesssim 0.01$ at $z \sim 0.5$, Ilbert et al., 2013), with the aid of the robust weighted adaptive kernel density estimator. The photo-z probability distribution function (PDF) of individual galaxies were carefully incorporated into the density field estimation in order to minimize the projection effect. At $z \sim 0.53$, we find a filament-like, significant overdensity of galaxies. Figure 5.1 (top panel), shows the estimated density field in the COSMOS field at $z \sim 0.52$-0.54. A large-scale structure with a thread-like morphology is evidently seen in the lower left side of Figure 5.1, with a significance of $\sigma \sim 8-18$ [1]. The same structure can also be seen in the density maps produced by Scoville et al. (2013) at $z \sim 0.53$.

To further investigate the reality of this structure, we used the 2D version of the Multi-Scale Morphology Filter (MMF) algorithm introduced in Chapter 2, which is able to disentangle the cosmic web into its components such as filaments and clusters. This algorithm describes the local geometry of each point in the density field based on the signs and the ratio of eigenvalues of the Hessian matrix (second order derivative of the density field). For example, if the local geometry of a point resembles a thread-like structure, this algorithm results in a large filamentary signal for the point. The filamentary signal value (a value between 0 and 1) shows the degree of resemblance to a filament, with higher values indicating more resemblance. We apply the MMF algorithm to our density field at $z \sim 0.53$, which results in large filamentary signal values (> 0.5) in the region covering the LSS (Figure 5.1, bottom panel).

The reality of this filamentary structure is further supported by the X-ray group catalogs of Finoguenov et al. (2007) and George et al. (2011) in the COSMOS field. There are at least

[1] Significance is defined as $\sigma = (\Sigma - \Sigma_{bg})/\sigma_{bg}$, where Σ is the estimated surface density, Σ_{bg} is the mean surface density, and σ_{bg} is the standard deviation around the mean surface density values.

five confirmed intermediate-density X-ray groups lying along, or in the proximity of this filamentary structure, in agreement with the expectations from the cosmic web simulations that galaxy groups/clusters are connected through the network of filaments (Bond et al., 1996). The X-ray groups are in the redshift range δz=0.527−0.530, with virial masses M_{200}=1.8−4.6×10^{13} M$\odot$ (George et al., 2011). This filamentary structure has a physical length of $\sim$ 8 Mpc and it might be even longer as it is located near the edge of the COSMOS field. According to simulations (Aragón-Calvo et al., 2010), such long filaments have $<$ 10% chance of being found in the density field, making them unique targets for the studies of the cosmic web and the LSS.

5.3 Spectroscopic Observations

5.3.1 Target Selection for Spectroscopy

In selecting the sources for spectroscopy, we define two samples. The first sample comprises the potential filament members and the second is a control sample of field galaxies at the same redshift. The main filament targets are selected to be in the vicinity of the filament, brighter than $i^+ < 22.5$ and to have $>$ 50% of their photo-z PDF lying within the redshift slice $\Delta z \sim$0.52−0.54 centered at z=0.53. The width of the redshift slice is $\sim$2 times the median photo-z uncertainty at $z \sim$0.5. The main field targets are selected similarly to those in the filament, except that they are located in a random point in the COSMOS field with no sign of overdensities. We also consider fillers as we design multi-object masks for spectroscopy. The filler sources on the filament mask are selected to be in the vicinity of the filament, brighter than $i^+ < 22.5$, with their photo-z in the range Δz=0.41−0.52 or Δz=0.54−0.65. The filler sources on the field mask are chosen in a similar way as that of the filament fillers except that they are located in the random position of the field mask. In selecting the sources (main targets and fillers, in filament and the field), we discard those flagged as potential AGN, based on the publicly available catalog of AGN candidates in the COSMOS field (Trump et al., 2007). Therefore, we expect little to no AGN contamination.

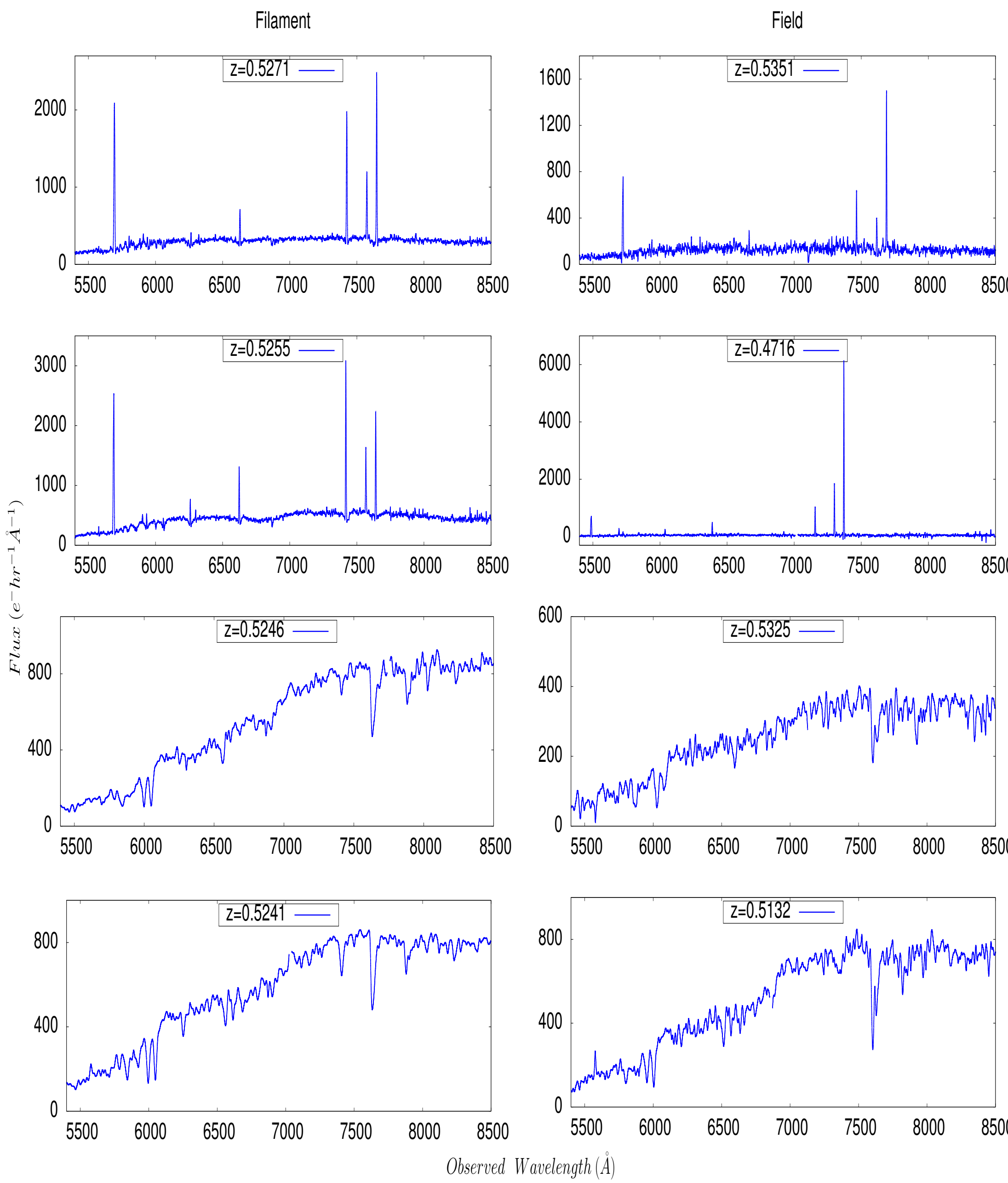

Figure 5.2: Some examples of the observed Keck/DEIMOS spectra, including quiescent and star-forming galaxies, in the filament and the field masks in the wavelength range 5400−8500 Å. The labels show the extracted redshift of the samples. Note the quality (high S/N) of the spectra.

Table 5.1: Observing Log and Spectroscopic Mask Properties

Mask Name	Date	R.A. J2000	Dec. J2000	Position Angle deg	Exp. Time ks	Number of Sources
Filament	28 Dec. 2014	10:00:59.36	+1:47:04.4	−42.0	5.4	52 targets, 46 fillers
Field	29 Dec. 2014	10:01:35.78	+2:32:08.0	+27.0	2.8	17 targets, 50 fillers

5.3.2 Observational Strategy

Spectroscopic observations were made on 28 and 29 December 2014 with the DEIMOS spectrograph on the Keck II telescope under clear conditions. We used a 600 line/mm diffraction grating (0.65 Å/px dipersion) with a spectral span of ∼5300 Å and a GG455 order blocking filter. Slit width is set to 0.75" for all sources. We select the central wavelength of λ_c=7200 Å which gives us an observed wavelength coverage ∼4550−9850 Å. Since the majority of the targets are expected to be at z ∼0.53, we achieve the rest-frame wavelength coverage ∼3000−6400 Å, given that all the slits are located at the center of the mask. This enables us to cover major spectroscopic features that can be potentially used to estimate SFR (e.g. [OII]λ3727, Hβ), metallicity ([OII]λ3727, [OIII]λ4959, [OIII]λ5007, Hβ), electron density ([OII]$\lambda\lambda$3726,3729 doublet), and ionization parameter ([OII]λ3727, [OIII]$\lambda\lambda$4959,5007) for the main targets. We designed two masks, one containing the filament targets and fillers and the other containing the control sample of field galaxies (targets and fillers). The masks were designed in such a manner to maximize the number of main targets.

The filament mask consisted of 52 main targets and 46 fillers and the field mask contained 17 main sources and 50 fillers [2]. The filament mask was observed on December 28 for 5.4 ks exposure time (4 individual exposures of 1.2 ks and one exposure of 0.6 ks), with the midpoint airmass of ∼1.1 and an average seeing of ∼0.5". We observed the field mask on December 29 for ∼2.8 ks total exposure time, with the midpoint airmass of ∼1.05 and an average seeing of ∼0.7". We note that after the spectroscopic redshift extraction, some fillers may turn out to be filament members or some fillers might be used as field galaxies.

[2] There is also one Lyman-α candidate in the filament and one in the field mask. The spectroscopic confirmation and analysis of these Lyman-α targets are presented in Matthee et al. (2015) and Sobral et al. (2015a).

We will use these extra possible sources to increase the sample size for our analysis. Table 5.3 summarizes the observing log.

5.3.3 Data Reduction and Calibration

In order to reduce the DEIMOS data, we use the *spec2d* package (Cooper et al., 2012; Newman et al., 2013). The reduction process involves flat fielding, cosmic ray removal, sky subtraction and wavelength calibration on a slit-by-slit basis. We used standard Kr, Xe, Ar, and Ne arc lamps for wavelength calibration. No dithering pattern was used for sky subtraction. The pipeline also extracts the 1D spectrum from the reduced 2D one per slit using the extraction algorithm of Horne (1986), which relies on the sum of fluxes at each wavelength in an optimised window around the 2D spectrum. We flux-calibrate the 1D spectra using the standard stars $Feige34$ and $Hz44$. The half-light radius of the sources is in the range $\sim$0.2$-$0.9". Therefore, we lose some flux at the 0.75" slit width due to the larger angular size of some of the sources and primarily, due to the seeing. We correct the flux-calibrated spectrum of each source (for the slit-loss) by scaling it with the observed photometry of the source. This is performed by integrating the spectra over the Subaru filter response profiles in broad (r and i^+), intermediate ($IB574$, $IB624$, $IB679$, $IB709$, $IB738$, $IB767$ and $IB827$), and narrow ($NB711$ and $NB816$) band filters and finding the required slit-loss correction term at each waveband. The median (estimated with the Hodges$-$Lehmann estimator) of the slit-loss correction scaling terms at these bands for each individual source is used as its slit-loss correction term. The *Subaru* multi-waveband magnitudes are extracted from the publicly available optical catalog of the COSMOS field (Capak et al., 2007b). Figure 5.2 shows examples of selected spectra in the filament and the field.

5.3.4 Spectroscopic completeness

The overall spectroscopic completeness for the main targets in the filamentary structure and the field are $\sim$74% and $\sim$77%, respectively. The spectroscopic completeness varies slightly with magnitude. For the main targets with $i^+ \leq 21.5$, we obtain a spectroscopic completeness of ∼76% (filament) and ∼73% (field). At $i^+ > 21.5$, the spectroscopic completeness becomes ∼72% (filament) and ∼82% (field). We obtain a spectroscopic success rate of ∼94% (89% for fillers) and 100% for the main targets in the filament and the field, respectively. The spectroscopic completeness is generally a function of position as well. However, due to the small sample size, we do not try to quantify it. We note that it is relatively uniform over the filament and the field regions.

5.3.5 Filament Spectroscopic Confirmation

We visually extract the spectroscopic redshifts using the *SpecPro* code (Masters and Capak, 2011). The main filament targets yield spectroscopic redshifts in the range z_{spec}=0.5067-0.5582 with a very sharp peak at $z \sim 0.53$ (see Figure 5.3). The filament fillers are spread in the range z_{spec}=0.4085−0.7797. Figure 5.3 shows the spectroscopic redshift distribution in the range $0.50 \leq z \leq 0.59$ for all the sources (main targets and fillers) in the filament mask (dashed blue line), as well as the main filament targets only (dashed red line). We clearly see a peak at $z \sim 0.53$, confirming the presence of the filamentary structure. The average spectroscopic redshift for the filament main targets is z_{avg}=0.5279, with standard deviation σ_z=0.0073. We fit a Gaussian function to the obtained redshift distribution of the main targets (solid green line). The Gaussian fit results in a peak redshift of z_{peak}=0.5283, with standard deviation σ=0.0015.

There is evidence for at least two individual nearby peaks centered at $z_1 \sim 0.528$ and $z_2 \sim 0.526$, as seen in the inner plot of Figure 5.3, indicating the existence of substructures along the filament. Fitting a double peaked Gaussian to the distribution of filament main targets yields redshifts z_1=0.5258±0.0008 and z_2=0.5287±0.0004 for these substructures. Note that there are only 4 (∼8%) main filament targets that yield spectroscopic redshifts outside the range $0.52 < z < 0.54$ originally adopted for main target selection, indicating a successful target selection process and a robust LSS extraction (Darvish et al., 2015).

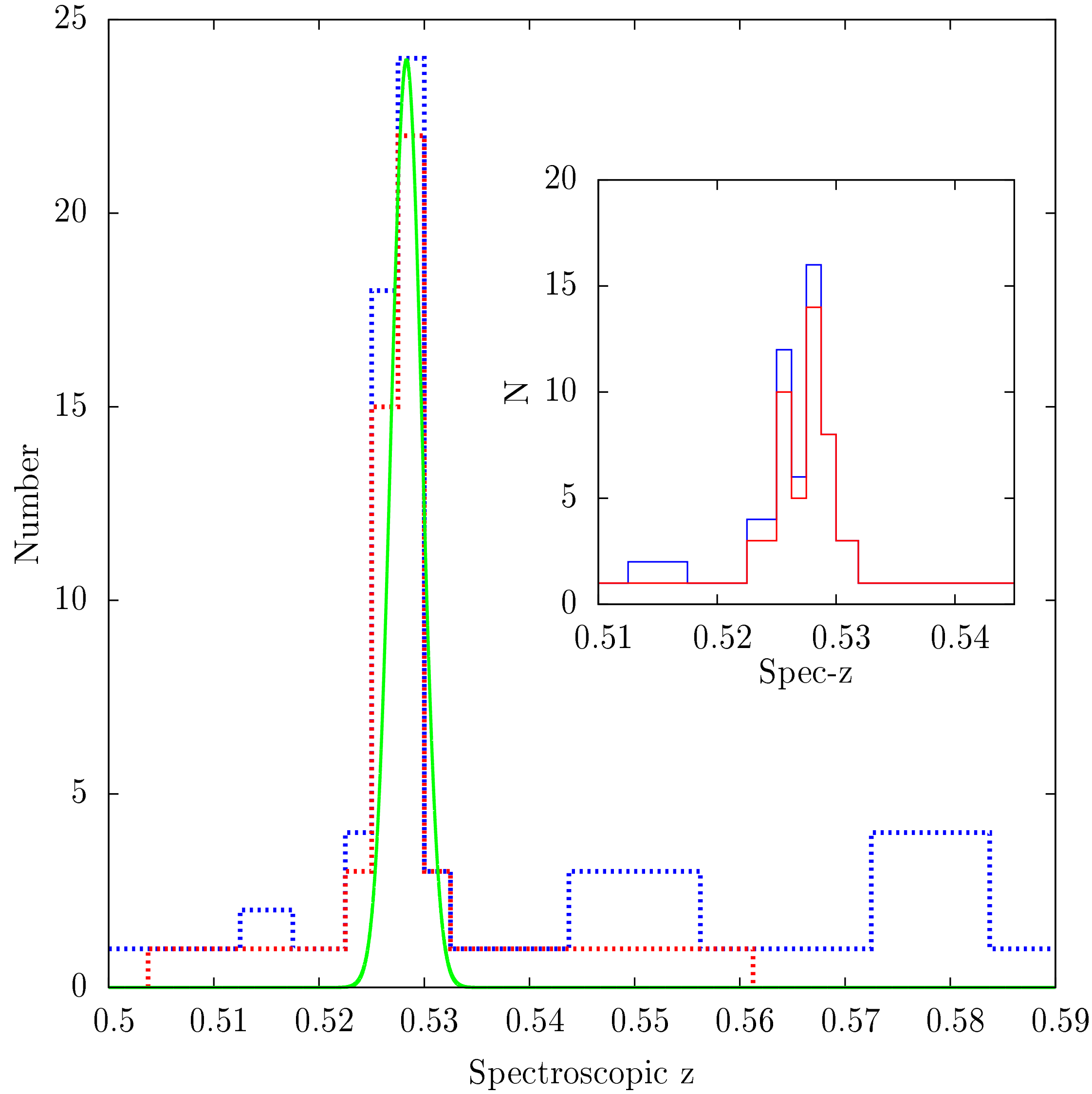

Figure 5.3: Spectroscopic redshift distribution in the range 0.50≤ z ≤0.59 for sources in the filament mask. Dashed blue line shows all the sources (main targets and fillers) in the filament mask, whereas the dashed red line indicates the main filament targets only. A peak at z ∼0.53 is seen, confirming the presence of the filament. Solid green line shows a Gaussian fit to the obtained redshift distribution of the main targets, peaking at z_{peak}=0.5283, with standard deviation σ=0.0015. The inner plot shows two individual nearby peaks at z_1=0.5258±0.0008 and z_2=0.5287±0.0004, showing the existence of possible substructures along the filament.

5.4 Selection of Star-forming, Emission-line Galaxies

In this work, we compare physical, chemical and dynamical properties of galaxies in the filament and the field that rely on strong emission lines. Therefore, we need to define a sample of star-forming emission line galaxies. We carefully investigate the obtained spectra and select those that visually have clear star-forming features, high quality, high Signal-to-Noise [OII], [OIII], and Hβ emission lines. We also make sure that filament sources have spectroscopic redshifts in the range z_{spec}=0.52−0.54 and field sources in the range z_{spec}=0.47−0.59. As we already mentioned in Section 5.3.2, after the spectroscopic redshift extraction of the sources, some fillers turned out to be filament members and some fillers can be used as field galaxies. We use these extra sources to increase the sample size of star-forming emission line galaxies. The final star-forming sample comprises 28 galaxies in the filament and 31 galaxies in the field [3].

5.4.1 Stellar Mass Estimation

Stellar masses were derived by Ilbert et al. (2013), using SED template fitting to the UV, optical, and mid-IR photometry. The synthetic templates were generated using BC03 (Bruzual and Charlot, 2003), assuming a Chabrier IMF, three different metallicities, an exponentially declining SFH with different e-folding time scales (τ=0.1−30 Gyr), and the Calzetti et al. (2000) extinction law. Contributions from nebular emission lines were included. Stellar masses are based on the median of the stellar mass PDF, marginalized over all other parameters.

The magnitude cut of $i^+ < 22.5$ used for sample selection, introduces a varying stellar mass completeness limit at different redshifts. We use the method developed by Pozzetti et al. (2010) to estimate the stellar mass completeness (see also Ilbert et al., 2013; Darvish et al., 2015). At $z \sim$0.5, we estimate the mass completeness to be ∼70%, 90%, and 95% at log(M/M$_\odot$)∼9.3, 9.6, and 9.7 respectively. In the low-mass bin (log(M/M$_\odot$)=9−9.5)

[3] We later discard one of the field sources as an AGN (Section 5.4.3), reducing the field sample size to 30 sources.

of our star-forming sample, the weighted average of the stellar mass is log($M/M_\odot$)$\sim$9.3. Therefore, in the lower mass range, our sample is $\sim$70% complete in stellar mass, while at higher mass bins, we achieve a completeness of $> 95\%$.

5.4.2 SFR Estimation

We estimate the SFR based on Hβ and [OII] luminosities. We convert dust-corrected Hβ luminosity ($L_{H\beta}$) to star-formation rate using the theoretical value of $L_{H\alpha}/L_{H\beta}$=2.86 for case B recombination (temperature T=10,000 K and electron density N_e=10^2 cm^{-3}, Osterbrock, 1989) and the relation between Hα dust-corrected luminosity and SFR given in Kennicutt (1998), modified for the Chabrier IMF:

$$SFR_{H\beta}(M_\odot yr^{-1}) = 1.27 \times 10^{-41} L_{H\beta}(ergs^{-1}) \tag{5.1}$$

The Hβ line is also affected by the Balmer continuum stellar absorption. For brighter galaxies with clear Balmer absorption feature in their spectrum, we correct the Hβ flux by directly fitting a Gaussian function to the the Balmer absorption and adding the missing flux to the Hβ line. For fainter sources where the stellar absorption is not clearly seen, we take the median EW of the Balmer absorption of brighter galaxies and use it to correct for fainter galaxies. The median EW of the Hβ Balmer absoprtion feature is $\sim$0.8 Å, in agreement with Zahid et al. (2011). Nevertheless, the Hβ stellar absorption only results in a 5%$-$10% correction to the Hβ flux, which is smaller or of the order of the uncertainty of the measured line flux itself.

The [OII] star-formation rate not only depends on dust-corrected [OII] luminosity but also on metallicity and ionisation state of the gas. Here, we use the metallicity-dependent equation given in Kewley et al. (2004), modified for the Chabrier IMF:

$$SFR_{[OII]}(M_\odot yr^{-1}) = \frac{4.44 \times 10^{-42} L_{[OII]}(ergs^{-1})}{(-1.75 \pm 0.25)[12 + log(O/H)] + 16.73 \pm 2.23} \tag{5.2}$$

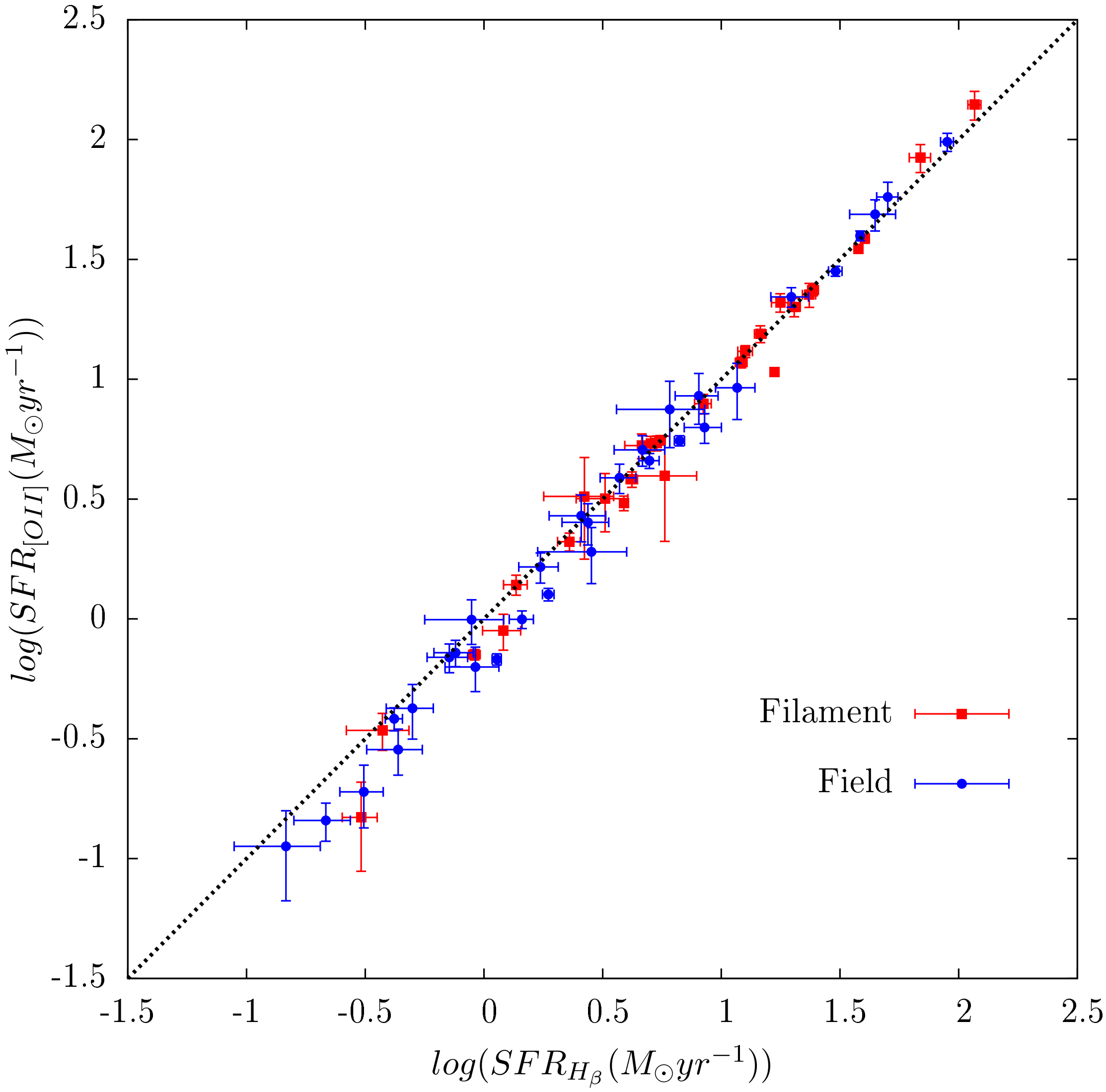

Figure 5.4: Dust-corrected [OII] versus Hβ SFRs for filament (red) and field (blue) star-forming galaxies. There is a good agreement between the estimated SFRs. The median SFR$_{[OII]}$ and SFR$_{H\beta}$ are consistent to within ∼0.01 dex (filament) and ∼0.03 dex (field) and the median absolute deviation between the two SFR indicators is only 0.03 dex.

where 12+log(O/H) is the oxygen abundance metallicity (Section 5.5.2), estimated based on the R_{23} diagnostic, via the R_{23}-metallicity relation of Zaritsky et al. (1994):

$$12 + log(O/H) = 9.265 - 0.33R_{23} - 0.202R_{23}^2 - 0.207R_{23}^3 - 0.333R_{23}^4 \quad (5.3)$$

where R_{23} metallicity diagnostic is defined as R_{23}=([OII]λ3727+[OIII]λ4959+[OIII]λ5007)/H_β.

We dust-correct the emission line fluxes ([OII], [OIII], Hβ) using the relation between the reddening of the ionized gas ($E(B-V)_{gas}$) and that of the stellar continuum ($E(B-V)_{star}$) presented in Calzetti et al. (2000):

$$E(B-V)_{gas} = 2.27E(B-V)_{star} \quad (5.4)$$

The stellar continuum is estimated in the SED Template-fitting procedure (Section 5.4.1), assuming the Calzetti et al. (2000) attenuation curve. Therefore, the dust-corrected, intrinsic emission line flux (F_{int}) is:

$$F_{int} = F_{obs} \times 10^{0.4k_\lambda E(B-V)_{gas}} \quad (5.5)$$

where k_λ is the reddening curve. The relation between stellar and gas extinction is quite uncertain at higher redshifts. While some studies nearly agree with the local universe relation (see e.g., Price et al., 2014 for z ~1.5 galaxies), others have shown that the $E(B-V)_{gas}$=$E(B-V)_{star}$ relation is preferable (see e.g., Shivaei et al., 2015 for z ~2 galaxies and Reddy et al., 2015 for z ~1.4−2.6 systems). However, choosing this new relation does not significantly affect many galaxy properties such as metallicity, ionization parameter, electron density, and gas velocity dispersion presented in Section 5.5. Moreover, at the redshift of our study (z ~0.5), Ly et al. (2012) have shown that assuming $E(B-V)_{gas} \sim 2E(B-V)_{star}$ for star-forming galaxies results in a better agreement between SED-based and Hα SFRs.

Figure 5.4 shows the comparison between dust-corrected [OII] and Hβ SFRs for filament and field samples, exhibiting a very good agreement. The median $SFR_{[OII]}$ and $SFR_{H\beta}$ are consistent to within ∼0.01 dex (filament) and ∼0.03 dex (field) and the median absolute deviation between the two SFR indicators is only 0.03 dex (filament and field).

We also compare the [OII] and SED-based SFRs (not shown here). This shows a larger dispersion of the order ∼0.3 dex. However, this is consistent with e.g., Steidel et al. (2014) (∼0.2 dex, Hα versus SED SFRs at $z \sim 2-3$) and Ciardullo et al. (2013) (∼0.3 dex, [OII] versus UV SFRs at $z \lesssim 0.5$). The source of discrepancy might be due to the stochasticity of the star-formation activity and the difference between the UV and [OII] star-formation timescales ($<$ 20 Myr for [OII] and $\sim$ 100 Myr for UV, Kennicutt, 1998), as the UV SFR is averaged out over a longer timescale.

5.4.3 AGN Contamination

As we discussed in Section 5.3.1, we originally discarded the potential AGN from the samples selected for spectroscopy (Trump et al., 2007). However, we check if the spectroscopic sample is contaminated by any remaining AGN using the available line ratios. Here, we use the [OIII]λ5007/Hβ versus [OII]λ3727/Hβ plot, as well as O_{32} versus R_{23} (O_{32} and R_{23} are defined in Section 5.5) plot to separate AGN from star-forming galaxies (Lamareille et al., 2004). Figure 5.5 shows the line ratios and the line separating star-forming galaxies from AGN. The separating curve is extracted from Lamareille et al. (2004) and the dashed lines are ±0.15 dex (±0.1 dex) uncertainties in the [OIII]λ5007/Hβ versus [OII]λ3727/Hβ (O_{32}-R_{23}) separation curve. According to Figure 5.5, all of our sources lie within the star-forming locus except one source. We jettison this source from our analysis in the following sections. We note that there are a few other sources in the field that lie close to the uncertainty curves. These sources do not change the results of this study.

5.4.4 Stacking Procedure

In order to obtain an average value of the physical quantities presented in Section 5.5, we stack the individual spectra in different environments, as well as stellar mass, SFR,

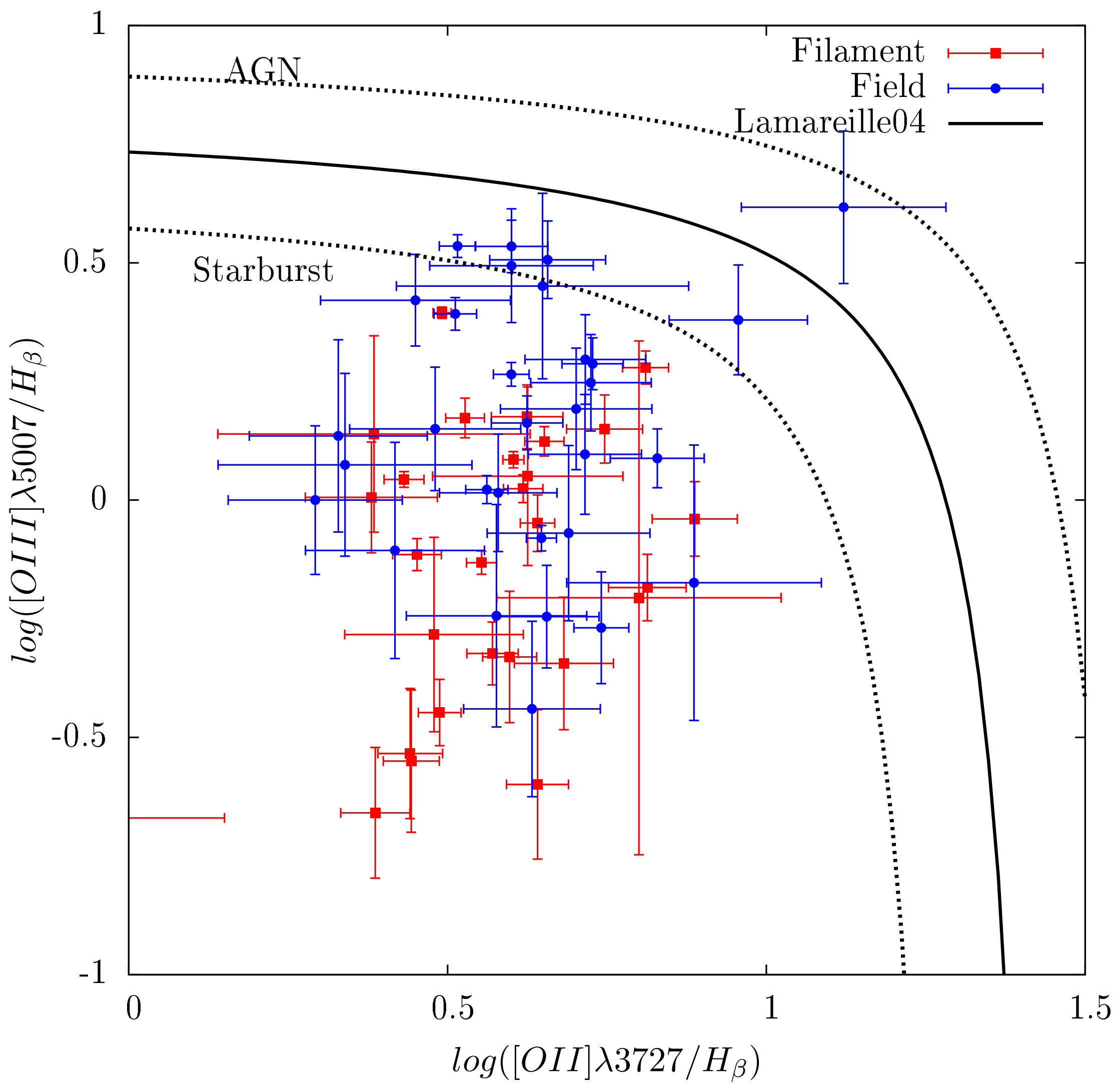

Figure 5.5: [OIII]λ5007/Hβ versus [OII]λ3727/Hβ (top) and O_{32} versus R_{23} (bottom) plots used to separate possible AGN from the filament (red) and field (blue) star-forming galaxies. The separating curve (solid line) is extracted from Lamareille et al. (2004) and the dashed lines are $\pm$0.15 dex ($\pm$0.1 dex) uncertainties in the [OIII]λ5007/Hβ versus [OII]λ3727/Hβ (O_{32}-R_{23}) separation curve. Only one source in the field is within the AGN region. We discard this source from our analysis.

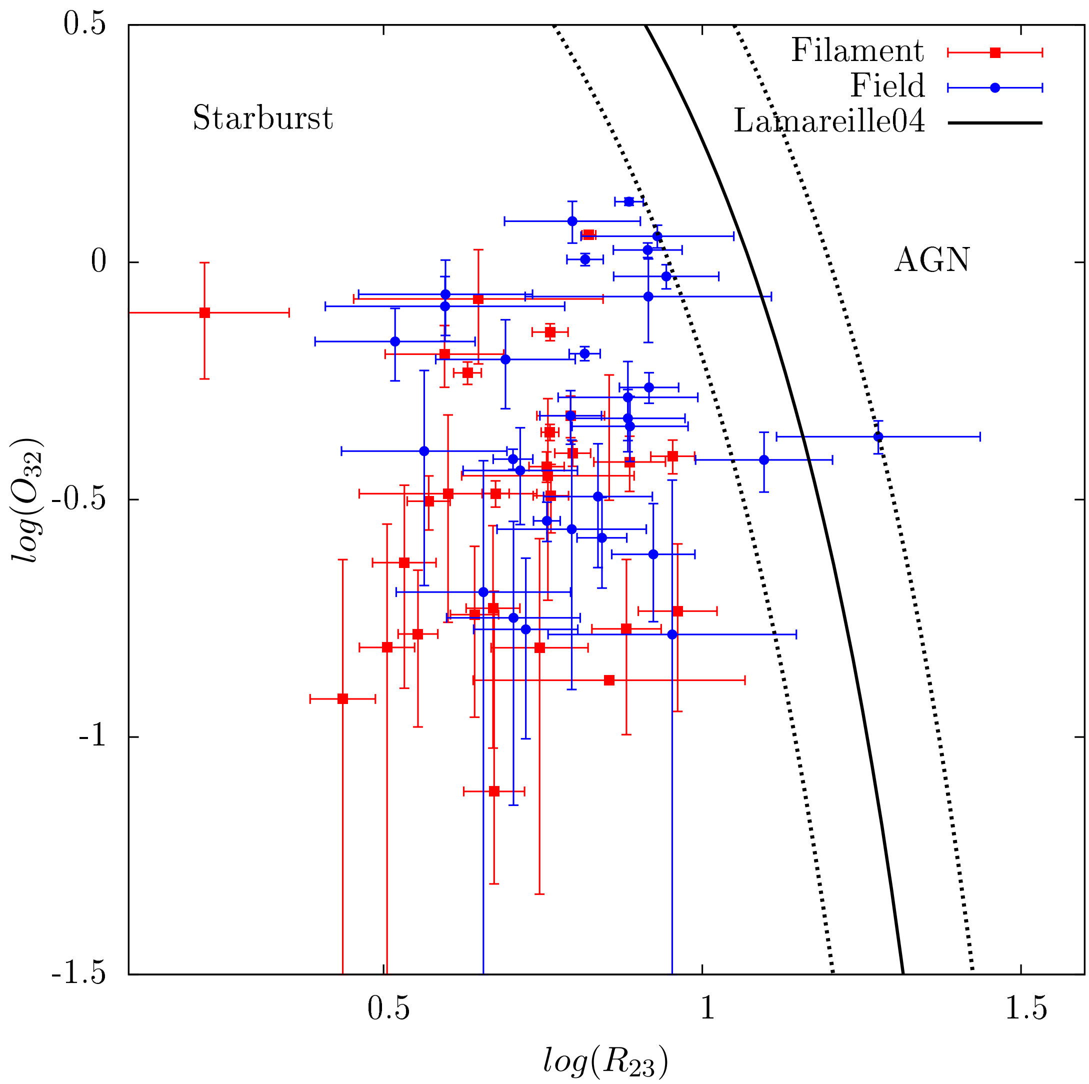

Figure 5.5: cont. (bottom)

sSFR, and $\mu_{0.32}$ bins (defined in Section 5.5.2). We first shift each flux calibrated spectrum to the rest-frame and normalize it to the flux of the Hβ line at the vacuum wavelength of $\lambda_{H\beta}$=4862.7 Å. We then take the weighted mean of each individual, normalized, rest-framed, flux-calibrated spectrum ($F_i(\lambda)$) by summing them up using:

$$F_{stack}(\lambda) = \frac{\sum_{i=1}^{N} w_i(\lambda)F_i(\lambda)}{\sum_{i=1}^{N} w_i(\lambda)} \tag{5.6}$$

where $w_i(\lambda)$ is the inverse variance of the normalized, rest-framed flux. We define three mass bins (log(M/M$_\odot$)=9−9.5, log(M/M$_\odot$)=9.5−10, and log(M/M$_\odot$)$>$ 10), two SFR bins (log([OII] SFR)$\leq$0.75 and (log([OII] SFR)$>$ 0.75), two sSFR bins (log(sSFR)≤ -9 and log(sSFR)> -9), and two $\mu_{0.32}$ bins ($\mu_{0.32}$ $\leq$9.5 and $\mu_{0.32}$ $>$9.5) and will use them in the following section for the analysis of the results.

5.5 Results

5.5.1 Electron Density

The average electron density (N_e) in a nebula can be estimated using the ratio of two lines of the same ion, emitted by different energy levels with almost the same excitation energy. Here, we use [OII]λ3726/λ3729 line ratio to estimate the average electron density (Osterbrock, 1989). Since the [OII]λ3726 and [OII]λ3729 lines are not fully separated in our stacked spectra, we fit a double Gaussian function of the following form to the [OII] doublet line flux:

$$f_\lambda = (\frac{a_1}{\sqrt{2\pi}\sigma_1}e^{-\frac{(\lambda-\lambda_1)^2}{2\sigma_1^2}} + \frac{a_2}{\sqrt{2\pi}\sigma_2}e^{-\frac{(\lambda-\lambda_2)^2}{2\sigma_2^2}}) + f_0 \tag{5.7}$$

We fix the parameters λ_1 and λ_2 to the vacuum wavelength of [OII] doublet lines, i.e., λ_1=3727.09 Å and λ_2=3729.88 Å. The [OII]λ3726/λ3729 flux ratio is therefore determined by the ratio of the normalization parameters, a_1/a_2. We estimate errors of a_1 and a_2 using a Monte-Carlo simulation. We assume that the true flux at each wavelength follows a Gaussian distribution with a sigma equal to the flux uncertainty. We fit the function f_λ to the flux values that are randomly selected from their Gaussian distribution at each wavelength. We perform the fitting procedure 100 times and the error of each free parameter is the standard deviation of the 100 estimated values. The [OII]λ3726/λ3729 flux ratio is converted to electron density using the $TEMDEN$ task of the $IRAF$ package (De Robertis et al., 1987; Shaw and Dufour, 1995). We assume an electron temperature of T_e=10,000 K as a typical temperature of star-forming regions with near-normal abundances (Osterbrock, 1989).

We find that the average electron density is significantly lower for star-forming galaxies in the filament compared to that of the field galaxies. The [OII] line ratio is [OII]λ3726/λ3729= 0.6909±0.0044 for the stacked spectra of filament star-forming galaxies, whereas for field star-forming systems, this ratio is [OII]λ3726/λ3729=1.0050±0.0104. These ratios correspond to the average electron densities of N_e=22±4 and 367±13 cm^{-3} for filament and field galaxies, respectively. The average electron density of the field star-forming galaxies is $\gtrsim$17 times that of star-forming systems in the filament.

We divide the sample into stellar mass, SFR, and sSFR bins and stack the spectra in each bin. We find that at each given mass, SFR, and sSFR bin, the average electron density of the stacked spectra for the filament galaxies is also significantly lower than that of the field galaxies. For example, in the mass range of log(M/M$_\odot$)=9−9.5, the average electron density is N_e=58±5 (filament) and 201±10 (field) cm^{-3}. For log(sSFR)> -9, the average electron density is N_e=15±4 (filament) and 405±15 (field) cm^{-3}, a factor of ∼27 larger for field galaxies. In other words, our result regarding the lower average electron density of star-forming galaxies in filament compared to the field does not change if the comparison is performed at fixed stellar mass, SFR, and sSFR bins in these two environments. Figure 5.6 shows the stacked [OII] intensity normalized to that of Hβ at $\lambda_{H\beta}$=4862.7 Å in filament and the field and in stellar mass, SFR, and sSFR bins (dotted lines). For comparison, the double Gaussian fits are also shown (solid lines). The difference is evident. Depending on the bin selected, electron densities vary in the range $\sim <10-75$ cm^{-3} for filament galaxies

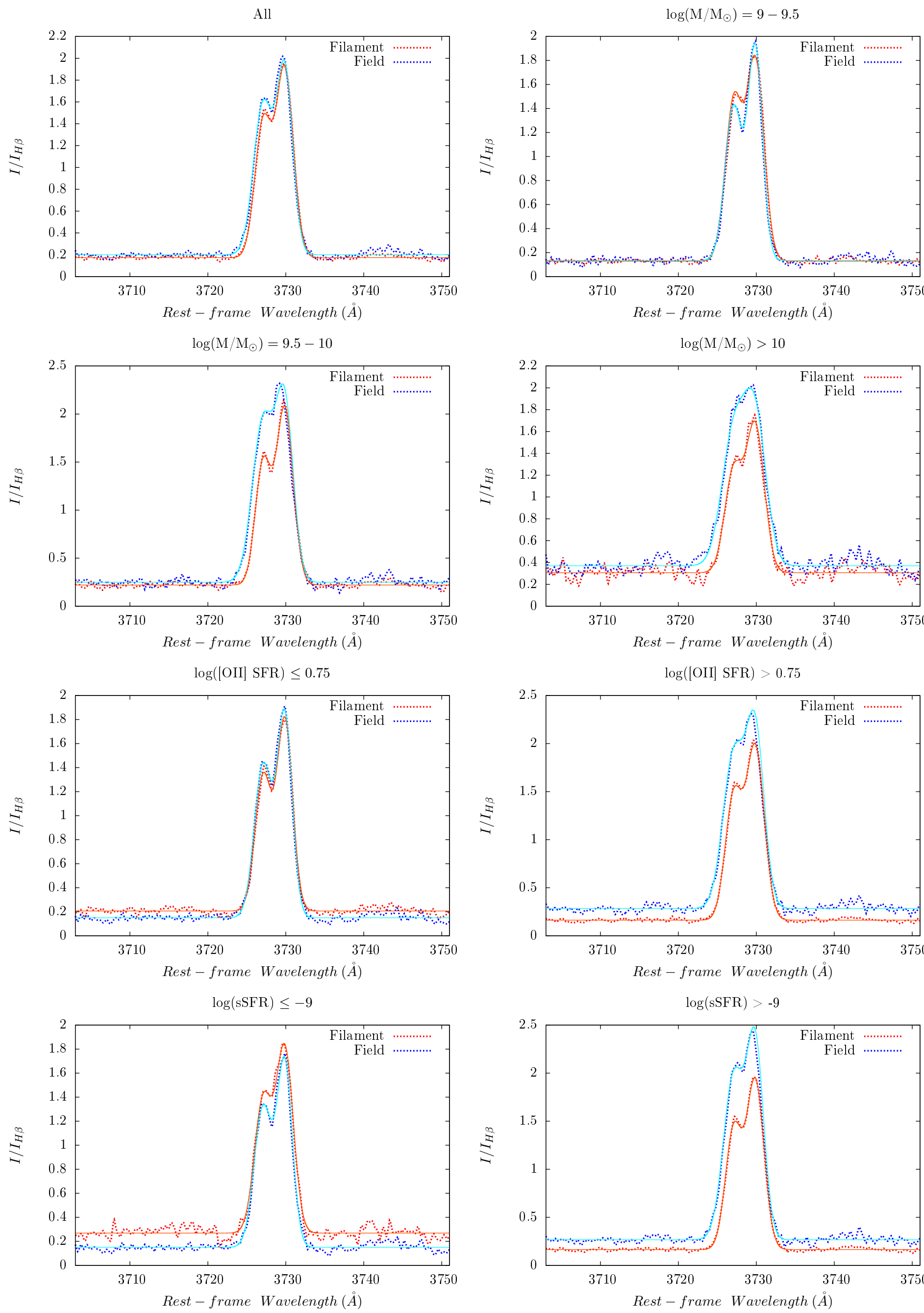

Figure 5.6: Stacked [OII] intensity normalized to that of Hβ at $\lambda_{H\beta}$=4862.7 Å in filament (red dotted line) and the field (blue dotted line) and in stellar mass, SFR, and sSFR bins. We fit the [OII] doublet with double Gaussian functions shown as solid lines. The difference between filament and field galaxies is evident. The [OII]λ3726/[OII]λ3729 ratios are converted to electron densities, assuming T$_e$=10,000 K. Depending on the bin selected, electron densities vary in the range $\sim$ <10−75 cm^{-3} for filament galaxies and in the range $\sim$ 200−740 cm^{-3} for galaxies in the field, significantly lower for filament galaxies.

and in the range $\sim 200-740$ cm^{-3} for galaxies in the field. The [OII] line ratios, as well as the estimated electron densities in different environments and for different mass, SFR, and sSFR bins of galaxies are given in Table 5.2.

Using [SII]λ6716/[SII]λ6761 line ratio, Sobral et al. (2015b) found that for a massive post-merger cluster at $z \sim$0.2 (Dawson et al., 2015; Stroe et al., 2015), electron densities are extremely low (< 5 cm^{-3}) for cluster star-forming galaxies, much smaller than star-forming galaxies in the outskirts and outside of the cluster. They also found that this is primarily driven by star-forming galaxies in the hottest regions of the cluster, thus likely caused by environmental effects. This is consistent with our result in this section (low to extremely low electron densities for filament galaxies) if we assume that the environment affects the electron densities in the sense that regions with higher local densities host galaxies with lower electron densities.

5.5.2 Metallicity

In order to estimate metallicities for filament and field star-forming galaxies, we use the R_{23} index defined as R_{23}=([OII]λ3727+[OIII]λ4959+[OIII]λ5007)/H_β (McGaugh, 1991; Tremonti et al., 2004; Kewley and Ellison, 2008). Here, we use the upper branch of the double-valued R_{23}-metallicity relation given by Tremonti et al. (2004):

$$12 + log(O/H) = 9.185 - 0.313x - 0.264x^2 - 0.321x^3 \qquad (5.8)$$

where x=log(R_{23}).

Using equation 5.8, we evaluate the average metallicity for the stacked spectra of star-forming galaxies in the filament and the field. The metallicity of the stacked spectra in the filament is 12+log(O/H)=8.766$\pm$0.004, about 0.13 dex larger than that of the field galaxies (12+log(O/H)=8.639$\pm$ 0.007). It is known that the metallicity is also a function of stellar mass and star-formation rate (Tremonti et al., 2004; Mannucci et al., 2010) and the metallicity difference between average filament and field star-forming galaxies might be due to different mass and/or SFR of galaxies in these two environments. In order to check this, we divide the star-forming galaxies into mass and SFR bins and stack their spectra. We find that at a given stellar mass bin, star-forming galaxies in the filament are more metal-enriched (by $\sim$0.1$-$0.15 dex) compared to those in the field (Figure 5.7). For example, at $\log(M/M_{\odot})$=9$-$9.5 mass bin, metallicities are 12+log(O/H)=8.708$\pm$0.004 and 8.541$\pm$0.007 in the filament and the field, respectively. Similar results are obtained at fixed SFR bins. That is, at fixed SFR bins, star-forming galaxies in the filament are more metal-enriched. For example, for log(SFR)$\leq$0.75, star-forming galaxies in the filament are $\sim$0.16 dex more enriched in metals than their field counterparts. Table 5.2 gives the metallicities of the stacked spectra for different subsamples.

Figure 5.7 shows the mass-metallicity relation for individual galaxies (red and blue empty points), as well as their stacked results in filament and the field (red and blue filled points). For comparison, we also show the local universe mass-metallicity relation from Tremonti et al. (2004) (modified for stellar masses based on the Chabrier IMF) and that of the Erb et al. (2006) at $z\sim$2 ($-$0.56 dex below the $z\sim$0 trend). Our obtained mass-metallicity relation at $z\sim 0.5$ lies between $z\sim$0 and $z\sim$2 trends. For filament galaxies, it lies $\sim$0.06$-$0.13 dex below the local universe trend, whereas for galaxies in the field, the difference is $\sim$0.21$-$0.23 dex. We fit the metallicity of individual data points in the filament and the field with a function of the form:

$$12 + log(O/H) = c(t - m_0)^2 + z_0 \tag{5.9}$$

where t=log(M/M$_{\odot}$). We fix the parameter c to that of Tremonti et al. (2004) relation (c=$-$0.08026). The fitting is performed using the robust nonlinear least-squares Marquardt-Levenberg algorithm. The estimated parameters are m_0=11.192$\pm$0.339 and z_0=8.955$\pm$0.094 in the filament and m_0=10.639$\pm$0.236 and z_0=8.698$\pm$0.041 in the field. The intrinsic metallicity scatter (after subtracting in quadrature the median observational uncertainties in measured metallicities) around the mean mass-metallicity relation is $\sim$0.17 dex (filament)

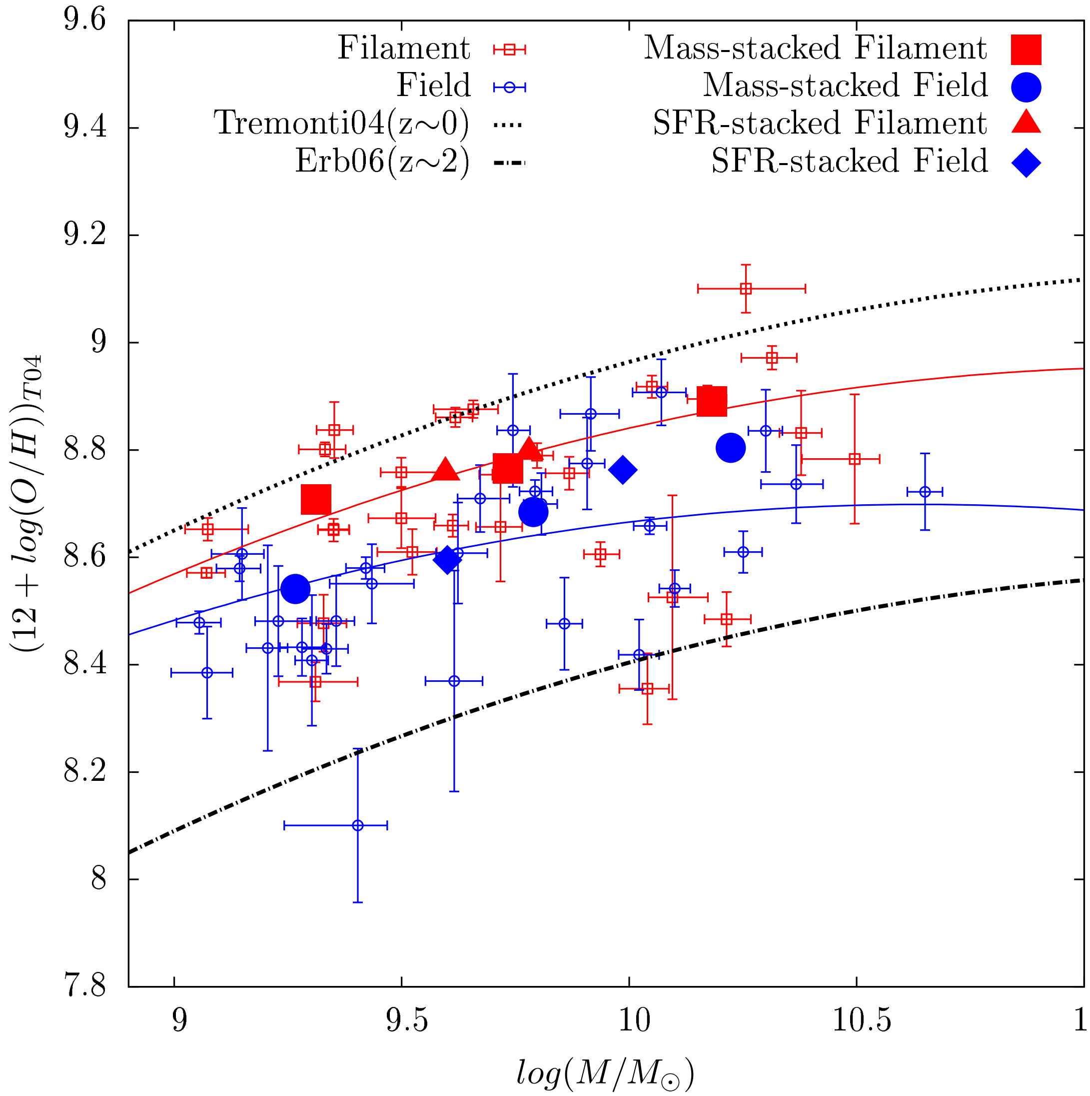

Figure 5.7: Mass-metallicity relation for filament (red empty points) and field (blue empty points) galaxies, along with mass-stacked and SFR-stacked spectra in the filament (red solid points) and the field (blue solid points). Red and blue solid lines represent the fit to the individual galaxies in the filament and the field, respectively. Mass-metallicity relation in the local universe from Tremonti et al. (2004) (dotted line) and that of Erb et al. (2006) at $z\sim2$ (dashed dotted line) are shown for comparison. The relation lies $\sim$0.06−0.13 dex below the local universe trend for filament galaxies and $\sim$0.21−0.23 dex for galaxies in the field. Filament galaxies are $\sim$ 0.1−0.15 dex more metal-enriched compared to galaxies in the field at a fixed stellar mass bin.

and ~0.13 dex (field). The results of the fits are shown in Figure 5.7. The fits to individual data points also show difference ($\sim 0.1-0.2$ dex) between metallicities in filament and the field at a given stellar mass, although the dispersion around the fitted lines is large.

In another attempt to quantify the environmental dependence of the mass-metallicity relation, we use the generalized two-dimensional K-S test (Fasano and Franceschini, 1987) to determine the probability that the populations of filament and field star-forming galaxies on the mass-metallicity plane are drawn from the same parent distribution. The derived p-value is p=0.04, implying that it is $< 4\%$ probable that the difference in mass-metallicity distributions in different environments is due to chance. In addition, we perform the one-dimensional K-S test for stellar mass and metallicity distributions in different environments. The derived p-value for the K-S test of stellar mass distributions in filament and the field is p=0.27, whereas it is p=0.03 for metallicity distributions. This indicates that it is unlikely that the stellar masses in filament and the field are drawn from a different parent distribution while there is a more significant difference between metallicity distributions.

As we already mentioned, the mass-metallicity relation is due to a more general mass-metallicity-SFR relation (the fundamental metallicity relation, Mannucci et al., 2010). As shown in Mannucci et al. (2010), by introducing the quantity $\mu_{0.32}$=log(M)−0.32log(SFR) that minimizes the dispersion of the projected fundamental metallicity relation, all galaxies out to $z \sim 2.5$ should follow the same $\mu_{0.32}$-metallicity relation. We define $\mu_{0.32}$=log(M/M$_\odot$)-0.32log([OII] SFR) and investigate the $\mu_{0.32}$-metallicity relation for filament and field galaxies. Figure 5.8 shows the relation between metallicity and $\mu_{0.32}$ for individual filament and field galaxies, along with stacked points. For comparison, the polynomial best fit from Mannucci et al. (2010) is also shown. Both filament and field galaxies nearly follow the Mannucci et al. (2010) trend. However, at a fixed $\mu_{0.32}$, filament galaxies are more metal-enriched. For example, at $\mu_{0.32} > 9.5$, the stacked spectra in the filament are about ~0.07 dex more metal-enhanced and at $\mu_{0.32} < 9.5$, filament galaxies show a metallicity enhancement of $\sim$ 0.16 dex compared to the field galaxies. The metallicities for the stacked spectra in different environments are presented in Table 5.2.

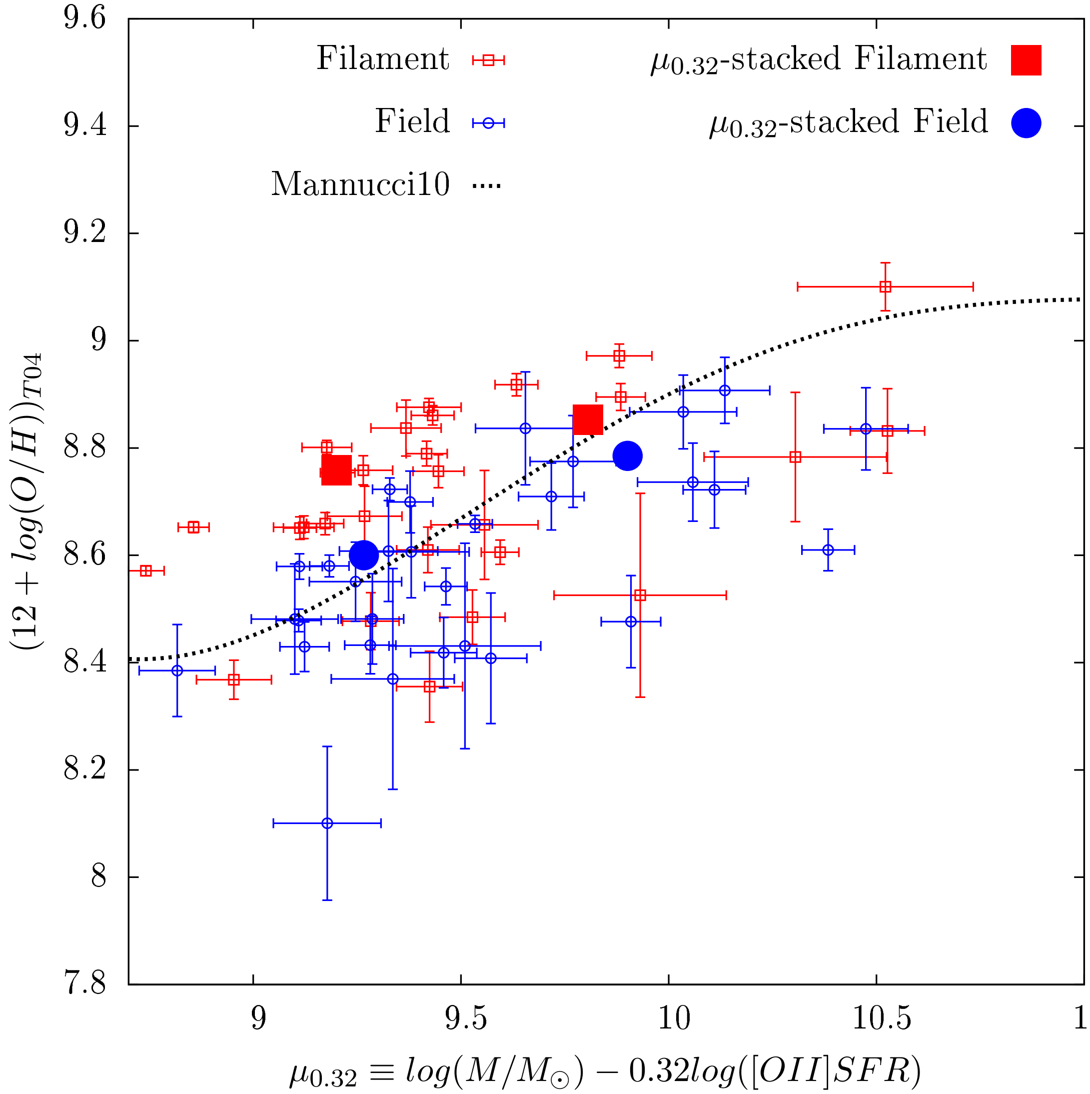

Figure 5.8: Relation between metallicity and $\mu_{0.32} \equiv \log(M/M_{\odot}) - 0.32\log([OII]\ SFR)$ for filament (red empty points) and field galaxies (blue empty points), together with $\mu_{0.32}$-stacked filament (red solid points) and field (blue solid points) spectra. For comparison, the polynomial best fit from Mannucci et al. (2010) is also shown. Both filament and field galaxies nearly follow the Mannucci et al. (2010) trend. However, at a fixed $\mu_{0.32}$, filament galaxies are more metal-enriched ($\sim$0.07$-$0.16 dex).

Our result regarding a deficit of metallicity in both filament (∼0.06−0.13 dex) and field (∼0.21−0.23 dex) galaxies at intermediate redshifts (z ∼0.5) compared to z ∼0, is in an overall qualitative agreement with Savaglio et al. (2005) (at least 0.1 dex at z ∼0.7), Cowie and Barger (2008) (∼0.2 dex at z ∼0.77 for $\log(M/M_\odot)=10-11$ galaxies), Maiolino et al. (2008) (∼0.1−0.2 dex at z ∼0.7 for $\log(M/M_\odot)=9-10$ galaxies), Lamareille et al. (2009) (∼0.2 dex at z ∼0.59), Moustakas et al. (2011) (∼0.16 dex at $0.45< z <0.55$ for $\log(M/M_\odot)=10.1-10.3$ galaxies), Zahid et al. (2011) (up to ∼0.15 dex at z ∼0.8 for $\log(M/M_\odot) < 10.5$ galaxies), Lara-López et al. (2013a) (∼0.1 dex at z ∼0.36), and Pérez-Montero et al. (2013) (0.14 dex at $0.4< z <0.6$). Qualitatively, our filament mass-metallicity relation evolution for stacked spectra resembles that of Moustakas et al. (2011) and Zahid et al. (2011), whereas for field galaxies, it is similar to that of Lamareille et al. (2009).

The metallicity enhancement (∼0.1−0.15 dex) in filament star-forming galaxies with respect to those in the field is consistent with several studies at low-z ($z\lesssim0.2$, Shields et al., 1991; Skillman et al., 1996; Mouhcine et al., 2007; Cooper et al., 2008b; Ellison et al., 2009; Scudder et al., 2012a; Petropoulou et al., 2012; Hughes et al., 2013; Alpaslan et al., 2015; Sobral et al., 2015b), intermediate-z (z∼1, Sobral et al., 2013b), and high-z (z∼2, Kulas et al., 2013; Shimakawa et al., 2015; Kacprzak et al., 2015), showing no or at best a small metallicity enrichment (∼ 0.05−0.2 dex) of galaxies in clusters relative to the field or galaxies in higher local densities with respect to those in low-density environments. Our result, together with these studies suggest that the internal processes are the primary driver of the chemical evolution of star-forming galaxies and the environment has a secondary role in the metallicity evolution of galaxies. However, we stress that some studies have found opposite environmental trends in the mass-metallicity relation. We will discuss it later in Section 5.6.

5.5.3 Ionization Parameter

The ionization parameter (q) —a measure of the number of H-ionizing photons per H atom— can be estimated using the O_{32} index defined as the [OIII]/[OII] line ratio (Kewley and Dopita, 2002; Nakajima et al., 2013). The [OIII]/[OII] ratio also depends strongly on metallicity (and stellar mass according to the mass-metallicity relation). Here, in order to estimate the ionization parameter, we use the equation given by Kobulnicky and Kewley (2004) (see also Nakajima and Ouchi, 2014) based on the photoionization model of Kewley and Dopita (2002):

$$
\begin{aligned}
log(q) &= \frac{A(O_{32}, 12 + log(O/H))}{B(O_{32}, 12 + log(O/H))} \\
A &= 32.81 - 1.153y^2 \\
&+ (12 + log(O/H))(-3.396 - 0.025y + 0.1444y^2) \\
B &= 4.603 - 0.3119y - 1.163y^2 \\
&+ (12 + log(O/H))(-0.48 + 0.0271y + 0.02037y^2) \qquad (5.10)
\end{aligned}
$$

where y=log(O_{32}), O_{32} is the [OIII]/[OII] line ratio, i.e., O_{32}=([OIII]λ4959+[OIII]λ5007)/ [OII]λ3727, and 12+log(O/H) is the gas phase oxygen abundance (metallicity). 12+log(O/H) metallicity is estimated in Section 5.5.2 using the R_{23} index and the equation given in Tremonti et al. (2004). The error of ionization parameter is estimated using the Monte-Carlo approach explained in Section 5.5.1, based on the uncertainties in estimated metallicity and the [OII] and [OIII] line fluxes. Line fluxes are estimated by fitting Gaussian functions to the line profiles. We note that the [OII] line is double-peaked and a better estimate of the flux can be achieved by fitting a double-peaked Gaussian function similar to Section 5.5.1. However, we found the difference between the flux estimated from single and double Gaussian functions to be negligible and use the single Gaussian fit to the [OII] line in this section.

Within the uncertainties, we do not find a significant difference between the average ionization parameter of the star-forming galaxies in the filament compared to that of the field galaxies. The ionization parameter is estimated to be q=7.352±0.086 and 7.397±0.099 cms^{-1} for stacked filament and field star-forming galaxies, respectively. We find that the

Table 5.2: Properties of the Stacked Spectra for Different Subsamples

Subsample	[OII]3726/[OII]3729	N_e cm^{-3}	[OIII]/[OII]	$\log(q)$ $\log(cms^{-1})$	$(12+\log(O/H))_{T04}$	$EW_{[OII]}$ Å
Filament all	0.6909±0.0044	22±4	0.3897±0.0079	7.352±0.086	8.766±0.004	30.4±0.7
$\log(M/M_\odot)=9-9.5$	0.7273±0.0054	58±5	0.7446±0.0163	7.574±0.085	8.708±0.004	33.3±0.9
$\log(M/M_\odot)=9.5-10$	0.6399±0.0065	<10	0.2457±0.0059	7.204±0.113	8.766±0.005	23.5±0.6
$\log(M/M_\odot)>10$	0.7008±0.0169	31±16	0.1399±0.0072	7.091±0.279	8.890±0.005	13.3±0.2
$\log(SFR)\leq0.75$	0.7322±0.0082	63±8	—	—	8.757±0.005	—
$\log(SFR)>0.75$	0.6737±0.0042	<10	—	—	8.796±0.003	—
$\log(sSFR)\leq -9$	0.7449±0.0132	76±14	—	—	—	17.0±0.4
$\log(sSFR)> -9$	0.6847±0.0043	15±4	—	—	—	41.4±0.8
$\mu_{0.32}\leq9.5$	—	—	—	—	8.759±0.003	—
$\mu_{0.32}>9.5$	—	—	—	—	8.853±0.004	—
Field all	1.0050±0.0104	367±13	0.5374±0.0135	7.397±0.099	8.639± 0.007	27.6±0.7
$\log(M/M_\odot)=9-9.5$	0.8621±0.0094	201±10	0.9496±0.0258	7.542±0.097	8.541±0.007	39.0±1.6
$\log(M/M_\odot)=9.5-10$	1.2822±0.0188	741±28	0.3413±0.0074	7.271±0.093	8.684±0.006	26.2±0.5
$\log(M/M_\odot)>10$	1.0105±0.0234	374±28	0.2464±0.0143	7.223±0.255	8.804±0.007	15.6±0.2
$\log(SFR)\leq0.75$	0.9055±0.0099	250±11	—	—	8.595±0.006	—
$\log(SFR)>0.75$	1.0528±0.0139	427±18	—	—	8.763±0.004	—
$\log(sSFR)\leq -9$	0.9074±0.0115	252±13	—	—	—	20.7±1.0
$\log(sSFR)> -9$	1.0354±0.0117	405±15	—	—	—	33.5±0.5
$\mu_{0.32}\leq9.5$	—	—	—	—	8.600±0.004	—
$\mu_{0.32}>9.5$	—	—	—	—	8.785±0.006	—

ionization parameter is a function of stellar mass (or metallicity) and decreases with increasing stellar mass (metallicity). However, at a fixed stellar mass, we do not find a significant difference between the average ionization parameter of galaxies in the filament and the field (Figure 5.9). The O_{32} values and the ionisation parameters for different environments and stellar mass bins are given in Table 5.2.

Recently, Sobral et al. (2015b) studied a merging cluster at $z \sim 0.2$ and did not find a significant difference between ionisation parameter of Hα star-forming galaxies in the field, the core, and the outskirts of the cluster at a fixed metallicity. Kewley et al. (2015) also compared the ISM of a sample of field and cluster star-forming galaxies at $z \sim 2$ and found no significant difference between their ionisation parameter. These are consistent with what we found in this section for our filament and field star-forming galaxies.

5.5.4 Line Equivalent Width

In this section, we study the equivalent width (EW) of [OII]λ3727, as well as that of Hβ in the filament and the field to investigate any environmental dependence. We also investigate the relation between EW, stellar mass, and sSFR and their dependence on environment.

We do not find a significant difference between EW distributions in different environments. The median [OII] EW for filament star-forming galaxies is $EW_{[OII]}$=29.9 Å, fully consistent with that of the field galaxies ($EW_{[OII]}$=29.1 Å). For the stacked spectra, we obtain $EW_{[OII]}$=30.4±0.7 Å in the filament and $EW_{[OII]}$=27.6±0.7 Å in the field. We obtain the same results based on other emission lines. For example, $EW_{H\beta}$ has a median value of $EW_{H\beta}$=6.0 and 8.2 Å in filament and the field (corrected for Balmer stellar absorption, see Section 5.4.2), correspondingly, with typically larger EW uncertainties compared to those of $EW_{[OII]}$. We perform K-S test to compare the distribution of EWs in different environments. The p-value is p=0.62 ([OII]) and p=0.40 (Hβ), meaning that it is unlikely that the distribution of EWs in filament and the field are drawn from different parent distributions.

The EW of an emission line is a measure of its intensity with respect to the stellar continuum. Since the flux of the emitting line is related to the recent star-formation activity

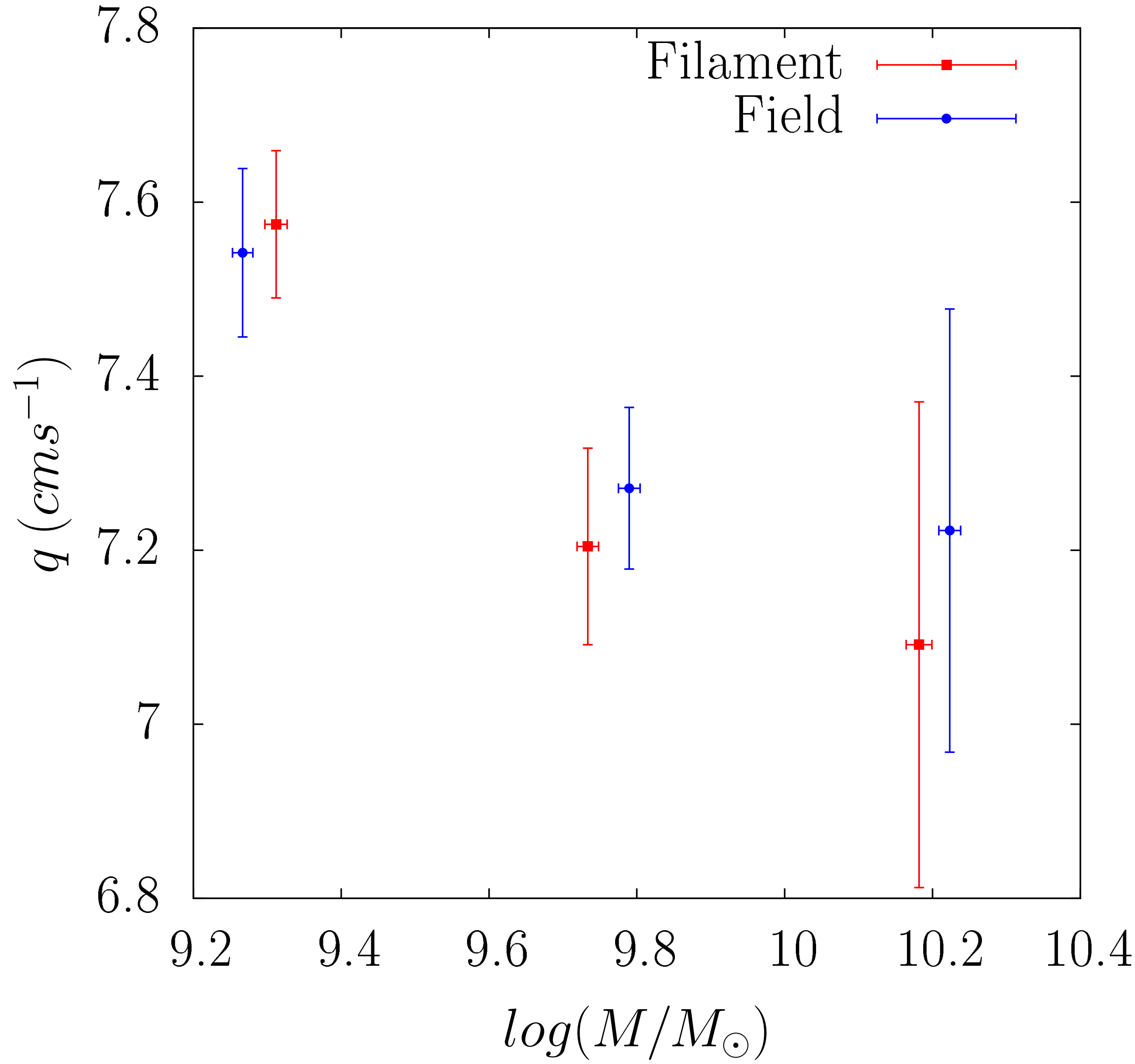

Figure 5.9: Ionization parameter estimated with O_{32} index for filament (red) and field (blue) galaxies as a function of stellar mass. Ionization parameter decreases with increasing stellar mass. However, within the uncertainties, there is no significant difference between ionization parameter of filament and field galaxies.

in galaxies and the stellar mass of a galaxy is predominantly determined by the overall mass of continuum stars, the EW of strong emission lines is a measure of the specific star-formation rate (sSFR) in galaxies (Fumagalli et al., 2012). Here, we investigate the environmental dependence of the relation between $EW_{[OII]}$ and [OII] specific star-formation rate ($sSFR_{[OII]}$). Figure 5.10 shows $\log(EW_{[OII]})$ versus $\log(sSFR_{[OII]})$ for filament and field galaxies and the sSFR-stacked spectra. We find that $sSFR_{[OII]}$ increases with $EW_{[OII]}$ for both filament and field star-forming galaxies. The $EW_{[OII]}$-$sSFR_{[OII]}$ relation appears to be independent of environment. We perform a linear fit ($\log(EW_{[OII]})=a[\log(sSFR_{[OII]})]+b$) to the $\log(EW_{[OII]})$-$\log(sSFR_{[OII]})$ relation for filament and field star-forming galaxies. Parameters of the best fit are a=0.285±0.064 and b=4.078±0.528 for filament star-forming galaxies, consistent with the field parameters (a=0.387±0.042 and b=5.001±0.364). The K-S test on the 2D distribution of galaxies in $\log(EW_{[OII]})$-$\log(sSFR_{[OII]})$ plane shows similarities between filament and field galaxies (p-value=0.13).

Many studies have shown a relatively tight correlation (typical dispersion of ∼0.2 dex) between SFR and stellar mass (Main-Sequence of star-forming galaxies), or equivalently between sSFR and stellar mass out to $z \sim 6$ (Brinchmann et al., 2004; Salim et al., 2007; Daddi et al., 2007; Elbaz et al., 2007; Noeske et al., 2007a; Karim et al., 2011; Whitaker et al., 2012; Reddy et al., 2012; Sobral et al., 2014; Salmon et al., 2015). Since we found that $EW_{[OII]}$ and $sSFR_{[OII]}$ are related, we expect to see a relation between $EW_{[OII]}$ and stellar mass. We investigate the environmental dependence of the $EW_{[OII]}$ and stellar mass for individual galaxies and our mass-stacked spectra, as shown in Figure 5.11. We see that $EW_{[OII]}$ decreases with increasing stellar mass. However, this trend looks similar for star-forming galaxies in the filament and the field. We linearly parameterize this relation ($\log(EW_{[OII]})=c[\log(M)]+d$) by fitting the stacked spectra, showing that the parameters are the same for filament (c=−0.473±0.055 and d=5.949±0.547) and the field galaxies (c=−0.462±0.064 and d=5.921±0.638), within the uncertainties.

The $EW_{[OII]}$-mass anti-correlation found here is consistent with other similar studies (Fumagalli et al., 2012; Sobral et al., 2014; Bridge et al., 2015). Using a sample of [OII]

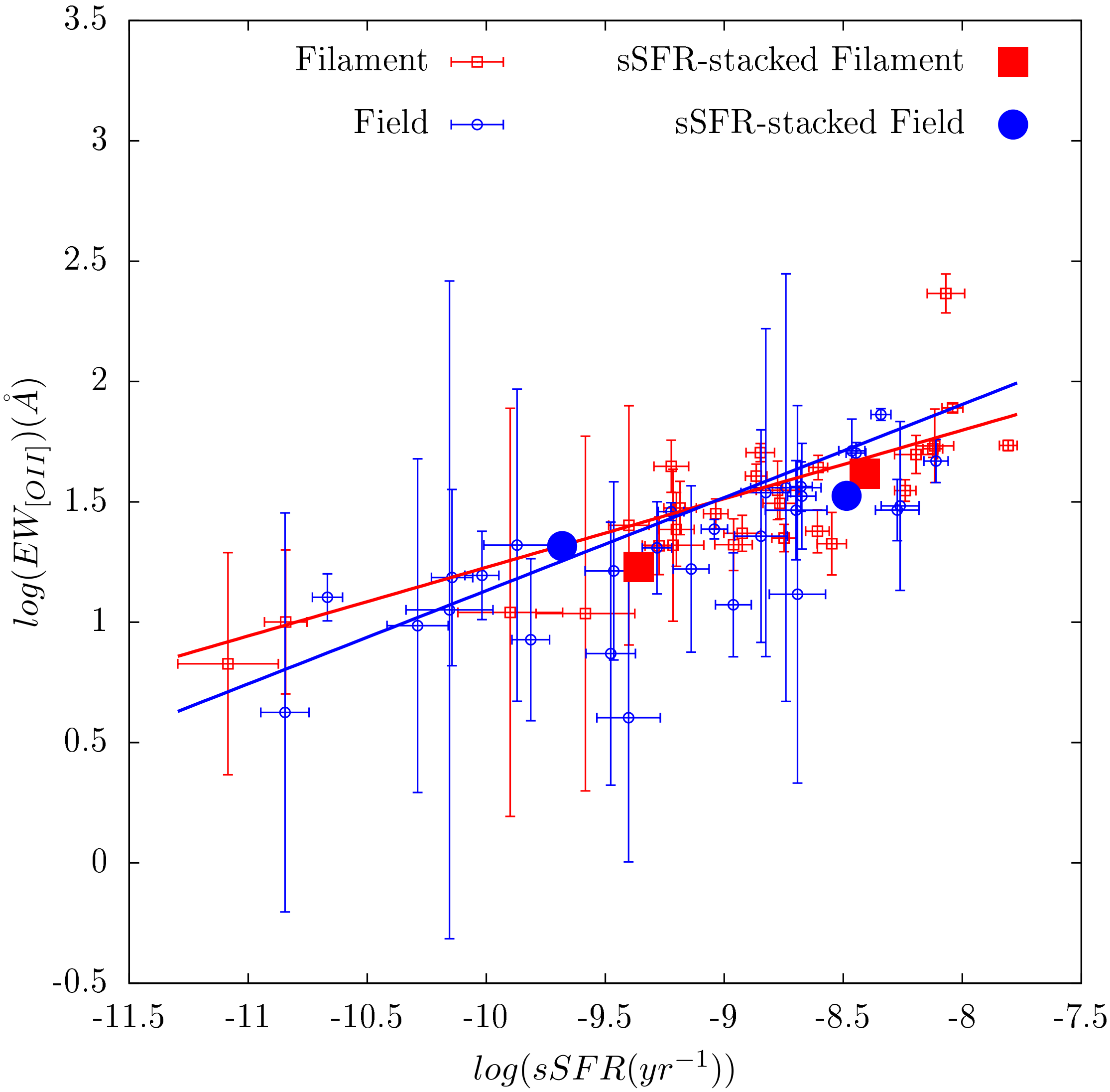

Figure 5.10: Relation between log(EW$_{[OII]}$) and log(sSFR$_{[OII]}$) for filament (red empty points) and field (blue empty points) galaxies and the sSFR-stacked spectra (solid points). Solid lines show the linear fit to the filament (red line) and field (blue line) data points. The sSFR$_{[OII]}$ increases with EW$_{[OII]}$ for both filament and field star-forming galaxies. However, the EW$_{[OII]}$-sSFR$_{[OII]}$ relation is independent of environment, within the uncertainties.

emitters at $z \lesssim 0.6$, Bridge et al. (2015) found a factor of $\sim$3 decline in the $EW_{[OII]}$ between their lowest and highest mass bin. Here, we find a factor of $\sim$2.5 decline between our lowest and highest mass bin, consistent with Bridge et al. (2015) given their wider mass range at $z \sim 0.5$. Fumagalli et al. (2012) also found that galaxies in the lowest mass bin of their data, have on average, an $EW_{H\alpha}$ which is five times higher than those in their highest mass bin. Given their broader mass range compared to our study, it is qualitatively in agreement with our result. Sobral et al. (2014) found a slope of ~ -0.25 between $\log(EW_{H\alpha+[NII]})$ and log(M), shallower than what we found. However, this might be due to differences in selection functions and $EW_{H\alpha+[NII]}$ versus $EW_{[OII]}$. Nonetheless, our work agrees qualitatively with that of Sobral et al. (2014). We highlight that we found that the $EW_{[OII]}$-mass anti-correlation is independent of environment and it is another manifestation of the environmental invariance of the SFR$-$mass relation for star-forming galaxies, consistent with Darvish et al. (2014).

The environmental invariance of $EW_{[OII]}$-$sSFR_{[OII]}$ and $EW_{[OII]}$-mass relations found here is consistent with several studies showing that on average, many properties of star-forming galaxies that are related to star-formation activity (such as color, SFR, sSFR and SFR$-$mass relation) are independent of their host environment, a result that appears to hold regardless of the redshift, the method used to define environment, and the star-formation activity indicator (Peng et al., 2010; Wijesinghe et al., 2012; Muzzin et al., 2012; Koyama et al., 2013b, 2014; Hayashi et al., 2014; Lin et al., 2014; Darvish et al., 2014). Hence, it has been argued that the major role of environment is to control the fraction of quiescent and star-forming systems (Peng et al., 2010; Sobral et al., 2011; Muzzin et al., 2012; Darvish et al., 2014), that is, it is more likely for galaxies to become quenched in denser environments. However, when they form stars, on average, their star-formation activity becomes independent of their host environment. In Section 5.6, we will discuss the possible role of star-formation histories in determining the fraction of star-forming galaxies in different environments.

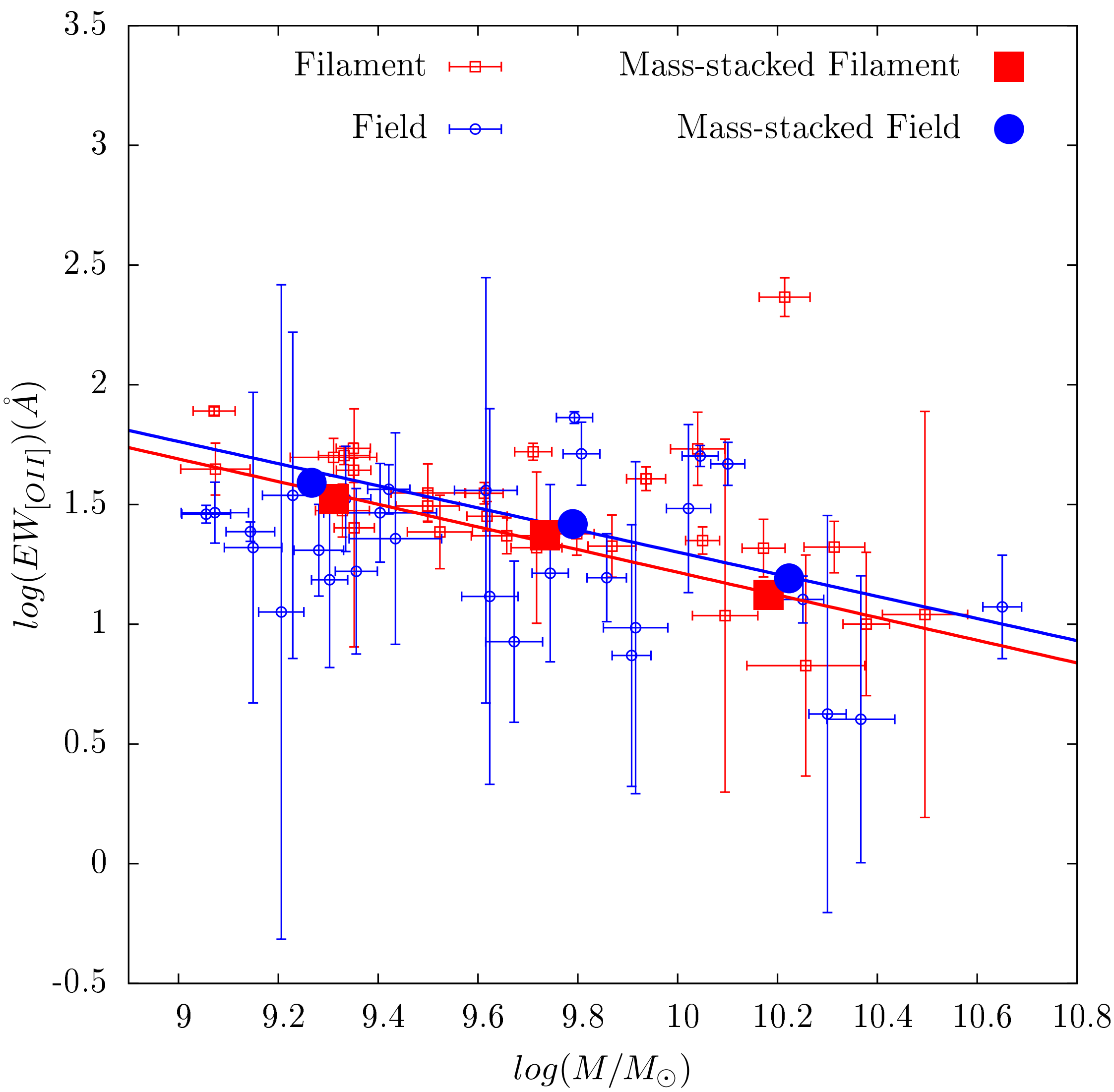

Figure 5.11: $EW_{[OII]}$-mass anti-correlation for individual filament (red empty points) and field (blue empty points) galaxies and the stellar mass-stacked spectra (solid points). Solid lines show the linear fit to the filament (red line) and field (blue line) data. The $EW_{[OII]}$ decreases with increasing stellar mass. However, this trend is similar for star-forming galaxies in the filament and the field.

5.5.5 Velocity Dispersion and Dynamical Mass

In order to estimate the line-of-sight gas velocity dispersion, we use the sigma of the fitted Gaussian functions to Hβ and [OIII]λ5007 line profiles. We need to subtract in quadrature the instrument velocity dispersion (σ_{inst}). The line-of-sight gas velocity dispersion is therefore:

$$\sigma = \sqrt{\sigma_t^2 - \sigma_{inst}^2} \tag{5.11}$$

where σ is the line-of-sight gas velocity dispersion (Hβ or [OIII]λ5007), σ_t is the directly measured (total) velocity dispersion from the spectra (using the sigma of the Gaussian fit to the line profiles), and σ_{inst} is the instrument velocity dispersion, measured from the width of the Arc lines. For the DEIMOS instrument (slit width 0.75", central wavelength λ_c=7200 Å), we achieve a resolution of ~1.5 Å, which is equivalent to σ_{inst}=62 kms^{-1}. For galaxies with $\sigma_t < \sigma_{inst}$, we use the instrument velocity dispersion as an upper limit for the velocity dispersion. We note that the velocity dispersions measured from the line width have some other contributions, such as the thermal broadening due to temperature of star-forming regions (at T~10^4 K, it is $\lesssim$10 kms^{-1} for Hβ and much smaller for [OIII]λ5007), mergers, and turbulent gas motions inside the HII regions (typically ~ 20 kms^{-1}, Shields, 1990). We do not subtract these smaller effects from the measured velocity dispersion and the measured values are a combination of these.

Figure 5.12 shows a comparison between estimated Hβ and [OIII]λ5007 velocity dispersions for star-forming galaxies in the filament and the field. There is a very good agreement between the estimated velocity dispersions. The median $\sigma_{H\beta}$ and median $\sigma_{[OIII]\lambda5007}$ are consistent to within ~5 (10) kms^{-1} for filament (field) galaxies, which are smaller than the median observational uncertainties of Hβ velocity dispersion ($\Delta\sigma_{H\beta}$ ~10 (20) kms^{-1} for filament (field) galaxies) and that of [OIII]λ5007 ($\Delta\sigma_{[OIII]\lambda5007}$ ~25 (15) kms^{-1} for filament (field) galaxies). The two velocity dispersion measurements also have a median absolute deviation of ~ 5 (15) kms^{-1}, smaller than the typical velocity dispersion uncertainties.

We do not find a significant difference between velocity dispersions in filament and the

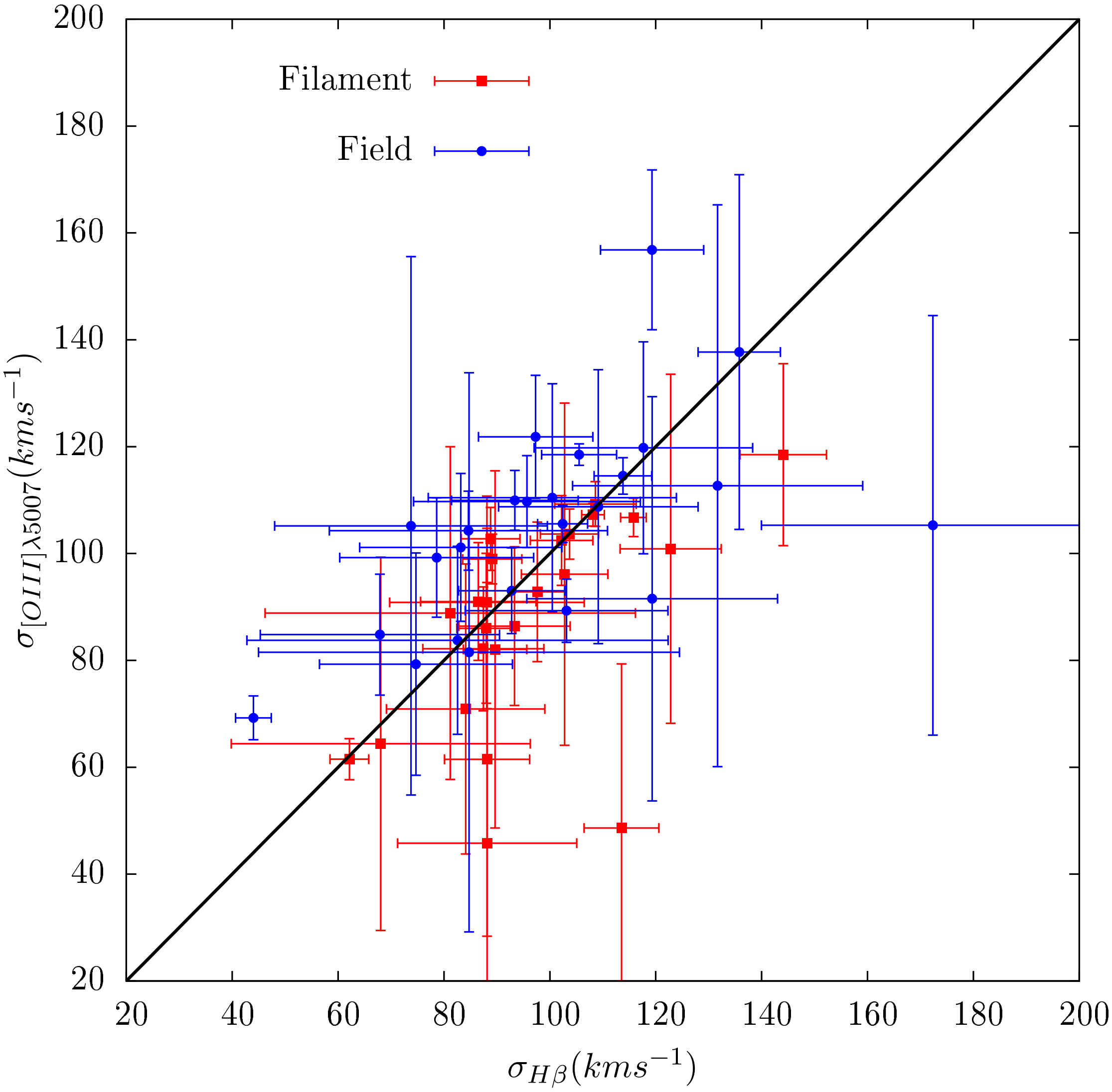

Figure 5.12: [OIII]λ5007 versus Hβ line-of-sight velocity dispersions for star-forming galaxies in the filament (red points) and the field (blue points). There is a very good agreement between the estimated velocity dispersions. The two velocity dispersion measurements have a median absolute deviation of ~ 5 (15) kms^{-1} in filament (field), smaller than the typical velocity dispersion uncertainties. We do not find a significant difference between velocity dispersions of the filament and field galaxies.

field. For example, the median Hβ velocity dispersion is $\sigma_{H\beta}$ ~90 kms^{-1} in the filament, whereas it is $\sigma_{H\beta}$ ~95 kms^{-1} in the field, consistent within the uncertainties. The K-S test p-values also show that it is unlikely that the distribution of $\sigma_{H\beta}$ (p=0.47), $\sigma_{[OIII]\lambda5007}$ (p=0.43), and $\sigma_{H\beta} - \sigma_{[OIII]\lambda5007}$ 2D distribution (p=0.43) in filament and the field are drawn from different parent distributions.

We compared our estimated velocity dispersions with that of Weiner et al. (2006) and found a relatively good agreement, within the uncertainties. We limited the sample of Weiner et al. (2006) to typical redshift (z ~0.5) and magnitude (i$^+$ ~21) of our own sample and found a velocity dispersion of ~75 kms^{-1}, comparable to our estimated value of ~90 kms^{-1} within our typical uncertainties (~10−15 km^{-1}). Our derived σ values also agree very well with those from Forbes et al. (1996) at ~0.5 (~90 kms^{-1}).

Given the velocity dispersion and the half-light radius of galaxies, we can estimate their dynamical mass (M$_{dyn}$) via:

$$M_{dyn} = \frac{\beta R_e \sigma^2}{G} \tag{5.12}$$

where β is a constant that depends on the mass distribution in a galaxy, R_e is the effective half-light radius, and G is the gravitational constant. The β value varies between ~2−6 (Rix et al., 1997; Pettini et al., 2001; Erb et al., 2003; Cappellari et al., 2006; Toft et al., 2012; Maseda et al., 2013; Erb et al., 2014; Rhoads et al., 2014; Beifiori et al., 2014) and is our major source of systematic uncertainty in dynamical mass measurements. Here, we use β=2 corresponding to the singular isothermal sphere mass profile (Keeton, 2001; Binney and Tremaine, 2008). However, we note that this could be as large as ~6. Therefore, our dynamical masses are lower limits and could become higher by a factor ~3. Half-light radii are extracted from the publicly available catalog of Leauthaud et al. (2007) in the COSMOS field, derived by running *Sextractor* (Bertin and Arnouts, 1996) on the HST/ACS $F814W$ images [4]. We use the Hβ velocity dispersion for dynamical mass measurements because the

[4] We also tried the public $ZEST$ catalog (Scarlata et al., 2007a) which extracts structural parameters (including effective radii) from HST/ACS $F814W$ images, using Simard (1998) $GIM2D$ $IRAF$ package. We found a relatively good agreement between the estimated effective radii from these two catalogs. Here, we only use the Leauthaud et al. (2007) values.

typical uncertainties in Hβ velocity dispersion is smaller than that of the [OIII]λ5007 line.

We find no significant evidence for different dynamical mass distributions for filament and field galaxies. The median dynamical mass is log($M_{dyn}/M_\odot$)$\sim$10.12 in filament while in the field, we have median log($M_{dyn}/M_\odot$)$\sim$10.06, with a median absolute deviation of $\sim$0.12 dex in both environments. Dynamical masses are in the range log($M_{dyn}/M_\odot$)$\sim$9.8$-$10.4 for filament galaxies and in the range log($M_{dyn}/M_\odot$)$\sim$9.4$-$10.8 for galaxies in the field. Dynamical masses for field galaxies have a slightly broader range. However, this might be due to a slightly wider stellar mass range in the field.

We also investigate the stellar-to-dynamical mass ratios (M_{star}/M_{dyn}) of star-forming galaxies in different environments and do not find a significant difference between them (Figure 5.13). For star-forming galaxies in the filament, the median stellar-to-dynamical mass ratio is M_{star}/M_{dyn} $\sim$0.45 with a median absolute deviation $\sim$0.31. The median ratio is M_{star}/M_{dyn} $\sim$0.30 in the field with a median standard deviation of $\sim$0.18. Given the relatively large absolute deviations, the stellar-to-dynamical mass ratios in filament and the field are consistent with each other.

Stellar-to-dynamical mass ratios in the filament are in the range M_{star}/M_{dyn} $\sim$0.08$-$3.88, and M_{star}/M_{dyn} $\sim$0.08$-$4.42 for field galaxies. $\sim$20% of star-forming galaxies in the filament and $\sim$15% in the field have unphysical M_{star}/M_{dyn} >1 (Figure 5.13). There might be several reasons for these unphysical values. Firstly, the uncertainties in the estimated M_{star}/M_{dyn} are quite large and the lower limit of their estimated M_{star}/M_{dyn} lies within the reasonable range for the majority of these sources. Secondly, we assumed a value of β=2 in estimating the dynamical masses. These sources might have a larger β value. Choosing β $\sim$5$-$6 brings all (except one with large error bar) the Stellar-to-dynamical mass ratios to the safe zone. Thirdly, the nebular gas dynamics may not be a complete representative of the total mass as the star-forming regions are mostly localized to inner regions of the disk.

In fact, if we discard the seemingly unphysical M_{star}/M_{dyn} >1 from our analysis, we find a much better agreement between stellar-to-dynamical mass ratios in filament and the field. The median stellar-to-dynamical mass ratio becomes M_{star}/M_{dyn} $\sim$0.28 (median absolute

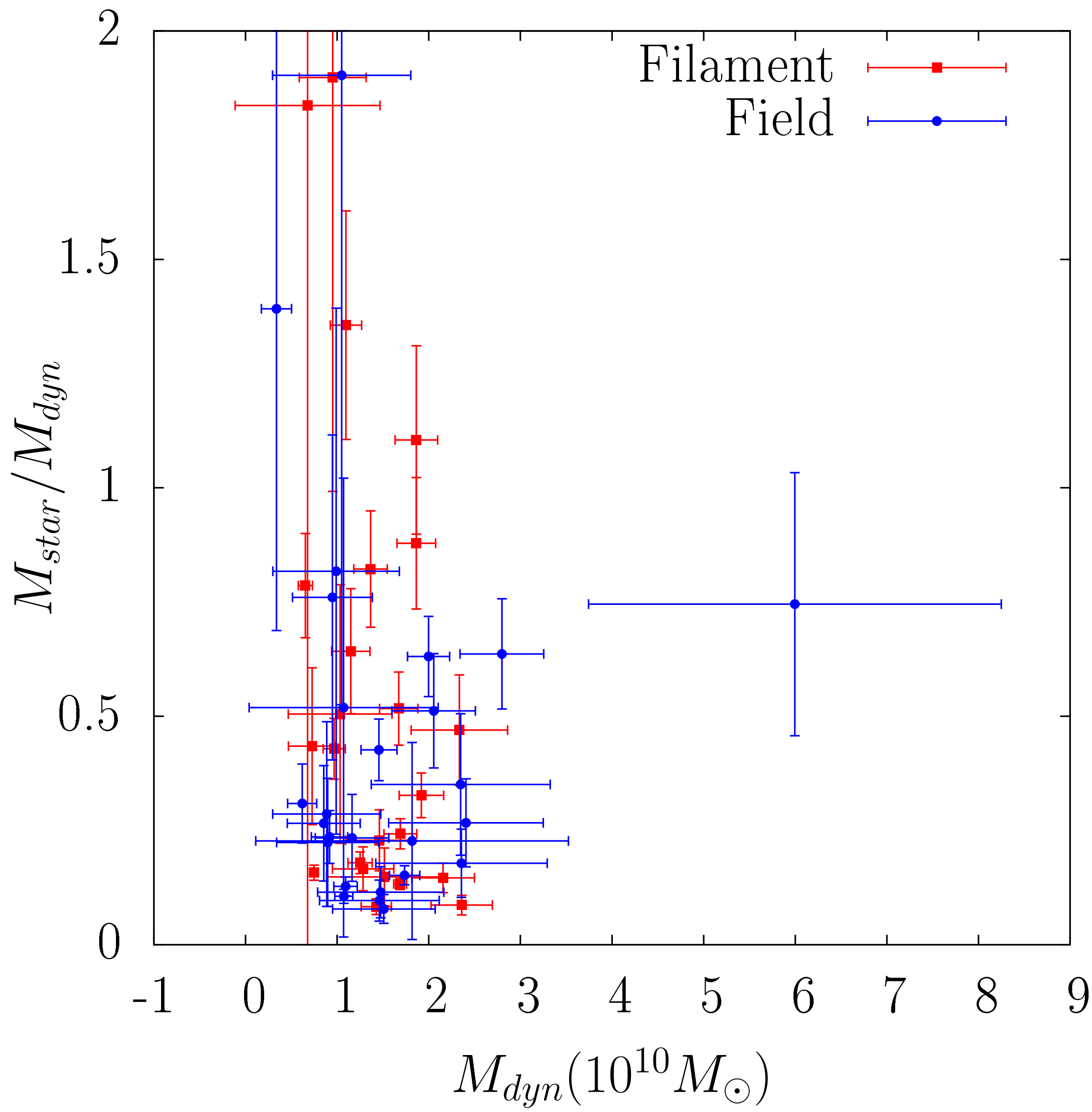

Figure 5.13: Stellar-to-dynamical mass ratio (M_{star}/M_{dyn}) as a function of dynamical mass for filament (red points) and the field (blue points) star-forming galaxies. We do not find a significant difference between them. After discarding the unphysical $M_{star}/M_{dyn} > 1$ data from our analysis, we find that for star-forming galaxies in the filament, the median stellar-to-dynamical mass ratio is $M_{star}/M_{dyn} \sim 0.28$ with a median absolute deviation ~ 0.15, fully consistent with the field star-forming galaxies with median $M_{star}/M_{dyn} \sim 0.27$ and median absolute deviation 0.15.

deviation $\sim$ 0.15) for filament star-forming galaxies, fully consistent with the field star-forming galaxies with median M_{star}/M_{dyn} ~0.27 and median absolute deviation 0.15. We also perform K-S test for the distributions of M_{star}/M_{dyn} in filament and the field, showing that it is unlikely (p-value=0.47) they are drawn from different parent distributions.

The estimated stellar-to-dynamical mass ratios in the filament and the field are consistent with each other (M_{star}/M_{dyn}=0.27−0.28) and with some previous studies, although these studies may cover a different stellar mass range, galaxy type, redshift, and selection function when compared to our study. For example, Maseda et al. (2013) found that for a sample of extreme emission line galaxies at z ~2 with stellar masses $\log(M/M_{\odot})$~8−9, the stellar-to-dynamical mass ratio is M_{star}/M_{dyn} ~0.27 (assuming β=3), in good agreement with our result. Using a sample of massive quiescent galaxies at z >1 and in the SDSS, Belli et al. (2014) showed that the average $\log(M_{star}/M_{dyn})$ is −0.13 for z >1 and −0.12 for the SDSS samples, assuming β=5. Adopting our value of β=2 in Belli et al. (2014) leads to the average value of M_{star}/M_{dyn} ~0.30 for SDSS and z >1 samples, fully consistent with our median value of (0.27−0.28) at z ~0.5.

Moreover, many studies of the Tully-Fisher relation out to z ~1 have shown no or at best very weak (for S0 galaxies and fainter systems) environmental dependence of its characteristics (Sakai et al., 2000; Nakamura et al., 2006; Pizagno et al., 2007; Jaffé et al., 2011; Mocz et al., 2012; Bösch et al., 2013; Rawle et al., 2013; Sobral et al., 2013b). Since maximum rotational velocity is related to velocity dispersion and absolute magnitude is proportional to stellar mass, the environmental invariance of stellar mass and velocity dispersion seen in our work is indirectly related to the environmental independence of the Tully-Fisher relation seen in these studies and obliquely agrees with them.

5.6 Discussion

In Section 5.5, we showed that some of the observable properties of filament and field star-forming galaxies such as their EW, EW-sSFR relation, velocity dispersion, dynamical mass, and ionization parameter are the same within the uncertainties. However, we found an enhancement of metallicity and a significant reduction of electron density for filament galaxies. What might be the cause of these differences?

We first need to discuss that the environmental dependence of the metallicity of star-forming galaxies may depend on the scale at which the environment is defined. At small scales (a few tens of kpc), there is substantial evidence from observations and simulations for a decrement of metallicity and an enhancement of star-formation activity in galaxy close pairs, merging, and interacting systems compared to isolated, field galaxies, mostly attributed to the interaction-induced inflow of metal-poor gas from the periphery of interacting galaxies to the center, diluting their metal content, and increasing their gas fuel for star-formation (Mihos and Hernquist, 1996; Kewley et al., 2006; Michel-Dansac et al., 2008; Ellison et al., 2008; Sol Alonso et al., 2010; Rupke et al., 2010; Perez et al., 2011; Scudder et al., 2012b; Ellison et al., 2013; Ly et al., 2014). At intermediate group scales where galaxy interactions are more common compared to cluster and field environments (Perez et al., 2009; Tonnesen and Cen, 2012) (due to a combination of (1) a lower velocity dispersion of group galaxies relative to their cluster counterparts and (2) a higher number density of group galaxies compared to the field systems, which provide an ideal condition for interactions), there is also evidence for a deficit of metals in group galaxies compared to control samples in the field (Lara-López et al., 2013b), possibly due to a higher fraction of interacting galaxies. At larger filamentary and cluster scales, the slight metal enhancement of galaxies relative to the field might be due to (1) the inflow of already enriched interafilamentary or interacluster gas into galaxies as observations and simulations have shown a more metal enriched IGM in cluster and filament environments compared to the field (Arnaud et al., 1994; Aracil et al., 2006; Stocke et al., 2006, 2007; Sato et al., 2007; Davé et al., 2011; Cen and Chisari, 2011; Oppenheimer et al., 2012), (2) the environmental strangulation (Larson et al., 1980; Peng et al., 2015) of low-metallicity diluting gas falling from the surrounding LSS cosmic web into galaxies, (3) the environmental ram pressure stripping (Gunn and Gott, 1972; Abadi et al., 1999) of the metal-poor diluting gas in the periphery of galaxies, and (4) trapping and recycling of metal-enriched outflows due to the hotter environment of filaments and clusters (Cen and Ostriker, 2006; Aracil et al., 2006; Werner et al., 2008) compared to the field.

However, among all the possibilities considered above, the inflow of the metal-enriched intrafilamentary gas into filament galaxies can better describe our observations in this work. Strangulation and ram pressure stripping would affect the gas content of filament galaxies which would eventually result in a reduced gas reservoir for galaxies, leading to a reduction of SFR in filament galaxies. However, we showed in Section 5.5.4 that the $EW_{[OII]}$-sSFR relation which is related to star-formation activity in galaxies is invariant to filament and field star-forming galaxies. Moreover, ram pressure stripping is practically effective for dwarf galaxies in denser environments of massive clusters with large velocity dispersions. Given the mass range of our sample galaxies and the environment of our filament, it is unlikely that ram pressure stripping would significantly affect the gas content of our filament galaxies.

The small environmental dependence of galaxy metallicity seen in this work and similar studies might be due to the selection of mostly brighter, central galaxies as highlighted by Peng and Maiolino (2014). Using a sample of galaxies in the SDSS, Peng and Maiolino (2014) showed that once central and satellites are carefully separated, there is a strong relation between overdensity and metallicity for satellite star-forming galaxies, whereas for central system, no such correlation was found. They attributed this correlation to the inflow of more metal-enriched gas in denser environments to satellite galaxies. Similarly, Pasquali et al. (2012) found that satellites have higher metallicities than equally massive centrals in the SDSS dataset.

We showed that on average, the ionization parameter is almost the same for filament and field galaxies, whereas the electron density is much lower for filament galaxies. The ionization parameter is defined as:

$$q = \frac{Q(H^0)}{4\pi r^2 N_H} \tag{5.13}$$

where $Q(H^0)$ is the number of Hydrogen photoionizing photons per second, passing through the surface area of $4\pi r^2$ with the Strömgren radius r, and N_H is the number density of Hydrogen atoms. Assuming ionization equilibrium, the photoioization rate is balanced out by the recombination rate:

$$Q(H^0) \propto r^3 N_H^2 \epsilon \tag{5.14}$$

where ϵ is the filling factor. Inserting equation 5.14 into 5.13 gives:

$$q \propto r N_H \epsilon \tag{5.15}$$

If the number density of hydrogen atoms is related to electron density, given the lower electron density in filament galaxies and similar ionization parameter between field and filament systems, the Strömgren radius and/or the filling factor of filament galaxies should change in such a way that leave the ionization parameter intact, according to equation 5.15. In other words, on average, filament galaxies might have bigger HII star-forming regions assuming ϵ is fixed, or the filling factor is larger for filament galaxies compared to the field assuming that r is the same in these two environments, or a combination of these.

Different star-formation histories between filament and field star-forming galaxies can explain some of the differences seen in this study. A longer, more constant star-formation timescale for filament star-forming galaxies compared to a shorter, burstier star-formation history for field star-forming galaxies is capable of sustaining a bigger HII region for a longer time. A bigger HII region reduces the pressure inside the region which leads to a lower electron density. A longer star-formation timescale for filament star-forming galaxies also suggests that at the time of observation, it is more likely to find a higher fraction of star-forming galaxies in filaments compared to the field. This is consistent with e.g., Darvish et al. (2014) who found a higher fraction of Hα star-forming galaxies in a filamentary structure at $z \sim 0.84$. It is still not clear what environmental effects (if any) might cause the difference in electron density, Strömgren radius, filling factor, and star-formation histories between filament and field galaxies. Whatever they are, they alter the ISM of galaxies in such a manner that affect the electron densities and leave the ionization parameter almost unchanged.

Since electron density measurements originate from HII regions with sizes up to a few hundred pc, a full understanding of them in different environments at intermediate and high redshifts requires sub-kpc resolution. Current space-based telescopes such as HST and ground-based integral field units (IFU) equipped with adaptive optics (AO) are able to provide information on kpc-scale star-forming regions in intermediate and high redshift galaxies (see e.g., Swinbank et al., 2012; Wuyts et al., 2013; Hemmati et al., 2014). However, with the next generation of telescopes such as TMT and E-ELT, sub-kpc resolution for intermediate- and high-z galaxies can be achieved through AO systems, enabling us to have a grasp of the properties of HII-regions in these galaxies located in different environments.

5.7 Summary and Conclusion

In this chapter, we spectroscopically confirm the presence of a large filamentary structure ($\sim$ 8 Mpc) in the COSMOS field at $z \sim$0.53. We extensively study the physical properties of the star-forming emission-line galaxies in this filament and compare them with a control sample of field galaxies at the same redshift. Our main results are:

1. We estimate the average electron density for filament and field star-forming galaxies using [OII]λ3726/λ3729 line ratio. We show that the average electron density is significantly lower (a factor of $\sim$ 17) for filament star-forming galaxies compared to that of the field systems. We obtain the same result if we perform the comparison in fixed stellar mass, SFR, and sSFR bins. Depending on the bin selected, electron densities vary in the range $\sim <10-75$ cm^{-3} for filament star-forming galaxies and in the range $\sim$ 200$-$740 cm^{-3} for star-forming galaxies in the field. The decrement of the electron densities in filament star-forming galaxies might be due to a longer star-formation timescale for filament star-forming systems.

2. We estimate the oxygen abundance metallicity using the R_{23} index. We show that our mass-metallicity relation at $z \sim 0.5$ for filament and field star-forming galaxies lies in between mass-metallicity relations at $z \sim 0$ and $z \sim 2$. We also show that our $\mu_{0.32}$-metallicity relation for filament and field star-forming galaxies nearly follows the Mannucci et al. (2010) trend at $z \sim 0$.

3. We show that at a fixed stellar mass, SFR, and $\mu_{0.32}$, filament star-forming galaxies are more metal-enriched ($\sim 0.1-0.15$ dex) compared to their field counterparts. The metallicity enhancement for filament star-forming galaxies compared to the field might be due to the inflow of the already enriched intrafilamentary gas into filament galaxies. The metallicity enhancement in denser environments suggests that environment has a secondary effect in the metal enrichment of galaxies and internal processes are the major driver of the chemical evolution in galaxies.

4. We estimate the average ionisation parameter of filament and field star-forming galaxies using the O_{32} index. Ionisation parameter depends on stellar mass and decreases with increasing stellar mass for both filament and field star-forming galaxies. However, within the uncertainties, we find insignificant difference between ionisation parameter of filament and field star-forming systems.

5. We show that $EW_{[OII]}$ correlates with sSFR and anti-correlates with stellar mass for filament and field star-forming galaxies. However, we show that within the uncertainties, $EW_{[OII]}$-sSFR and $EW_{[OII]}$-mass relations are the same for filament and field star-forming systems. The environmental independence of the $EW_{[OII]}$-mass anti-correlation is another manifestation of the environmental invariance of the SFR$-$mass relation for star-forming galaxies, seen in previous studies.

6. We estimate the line-of-sight velocity dispersion and dynamical masses for filament and field star-forming systems. We show that, on average, velocity dispersion, dy-

namical mass, and stellar-to-dynamical mass ratio are similar for filament and field star-forming galaxies.

Assuming ionisation equilibrium within HII star-forming regions, we can show that the ionisation parameter directly depends on the electron density, the diameter of the HII region, and the volume filling factor. Since we showed that, on average, the ionisation parameter is similar for filament and field star-forming galaxies and the electron density is much lower for filament star-forming systems, this suggests that, on average, filament star-forming galaxies might have larger HII regions compared to their field counterparts if we assume that the filling factor is the same for them. However, HII regions have sub-kpc sizes and a full understanding of their sizes in different environments at higher redshifts requires the next generation of telescopes such as TMT that are equipped with the IFU systems and assisted by the AO technology.

Chapter 6

Summary and Conclusions

Summary of Chapter 2

We used a K_s-band selected sample of galaxies with accurate photometric redshifts in the COSMOS field at z=0.1−3.1 in order to estimate the density field. The density field was determined with the weighted versions of the adaptive kernel smoothing, tenth and fifth NN, Voronoi tessellation and Delaunay triangulation methods. We evaluated the performance of each density estimator using extensive realistic and Monte-Carlo simulations. We found an overall good agreement between the density field estimated with different methods over ∼2 orders of magnitude. We performed extensive simulations to show that the adaptive kernel smoothing and Voronoi tessellation outperformed other methods in estimating the density field of galaxies. We recommend using these estimators as a more reliable and robust substitute for the widely-used NN or count in aperture methods. We introduced the robust MMF algorithm which was able to disentangle the cosmic web into its components. The algorithms developed in this chapter were extensively used in other chapters that dealt mostly with the effects of environment on properties of galaxies.

Summary of Chapter 3

In this chapter, we studied the effects of the environment on a mass complete sample of quiescent and star-forming galaxies out to z∼3 in the COSMOS field. The rest-frame

NUV$-r^{+}-$J color-color plots were used to separate the galaxy population into quiescent and star-forming systems. We investigated the median SFR, sSFR, quiescent fraction, rest-frame color, and the comoving number and mass density of galaxies as a function of their environment (overdensity), stellar mass, galaxy type, and redshift. Our main results are:

1. The median SFR and sSFR of galaxies are strong functions of environment at $z \lesssim 1$, in a sense that they both decrease with increasing overdensity at $z \lesssim 1$. However, at $z \gtrsim 1$, they are almost independent of the environment.

2. When we only consider the star-forming galaxies, their median SFR and sSFR do not significantly change with environment out to $z \sim 3$. In other words, if a galaxy is star-forming, on average, its SFR and sSFR are unaltered by its host environment. However, denser environments increase the chance of a galaxy to become quiescent. Hence, the role of environment seems to control the fraction of star-forming and quiescent galaxies.

3. At a given overdensity, the median SFR and sSFR of galaxies (quiescent and star-forming) are higher at higher redshifts compared to lower-z samples, indicating an overall decline in the global star-formation activity in galaxies since $z \sim$2-3.

4. The fraction of quiescent galaxies significantly changes with environment (overdensity) at $z \lesssim 1$, and it is higher in denser regions. However, at $z \gtrsim 1$, it is almost independent of the environment. At a given overdensity, the fraction of quiescent galaxies is always higher at lower redshifts. This is an indication of the Butcher-Oemler effect.

5. The quiescent fraction growth rate is almost independent of environment at look-back time $\gtrsim$8 Gyr. However, at lower redshifts (look-back time $\lesssim$8 Gyr), it increases with increasing overdensity. Galaxies become quenched more rapidly in denser environments compared to less-dense regions.

6. The fraction of quiescent galaxies depends on stellar mass at all the redshifts considered in this study ($0.1< z <3.1$), and it is higher for more massive systems. At

a given stellar mass, the fraction of quiescent galaxies is higher at lower redshifts. This is another manifestation of the galaxy mass-downsizing. We estimate the typical time delay between the quenching of less massive ($\log(M/M_{\odot})\sim10$) and more massive ($\log(M/M_{\odot})\sim11$) galaxies to be $\Delta t\sim3.4\pm0.9$ Gyr.

7. At all the redshifts considered in this study ($0.1< z <3.1$), the fraction of quiescent galaxies at a fixed environment strongly depends on stellar mass, i.e., the fraction of quiescent galaxies at all fixed density levels is always higher for more massive galaxies compared to less massive systems out to z$\sim$3. However, at a fixed stellar mass, quiescent fraction depends on environment (overdensity) only at $z\lesssim1$ and not significantly at higher redshifts. At a fixed stellar mass and at z$\lesssim$1, this fraction is higher in denser regions. All these results suggest that environmental quenching is practically important at $z\lesssim1$, whereas mass quenching is the major factor of star-formation truncation in galaxies at $z\gtrsim1$.

8. At a given stellar mass, the median rest-frame u^*-B_J color of quiescent galaxies is independent of the environment in which they reside. Quiescent galaxies become redder with cosmic time and their color evolution is independent of their environment. Since $z\sim3$, more massive quiescent galaxies ($\log(M/M_{\odot})\gtrsim10$) have become $\sim$0.2 mag redder in rest-frame u^*-B_J, whereas less massive quiescent systems have reddened by $\sim$0.1 mag since $z\sim1$.

9. On average, more massive quiescent galaxies are redder compared to less massive ones at any given redshift, regardless of their environment. The lack of a correlation between color and environment at fixed stellar mass for quiescent galaxies suggests that the relation between stellar mass and the local density of the galaxies is more fundamental than the color$-$density relation.

10. The average comoving number and mass density of massive ($\log(M/M_{\odot})>11$) star-forming galaxies have not evolved much since $z\sim3$. However, for massive quiescent

galaxies, number and mass densities rise sharply from $z \sim 3$ to $z \sim 1$ and remain almost unchanged since then.

11. The evolution of the comoving number and mass density of massive star-forming galaxies do not depend on their environment. They remain almost unchanged since $z \sim 3$, regardless of their host environment. The situation is different for massive quiescent galaxies. The comoving number and mass density of massive quiescent galaxies do not change much with environment and redshift from $z \sim 3$ to $z \sim 1.3$, which is similar to those of star-forming galaxies. However, at lower redshifts ($z \lesssim 1.3$), we find a significant evolution in the number and mass density of massive quiescent galaxies in denser environments compared with less-dense regions. Dense environments at lower redshifts are populated with massive quiescent galaxies, which signifies the role of the environment in quenching the star-formation activity in galaxies at lower redshifts.

Summary of Chapter 4

1. Our results improve previous studies based on intermediate environments and agree quantitatively and qualitatively with them, but show that what are often called "intermediate" densities and/or "group" environments are likely to be filaments.

2. Our results show that the observed fraction of star-forming galaxies is enhanced in filaments, relative to the field and cluster environments at $z \sim 0.8-0.9$. This enhancement in the fraction of star-forming galaxies in filaments is either intrinsic and/or due to a boost in the SFR of star-forming galaxies in filaments when combined with the selection biases. A possible physical interpretation for this trend is mild galaxy−galaxy interactions.

3. We also find that —in agreement with other studies— the observed SFR−mass relation and its intrinsic scatter, median SFR, stellar mass, and sSFR is mostly independent of environment for selected Hα emitters and underlying star-forming galaxies at $z \sim 0.8-0.9$. However, we mention that the environmental independence of the median

SFR and the SFR−mass relation for star-forming galaxies is affected by the selection biases, i.e., the intrinsic SFR of star-forming galaxies might vary with environment without being observed in the median values or the SFR−mass relation, as a result of selection effects. Indeed, if the environmental invariance of SFR−mass relation turns out to be real (and not much affected by the selection biases), this means that the environment is most relevant to set the star-forming fraction, or to determine if a galaxy is actively forming stars or not (but when it forms stars, on average, it lies on the same relation across environments). This implies that the physical processes involved in triggering/quenching star-formation should act on a relatively short timescale (assuming the SFR−mass relation is actually independent of environment and not much affected by selection biases).

4. Since our analysis is limited to a narrow redshift slice (Δz=0.03, equivalent to a comoving radial length of ∼80 Mpc at z ∼0.84), we discriminate against filaments oriented radially and we miss possible sub-structures along the line of sight. However, this is a limitation to all other similar photo-z-based studies. A better understanding of the geometry of structures can be achieved by 3D reconstruction of them using a large spectroscopic sample.

Summary of Chapter 5

We spectroscopically confirmed the presence of a large filamentary structure (∼ 8 Mpc) in the COSMOS field at z ∼0.53. We extensively studied the physical properties of the star-forming emission-line galaxies in this filament and compared them with a control sample of field galaxies at the same redshift. Our main results are:

1. We estimate the average electron density for filament and field star-forming galaxies using [OII]λ3726/λ3729 line ratio. We show that the average electron density is significantly lower (a factor of ∼ 17) for filament star-forming galaxies compared to that of the field systems. We obtain the same result if we perform the comparison

in fixed stellar mass, SFR, and sSFR bins. Depending on the bin selected, electron densities vary in the range $\sim <10-75$ cm^{-3} for filament star-forming galaxies and in the range $\sim 200-740$ cm^{-3} for star-forming galaxies in the field. The decrement of the electron densities in filament star-forming galaxies might be due to a longer star-formation timescale for filament star-forming systems.

2. We estimate the oxygen abundance metallicity using the R_{23} index. We show that our mass-metallicity relation at $z \sim 0.5$ for filament and field star-forming galaxies lies in between mass-metallicity relations at $z \sim 0$ and $z \sim 2$. We also show that our $\mu_{0.32}$-metallicity relation for filament and field star-forming galaxies nearly follows the Mannucci et al. (2010) trend at $z \sim 0$.

3. We show that at a fixed stellar mass, SFR, and $\mu_{0.32}$, filament star-forming galaxies are more metal-enriched ($\sim$0.1$-$0.15 dex) compared to their field counterparts. The metallicity enhancement for filament star-forming galaxies compared to the field might be due to the inflow of the already enriched intrafilamentary gas into filament galaxies. The metallicity enhancement in denser environments suggests that environment has a secondary effect in the metal enrichment of galaxies and internal processes are the major driver of the chemical evolution in galaxies.

4. We estimate the average ionisation parameter of filament and field star-forming galaxies using the O_{32} index. Ionisation parameter depends on stellar mass and decreases with increasing stellar mass for both filament and field star-forming galaxies. However, within the uncertainties, we find insignificant difference between ionisation parameter of filament and field star-forming systems.

5. We show that $EW_{[OII]}$ correlates with sSFR and anti-correlates with stellar mass for filament and field star-forming galaxies. However, we show that within the uncertainties, $EW_{[OII]}$-sSFR and $EW_{[OII]}$-mass relations are the same for filament and field star-forming systems. The environmental independence of the $EW_{[OII]}$-mass anti-

correlation is another manifestation of the environmental invariance of the SFR−mass relation for star-forming galaxies, seen in previous studies.

6. We estimate the line-of-sight velocity dispersion and dynamical masses for filament and field star-forming systems. We show that, on average, velocity dispersion, dynamical mass, and stellar-to-dynamical mass ratio are similar for filament and field star-forming galaxies.

Assuming ionisation equilibrium within HII star-forming regions, we can show that the ionisation parameter directly depends on the electron density, the diameter of the HII region, and the volume filling factor. Since we showed that, on average, the ionisation parameter is similar for filament and field star-forming galaxies and the electron density is much lower for filament star-forming systems, this suggests that, on average, filament star-forming galaxies might have larger HII regions compared to their field counterparts if we assume that the filling factor is the same for them. However, HII regions have sub-kpc sizes and a full understanding of their sizes in different environments at higher redshifts requires the next generation of telescopes such as TMT that are equipped with the IFU systems and assisted by the AO technology.

References

Abadi, M. G., Moore, B., and Bower, R. G.: 1999, *MNRAS* **308**, 947

Alpaslan, M., Driver, S., Robotham, A. S. G., Obreschkow, D., Andrae, E., Cluver, M., Kelvin, L. S., Lange, R., Owers, M., Taylor, E. N., Andrews, S. K., Bamford, S., Bland-Hawthorn, J., Brough, S., Brown, M. J. I., Colless, M., Davies, L. J. M., Eardley, E., Grootes, M. W., Hopkins, A. M., Kennedy, R., Liske, J., Lara-López, M. A., López-Sánchez, Á. R., Loveday, J., Madore, B. F., Mahajan, S., Meyer, M., Moffett, A., Norberg, P., Penny, S., Pimbblet, K. A., Popescu, C. C., Seibert, M., and Tuffs, R.: 2015, *MNRAS* **451**, 3249

Alpaslan, M., Robotham, A. S. G., Driver, S., Norberg, P., Baldry, I., Bauer, A. E., Bland-Hawthorn, J., Brown, M., Cluver, M., Colless, M., Foster, C., Hopkins, A., Van Kampen, E., Kelvin, L., Lara-Lopez, M. A., Liske, J., Lopez-Sanchez, A. R., Loveday, J., McNaught-Roberts, T., Merson, A., and Pimbblet, K.: 2014, *MNRAS* **438**, 177

Aracil, B., Tripp, T. M., Bowen, D. V., Prochaska, J. X., Chen, H.-W., and Frye, B. L.: 2006, *MNRAS* **367**, 139

Aragón-Calvo, M. A., Jones, B. J. T., van de Weygaert, R., and van der Hulst, J. M.: 2007, *Astronomy and Astrophysics* **474**, 315

Aragón-Calvo, M. A., van de Weygaert, R., and Jones, B. J. T.: 2010, *MNRAS* **408**, 2163

Aragon-Salamanca, A., Ellis, R. S., Couch, W. J., and Carter, D.: 1993, *MNRAS* **262**, 764

Arnaud, K. A., Mushotzky, R. F., Ezawa, H., Fukazawa, Y., Ohashi, T., Bautz, M. W., Crewe, G. B., Gendreau, K. C., Yamashita, K., Kamata, Y., and Akimoto, F.: 1994, *ApJl* **436**, L67

Arnouts, S., Moscardini, L., Vanzella, E., Colombi, S., Cristiani, S., Fontana, A., Giallongo, E., Matarrese, S., and Saracco, P.: 2002, *MNRAS* **329**, 355

Baldry, I. K., Balogh, M. L., Bower, R. G., Glazebrook, K., Nichol, R. C., Bamford, S. P., and Budavari, T.: 2006, *MNRAS* **373**, 469

Balogh, M., Eke, V., Miller, C., Lewis, I., Bower, R., Couch, W., Nichol, R., Bland-Hawthorn, J., Baldry, I. K., Baugh, C., Bridges, T., Cannon, R., Cole, S., Colless, M., Collins, C., Cross, N., Dalton, G., de Propris, R., Driver, S. P., Efstathiou, G., Ellis, R. S., Frenk, C. S., Glazebrook, K., Gomez, P., Gray, A., Hawkins, E., Jackson, C., Lahav, O., Lumsden, S., Maddox, S., Madgwick, D., Norberg, P., Peacock, J. A., Percival, W., Peterson, B. A., Sutherland, W., and Taylor, K.: 2004, *MNRAS* **348**, 1355

Balogh, M. L., Navarro, J. F., and Morris, S. L.: 2000, *ApJ* **540**, 113

Bamford, S. P., Nichol, R. C., Baldry, I. K., Land, K., Lintott, C. J., Schawinski, K., Slosar, A., Szalay, A. S., Thomas, D., Torki, M., Andreescu, D., Edmondson, E. M., Miller, C. J., Murray, P., Raddick, M. J., and Vandenberg, J.: 2009, *MNRAS* **393**, 1324

Barnes, and Hernquist, L. E.: 1991, *ApJl* **370**, L65

Bassett, R., Papovich, C., Lotz, J. M., Bell, E. F., Finkelstein, S. L., Newman, J. A., Tran, K.-V., Almaini, O., Lani, C., Cooper, M., Croton, D., Dekel, A., Ferguson, H. C., Kocevski, D. D., Koekemoer, A. M., Koo, D. C., McGrath, E. J., McIntosh, D. H., and Wechsler, R.: 2013, *ApJ* **770**, 58

Beifiori, A., Thomas, D., Maraston, C., Steele, O., Masters, K. L., Pforr, J., Saglia, R. P., Bender, R., Tojeiro, R., Chen, Y.-M., Bolton, A., Brownstein, J. R., Johansson, J., Leauthaud, A., Nichol, R. C., Schneider, D. P., Senger, R., Skibba, R., Wake, D., Pan, K., Snedden, S., Bizyaev, D., Brewington, H., Malanushenko, V., Malanushenko, E., Oravetz, D., Simmons, A., Shelden, A., and Ebelke, G.: 2014, *ApJ* **789**, 92

Bell, E. F., Wolf, C., Meisenheimer, K., Rix, H.-W., Borch, A., Dye, S., Kleinheinrich, M., Wisotzki, L., and McIntosh, D. H.: 2004, *ApJ* **608**, 752

Belli, S., Newman, A. B., Ellis, R. S., and Konidaris, N. P.: 2014, *ApJl* **788**, L29

Benítez-Llambay, A., Navarro, J. F., Abadi, M. G., Gottlöber, S., Yepes, G., Hoffman, Y., and Steinmetz, M.: 2013, *ApJl* **763**, L41

Bernardeau, F. and van de Weygaert, R.: 1996, *MNRAS* **279**, 693

Bertin, E. and Arnouts, S.: 1996, **117**, 393

Best, P. N.: 2004, *MNRAS* **351**, 70

Binney, J. and Tremaine, S.: 2008, *Galactic Dynamics: Second Edition*, Princeton University Press

Birnboim, Y. and Dekel, A.: 2003, *MNRAS* **345**, 349

Biviano, A., Fadda, D., Durret, F., Edwards, L. O. V., and Marleau, F.: 2011, *Astronomy and Astrophysics* **532**, A77

Blakeslee, J. P., Franx, M., Postman, M., Rosati, P., Holden, B. P., Illingworth, G. D., Ford, H. C., Cross, N. J. G., Gronwall, C., Benítez, N., Bouwens, R. J., Broadhurst, T. J., Clampin, M., Demarco, R., Golimowski, D. A., Hartig, G. F., Infante, L., Martel, A. R., Miley, G. K., Menanteau, F., Meurer, G. R., Sirianni, M., and White, R. L.: 2003, *ApJl* **596**, L143

Blanton, M. R., Eisenstein, D., Hogg, D. W., and Zehavi, I.: 2006, *ApJ* **645**, 977

Böhringer, H., Schuecker, P., Guzzo, L., Collins, C. A., Voges, W., Cruddace, R. G., Ortiz-Gil, A., Chincarini, G., De Grandi, S., Edge, A. C., MacGillivray, H. T., Neumann, D. M., Schindler, S., and Shaver, P.: 2004, *Astronomy and Astrophysics* **425**, 367

Böhringer, H., Voges, W., Huchra, J. P., McLean, B., Giacconi, R., Rosati, P., Burg, R., Mader, J., Schuecker, P., Simiç, D., Komossa, S., Reiprich, T. H., Retzlaff, J., and Trümper, J.: 2000, *ApJl Supp.* **129**, 435

Bolzonella, M., Kovač, K., Pozzetti, L., Zucca, E., Cucciati, O., Lilly, S. J., Peng, Y., Iovino, A., Zamorani, G., Vergani, D., Tasca, L. A. M., Lamareille, F., Oesch, P., Caputi, K., Kampczyk, P., Bardelli, S., Maier, C., Abbas, U., Knobel, C., Scodeggio, M., Carollo, C. M., Contini, T., Kneib, J.-P., Le Fèvre, O., Mainieri, V., Renzini, A., Bongiorno, A., Coppa, G., de la Torre, S., de Ravel, L., Franzetti, P., Garilli, B., Le Borgne, J.-F., Le Brun, V., Mignoli, M., Pelló, R., Perez-Montero, E., Ricciardelli, E., Silverman, J. D., Tanaka, M., Tresse, L., Bottini, D., Cappi, A., Cassata, P., Cimatti, A., Guzzo, L., Koekemoer, A. M., Leauthaud, A., Maccagni, D., Marinoni, C., McCracken, H. J., Memeo, P., Meneux, B., Porciani, C., Scaramella, R., Aussel, H., Capak, P., Halliday, C., Ilbert, O., Kartaltepe, J., Salvato, M., Sanders, D., Scarlata, C., Scoville, N., Taniguchi, Y., and Thompson, D.: 2010, *Astronomy and Astrophysics* **524**, A76

Bond, J. R., Kofman, L., and Pogosyan, D.: 1996, *Nature* **380**, 603

Bösch, B., Böhm, A., Wolf, C., Aragón-Salamanca, A., Ziegler, B. L., Barden, M., Gray, M. E., Balogh, M., Meisenheimer, K., and Schindler, S.: 2013, *Astronomy and Astrophysics* **554**, A97

Boselli, A., Boissier, S., Cortese, L., and Gavazzi, G.: 2008, *ApJ* **674**, 742

Boselli, A. and Gavazzi, G.: 2006, *Publications of the Astronomical Society of the Pacific* **118**, 517

Boselli, A. and Gavazzi, G.: 2014, **22**, 74

Bothwell, M. S., Maiolino, R., Kennicutt, R., Cresci, G., Mannucci, F., Marconi, A., and Cicone, C.: 2013, *MNRAS* **433**, 1425

Bouché, N. and Lowenthal, J. D.: 2005, *ApJl* **623**, L75

Bower, R. G., Lucey, J. R., and Ellis, R. S.: 1992, *MNRAS* **254**, 589

Boylan-Kolchin, M., Springel, V., White, S. D. M., Jenkins, A., and Lemson, G.: 2009, *MNRAS* **398**, 1150

Brammer, G. B., Whitaker, K. E., van Dokkum, P. G., Marchesini, D., Franx, M., Kriek, M., Labbé, I., Lee, K.-S., Muzzin, A., Quadri, R. F., Rudnick, G., and Williams, R.: 2011, *ApJ* **739**, 24

Brammer, G. B., Whitaker, K. E., van Dokkum, P. G., Marchesini, D., Labbé, I., Franx, M., Kriek, M., Quadri, R. F., Illingworth, G., Lee, K.-S., Muzzin, A., and Rudnick, G.: 2009, *ApJl* **706**, L173

Bridge, J. S., Gronwall, C., Ciardullo, R., Hagen, A., Zeimann, G., Malz, A. I., Acquaviva, V., Schneider, D. P., Drory, N., Gebhardt, K., and Jogee, S.: 2015, *ApJ* **799**, 205

Brinchmann, J., Charlot, S., White, S. D. M., Tremonti, C., Kauffmann, G., Heckman, T., and Brinkmann, J.: 2004, *MNRAS* **351**, 1151

Brodwin, M., Stanford, S. A., Gonzalez, A. H., Zeimann, G. R., Snyder, G. F., Mancone, C. L., Pope, A., Eisenhardt, P. R., Stern, D., Alberts, S., Ashby, M. L. N., Brown, M. J. I., Chary, R.-R., Dey, A., Galametz, A., Gettings, D. P., Jannuzi, B. T., Miller, E. D., Moustakas, J., and Moustakas, L. A.: 2013, *ApJ* **779**, 138

Bruzual, G.: 2007, in A. Vallenari, R. Tantalo, L. Portinari, and A. Moretti (eds.), *From Stars to Galaxies: Building the Pieces to Build Up the Universe*, Vol. 374 of *Astronomical Society of the Pacific Conference Series*, p. 303

Bruzual, G. and Charlot, S.: 2003, *MNRAS* **344**, 1000

Bundy, K., Ellis, R. S., Conselice, C. J., Taylor, J. E., Cooper, M. C., Willmer, C. N. A., Weiner, B. J., Coil, A. L., Noeske, K. G., and Eisenhardt, P. R. M.: 2006, *ApJ* **651**, 120

Butcher, H. and Oemler, Jr., A.: 1978, *ApJ* **219**, 18

Calzetti, D., Armus, L., Bohlin, R. C., Kinney, A. L., Koornneef, J., and Storchi-Bergmann, T.: 2000, *ApJ* **533**, 682

Cantalupo, S., Arrigoni-Battaia, F., Prochaska, J. X., Hennawi, J. F., and Madau, P.: 2014, *Nature* **506**, 63

Capak, P., Abraham, R. G., Ellis, R. S., Mobasher, B., Scoville, N., Sheth, K., and Koekemoer, A.: 2007a, *ApJl Supp.* **172**, 284

Capak, P., Aussel, H., Ajiki, M., McCracken, H. J., Mobasher, B., Scoville, N., Shopbell, P., Taniguchi, Y., Thompson, D., Tribiano, S., Sasaki, S., Blain, A. W., Brusa, M., Carilli, C., Comastri, A., Carollo, C. M., Cassata, P., Colbert, J., Ellis, R. S., Elvis, M., Giavalisco, M., Green, W., Guzzo, L., Hasinger, G., Ilbert, O., Impey, C., Jahnke, K., Kartaltepe, J., Kneib, J.-P., Koda, J., Koekemoer, A., Komiyama, Y., Leauthaud, A., Le Fevre, O., Lilly, S., Liu, C., Massey, R., Miyazaki, S., Murayama, T., Nagao, T., Peacock, J. A., Pickles, A., Porciani, C., Renzini, A., Rhodes, J., Rich, M., Salvato, M., Sanders, D. B., Scarlata, C., Schiminovich, D., Schinnerer, E., Scodeggio, M., Sheth, K., Shioya, Y., Tasca, L. A. M., Taylor, J. E., Yan, L., and Zamorani, G.: 2007b, *ApJl Supp.* **172**, 99

Capozzi, D., Collins, C. A., and Stott, J. P.: 2010, *MNRAS* **403**, 1274

Cappellari, M., Bacon, R., Bureau, M., Damen, M. C., Davies, R. L., de Zeeuw, P. T., Emsellem, E., Falcón-Barroso, J., Krajnović, D., Kuntschner, H., McDermid, R. M., Peletier, R. F., Sarzi, M., van den Bosch, R. C. E., and van de Ven, G.: 2006, *MNRAS* **366**, 1126

Cappelluti, N., Cappi, M., Dadina, M., Malaguti, G., Branchesi, M., D'Elia, V., and Palumbo, G. G. C.: 2005, *Astronomy and Astrophysics* **430**, 39

Cassata, P., Guzzo, L., Franceschini, A., Scoville, N., Capak, P., Ellis, R. S., Koekemoer, A., McCracken, H. J., Mobasher, B., Renzini, A., Ricciardelli, E., Scodeggio, M., Taniguchi, Y., and Thompson, D.: 2007, *ApJl Supp.* **172**, 270

Cayatte, V., van Gorkom, J. H., Balkowski, C., and Kotanyi, C.: 1990, *The Astronomical Journal* **100**, 604

Cen, R. and Chisari, N. E.: 2011, *ApJ* **731**, 11

Cen, R. and Ostriker, J. P.: 1999, *ApJ* **514**, 1

Cen, R. and Ostriker, J. P.: 2006, *ApJ* **650**, 560

Chabrier, G.: 2003, *Publications of the Astronomical Society of the Pacific* **115**, 763

Chiang, Y.-K., Overzier, R., and Gebhardt, K.: 2014, *ApJl* **782**, L3

Ciardullo, R., Gronwall, C., Adams, J. J., Blanc, G. A., Gebhardt, K., Finkelstein, S. L., Jogee, S., Hill, G. J., Drory, N., Hopp, U., Schneider, D. P., Zeimann, G. R., and Dalton, G. B.: 2013, *ApJ* **769**, 83

Colberg, J. M., Krughoff, K. S., and Connolly, A. J.: 2005, *MNRAS* **359**, 272

Colless, M., Dalton, G., Maddox, S., Sutherland, W., Norberg, P., Cole, S., Bland-Hawthorn, J., Bridges, T., Cannon, R., Collins, C., Couch, W., Cross, N., Deeley, K., De Propris, R., Driver, S. P., Efstathiou, G., Ellis, R. S., Frenk, C. S., Glazebrook, K., Jackson, C., Lahav, O., Lewis, I., Lumsden, S., Madgwick, D., Peacock, J. A., Peterson, B. A., Price, I., Seaborne, M., and Taylor, K.: 2001, *MNRAS* **328**, 1039

Cool, R. J., Eisenstein, D. J., Fan, X., Fukugita, M., Jiang, L., Maraston, C., Meiksin, A., Schneider, D. P., and Wake, D. A.: 2008, *ApJ* **682**, 919

Cooper, M. C., Newman, J. A., Coil, A. L., Croton, D. J., Gerke, B. F., Yan, R., Davis, M., Faber, S. M., Guhathakurta, P., Koo, D. C., Weiner, B. J., and Willmer, C. N. A.: 2007, *MNRAS* **376**, 1445

Cooper, M. C., Newman, J. A., Davis, M., Finkbeiner, D. P., and Gerke, B. F.: 2012, *spec2d: DEEP2 DEIMOS Spectral Pipeline*, Astrophysics Source Code Library

Cooper, M. C., Newman, J. A., Madgwick, D. S., Gerke, B. F., Yan, R., and Davis, M.: 2005, *ApJ* **634**, 833

Cooper, M. C., Newman, J. A., Weiner, B. J., Yan, R., Willmer, C. N. A., Bundy, K., Coil, A. L., Conselice, C. J., Davis, M., Faber, S. M., Gerke, B. F., Guhathakurta, P., Koo, D. C., and Noeske, K. G.: 2008a, *MNRAS* **383**, 1058

Cooper, M. C., Tremonti, C. A., Newman, J. A., and Zabludoff, A. I.: 2008b, *MNRAS* **390**, 245

Coppin, K. E. K., Geach, J. E., Webb, T. M. A., Faloon, A., Yan, R., O'Donnell, D., Ouellette, N., Egami, E., Ellingson, E., Gilbank, D., Hicks, A., Barrientos, L. F., Yee, H. K. C., and Gladders, M.: 2012, *ApJl* **749**, L43

Cortese, L., Ciesla, L., Boselli, A., Bianchi, S., Gomez, H., Smith, M. W. L., Bendo, G. J., Eales, S., Pohlen, M., Baes, M., Corbelli, E., Davies, J. I., Hughes, T. M., Hunt, L. K., Madden, S. C., Pierini, D., di Serego Alighieri, S., Zibetti, S., Boquien, M., Clements, D. L., Cooray, A., Galametz, M., Magrini, L., Pappalardo, C., Spinoglio, L., and Vlahakis, C.: 2012, *Astronomy and Astrophysics* **540**, A52

Cortese, L., Davies, J. I., Pohlen, M., Baes, M., Bendo, G. J., Bianchi, S., Boselli, A., De Looze, I., Fritz, J., Verstappen, J., Bomans, D. J., Clemens, M., Corbelli, E., Dariush, A., di Serego Alighieri, S., Fadda, D., Garcia-Appadoo, D. A., Gavazzi, G., Giovanardi, C., Grossi, M., Hughes, T. M., Hunt, L. K., Jones, A. P., Madden, S., Pierini, D., Sabatini, S., Smith, M. W. L., Vlahakis, C., Xilouris, E. M., and Zibetti, S.: 2010, *Astronomy and Astrophysics* **518**, L49

Couch, W. J. and Sharples, R. M.: 1987, *MNRAS* **229**, 423

Cowie, L. L. and Barger, A. J.: 2008, *ApJ* **686**, 72

Cowie, L. L., Hu, E. M., Jenkins, E. B., and York, D. G.: 1983, *ApJ* **272**, 29

Cowie, L. L. and Songaila, A.: 1977, *Nature* **266**, 501

Cowie, L. L., Songaila, A., Hu, E. M., and Cohen, J. G.: 1996, *The Astronomical Journal* **112**, 839

Cox, T. J., Jonsson, P., Somerville, R. S., Primack, J. R., and Dekel, A.: 2008, *MNRAS* **384**, 386

Crawford, C. S., Allen, S. W., Ebeling, H., Edge, A. C., and Fabian, A. C.: 1999, *MNRAS* **306**, 857

Cucciati, O., Iovino, A., Kovač, K., Scodeggio, M., Lilly, S. J., Bolzonella, M., Bardelli, S., Vergani, D., Tasca, L. A. M., Zucca, E., Zamorani, G., Pozzetti, L., Knobel, C., Oesch, P., Lamareille, F., Caputi, K., Kampczyk, P., Tresse, L., Maier, C., Carollo, C. M., Contini, T., Kneib, J.-P., Le Fèvre, O., Mainieri, V., Renzini, A., Bongiorno, A., Coppa, G., de la Torre, S., de Ravel, L., Franzetti, P., Garilli, B., Le Borgne, J.-F., Le Brun, V., Mignoli, M., Pellò, R., Peng, Y., Perez-Montero, E., Ricciardelli, E., Silverman, J. D., Tanaka, M., Koekemoer, A. M., Scoville, N., Abbas, U., Bottini, D., Cappi, A., Cassata, P., Cimatti, A., Guzzo, L., Leauthaud, A., Maccagni, D., Marinoni, C., McCracken, H. J., Memeo, P., Meneux, B., Porciani, C., and Scaramella, R.: 2010, *Astronomy and Astrophysics* **524**, A2

Daddi, E., Dickinson, M., Morrison, G., Chary, R., Cimatti, A., Elbaz, D., Frayer, D., Renzini, A., Pope, A., Alexander, D. M., Bauer, F. E., Giavalisco, M., Huynh, M., Kurk, J., and Mignoli, M.: 2007, *ApJ* **670**, 156

Danforth, C. W., Keeney, B. A., Stocke, J. T., Shull, J. M., and Yao, Y.: 2010, *ApJ* **720**, 976

Darvish, B., Mobasher, B., Sobral, D., Scoville, N., and Aragon-Calvo, M.: 2015, *ApJ* **805**, 121

Darvish, B., Sobral, D., Mobasher, B., Scoville, N. Z., Best, P., Sales, L. V., and Smail, I.: 2014, *ApJ* **796**, 51

Davé, R., Cen, R., Ostriker, J. P., Bryan, G. L., Hernquist, L., Katz, N., Weinberg, D. H., Norman, M. L., and O'Shea, B.: 2001, *ApJ* **552**, 473

Davé, R., Finlator, K., and Oppenheimer, B. D.: 2011, *MNRAS* **416**, 1354

Davé, R., Oppenheimer, B. D., Katz, N., Kollmeier, J. A., and Weinberg, D. H.: 2010, *MNRAS* **408**, 2051

Davidzon, I., Bolzonella, M., Coupon, J., Ilbert, O., Arnouts, S., de la Torre, S., Fritz, A., De Lucia, G., Iovino, A., Granett, B. R., Zamorani, G., Guzzo, L., Abbas, U., Adami, C., Bel, J., Bottini, D., Branchini, E., Cappi, A., Cucciati, O., Franzetti, P., Fumana, M., Garilli, B., Krywult, J., Le Brun, V., Le Fèvre, O., Maccagni, D., Małek, K., Marulli, F., McCracken, H. J., Paioro, L., Peacock, J. A., Polletta, M., Pollo, A., Schlagenhaufer, H., Scodeggio, M., Tasca, L. A. M., Tojeiro, R., Vergani, D., Zanichelli, A., Burden, A., Di

Porto, C., Marchetti, A., Marinoni, C., Mellier, Y., Moscardini, L., Moutard, T., Nichol, R. C., Percival, W. J., Phleps, S., and Wolk, M.: 2013, *Astronomy and Astrophysics* **558**, A23

Dawson, W. A., Jee, M. J., Stroe, A., Ng, Y. K., Golovich, N., Wittman, D., Sobral, D., Brüggen, M., Röttgering, H. J. A., and van Weeren, R. J.: 2015, *ApJ* **805**, 143

de los Reyes, M. A., Ly, C., Lee, J. C., Salim, S., Peeples, M. S., Momcheva, I., Feddersen, J., Dale, D. A., Ouchi, M., Ono, Y., and Finn, R.: 2015, *The Astronomical Journal* **149**, 79

De Lucia, G., Poggianti, B. M., Aragón-Salamanca, A., White, S. D. M., Zaritsky, D., Clowe, D., Halliday, C., Jablonka, P., von der Linden, A., Milvang-Jensen, B., Pelló, R., Rudnick, G., Saglia, R. P., and Simard, L.: 2007, *MNRAS* **374**, 809

De Robertis, M. M., Dufour, R. J., and Hunt, R. W.: 1987, **81**, 195

Dekel, A. and Birnboim, Y.: 2006, *MNRAS* **368**, 2

Dekel, A., Birnboim, Y., Engel, G., Freundlich, J., Goerdt, T., Mumcuoglu, M., Neistein, E., Pichon, C., Teyssier, R., and Zinger, E.: 2009a, *Nature* **457**, 451

Dekel, A., Sari, R., and Ceverino, D.: 2009b, *ApJ* **703**, 785

Dietrich, J. P., Erben, T., Lamer, G., Schneider, P., Schwope, A., Hartlap, J., and Maturi, M.: 2007, *Astronomy and Astrophysics* **470**, 821

Dietrich, J. P., Werner, N., Clowe, D., Finoguenov, A., Kitching, T., Miller, L., and Simionescu, A.: 2012, *Nature* **487**, 202

Domínguez, A., Siana, B., Henry, A. L., Scarlata, C., Bedregal, A. G., Malkan, M., Atek, H., Ross, N. R., Colbert, J. W., Teplitz, H. I., Rafelski, M., McCarthy, P., Bunker, A., Hathi, N. P., Dressler, A., Martin, C. L., and Masters, D.: 2013, *ApJ* **763**, 145

Domínguez Sánchez, H., Pozzi, F., Gruppioni, C., Cimatti, A., Ilbert, O., Pozzetti, L., McCracken, H., Capak, P., Le Floch, E., Salvato, M., Zamorani, G., Carollo, C. M., Contini, T., Kneib, J.-P., Le Fèvre, O., Lilly, S. J., Mainieri, V., Renzini, A., Scodeggio, M., Bardelli, S., Bolzonella, M., Bongiorno, A., Caputi, K., Coppa, G., Cucciati, O., de la Torre, S., de Ravel, L., Franzetti, P., Garilli, B., Iovino, A., Kampczyk, P., Knobel, C., Kovač, K., Lamareille, F., Le Borgne, J.-F., Le Brun, V., Maier, C., Mignoli, M., Pelló, R., Peng, Y., Perez-Montero, E., Ricciardelli, E., Silverman, J. D., Tanaka, M., Tasca, L. A. M., Tresse, L., Vergani, D., and Zucca, E.: 2011, *MNRAS* **417**, 900

Dressler, A.: 1980, *ApJ* **236**, 351

Dressler, A. and Gunn, J. E.: 1983, *ApJ* **270**, 7

Dressler, A., Oemler, Jr., A., Butcher, H. R., and Gunn, J. E.: 1994, *ApJ* **430**, 107

Dressler, A., Smail, I., Poggianti, B. M., Butcher, H., Couch, W. J., Ellis, R. S., and Oemler, Jr., A.: 1999, *ApJl Supp.* **122**, 51

Driver, S. P., Hill, D. T., Kelvin, L. S., Robotham, A. S. G., Liske, J., Norberg, P., Baldry, I. K., Bamford, S. P., Hopkins, A. M., Loveday, J., Peacock, J. A., Andrae, E., Bland-Hawthorn, J., Brough, S., Brown, M. J. I., Cameron, E., Ching, J. H. Y., Colless, M., Conselice, C. J., Croom, S. M., Cross, N. J. G., de Propris, R., Dye, S., Drinkwater, M. J., Ellis, S., Graham, A. W., Grootes, M. W., Gunawardhana, M., Jones, D. H., van Kampen, E., Maraston, C., Nichol, R. C., Parkinson, H. R., Phillipps, S., Pimbblet, K., Popescu, C. C., Prescott, M., Roseboom, I. G., Sadler, E. M., Sansom, A. E., Sharp, R. G., Smith, D. J. B., Taylor, E., Thomas, D., Tuffs, R. J., Wijesinghe, D., Dunne, L., Frenk, C. S., Jarvis, M. J., Madore, B. F., Meyer, M. J., Seibert, M., Staveley-Smith, L., Sutherland, W. J., and Warren, S. J.: 2011, *MNRAS* **413**, 971

Dutton, A. A., van den Bosch, F. C., and Dekel, A.: 2010, *MNRAS* **405**, 1690

Ebeling, H., Barrett, E., and Donovan, D.: 2004, *ApJl* **609**, L49

Ebeling, H., Edge, A. C., Bohringer, H., Allen, S. W., Crawford, C. S., Fabian, A. C., Voges, W., and Huchra, J. P.: 1998, *MNRAS* **301**, 881

Ebeling, H., Edge, A. C., and Henry, J. P.: 2001, *ApJ* **553**, 668

Ebeling, H. and Wiedenmann, G.: 1993, **47**, 704

Elbaz, D., Daddi, E., Le Borgne, D., Dickinson, M., Alexander, D. M., Chary, R.-R., Starck, J.-L., Brandt, W. N., Kitzbichler, M., MacDonald, E., Nonino, M., Popesso, P., Stern, D., and Vanzella, E.: 2007, *Astronomy and Astrophysics* **468**, 33

Ellison, S. L., Mendel, J. T., Patton, D. R., and Scudder, J. M.: 2013, *MNRAS* **435**, 3627

Ellison, S. L., Patton, D. R., Simard, L., and McConnachie, A. W.: 2008, *The Astronomical Journal* **135**, 1877

Ellison, S. L., Simard, L., Cowan, N. B., Baldry, I. K., Patton, D. R., and McConnachie, A. W.: 2009, *MNRAS* **396**, 1257

Erb, D. K., Shapley, A. E., Pettini, M., Steidel, C. C., Reddy, N. A., and Adelberger, K. L.: 2006, *ApJ* **644**, 813

Erb, D. K., Shapley, A. E., Steidel, C. C., Pettini, M., Adelberger, K. L., Hunt, M. P., Moorwood, A. F. M., and Cuby, J.-G.: 2003, *ApJ* **591**, 101

Erb, D. K., Steidel, C. C., Trainor, R. F., Bogosavljević, M., Shapley, A. E., Nestor, D. B., Kulas, K. R., Law, D. R., Strom, A. L., Rudie, G. C., Reddy, N. A., Pettini, M., Konidaris, N. P., Mace, G., Matthews, K., and McLean, I. S.: 2014, *ApJ* **795**, 33

Fadda, D., Biviano, A., Marleau, F. R., Storrie-Lombardi, L. J., and Durret, F.: 2008, *ApJl* **672**, L9

Fasano, G. and Franceschini, A.: 1987, *MNRAS* **225**, 155

Feruglio, C., Aussel, H., Le Floc'h, E., Ilbert, O., Salvato, M., Capak, P., Fiore, F., Kartaltepe, J., Sanders, D., Scoville, N., Koekemoer, A. M., and Ideue, Y.: 2010, *ApJ* **721**, 607

Finoguenov, A., Briel, U. G., and Henry, J. P.: 2003, *Astronomy and Astrophysics* **410**, 777

Finoguenov, A., Guzzo, L., Hasinger, G., Scoville, N. Z., Aussel, H., Böhringer, H., Brusa, M., Capak, P., Cappelluti, N., Comastri, A., Giodini, S., Griffiths, R. E., Impey, C., Koekemoer, A. M., Kneib, J.-P., Leauthaud, A., Le Fèvre, O., Lilly, S., Mainieri, V., Massey, R., McCracken, H. J., Mobasher, B., Murayama, T., Peacock, J. A., Sakelliou, I., Schinnerer, E., Silverman, J. D., Smolčić, V., Taniguchi, Y., Tasca, L., Taylor, J. E., Trump, J. R., and Zamorani, G.: 2007, *ApJl Supp.* **172**, 182

Forbes, D. A., Phillips, A. C., Koo, D. C., and Illingworth, G. D.: 1996, *ApJ* **462**, 89

Ford, H. C. and Butcher, H.: 1979, *ApJl Supp.* **41**, 147

Foster, C., Hopkins, A. M., Gunawardhana, M., Lara-López, M. A., Sharp, R. G., Steele, O., Taylor, E. N., Driver, S. P., Baldry, I. K., Bamford, S. P., Liske, J., Loveday, J., Norberg, P., Peacock, J. A., Alpaslan, M., Bauer, A. E., Bland-Hawthorn, J., Brough, S., Cameron, E., Colless, M., Conselice, C. J., Croom, S. M., Frenk, C. S., Hill, D. T., Jones, D. H., Kelvin, L. S., Kuijken, K., Nichol, R. C., Owers, M. S., Parkinson, H. R., Pimbblet, K. A., Popescu, C. C., Prescott, M., Robotham, A. S. G., Lopez-Sanchez, A. R., Sutherland, W. J., Thomas, D., Tuffs, R. J., van Kampen, E., and Wijesinghe, D.: 2012, *Astronomy and Astrophysics* **547**, A79

Frenk, C. S., Evrard, A. E., White, S. D. M., and Summers, F. J.: 1996, *ApJ* **472**, 460

Fujita, Y.: 1998, *ApJ* **509**, 587

Fumagalli, M., Krumholz, M. R., Prochaska, J. X., Gavazzi, G., and Boselli, A.: 2009, *ApJ* **697**, 1811

Fumagalli, M., Patel, S. G., Franx, M., Brammer, G., van Dokkum, P., da Cunha, E., Kriek, M., Lundgren, B., Momcheva, I., Rix, H.-W., Schmidt, K. B., Skelton, R. E., Whitaker, K. E., Labbe, I., and Nelson, E.: 2012, *ApJl* **757**, L22

Gabor, J. M. and Davé, R.: 2015, *MNRAS* **447**, 374

Gallazzi, A., Bell, E. F., Wolf, C., Gray, M. E., Papovich, C., Barden, M., Peng, C. Y., Meisenheimer, K., Heymans, C., van Kampen, E., Gilmour, R., Balogh, M., McIntosh, D. H., Bacon, D., Barazza, F. D., Böhm, A., Caldwell, J. A. R., Häußler, B., Jahnke, K., Jogee, S., Lane, K., Robaina, A. R., Sanchez, S. F., Taylor, A., Wisotzki, L., and Zheng, X.: 2009, *ApJ* **690**, 1883

Garn, T. and Best, P. N.: 2010, *MNRAS* **409**, 421

Gavazzi, G., Boselli, A., van Driel, W., and O'Neil, K.: 2005, *Astronomy and Astrophysics* **429**, 439

Gavazzi, R. and Soucail, G.: 2007, *Astronomy and Astrophysics* **462**, 459

Geach, J. E., Ellis, R. S., Smail, I., Rawle, T. D., and Moran, S. M.: 2011, *MNRAS* **413**, 177

Geach, J. E., Smail, I., Best, P. N., Kurk, J., Casali, M., Ivison, R. J., and Coppin, K.: 2008, *MNRAS* **388**, 1473

George, M. R., Leauthaud, A., Bundy, K., Finoguenov, A., Tinker, J., Lin, Y.-T., Mei, S., Kneib, J.-P., Aussel, H., Behroozi, P. S., Busha, M. T., Capak, P., Coccato, L., Covone, G., Faure, C., Fiorenza, S. L., Ilbert, O., Le Floc'h, E., Koekemoer, A. M., Tanaka, M., Wechsler, R. H., and Wolk, M.: 2011, *ApJ* **742**, 125

Gilbank, D. G. and Balogh, M. L.: 2008, *MNRAS* **385**, L116

Gill, S. P. D., Knebe, A., and Gibson, B. K.: 2005, *MNRAS* **356**, 1327

Gilmour, R., Gray, M. E., Almaini, O., Best, P., Wolf, C., Meisenheimer, K., Papovich, C., and Bell, E.: 2007, *MNRAS* **380**, 1467

Gioia, I. M., Henry, J. P., Maccacaro, T., Morris, S. L., Stocke, J. T., and Wolter, A.: 1990, *ApJl* **356**, L35

Gladders, M. D. and Yee, H. K. C.: 2000, *The Astronomical Journal* **120**, 2148

Gladders, M. D. and Yee, H. K. C.: 2005, *ApJl Supp.* **157**, 1

Goto, T., Sekiguchi, M., Nichol, R. C., Bahcall, N. A., Kim, R. S. J., Annis, J., Ivezić, Ž., Brinkmann, J., Hennessy, G. S., Szokoly, G. P., and Tucker, D. L.: 2002, *The Astronomical Journal* **123**, 1807

Grützbauch, R., Conselice, C. J., Bauer, A. E., Bluck, A. F. L., Chuter, R. W., Buitrago, F., Mortlock, A., Weinzirl, T., and Jogee, S.: 2011, *MNRAS* **418**, 938

Gunn, J. E. and Gott, III, J. R.: 1972, *ApJ* **176**, 1

Guzzo, L. and The Vipers Team: 2013, *The Messenger* **151**, 41

Hao, J., McKay, T. A., Koester, B. P., Rykoff, E. S., Rozo, E., Annis, J., Wechsler, R. H., Evrard, A., Siegel, S. R., Becker, M., Busha, M., Gerdes, D., Johnston, D. E., and Sheldon, E.: 2010, *ApJl Supp.* **191**, 254

Hayashi, M., Kodama, T., Koyama, Y., Tadaki, K.-I., and Tanaka, I.: 2011, *MNRAS* **415**, 2670

Hayashi, M., Kodama, T., Koyama, Y., Tadaki, K.-i., Tanaka, I., Shimakawa, R., Matsuda, Y., Sobral, D., Best, P. N., and Smail, I.: 2014, *MNRAS* **439**, 2571

Heckman, T. M., Baum, S. A., van Breugel, W. J. M., and McCarthy, P.: 1989, *ApJ* **338**, 48

Hemmati, S., Miller, S. H., Mobasher, B., Nayyeri, H., Ferguson, H. C., Guo, Y., Koekemoer, A. M., Koo, D. C., and Papovich, C.: 2014, *ApJ* **797**, 108

Henry, A., Scarlata, C., Domínguez, A., Malkan, M., Martin, C. L., Siana, B., Atek, H., Bedregal, A. G., Colbert, J. W., Rafelski, M., Ross, N., Teplitz, H., Bunker, A. J., Dressler, A., Hathi, N., Masters, D., McCarthy, P., and Straughn, A.: 2013, *ApJl* **776**, L27

Higuchi, Y., Oguri, M., Tanaka, M., and Sakurai, J.: 2015, *ArXiv e-prints*

Hogg, D. W., Blanton, M. R., Brinchmann, J., Eisenstein, D. J., Schlegel, D. J., Gunn, J. E., McKay, T. A., Rix, H.-W., Bahcall, N. A., Brinkmann, J., and Meiksin, A.: 2004, *ApJl* **601**, L29

Horne, K.: 1986, *Publications of the Astronomical Society of the Pacific* **98**, 609

Hu, E. M., Cowie, L. L., and Wang, Z.: 1985, *ApJl Supp.* **59**, 447

Hughes, T. M., Cortese, L., Boselli, A., Gavazzi, G., and Davies, J. I.: 2013, *Astronomy and Astrophysics* **550**, A115

Ibar, E., Sobral, D., Best, P. N., Ivison, R. J., Smail, I., Arumugam, V., Berta, S., Béthermin, M., Bock, J., Cava, A., Conley, A., Farrah, D., Geach, J., Ikarashi, S., Kohno, K., Le Floc'h, E., Lutz, D., Magdis, G., Magnelli, B., Marsden, G., Oliver, S. J., Page, M. J., Pozzi, F., Riguccini, L., Schulz, B., Seymour, N., Smith, A. J., Symeonidis, M., Wang, L., Wardlow, J., and Zemcov, M.: 2013, *MNRAS* **434**, 3218

Ideue, Y., Taniguchi, Y., Nagao, T., Shioya, Y., Kajisawa, M., Trump, J. R., Vergani, D., Iovino, A., Koekemoer, A. M., Le Fèvre, O., Ilbert, O., and Scoville, N. Z.: 2012, *ApJ* **747**, 42

Ilbert, O., Arnouts, S., McCracken, H. J., Bolzonella, M., Bertin, E., Le Fèvre, O., Mellier, Y., Zamorani, G., Pellò, R., Iovino, A., Tresse, L., Le Brun, V., Bottini, D., Garilli, B., Maccagni, D., Picat, J. P., Scaramella, R., Scodeggio, M., Vettolani, G., Zanichelli, A., Adami, C., Bardelli, S., Cappi, A., Charlot, S., Ciliegi, P., Contini, T., Cucciati, O., Foucaud, S., Franzetti, P., Gavignaud, I., Guzzo, L., Marano, B., Marinoni, C., Mazure, A., Meneux, B., Merighi, R., Paltani, S., Pollo, A., Pozzetti, L., Radovich, M., Zucca, E., Bondi, M., Bongiorno, A., Busarello, G., de La Torre, S., Gregorini, L., Lamareille, F., Mathez, G., Merluzzi, P., Ripepi, V., Rizzo, D., and Vergani, D.: 2006, *Astronomy and Astrophysics* **457**, 841

Ilbert, O., Capak, P., Salvato, M., Aussel, H., McCracken, H. J., Sanders, D. B., Scoville, N., Kartaltepe, J., Arnouts, S., Le Floc'h, E., Mobasher, B., Taniguchi, Y., Lamareille, F., Leauthaud, A., Sasaki, S., Thompson, D., Zamojski, M., Zamorani, G., Bardelli, S., Bolzonella, M., Bongiorno, A., Brusa, M., Caputi, K. I., Carollo, C. M., Contini, T., Cook, R., Coppa, G., Cucciati, O., de la Torre, S., de Ravel, L., Franzetti, P., Garilli, B., Hasinger, G., Iovino, A., Kampczyk, P., Kneib, J.-P., Knobel, C., Kovac, K., Le Borgne, J. F., Le Brun, V., Fèvre, O. L., Lilly, S., Looper, D., Maier, C., Mainieri, V., Mellier, Y., Mignoli, M., Murayama, T., Pellò, R., Peng, Y., Pérez-Montero, E., Renzini, A., Ricciardelli, E., Schiminovich, D., Scodeggio, M., Shioya, Y., Silverman, J., Surace, J., Tanaka, M., Tasca, L., Tresse, L., Vergani, D., and Zucca, E.: 2009, *ApJ* **690**, 1236

Ilbert, O., McCracken, H. J., Le Fèvre, O., Capak, P., Dunlop, J., Karim, A., Renzini, M. A., Caputi, K., Boissier, S., Arnouts, S., Aussel, H., Comparat, J., Guo, Q., Hudelot, P., Kartaltepe, J., Kneib, J. P., Krogager, J. K., Le Floc'h, E., Lilly, S., Mellier, Y., Milvang-Jensen, B., Moutard, T., Onodera, M., Richard, J., Salvato, M., Sanders, D. B., Scoville, N., Silverman, J. D., Taniguchi, Y., Tasca, L., Thomas, R., Toft, S., Tresse, L., Vergani, D., Wolk, M., and Zirm, A.: 2013, *Astronomy and Astrophysics* **556**, A55

Jaffé, Y. L., Aragón-Salamanca, A., Kuntschner, H., Bamford, S., Hoyos, C., De Lucia, G., Halliday, C., Milvang-Jensen, B., Poggianti, B., Rudnick, G., Saglia, R. P., Sanchez-Blazquez, P., and Zaritsky, D.: 2011, *MNRAS* **417**, 1996

Jauzac, M., Jullo, E., Kneib, J.-P., Ebeling, H., Leauthaud, A., Ma, C.-J., Limousin, M., Massey, R., and Richard, J.: 2012, *MNRAS* **426**, 3369

Kaastra, J. S., Lieu, R., Tamura, T., Paerels, F. B. S., and den Herder, J. W.: 2003, *Astronomy and Astrophysics* **397**, 445

Kacprzak, G. G., Yuan, T., Nanayakkara, T., Kobayashi, C., Tran, K.-V. H., Kewley, L. J., Glazebrook, K., Spitler, L., Taylor, P., Cowley, M., Labbe, I., Straatman, C., and Tomczak, A.: 2015, *ApJl* **802**, L26

Karim, A., Schinnerer, E., Martínez-Sansigre, A., Sargent, M. T., van der Wel, A., Rix, H.-W., Ilbert, O., Smolčić, V., Carilli, C., Pannella, M., Koekemoer, A. M., Bell, E. F., and Salvato, M.: 2011, *ApJ* **730**, 61

Kartaltepe, J. S., Ebeling, H., Ma, C. J., and Donovan, D.: 2008, *MNRAS* **389**, 1240

Kauffmann, G., White, S. D. M., Heckman, T. M., Ménard, B., Brinchmann, J., Charlot, S., Tremonti, C., and Brinkmann, J.: 2004, *MNRAS* **353**, 713

Keeton, C. R.: 2001, *ArXiv Astrophysics e-prints*

Kennicutt, Jr., R. C.: 1998, *Annual Reviews of Astronomy and Astrophysics* **36**, 189

Kewley, L. J. and Dopita, M. A.: 2002, *ApJl Supp.* **142**, 35

Kewley, L. J. and Ellison, S. L.: 2008, *ApJ* **681**, 1183

Kewley, L. J., Geller, M. J., and Barton, E. J.: 2006, *The Astronomical Journal* **131**, 2004

Kewley, L. J., Geller, M. J., and Jansen, R. A.: 2004, *The Astronomical Journal* **127**, 2002

Kewley, L. J., Yuan, T., Nanayakkara, T., Kacprzak, G. G., Tran, K.-V. H., Glazebrook, K., Spitler, L., Cowley, M., Dopita, M., Straatman, C., Labbe, I., and Tomczak, A.: 2015, *ArXiv e-prints*

Klar, J. S. and Mücket, J. P.: 2012, *MNRAS* **423**, 304

Knobel, C., Lilly, S. J., Iovino, A., Kovač, K., Bschorr, T. J., Presotto, V., Oesch, P. A., Kampczyk, P., Carollo, C. M., Contini, T., Kneib, J.-P., Le Fevre, O., Mainieri, V., Renzini, A., Scodeggio, M., Zamorani, G., Bardelli, S., Bolzonella, M., Bongiorno, A., Caputi, K., Cucciati, O., de la Torre, S., de Ravel, L., Franzetti, P., Garilli, B., Lamareille, F., Le Borgne, J.-F., Le Brun, V., Maier, C., Mignoli, M., Pello, R., Peng, Y., Perez Montero, E., Silverman, J., Tanaka, M., Tasca, L., Tresse, L., Vergani, D., Zucca, E., Barnes, L., Bordoloi, R., Cappi, A., Cimatti, A., Coppa, G., Koekemoer, A. M., López-Sanjuan, C., McCracken, H. J., Moresco, M., Nair, P., Pozzetti, L., and Welikala, N.: 2012, *ApJ* **753**, 121

Knobel, C., Lilly, S. J., Iovino, A., Porciani, C., Kovač, K., Cucciati, O., Finoguenov, A., Kitzbichler, M. G., Carollo, C. M., Contini, T., Kneib, J.-P., Le Fèvre, O., Mainieri, V., Renzini, A., Scodeggio, M., Zamorani, G., Bardelli, S., Bolzonella, M., Bongiorno, A., Caputi, K., Coppa, G., de la Torre, S., de Ravel, L., Franzetti, P., Garilli, B., Kampczyk, P., Lamareille, F., Le Borgne, J.-F., Le Brun, V., Maier, C., Mignoli, M., Pello, R., Peng, Y., Perez Montero, E., Ricciardelli, E., Silverman, J. D., Tanaka, M., Tasca, L., Tresse, L., Vergani, D., Zucca, E., Abbas, U., Bottini, D., Cappi, A., Cassata, P., Cimatti, A., Fumana, M., Guzzo, L., Koekemoer, A. M., Leauthaud, A., Maccagni, D., Marinoni, C., McCracken, H. J., Memeo, P., Meneux, B., Oesch, P., Pozzetti, L., and Scaramella, R.:

2009, *ApJ* **697**, 1842

Kobulnicky, H. A. and Kewley, L. J.: 2004, *ApJ* **617**, 240

Kocevski, D. D., Lubin, L. M., Lemaux, B. C., Gal, R. R., Fassnacht, C. D., Lin, R., and Squires, G. K.: 2009, *ApJ* **700**, 901

Kodama, T., Smail, I., Nakata, F., Okamura, S., and Bower, R. G.: 2001, *ApJl* **562**, L9

Kodama, T., Tanaka, M., Tamura, T., Yahagi, H., Nagashima, M., Tanaka, I., Arimoto, N., Futamase, T., Iye, M., Karasawa, Y., Kashikawa, N., Kawasaki, W., Kitayama, T., Matsuhara, H., Nakata, F., Ohashi, T., Ohta, K., Okamoto, T., Okamura, S., Shimasaku, K., Suto, Y., Tamura, N., Umetsu, K., and Yamada, T.: 2005, *PASJ* **57**, 309

Koester, B. P., McKay, T. A., Annis, J., Wechsler, R. H., Evrard, A., Bleem, L., Becker, M., Johnston, D., Sheldon, E., Nichol, R., Miller, C., Scranton, R., Bahcall, N., Barentine, J., Brewington, H., Brinkmann, J., Harvanek, M., Kleinman, S., Krzesinski, J., Long, D., Nitta, A., Schneider, D. P., Sneddin, S., Voges, W., and York, D.: 2007, *ApJ* **660**, 239

Kovač, K., Lilly, S. J., Cucciati, O., Porciani, C., Iovino, A., Zamorani, G., Oesch, P., Bolzonella, M., Knobel, C., Finoguenov, A., Peng, Y., Carollo, C. M., Pozzetti, L., Caputi, K., Silverman, J. D., Tasca, L. A. M., Scodeggio, M., Vergani, D., Scoville, N. Z., Capak, P., Contini, T., Kneib, J.-P., Le Fèvre, O., Mainieri, V., Renzini, A., Bardelli, S., Bongiorno, A., Coppa, G., de la Torre, S., de Ravel, L., Franzetti, P., Garilli, B., Guzzo, L., Kampczyk, P., Lamareille, F., Le Borgne, J.-F., Le Brun, V., Maier, C., Mignoli, M., Pello, R., Perez Montero, E., Ricciardelli, E., Tanaka, M., Tresse, L., Zucca, E., Abbas, U., Bottini, D., Cappi, A., Cassata, P., Cimatti, A., Fumana, M., Koekemoer, A. M., Maccagni, D., Marinoni, C., McCracken, H. J., Memeo, P., Meneux, B., and Scaramella, R.: 2010, *ApJ* **708**, 505

Koyama, Y., Kodama, T., Nakata, F., Shimasaku, K., and Okamura, S.: 2011, *ApJ* **734**, 66

Koyama, Y., Kodama, T., Shimasaku, K., Hayashi, M., Okamura, S., Tanaka, I., and Tokoku, C.: 2010, *MNRAS* **403**, 1611

Koyama, Y., Kodama, T., Shimasaku, K., Okamura, S., Tanaka, M., Lee, H. M., Im, M., Matsuhara, H., Takagi, T., Wada, T., and Oyabu, S.: 2008, *MNRAS* **391**, 1758

Koyama, Y., Kodama, T., Tadaki, K.-i., Hayashi, M., Tanaka, I., and Shimakawa, R.: 2014, *ApJ* **789**, 18

Koyama, Y., Kodama, T., Tadaki, K.-i., Hayashi, M., Tanaka, M., Smail, I., Tanaka, I., and Kurk, J.: 2013a, *MNRAS* **428**, 1551

Koyama, Y., Smail, I., Kurk, J., Geach, J. E., Sobral, D., Kodama, T., Nakata, F., Swinbank, A. M., Best, P. N., Hayashi, M., and Tadaki, K.-i.: 2013b, *MNRAS* **434**, 423

Kriek, M., van der Wel, A., van Dokkum, P. G., Franx, M., and Illingworth, G. D.: 2008, *ApJ* **682**, 896

Kulas, K. R., McLean, I. S., Shapley, A. E., Steidel, C. C., Konidaris, N. P., Matthews, K., Mace, G. N., Rudie, G. C., Trainor, R. F., and Reddy, N. A.: 2013, *ApJ* **774**, 130

Lamareille, F., Brinchmann, J., Contini, T., Walcher, C. J., Charlot, S., Pérez-Montero, E., Zamorani, G., Pozzetti, L., Bolzonella, M., Garilli, B., Paltani, S., Bongiorno, A., Le Fèvre, O., Bottini, D., Le Brun, V., Maccagni, D., Scaramella, R., Scodeggio, M., Tresse, L., Vettolani, G., Zanichelli, A., Adami, C., Arnouts, S., Bardelli, S., Cappi, A., Ciliegi, P., Foucaud, S., Franzetti, P., Gavignaud, I., Guzzo, L., Ilbert, O., Iovino, A., McCracken, H. J., Marano, B., Marinoni, C., Mazure, A., Meneux, B., Merighi, R., Pellò, R., Pollo, A., Radovich, M., Vergani, D., Zucca, E., Romano, A., Grado, A., and Limatola, L.: 2009, *Astronomy and Astrophysics* **495**, 53

Lamareille, F., Mouhcine, M., Contini, T., Lewis, I., and Maddox, S.: 2004, *MNRAS* **350**, 396

Lara-López, M. A., Hopkins, A. M., López-Sánchez, A. R., Brough, S., Gunawardhana, M. L. P., Colless, M., Robotham, A. S. G., Bauer, A. E., Bland-Hawthorn, J., Cluver, M., Driver, S., Foster, C., Kelvin, L. S., Liske, J., Loveday, J., Owers, M. S., Ponman, T. J., Sharp, R. G., Steele, O., Taylor, E. N., and Thomas, D.: 2013a, *MNRAS* **434**, 451

Lara-López, M. A., Hopkins, A. M., Robotham, A., Owers, M. S., Colless, M., Brough, S., Norberg, P., Steele, O., Taylor, E. N., and Thomas, D.: 2013b, *Astronomische Nachrichten* **334**, 466

Larson, R. B., Tinsley, B. M., and Caldwell, C. N.: 1980, *ApJ* **237**, 692

Lavery, R. J. and Henry, J. P.: 1988, *ApJ* **330**, 596

Le Floc'h, E., Aussel, H., Ilbert, O., Riguccini, L., Frayer, D. T., Salvato, M., Arnouts, S., Surace, J., Feruglio, C., Rodighiero, G., Capak, P., Kartaltepe, J., Heinis, S., Sheth, K., Yan, L., McCracken, H. J., Thompson, D., Sanders, D., Scoville, N., and Koekemoer, A.: 2009, *ApJ* **703**, 222

Leauthaud, A., Massey, R., Kneib, J.-P., Rhodes, J., Johnston, D. E., Capak, P., Heymans, C., Ellis, R. S., Koekemoer, A. M., Le Fèvre, O., Mellier, Y., Réfrégier, A., Robin, A. C., Scoville, N., Tasca, L., Taylor, J. E., and Van Waerbeke, L.: 2007, *ApJl Supp.* **172**, 219

Lilly, S. J., Carollo, C. M., Pipino, A., Renzini, A., and Peng, Y.: 2013, *ApJ* **772**, 119

Lilly, S. J., Le Fèvre, O., Renzini, A., Zamorani, G., Scodeggio, M., Contini, T., Carollo, C. M., Hasinger, G., Kneib, J.-P., Iovino, A., Le Brun, V., Maier, C., Mainieri, V., Mignoli, M., Silverman, J., Tasca, L. A. M., Bolzonella, M., Bongiorno, A., Bottini, D., Capak, P., Caputi, K., Cimatti, A., Cucciati, O., Daddi, E., Feldmann, R., Franzetti, P., Garilli, B., Guzzo, L., Ilbert, O., Kampczyk, P., Kovac, K., Lamareille, F., Leauthaud, A., Borgne, J.-F. L., McCracken, H. J., Marinoni, C., Pello, R., Ricciardelli, E., Scarlata, C., Vergani, D., Sanders, D. B., Schinnerer, E., Scoville, N., Taniguchi, Y., Arnouts, S., Aussel, H., Bardelli, S., Brusa, M., Cappi, A., Ciliegi, P., Finoguenov, A., Foucaud, S., Franceschini, A., Halliday, C., Impey, C., Knobel, C., Koekemoer, A., Kurk, J., Maccagni, D., Maddox, S., Marano, B., Marconi, G., Meneux, B., Mobasher, B., Moreau, C., Peacock, J. A., Porciani, C., Pozzetti, L., Scaramella, R., Schiminovich, D., Shopbell, P., Smail, I., Thompson, D., Tresse, L., Vettolani, G., Zanichelli, A., and Zucca, E.: 2007, *ApJl Supp.* **172**, 70

Lin, L., Jian, H.-Y., Foucaud, S., Norberg, P., Bower, R. G., Cole, S., Arnalte-Mur, P., Chen, C.-W., Coupon, J., Hsieh, B.-C., Heinis, S., Phleps, S., Chen, W.-P., Lee, C.-H., Burgett, W., Chambers, K. C., Denneau, L., Draper, P., Flewelling, H., Hodapp, K. W., Huber, M. E., Kaiser, N., Kudritzki, R.-P., Magnier, E. A., Metcalfe, N., Price, P. A., Tonry, J. L., Wainscoat, R. J., and Waters, C.: 2014, *ApJ* **782**, 33

Lubin, L. M., Gal, R. R., Lemaux, B. C., Kocevski, D. D., and Squires, G. K.: 2009, *The Astronomical Journal* **137**, 4867

Ly, C., Malkan, M. A., Kashikawa, N., Ota, K., Shimasaku, K., Iye, M., and Currie, T.: 2012, *ApJl* **747**, L16

Ly, C., Malkan, M. A., Nagao, T., Kashikawa, N., Shimasaku, K., and Hayashi, M.: 2014, *ApJ* **780**, 122

Madau, P. and Dickinson, M.: 2014, *Annual Reviews of Astronomy and Astrophysics* **52**, 415

Mahajan, S., Raychaudhury, S., and Pimbblet, K. A.: 2012, *MNRAS* **427**, 1252

Maier, C., Lilly, S. J., Ziegler, B. L., Contini, T., Pérez Montero, E., Peng, Y., and Balestra, I.: 2014, *ApJ* **792**, 3

Maier, C., Ziegler, B. L., Lilly, S. J., Contini, T., Pérez-Montero, E., Lamareille, F., Bolzonella, M., and Le Floc'h, E.: 2015, *Astronomy and Astrophysics* **577**, A14

Maiolino, R., Nagao, T., Grazian, A., Cocchia, F., Marconi, A., Mannucci, F., Cimatti, A., Pipino, A., Ballero, S., Calura, F., Chiappini, C., Fontana, A., Granato, G. L., Matteucci, F., Pastorini, G., Pentericci, L., Risaliti, G., Salvati, M., and Silva, L.: 2008, *Astronomy and Astrophysics* **488**, 463

Mamon, G. A., Sanchis, T., Salvador-Solé, E., and Solanes, J. M.: 2004, *Astronomy and Astrophysics* **414**, 445

Mannucci, F., Cresci, G., Maiolino, R., Marconi, A., and Gnerucci, A.: 2010, *MNRAS* **408**, 2115

Marriage, T. A., Acquaviva, V., Ade, P. A. R., Aguirre, P., Amiri, M., Appel, J. W., Barrientos, L. F., Battistelli, E. S., Bond, J. R., Brown, B., Burger, B., Chervenak, J., Das, S., Devlin, M. J., Dicker, S. R., Bertrand Doriese, W., Dunkley, J., Dünner, R., Essinger-Hileman, T., Fisher, R. P., Fowler, J. W., Hajian, A., Halpern, M., Hasselfield, M., Hernández-Monteagudo, C., Hilton, G. C., Hilton, M., Hincks, A. D., Hlozek, R., Huffenberger, K. M., Handel Hughes, D., Hughes, J. P., Infante, L., Irwin, K. D., Baptiste Juin, J., Kaul, M., Klein, J., Kosowsky, A., Lau, J. M., Limon, M., Lin, Y.-T., Lupton, R. H., Marsden, D., Martocci, K., Mauskopf, P., Menanteau, F., Moodley, K., Moseley, H., Netterfield, C. B., Niemack, M. D., Nolta, M. R., Page, L. A., Parker, L., Partridge, B., Quintana, H., Reese, E. D., Reid, B., Sehgal, N., Sherwin, B. D., Sievers, J., Spergel, D. N., Staggs, S. T., Swetz, D. S., Switzer, E. R., Thornton, R., Trac, H., Tucker, C., Warne, R., Wilson, G., Wollack, E., and Zhao, Y.: 2011, *ApJ* **737**, 61

Martin, D. C., Chang, D., Matuszewski, M., Morrissey, P., Rahman, S., Moore, A., and Steidel, C. C.: 2014a, *ApJ* **786**, 106

Martin, D. C., Chang, D., Matuszewski, M., Morrissey, P., Rahman, S., Moore, A., Steidel, C. C., and Matsuda, Y.: 2014b, *ApJ* **786**, 107

Martin, D. C., Wyder, T. K., Schiminovich, D., Barlow, T. A., Forster, K., Friedman, P. G., Morrissey, P., Neff, S. G., Seibert, M., Small, T., Welsh, B. Y., Bianchi, L., Donas, J., Heckman, T. M., Lee, Y.-W., Madore, B. F., Milliard, B., Rich, R. M., Szalay, A. S., and

Yi, S. K.: 2007, *ApJl Supp.* **173**, 342

Maseda, M. V., van der Wel, A., da Cunha, E., Rix, H.-W., Pacifici, C., Momcheva, I., Brammer, G. B., Franx, M., van Dokkum, P., Bell, E. F., Fumagalli, M., Grogin, N. A., Kocevski, D. D., Koekemoer, A. M., Lundgren, B. F., Marchesini, D., Nelson, E. J., Patel, S. G., Skelton, R. E., Straughn, A. N., Trump, J. R., Weiner, B. J., Whitaker, K. E., and Wuyts, S.: 2013, *ApJl* **778**, L22

Massey, R., Rhodes, J., Ellis, R., Scoville, N., Leauthaud, A., Finoguenov, A., Capak, P., Bacon, D., Aussel, H., Kneib, J.-P., Koekemoer, A., McCracken, H., Mobasher, B., Pires, S., Refregier, A., Sasaki, S., Starck, J.-L., Taniguchi, Y., Taylor, A., and Taylor, J.: 2007, *Nature* **445**, 286

Masters, D. and Capak, P.: 2011, *Publications of the Astronomical Society of the Pacific* **123**, 638

Masters, D., McCarthy, P., Siana, B., Malkan, M., Mobasher, B., Atek, H., Henry, A., Martin, C. L., Rafelski, M., Hathi, N. P., Scarlata, C., Ross, N. R., Bunker, A. J., Blanc, G., Bedregal, A. G., Domínguez, A., Colbert, J., Teplitz, H., and Dressler, A.: 2014, *ApJ* **785**, 153

Matthee, J., Sobral, D., Santos, S., Röttgering, H., Darvish, B., and Mobasher, B.: 2015, *MNRAS* **451**, 4919

McCracken, H. J., Milvang-Jensen, B., Dunlop, J., Franx, M., Fynbo, J. P. U., Le Fèvre, O., Holt, J., Caputi, K. I., Goranova, Y., Buitrago, F., Emerson, J. P., Freudling, W., Hudelot, P., López-Sanjuan, C., Magnard, F., Mellier, Y., Møller, P., Nilsson, K. K., Sutherland, W., Tasca, L., and Zabl, J.: 2012, *Astronomy and Astrophysics* **544**, A156

McDonald, M. and Veilleux, S.: 2009, *ApJl* **703**, L172

McDonald, M., Veilleux, S., and Mushotzky, R.: 2011, *ApJ* **731**, 33

McDonald, M., Veilleux, S., Rupke, D. S. N., and Mushotzky, R.: 2010, *ApJ* **721**, 1262

McGaugh, S. S.: 1991, *ApJ* **380**, 140

Mehrtens, N., Romer, A. K., Hilton, M., Lloyd-Davies, E. J., Miller, C. J., Stanford, S. A., Hosmer, M., Hoyle, B., Collins, C. A., Liddle, A. R., Viana, P. T. P., Nichol, R. C., Stott, J. P., Dubois, E. N., Kay, S. T., Sahlén, M., Young, O., Short, C. J., Christodoulou, L., Watson, W. A., Davidson, M., Harrison, C. D., Baruah, L., Smith, M., Burke, C., Mayers, J. A., Deadman, P.-J., Rooney, P. J., Edmondson, E. M., West, M., Campbell, H. C., Edge, A. C., Mann, R. G., Sabirli, K., Wake, D., Benoist, C., da Costa, L., Maia, M. A. G., and Ogando, R.: 2012, *MNRAS* **423**, 1024

Mei, S., Holden, B. P., Blakeslee, J. P., Ford, H. C., Franx, M., Homeier, N. L., Illingworth, G. D., Jee, M. J., Overzier, R., Postman, M., Rosati, P., Van der Wel, A., and Bartlett, J. G.: 2009, *ApJ* **690**, 42

Merritt, D.: 1984, *ApJ* **276**, 26

Michel-Dansac, L., Lambas, D. G., Alonso, M. S., and Tissera, P.: 2008, *MNRAS* **386**, L82

Mihos, J. C. and Hernquist, L.: 1996, *ApJ* **464**, 641

Mihos, J. C., Richstone, D. O., and Bothun, G. D.: 1992, *ApJ* **400**, 153

Miller, C. J., Nichol, R. C., Reichart, D., Wechsler, R. H., Evrard, A. E., Annis, J., McKay, T. A., Bahcall, N. A., Bernardi, M., Boehringer, H., Connolly, A. J., Goto, T., Kniazev, A., Lamb, D., Postman, M., Schneider, D. P., Sheth, R. K., and Voges, W.: 2005, *The Astronomical Journal* **130**, 968

Miyazaki, S., Hamana, T., Ellis, R. S., Kashikawa, N., Massey, R. J., Taylor, J., and Refregier, A.: 2007, *ApJ* **669**, 714

Mobasher, B., Capak, P., Scoville, N. Z., Dahlen, T., Salvato, M., Aussel, H., Thompson, D. J., Feldmann, R., Tasca, L., Le Fevre, O., Lilly, S., Carollo, C. M., Kartaltepe, J. S., McCracken, H., Mould, J., Renzini, A., Sanders, D. B., Shopbell, P. L., Taniguchi, Y., Ajiki, M., Shioya, Y., Contini, T., Giavalisco, M., Ilbert, O., Iovino, A., Le Brun, V., Mainieri, V., Mignoli, M., and Scodeggio, M.: 2007, *ApJl Supp.* **172**, 117

Mocz, P., Green, A., Malacari, M., and Glazebrook, K.: 2012, *MNRAS* **425**, 296

Moore, B., Katz, N., Lake, G., Dressler, A., and Oemler, A.: 1996, *Nature* **379**, 613

Moore, B., Lake, G., and Katz, N.: 1998, *ApJ* **495**, 139

Moresco, M., Pozzetti, L., Cimatti, A., Zamorani, G., Mignoli, M., di Cesare, S., Bolzonella, M., Zucca, E., Lilly, S., Kovač, K., Scodeggio, M., Cassata, P., Tasca, L., Vergani, D., Halliday, C., Carollo, M., Contini, T., Kneib, J.-P., Le Févre, O., Mainieri, V., Renzini, A., Bardelli, S., Bongiorno, A., Caputi, K., Coppa, G., Cucciati, O., de la Torre, S., de Ravel, L., Franzetti, P., Garilli, B., Iovino, A., Kampczyk, P., Knobel, C., Lamareille, F., Le Borgne, J.-F., Le Brun, V., Maier, C., Pellò, R., Peng, Y., Perez Montero, E., Ricciardelli, E., Silverman, J. D., Tanaka, M., Tresse, L., Abbas, U., Bottini, D., Cappi, A., Guzzo, L., Koekemoer, A. M., Leauthaud, A., Maccagni, D., Marinoni, C., McCracken, H. J., Memeo, P., Meneux, B., Nair, P., Oesch, P., Porciani, C., Scaramella, R., Scarlata, C., and Scoville, N.: 2010, *Astronomy and Astrophysics* **524**, A67

Mortlock, A., Conselice, C. J., Hartley, W. G., Duncan, K., Lani, C., Ownsworth, J. R., Almaini, O., Wel, A. v. d., Huang, K.-H., Ashby, M. L. N., Willner, S. P., Fontana, A., Dekel, A., Koekemoer, A. M., Ferguson, H. C., Faber, S. M., Grogin, N. A., and Kocevski, D. D.: 2015, *MNRAS* **447**, 2

Moss, C.: 2006, *MNRAS* **373**, 167

Moster, B. P., Somerville, R. S., Newman, J. A., and Rix, H.-W.: 2011, *ApJ* **731**, 113

Mouhcine, M., Baldry, I. K., and Bamford, S. P.: 2007, *MNRAS* **382**, 801

Moustakas, J., Coil, A. L., Aird, J., Blanton, M. R., Cool, R. J., Eisenstein, D. J., Mendez, A. J., Wong, K. C., Zhu, G., and Arnouts, S.: 2013, *ApJ* **767**, 50

Moustakas, J., Zaritsky, D., Brown, M., Cool, R., Dey, A., Eisenstein, D. J., Gonzalez, A. H., Jannuzi, B., Jones, C., Kochanek, C. S., Murray, S. S., and Wild, V.: 2011, *ArXiv e-prints*

Muzzin, A., Marchesini, D., Stefanon, M., Franx, M., McCracken, H. J., Milvang-Jensen, B., Dunlop, J. S., Fynbo, J. P. U., Brammer, G., Labbé, I., and van Dokkum, P. G.: 2013a, *ApJ* **777**, 18

Muzzin, A., Wilson, G., Demarco, R., Lidman, C., Nantais, J., Hoekstra, H., Yee, H. K. C., and Rettura, A.: 2013b, *ApJ* **767**, 39

Muzzin, A., Wilson, G., Yee, H. K. C., Gilbank, D., Hoekstra, H., Demarco, R., Balogh, M., van Dokkum, P., Franx, M., Ellingson, E., Hicks, A., Nantais, J., Noble, A., Lacy, M., Lidman, C., Rettura, A., Surace, J., and Webb, T.: 2012, *ApJ* **746**, 188

Nakajima, K. and Ouchi, M.: 2014, *MNRAS* **442**, 900

Nakajima, K., Ouchi, M., Shimasaku, K., Hashimoto, T., Ono, Y., and Lee, J. C.: 2013, *ApJ* **769**, 3

Nakamura, O., Aragón-Salamanca, A., Milvang-Jensen, B., Arimoto, N., Ikuta, C., and Bamford, S. P.: 2006, *MNRAS* **366**, 144

Newman, J. A., Cooper, M. C., Davis, M., Faber, S. M., Coil, A. L., Guhathakurta, P., Koo, D. C., Phillips, A. C., Conroy, C., Dutton, A. A., Finkbeiner, D. P., Gerke, B. F., Rosario, D. J., Weiner, B. J., Willmer, C. N. A., Yan, R., Harker, J. J., Kassin, S. A., Konidaris, N. P., Lai, K., Madgwick, D. S., Noeske, K. G., Wirth, G. D., Connolly, A. J., Kaiser, N., Kirby, E. N., Lemaux, B. C., Lin, L., Lotz, J. M., Luppino, G. A., Marinoni, C., Matthews, D. J., Metevier, A., and Schiavon, R. P.: 2013, *ApJl Supp.* **208**, 5

Nicastro, F., Krongold, Y., Fields, D., Conciatore, M. L., Zappacosta, L., Elvis, M., Mathur, S., and Papadakis, I.: 2010, *ApJ* **715**, 854

Nicastro, F., Mathur, S., Elvis, M., Drake, J., Fang, T., Fruscione, A., Krongold, Y., Marshall, H., Williams, R., and Zezas, A.: 2005a, *Nature* **433**, 495

Nicastro, F., Mathur, S., Elvis, M., Drake, J., Fiore, F., Fang, T., Fruscione, A., Krongold, Y., Marshall, H., and Williams, R.: 2005b, *ApJ* **629**, 700

Nicol, M.-H., Meisenheimer, K., Wolf, C., and Tapken, C.: 2011, *ApJ* **727**, 51

Noeske, K. G., Faber, S. M., Weiner, B. J., Koo, D. C., Primack, J. R., Dekel, A., Papovich, C., Conselice, C. J., Le Floc'h, E., Rieke, G. H., Coil, A. L., Lotz, J. M., Somerville, R. S., and Bundy, K.: 2007a, *ApJl* **660**, L47

Noeske, K. G., Weiner, B. J., Faber, S. M., Papovich, C., Koo, D. C., Somerville, R. S., Bundy, K., Conselice, C. J., Newman, J. A., Schiminovich, D., Le Floc'h, E., Coil, A. L., Rieke, G. H., Lotz, J. M., Primack, J. R., Barmby, P., Cooper, M. C., Davis, M., Ellis, R. S., Fazio, G. G., Guhathakurta, P., Huang, J., Kassin, S. A., Martin, D. C., Phillips, A. C., Rich, R. M., Small, T. A., Willmer, C. N. A., and Wilson, G.: 2007b, *ApJl* **660**, L43

Oppenheimer, B. D., Davé, R., Katz, N., Kollmeier, J. A., and Weinberg, D. H.: 2012, *MNRAS* **420**, 829

Osterbrock, D. E.: 1989, *Astrophysics of gaseous nebulae and active galactic nuclei*

Papovich, C., Momcheva, I., Willmer, C. N. A., Finkelstein, K. D., Finkelstein, S. L., Tran, K.-V., Brodwin, M., Dunlop, J. S., Farrah, D., Khan, S. A., Lotz, J., McCarthy, P., McLure, R. J., Rieke, M., Rudnick, G., Sivanandam, S., Pacaud, F., and Pierre, M.: 2010, *ApJ* **716**, 1503

Park, C., Choi, Y.-Y., Vogeley, M. S., Gott, III, J. R., Blanton, M. R., and SDSS Collaboration: 2007, *ApJ* **658**, 898

Pasquali, A., Gallazzi, A., and van den Bosch, F. C.: 2012, *MNRAS* **425**, 273

Patel, S. G., Holden, B. P., Kelson, D. D., Illingworth, G. D., and Franx, M.: 2009, *ApJl* **705**, L67

Peng, Y., Maiolino, R., and Cochrane, R.: 2015, *Nature* **521**, 192

Peng, Y.-j., Lilly, S. J., Kovač, K., Bolzonella, M., Pozzetti, L., Renzini, A., Zamorani, G., Ilbert, O., Knobel, C., Iovino, A., Maier, C., Cucciati, O., Tasca, L., Carollo, C. M., Silverman, J., Kampczyk, P., de Ravel, L., Sanders, D., Scoville, N., Contini, T., Mainieri, V., Scodeggio, M., Kneib, J.-P., Le Fèvre, O., Bardelli, S., Bongiorno, A., Caputi, K., Coppa, G., de la Torre, S., Franzetti, P., Garilli, B., Lamareille, F., Le Borgne, J.-F., Le Brun, V., Mignoli, M., Perez Montero, E., Pello, R., Ricciardelli, E., Tanaka, M., Tresse, L., Vergani, D., Welikala, N., Zucca, E., Oesch, P., Abbas, U., Barnes, L., Bordoloi, R., Bottini, D., Cappi, A., Cassata, P., Cimatti, A., Fumana, M., Hasinger, G., Koekemoer, A., Leauthaud, A., Maccagni, D., Marinoni, C., McCracken, H., Memeo, P., Meneux, B., Nair, P., Porciani, C., Presotto, V., and Scaramella, R.: 2010, *ApJ* **721**, 193

Peng, Y.-j., Lilly, S. J., Renzini, A., and Carollo, M.: 2012, *ApJ* **757**, 4

Peng, Y.-j. and Maiolino, R.: 2014, *MNRAS* **438**, 262

Perez, J., Michel-Dansac, L., and Tissera, P. B.: 2011, *MNRAS* **417**, 580

Perez, J., Tissera, P., Padilla, N., Alonso, M. S., and Lambas, D. G.: 2009, *MNRAS* **399**, 1157

Pérez-Montero, E., Contini, T., Lamareille, F., Maier, C., Carollo, C. M., Kneib, J.-P., Le Fèvre, O., Lilly, S., Mainieri, V., Renzini, A., Scodeggio, M., Zamorani, G., Bardelli, S., Bolzonella, M., Bongiorno, A., Caputi, K., Cucciati, O., de la Torre, S., de Ravel, L., Franzetti, P., Garilli, B., Iovino, A., Kampczyk, P., Knobel, C., Kovač, K., Le Borgne, J.-F., Le Brun, V., Mignoli, M., Pellò, R., Peng, Y., Presotto, V., Ricciardelli, E., Silverman, J. D., Tanaka, M., Tasca, L. A. M., Tresse, L., Vergani, D., and Zucca, E.: 2013, *Astronomy and Astrophysics* **549**, A25

Petropoulou, V., Vílchez, J., and Iglesias-Páramo, J.: 2012, *ApJ* **749**, 133

Pettini, M., Shapley, A. E., Steidel, C. C., Cuby, J.-G., Dickinson, M., Moorwood, A. F. M., Adelberger, K. L., and Giavalisco, M.: 2001, *ApJ* **554**, 981

Pimbblet, K. A.: 2011, *MNRAS* **411**, 2637

Pimbblet, K. A., Drinkwater, M. J., and Hawkrigg, M. C.: 2004, *MNRAS* **354**, L61

Pintos-Castro, I., Sánchez-Portal, M., Cepa, J., Santos, J. S., Altieri, B., Pérez Martínez, R., Alfaro, E. J., Bongiovanni, Á., Coia, D., Conversi, L., Domínguez-Sánchez, H., Ederoclite, A., González-Serrano, J. I., Metcalfe, L., Oteo, I., Pérez García, A. M., Polednikova, J., Rawle, T. D., and Valtchanov, I.: 2013, *Astronomy and Astrophysics* **558**, A100

Pizagno, J., Prada, F., Weinberg, D. H., Rix, H.-W., Pogge, R. W., Grebel, E. K., Harbeck, D., Blanton, M., Brinkmann, J., and Gunn, J. E.: 2007, *The Astronomical Journal* **134**, 945

Planck Collaboration, Ade, P. A. R., Aghanim, N., Arnaud, M., Ashdown, M., Aumont, J., Baccigalupi, C., Balbi, A., Banday, A. J., Barreiro, R. B., and et al.: 2011, *Astronomy and Astrophysics* **536**, A8

Platen, E., van de Weygaert, R., Jones, B. J. T., Vegter, G., and Calvo, M. A. A.: 2011, *MNRAS* **416**, 2494

Poggianti, B. M., Aragón-Salamanca, A., Zaritsky, D., De Lucia, G., Milvang-Jensen, B., Desai, V., Jablonka, P., Halliday, C., Rudnick, G., Varela, J., Bamford, S., Best, P., Clowe, D., Noll, S., Saglia, R., Pelló, R., Simard, L., von der Linden, A., and White, S.: 2009, *ApJ* **693**, 112

Popesso, P., Rodighiero, G., Saintonge, A., Santini, P., Grazian, A., Lutz, D., Brusa, M., Altieri, B., Andreani, P., Aussel, H., Berta, S., Bongiovanni, A., Cava, A., Cepa, J., Cimatti, A., Daddi, E., Dominguez, H., Elbaz, D., Förster Schreiber, N., Genzel, R., Gruppioni, C., Magdis, G., Maiolino, R., Magnelli, B., Nordon, R., Pérez García, A. M., Poglitsch, A., Pozzi, F., Riguccini, L., Sanchez-Portal, M., Shao, L., Sturm, E., Tacconi, L., Valtchanov, I., Wieprecht, E., and Wetzstein, M.: 2011, *Astronomy and Astrophysics* **532**, A145

Porter, S. C. and Raychaudhury, S.: 2007, *MNRAS* **375**, 1409

Porter, S. C., Raychaudhury, S., Pimbblet, K. A., and Drinkwater, M. J.: 2008, *MNRAS* **388**, 1152

Postman, M., Franx, M., Cross, N. J. G., Holden, B., Ford, H. C., Illingworth, G. D., Goto, T., Demarco, R., Rosati, P., Blakeslee, J. P., Tran, K.-V., Benítez, N., Clampin, M., Hartig, G. F., Homeier, N., Ardila, D. R., Bartko, F., Bouwens, R. J., Bradley, L. D., Broadhurst, T. J., Brown, R. A., Burrows, C. J., Cheng, E. S., Feldman, P. D., Golimowski, D. A., Gronwall, C., Infante, L., Kimble, R. A., Krist, J. E., Lesser, M. P., Martel, A. R., Mei, S., Menanteau, F., Meurer, G. R., Miley, G. K., Motta, V., Sirianni, M., Sparks, W. B., Tran, H. D., Tsvetanov, Z. I., White, R. L., and Zheng, W.: 2005, *ApJ* **623**, 721

Pozzetti, L., Bolzonella, M., Zucca, E., Zamorani, G., Lilly, S., Renzini, A., Moresco, M., Mignoli, M., Cassata, P., Tasca, L., Lamareille, F., Maier, C., Meneux, B., Halliday, C., Oesch, P., Vergani, D., Caputi, K., Kovač, K., Cimatti, A., Cucciati, O., Iovino, A., Peng, Y., Carollo, M., Contini, T., Kneib, J.-P., Le Févre, O., Mainieri, V., Scodeggio, M., Bardelli, S., Bongiorno, A., Coppa, G., de la Torre, S., de Ravel, L., Franzetti, P., Garilli, B., Kampczyk, P., Knobel, C., Le Borgne, J.-F., Le Brun, V., Pellò, R., Perez Montero, E., Ricciardelli, E., Silverman, J. D., Tanaka, M., Tresse, L., Abbas, U., Bottini, D., Cappi, A., Guzzo, L., Koekemoer, A. M., Leauthaud, A., Maccagni, D., Marinoni, C., McCracken, H. J., Memeo, P., Porciani, C., Scaramella, R., Scarlata, C., and Scoville, N.: 2010, *Astronomy and Astrophysics* **523**, A13

Price, S. H., Kriek, M., Brammer, G. B., Conroy, C., Förster Schreiber, N. M., Franx, M., Fumagalli, M., Lundgren, B., Momcheva, I., Nelson, E. J., Skelton, R. E., van Dokkum, P. G., Whitaker, K. E., and Wuyts, S.: 2014, *ApJ* **788**, 86

Rawle, T. D., Lucey, J. R., Smith, R. J., and Head, J. T. C. G.: 2013, *MNRAS* **433**, 2667

Reddy, N. A., Kriek, M., Shapley, A. E., Freeman, W. R., Siana, B., Coil, A. L., Mobasher, B., Price, S. H., Sanders, R. L., and Shivaei, I.: 2015, *ApJ* **806**, 259

Reddy, N. A., Pettini, M., Steidel, C. C., Shapley, A. E., Erb, D. K., and Law, D. R.: 2012, *ApJ* **754**, 25

Reichardt, C. L., Stalder, B., Bleem, L. E., Montroy, T. E., Aird, K. A., Andersson, K., Armstrong, R., Ashby, M. L. N., Bautz, M., Bayliss, M., Bazin, G., Benson, B. A., Brodwin, M., Carlstrom, J. E., Chang, C. L., Cho, H. M., Clocchiatti, A., Crawford, T. M., Crites, A. T., de Haan, T., Desai, S., Dobbs, M. A., Dudley, J. P., Foley, R. J., Forman, W. R., George, E. M., Gladders, M. D., Gonzalez, A. H., Halverson, N. W., Harrington, N. L., High, F. W., Holder, G. P., Holzapfel, W. L., Hoover, S., Hrubes, J. D., Jones, C., Joy, M., Keisler, R., Knox, L., Lee, A. T., Leitch, E. M., Liu, J., Lueker, M., Luong-Van, D., Mantz, A., Marrone, D. P., McDonald, M., McMahon, J. J., Mehl, J., Meyer, S. S., Mocanu, L., Mohr, J. J., Murray, S. S., Natoli, T., Padin, S., Plagge, T., Pryke, C., Rest, A., Ruel, J., Ruhl, J. E., Saliwanchik, B. R., Saro, A., Sayre, J. T., Schaffer, K. K., Shaw, L., Shirokoff, E., Song, J., Spieler, H. G., Staniszewski, Z., Stark, A. A., Story, K., Stubbs, C. W., Šuhada, R., van Engelen, A., Vanderlinde, K., Vieira, J. D., Vikhlinin, A., Williamson, R., Zahn, O., and Zenteno, A.: 2013, *ApJ* **763**, 127

Rhoads, J. E., Malhotra, S., Richardson, M. L. A., Finkelstein, S. L., Fynbo, J. P. U., McLinden, E. M., and Tilvi, V. S.: 2014, *ApJ* **780**, 20

Rieke, G. H., Alonso-Herrero, A., Weiner, B. J., Pérez-González, P. G., Blaylock, M., Donley, J. L., and Marcillac, D.: 2009, *ApJ* **692**, 556

Rix, H.-W., Guhathakurta, P., Colless, M., and Ing, K.: 1997, *MNRAS* **285**, 779

Rupke, D. S. N., Kewley, L. J., and Chien, L.-H.: 2010, *ApJ* **723**, 1255

Sakai, S., Mould, J. R., Hughes, S. M. G., Huchra, J. P., Macri, L. M., Kennicutt, Jr., R. C., Gibson, B. K., Ferrarese, L., Freedman, W. L., Han, M., Ford, H. C., Graham, J. A., Illingworth, G. D., Kelson, D. D., Madore, B. F., Sebo, K., Silbermann, N. A., and Stetson, P. B.: 2000, *ApJ* **529**, 698

Salim, S., Rich, R. M., Charlot, S., Brinchmann, J., Johnson, B. D., Schiminovich, D., Seibert, M., Mallery, R., Heckman, T. M., Forster, K., Friedman, P. G., Martin, D. C., Morrissey, P., Neff, S. G., Small, T., Wyder, T. K., Bianchi, L., Donas, J., Lee, Y.-W., Madore, B. F., Milliard, B., Szalay, A. S., Welsh, B. Y., and Yi, S. K.: 2007, *ApJl Supp.* **173**, 267

Salmon, B., Papovich, C., Finkelstein, S. L., Tilvi, V., Finlator, K., Behroozi, P., Dahlen, T., Davé, R., Dekel, A., Dickinson, M., Ferguson, H. C., Giavalisco, M., Long, J., Lu, Y., Mobasher, B., Reddy, N., Somerville, R. S., and Wechsler, R. H.: 2015, *ApJ* **799**, 183

Sánchez, S. F., Rosales-Ortega, F. F., Jungwiert, B., Iglesias-Páramo, J., Vílchez, J. M., Marino, R. A., Walcher, C. J., Husemann, B., Mast, D., Monreal-Ibero, A., Cid Fernandes, R., Pérez, E., González Delgado, R., García-Benito, R., Galbany, L., van de Ven, G., Jahnke, K., Flores, H., Bland-Hawthorn, J., López-Sánchez, A. R., Stanishev, V., Miralles-Caballero, D., Díaz, A. I., Sánchez-Blazquez, P., Mollá, M., Gallazzi, A., Papaderos, P., Gomes, J. M., Gruel, N., Pérez, I., Ruiz-Lara, T., Florido, E., de Lorenzo-

Cáceres, A., Mendez-Abreu, J., Kehrig, C., Roth, M. M., Ziegler, B., Alves, J., Wisotzki, L., Kupko, D., Quirrenbach, A., Bomans, D., and Califa Collaboration: 2013, *Astronomy and Astrophysics* **554**, A58

Sanders, D. B., Salvato, M., Aussel, H., Ilbert, O., Scoville, N., Surace, J. A., Frayer, D. T., Sheth, K., Helou, G., Brooke, T., Bhattacharya, B., Yan, L., Kartaltepe, J. S., Barnes, J. E., Blain, A. W., Calzetti, D., Capak, P., Carilli, C., Carollo, C. M., Comastri, A., Daddi, E., Ellis, R. S., Elvis, M., Fall, S. M., Franceschini, A., Giavalisco, M., Hasinger, G., Impey, C., Koekemoer, A., Le Fèvre, O., Lilly, S., Liu, M. C., McCracken, H. J., Mobasher, B., Renzini, A., Rich, M., Schinnerer, E., Shopbell, P. L., Taniguchi, Y., Thompson, D. J., Urry, C. M., and Williams, J. P.: 2007, *ApJl Supp.* **172**, 86

Sanders, R. L., Shapley, A. E., Kriek, M., Reddy, N. A., Freeman, W. R., Coil, A. L., Siana, B., Mobasher, B., Shivaei, I., Price, S. H., and de Groot, L.: 2015, *ApJ* **799**, 138

Santos, J. S., Altieri, B., Tanaka, M., Valtchanov, I., Saintonge, A., Dickinson, M., Foucaud, S., Kodama, T., Rawle, T. D., and Tadaki, K.: 2014, *MNRAS* **438**, 2565

Sato, K., Yamasaki, N. Y., Ishida, M., Ishisaki, Y., Ohashi, T., Kawahara, H., Kitaguchi, T., Kawaharada, M., Kokubun, M., Makishima, K., Ota, N., Nakazawa, K., Tamura, T., Matsushita, K., Kawano, N., Fukazawa, Y., and Hughes, J. P.: 2007, *PASJ* **59**, 299

Savaglio, S., Glazebrook, K., Le Borgne, D., Juneau, S., Abraham, R. G., Chen, H.-W., Crampton, D., McCarthy, P. J., Carlberg, R. G., Marzke, R. O., Roth, K., Jørgensen, I., and Murowinski, R.: 2005, *ApJ* **635**, 260

Scarlata, C., Carollo, C. M., Lilly, S., Sargent, M. T., Feldmann, R., Kampczyk, P., Porciani, C., Koekemoer, A., Scoville, N., Kneib, J.-P., Leauthaud, A., Massey, R., Rhodes, J., Tasca, L., Capak, P., Maier, C., McCracken, H. J., Mobasher, B., Renzini, A., Taniguchi, Y., Thompson, D., Sheth, K., Ajiki, M., Aussel, H., Murayama, T., Sanders, D. B., Sasaki, S., Shioya, Y., and Takahashi, M.: 2007a, *ApJl Supp.* **172**, 406

Scarlata, C., Carollo, C. M., Lilly, S. J., Feldmann, R., Kampczyk, P., Renzini, A., Cimatti, A., Halliday, C., Daddi, E., Sargent, M. T., Koekemoer, A., Scoville, N., Kneib, J.-P., Leauthaud, A., Massey, R., Rhodes, J., Tasca, L., Capak, P., McCracken, H. J., Mobasher, B., Taniguchi, Y., Thompson, D., Ajiki, M., Aussel, H., Murayama, T., Sanders, D. B., Sasaki, S., Shioya, Y., and Takahashi, M.: 2007b, *ApJl Supp.* **172**, 494

Schaap, W. E. and van de Weygaert, R.: 2000, *Astronomy and Astrophysics* **363**, L29

Scharf, C., Donahue, M., Voit, G. M., Rosati, P., and Postman, M.: 2000, *ApJl* **528**, L73

Scodeggio, M., Vergani, D., Cucciati, O., Iovino, A., Franzetti, P., Garilli, B., Lamareille, F., Bolzonella, M., Pozzetti, L., Abbas, U., Marinoni, C., Contini, T., Bottini, D., Le Brun, V., Le Fèvre, O., Maccagni, D., Scaramella, R., Tresse, L., Vettolani, G., Zanichelli, A., Adami, C., Arnouts, S., Bardelli, S., Cappi, A., Charlot, S., Ciliegi, P., Foucaud, S., Gavignaud, I., Guzzo, L., Ilbert, O., McCracken, H. J., Marano, B., Mazure, A., Meneux, B., Merighi, R., Paltani, S., Pellò, R., Pollo, A., Radovich, M., Zamorani, G., Zucca, E., Bondi, M., Bongiorno, A., Brinchmann, J., de La Torre, S., de Ravel, L., Gregorini, L., Memeo, P., Perez-Montero, E., Mellier, Y., Temporin, S., and Walcher, C. J.: 2009, *Astronomy and Astrophysics* **501**, 21

Scoville, N., Arnouts, S., Aussel, H., Benson, A., Bongiorno, A., Bundy, K., Calvo, M. A. A., Capak, P., Carollo, M., Civano, F., Dunlop, J., Elvis, M., Faisst, A., Finoguenov, A., Fu, H., Giavalisco, M., Guo, Q., Ilbert, O., Iovino, A., Kajisawa, M., Kartaltepe, J., Leauthaud, A., Le Fèvre, O., LeFloch, E., Lilly, S. J., Liu, C. T.-C., Manohar, S., Massey, R., Masters, D., McCracken, H. J., Mobasher, B., Peng, Y.-J., Renzini, A., Rhodes, J., Salvato, M., Sanders, D. B., Sarvestani, B. D., Scarlata, C., Schinnerer, E., Sheth, K., Shopbell, P. L., Smolčić, V., Taniguchi, Y., Taylor, J. E., White, S. D. M., and Yan, L.: 2013, *ApJl Supp.* **206**, 3

Scoville, N., Aussel, H., Benson, A., Blain, A., Calzetti, D., Capak, P., Ellis, R. S., El-Zant, A., Finoguenov, A., Giavalisco, M., Guzzo, L., Hasinger, G., Koda, J., Le Fèvre, O., Massey, R., McCracken, H. J., Mobasher, B., Renzini, A., Rhodes, J., Salvato, M., Sanders, D. B., Sasaki, S. S., Schinnerer, E., Sheth, K., Shopbell, P. L., Taniguchi, Y., Taylor, J. E., and Thompson, D. J.: 2007a, *ApJl Supp.* **172**, 150

Scoville, N., Aussel, H., Brusa, M., Capak, P., Carollo, C. M., Elvis, M., Giavalisco, M., Guzzo, L., Hasinger, G., Impey, C., Kneib, J.-P., LeFevre, O., Lilly, S. J., Mobasher, B., Renzini, A., Rich, R. M., Sanders, D. B., Schinnerer, E., Schminovich, D., Shopbell, P., Taniguchi, Y., and Tyson, N. D.: 2007b, *ApJl Supp.* **172**, 1

Scudder, J. M., Ellison, S. L., and Mendel, J. T.: 2012a, *MNRAS* **423**, 2690

Scudder, J. M., Ellison, S. L., Torrey, P., Patton, D. R., and Mendel, J. T.: 2012b, *MNRAS* **426**, 549

Shandarin, S. F. and Zeldovich, Y. B.: 1989, *Reviews of Modern Physics* **61**, 185

Shaw, R. A. and Dufour, R. J.: 1995, *Publications of the Astronomical Society of the Pacific* **107**, 896

Shields, G. A.: 1990, *Annual Reviews of Astronomy and Astrophysics* **28**, 525

Shields, G. A., Skillman, E. D., and Kennicutt, Jr., R. C.: 1991, *ApJ* **371**, 82

Shimakawa, R., Kodama, T., Tadaki, K.-i., Hayashi, M., Koyama, Y., and Tanaka, I.: 2015, *MNRAS* **448**, 666

Shivaei, I., Reddy, N. A., Steidel, C. C., and Shapley, A. E.: 2015, *ApJ* **804**, 149

Silverman, B. W.: 1986, *Density estimation for statistics and data analysis*

Simard, L.: 1998, in R. Albrecht, R. N. Hook, and H. A. Bushouse (eds.), *Astronomical Data Analysis Software and Systems VII*, Vol. 145 of *Astronomical Society of the Pacific Conference Series*, p. 108

Skillman, E. D., Kennicutt, Jr., R. C., Shields, G. A., and Zaritsky, D.: 1996, *ApJ* **462**, 147

Smail, I., Geach, J. E., Swinbank, A. M., Tadaki, K., Arumugam, V., Hartley, W., Almaini, O., Bremer, M. N., Chapin, E., Chapman, S. C., Danielson, A. L. R., Edge, A. C., Scott, D., Simpson, C. J., Simpson, J. M., Conselice, C., Dunlop, J. S., Ivison, R. J., Karim, A., Kodama, T., Mortlock, A., Robson, E. I., Roseboom, I., Thomson, A. P., van der Werf, P. P., and Webb, T. M. A.: 2014, *ApJ* **782**, 19

Smail, I., Morrison, G., Gray, M. E., Owen, F. N., Ivison, R. J., Kneib, J.-P., and Ellis, R. S.: 1999, *ApJ* **525**, 609

Sobral, D., Best, P. N., Geach, J. E., Smail, I., Cirasuolo, M., Garn, T., Dalton, G. B., and Kurk, J.: 2010, *MNRAS* **404**, 1551

Sobral, D., Best, P. N., Geach, J. E., Smail, I., Kurk, J., Cirasuolo, M., Casali, M., Ivison, R. J., Coppin, K., and Dalton, G. B.: 2009, *MNRAS* **398**, 75

Sobral, D., Best, P. N., Matsuda, Y., Smail, I., Geach, J. E., and Cirasuolo, M.: 2012, *MNRAS* **420**, 1926

Sobral, D., Best, P. N., Smail, I., Geach, J. E., Cirasuolo, M., Garn, T., and Dalton, G. B.: 2011, *MNRAS* **411**, 675

Sobral, D., Best, P. N., Smail, I., Mobasher, B., Stott, J., and Nisbet, D.: 2014, *MNRAS* **437**, 3516

Sobral, D., Matthee, J., Darvish, B., Schaerer, D., Mobasher, B., Röttgering, H., Santos, S., and Hemmati, S.: 2015a, *ArXiv e-prints*

Sobral, D., Smail, I., Best, P. N., Geach, J. E., Matsuda, Y., Stott, J. P., Cirasuolo, M., and Kurk, J.: 2013a, *MNRAS* **428**, 1128

Sobral, D., Stroe, A., Dawson, W. A., Wittman, D., Jee, M. J., Röttgering, H., van Weeren, R. J., and Brüggen, M.: 2015b, *MNRAS* **450**, 630

Sobral, D., Swinbank, A. M., Stott, J. P., Matthee, J., Bower, R. G., Smail, I., Best, P., Geach, J. E., and Sharples, R. M.: 2013b, *ApJ* **779**, 139

Sol Alonso, M., Michel-Dansac, L., and Lambas, D. G.: 2010, *Astronomy and Astrophysics* **514**, A57

Speagle, J. S., Steinhardt, C. L., Capak, P. L., and Silverman, J. D.: 2014, *ArXiv e-prints*

Springel, V.: 2000, *MNRAS* **312**, 859

Springel, V., White, S. D. M., Jenkins, A., Frenk, C. S., Yoshida, N., Gao, L., Navarro, J., Thacker, R., Croton, D., Helly, J., Peacock, J. A., Cole, S., Thomas, P., Couchman, H., Evrard, A., Colberg, J., and Pearce, F.: 2005, *Nature* **435**, 629

Steidel, C. C., Rudie, G. C., Strom, A. L., Pettini, M., Reddy, N. A., Shapley, A. E., Trainor, R. F., Erb, D. K., Turner, M. L., Konidaris, N. P., Kulas, K. R., Mace, G., Matthews, K., and McLean, I. S.: 2014, *ApJ* **795**, 165

Stocke, J. T., Danforth, C. W., Shull, J. M., Penton, S. V., and Giroux, M. L.: 2007, *ApJ* **671**, 146

Stocke, J. T., Penton, S. V., Danforth, C. W., Shull, J. M., Tumlinson, J., and McLin, K. M.: 2006, *ApJ* **641**, 217

Stoica, R. S., Martínez, V. J., Mateu, J., and Saar, E.: 2005, *Astronomy and Astrophysics* **434**, 423

Stott, J. P., Smail, I., Edge, A. C., Ebeling, H., Smith, G. P., Kneib, J.-P., and Pimbblet, K. A.: 2007, *ApJ* **661**, 95

Stott, J. P., Sobral, D., Bower, R., Smail, I., Best, P. N., Matsuda, Y., Hayashi, M., Geach, J. E., and Kodama, T.: 2013, *MNRAS* **436**, 1130

Stroe, A., Sobral, D., Dawson, W., Jee, M. J., Hoekstra, H., Wittman, D., van Weeren, R. J., Brüggen, M., and Röttgering, H. J. A.: 2015, *MNRAS* **450**, 646

Stroe, A., Sobral, D., Röttgering, H. J. A., and van Weeren, R. J.: 2014, *MNRAS* **438**, 1377

Swinbank, A. M., Smail, I., Sobral, D., Theuns, T., Best, P. N., and Geach, J. E.: 2012, *ApJ* **760**, 130

Tanaka, M., Goto, T., Okamura, S., Shimasaku, K., and Brinkmann, J.: 2004, *The Astronomical Journal* **128**, 2677

Tempel, E., Stoica, R. S., Martínez, V. J., Liivamägi, L. J., Castellan, G., and Saar, E.: 2014, *MNRAS* **438**, 3465

Toft, S., Gallazzi, A., Zirm, A., Wold, M., Zibetti, S., Grillo, C., and Man, A.: 2012, *ApJ* **754**, 3

Tonnesen, S. and Cen, R.: 2012, *MNRAS* **425**, 2313

Tran, K.-V. H., Papovich, C., Saintonge, A., Brodwin, M., Dunlop, J. S., Farrah, D., Finkelstein, K. D., Finkelstein, S. L., Lotz, J., McLure, R. J., Momcheva, I., and Willmer, C. N. A.: 2010, *ApJl* **719**, L126

Tran, K.-V. H., Saintonge, A., Moustakas, J., Bai, L., Gonzalez, A. H., Holden, B. P., Zaritsky, D., and Kautsch, S. J.: 2009, *ApJ* **705**, 809

Tremonti, C. A., Heckman, T. M., Kauffmann, G., Brinchmann, J., Charlot, S., White, S. D. M., Seibert, M., Peng, E. W., Schlegel, D. J., Uomoto, A., Fukugita, M., and Brinkmann, J.: 2004, *ApJ* **613**, 898

Trump, J. R., Impey, C. D., McCarthy, P. J., Elvis, M., Huchra, J. P., Brusa, M., Hasinger, G., Schinnerer, E., Capak, P., Lilly, S. J., and Scoville, N. Z.: 2007, *ApJl Supp.* **172**, 383

Valentino, F., Daddi, E., Strazzullo, V., Gobat, R., Onodera, M., Bournaud, F., Juneau, S., Renzini, A., Arimoto, N., Carollo, M., and Zanella, A.: 2015, *ApJ* **801**, 132

Villar, V., Gallego, J., Pérez-González, P. G., Pascual, S., Noeske, K., Koo, D. C., Barro, G., and Zamorano, J.: 2008, *ApJ* **677**, 169

Vogelsberger, M., Genel, S., Springel, V., Torrey, P., Sijacki, D., Xu, D., Snyder, G., Bird, S., Nelson, D., and Hernquist, L.: 2014, *Nature* **509**, 177

Weiner, B. J., Willmer, C. N. A., Faber, S. M., Melbourne, J., Kassin, S. A., Phillips, A. C., Harker, J., Metevier, A. J., Vogt, N. P., and Koo, D. C.: 2006, *ApJ* **653**, 1027

Werner, N., Finoguenov, A., Kaastra, J. S., Simionescu, A., Dietrich, J. P., Vink, J., and Böhringer, H.: 2008, *Astronomy and Astrophysics* **482**, L29

Whitaker, K. E., van Dokkum, P. G., Brammer, G., and Franx, M.: 2012, *ApJl* **754**, L29

Wijesinghe, D. B., Hopkins, A. M., Brough, S., Taylor, E. N., Norberg, P., Bauer, A., Brown, M. J. I., Cameron, E., Conselice, C. J., Croom, S., Driver, S., Grootes, M. W., Jones, D. H., Kelvin, L., Loveday, J., Pimbblet, K. A., Popescu, C. C., Prescott, M., Sharp, R., Baldry, I., Sadler, E. M., Liske, J., Robotham, A. S. G., Bamford, S., Bland-Hawthorn, J., Gunawardhana, M., Meyer, M., Parkinson, H., Drinkwater, M. J., Peacock, J., and Tuffs, R.: 2012, *MNRAS* **423**, 3679

Williams, R. J., Quadri, R. F., Franx, M., van Dokkum, P., and Labbé, I.: 2009, *ApJ* **691**, 1879

Williamson, R., Benson, B. A., High, F. W., Vanderlinde, K., Ade, P. A. R., Aird, K. A., Andersson, K., Armstrong, R., Ashby, M. L. N., Bautz, M., Bazin, G., Bertin, E., Bleem, L. E., Bonamente, M., Brodwin, M., Carlstrom, J. E., Chang, C. L., Chapman, S. C., Clocchiatti, A., Crawford, T. M., Crites, A. T., de Haan, T., Desai, S., Dobbs, M. A., Dudley, J. P., Fazio, G. G., Foley, R. J., Forman, W. R., Garmire, G., George, E. M., Gladders, M. D., Gonzalez, A. H., Halverson, N. W., Holder, G. P., Holzapfel, W. L., Hoover, S., Hrubes, J. D., Jones, C., Joy, M., Keisler, R., Knox, L., Lee, A. T., Leitch, E. M., Lueker, M., Luong-Van, D., Marrone, D. P., McMahon, J. J., Mehl, J., Meyer, S. S., Mohr, J. J., Montroy, T. E., Murray, S. S., Padin, S., Plagge, T., Pryke, C., Reichardt, C. L., Rest, A., Ruel, J., Ruhl, J. E., Saliwanchik, B. R., Saro, A., Schaffer, K. K., Shaw, L., Shirokoff, E., Song, J., Spieler, H. G., Stalder, B., Stanford, S. A., Staniszewski, Z., Stark, A. A., Story, K., Stubbs, C. W., Vieira, J. D., Vikhlinin, A., and Zenteno, A.: 2011, *ApJ* **738**, 139

Wilson, G., Muzzin, A., Yee, H. K. C., Lacy, M., Surace, J., Gilbank, D., Blindert, K., Hoekstra, H., Majumdar, S., Demarco, R., Gardner, J. P., Gladders, M. D., and Lonsdale, C.: 2009, *ApJ* **698**, 1943

Wolf, C., Gray, M. E., and Meisenheimer, K.: 2005, *Astronomy and Astrophysics* **443**, 435

Wuyts, S., Förster Schreiber, N. M., Nelson, E. J., van Dokkum, P. G., Brammer, G., Chang, Y.-Y., Faber, S. M., Ferguson, H. C., Franx, M., Fumagalli, M., Genzel, R., Grogin, N. A., Kocevski, D. D., Koekemoer, A. M., Lundgren, B., Lutz, D., McGrath, E. J., Momcheva, I., Rosario, D., Skelton, R. E., Tacconi, L. J., van der Wel, A., and Whitaker, K. E.: 2013, *ApJ* **779**, 135

Xia, L., Malhotra, S., Rhoads, J., Pirzkal, N., Straughn, A., Finkelstein, S., Cohen, S., Kuntschner, H., Kümmel, M., Walsh, J., Windhorst, R. A., and O'Connell, R.: 2012, *The Astronomical Journal* **144**, 28

Yabe, K., Ohta, K., Iwamuro, F., Akiyama, M., Tamura, N., Yuma, S., Kimura, M., Takato, N., Moritani, Y., Sumiyoshi, M., Maihara, T., Silverman, J., Dalton, G., Lewis, I., Bonfield, D., Lee, H., Curtis-Lake, E., Macaulay, E., and Clarke, F.: 2014, *MNRAS* **437**, 3647

York, D. G., Adelman, J., Anderson, Jr., J. E., Anderson, S. F., Annis, J., Bahcall, N. A., Bakken, J. A., Barkhouser, R., Bastian, S., Berman, E., Boroski, W. N., Bracker, S., Briegel, C., Briggs, J. W., Brinkmann, J., Brunner, R., Burles, S., Carey, L., Carr, M. A., Castander, F. J., Chen, B., Colestock, P. L., Connolly, A. J., Crocker, J. H., Csabai, I., Czarapata, P. C., Davis, J. E., Doi, M., Dombeck, T., Eisenstein, D., Ellman, N., Elms, B. R., Evans, M. L., Fan, X., Federwitz, G. R., Fiscelli, L., Friedman, S., Frieman, J. A., Fukugita, M., Gillespie, B., Gunn, J. E., Gurbani, V. K., de Haas, E., Haldeman, M., Harris, F. H., Hayes, J., Heckman, T. M., Hennessy, G. S., Hindsley, R. B., Holm, S., Holmgren, D. J., Huang, C.-h., Hull, C., Husby, D., Ichikawa, S.-I., Ichikawa, T., Ivezić, Ž., Kent, S., Kim, R. S. J., Kinney, E., Klaene, M., Kleinman, A. N., Kleinman, S., Knapp, G. R., Korienek, J., Kron, R. G., Kunszt, P. Z., Lamb, D. Q., Lee, B., Leger, R. F., Limmongkol, S., Lindenmeyer, C., Long, D. C., Loomis, C., Loveday, J., Lucinio, R., Lupton, R. H., MacKinnon, B., Mannery, E. J., Mantsch, P. M., Margon, B., McGehee, P., McKay, T. A., Meiksin, A., Merelli, A., Monet, D. G., Munn, J. A., Narayanan, V. K., Nash, T., Neilsen, E., Neswold, R., Newberg, H. J., Nichol, R. C., Nicinski, T., Nonino, M., Okada, N., Okamura, S., Ostriker, J. P., Owen, R., Pauls, A. G., Peoples, J., Peterson, R. L., Petravick, D., Pier, J. R., Pope, A., Pordes, R., Prosapio, A., Rechenmacher, R., Quinn, T. R., Richards, G. T., Richmond, M. W., Rivetta, C. H., Rockosi, C. M., Ruthmansdorfer, K., Sandford, D., Schlegel, D. J., Schneider, D. P., Sekiguchi, M., Sergey, G., Shimasaku, K., Siegmund, W. A., Smee, S., Smith, J. A., Snedden, S., Stone, R., Stoughton, C., Strauss, M. A., Stubbs, C., SubbaRao, M., Szalay, A. S., Szapudi, I., Szokoly, G. P., Thakar, A. R., Tremonti, C., Tucker, D. L., Uomoto, A., Vanden Berk, D., Vogeley, M. S., Waddell, P., Wang, S.-i., Watanabe, M., Weinberg, D. H., Yanny, B., Yasuda, N., and SDSS Collaboration: 2000, *The Astronomical Journal* **120**, 1579

Zahid, H. J., Geller, M. J., Kewley, L. J., Hwang, H. S., Fabricant, D. G., and Kurtz, M. J.: 2013, *ApJl* **771**, L19

Zahid, H. J., Kewley, L. J., and Bresolin, F.: 2011, *ApJ* **730**, 137

Zamojski, M. A., Schiminovich, D., Rich, R. M., Mobasher, B., Koekemoer, A. M., Capak, P., Taniguchi, Y., Sasaki, S. S., McCracken, H. J., Mellier, Y., Bertin, E., Aussel, H., Sanders, D. B., Le Fèvre, O., Ilbert, O., Salvato, M., Thompson, D. J., Kartaltepe, J. S., Scoville, N., Barlow, T. A., Forster, K., Friedman, P. G., Martin, D. C., Morrissey, P., Neff, S. G., Seibert, M., Small, T., Wyder, T. K., Bianchi, L., Donas, J., Heckman, T. M., Lee, Y.-W., Madore, B. F., Milliard, B., Szalay, A. S., Welsh, B. Y., and Yi, S. K.: 2007, *ApJl Supp.* **172**, 468

Zappacosta, L., Mannucci, F., Maiolino, R., Gilli, R., Ferrara, A., Finoguenov, A., Nagar, N. M., and Axon, D. J.: 2002, *Astronomy and Astrophysics* **394**, 7

Zappacosta, L., Nicastro, F., Maiolino, R., Tagliaferri, G., Buote, D. A., Fang, T., Humphrey, P. J., and Gastaldello, F.: 2010, *ApJ* **717**, 74

Zaritsky, D., Kennicutt, Jr., R. C., and Huchra, J. P.: 1994, *ApJ* **420**, 87

Zeimann, G. R., Stanford, S. A., Brodwin, M., Gonzalez, A. H., Mancone, C., Snyder, G. F., Stern, D., Eisenhardt, P., Dey, A., and Moustakas, J.: 2013, *ApJ* **779**, 137

Zel'dovich, Y. B.: 1970, *Astronomy and Astrophysics* **5**, 84

Ziparo, F., Popesso, P., Finoguenov, A., Biviano, A., Wuyts, S., Wilman, D., Salvato, M., Tanaka, M., Nandra, K., Lutz, D., Elbaz, D., Dickinson, M., Altieri, B., Aussel, H., Berta, S., Cimatti, A., Fadda, D., Genzel, R., Le Floc'h, E., Magnelli, B., Nordon, R., Poglitsch, A., Pozzi, F., Portal, M. S., Tacconi, L., Bauer, F. E., Brandt, W. N., Cappelluti, N., Cooper, M. C., and Mulchaey, J. S.: 2014, *MNRAS* **437**, 458

Appendix

A1 Effect of Density Field Estimation based on Different Sample Selections

In Chapter 3 Section 2.2, we used a flux-limited (K_s <24) sample of galaxies in order to estimate the density field. All the main results presented in Chapter 3 Section 3.3 were based on this flux-limited sample used for density estimation. Here, we try two other samples of galaxies to estimate the density field and investigate their effects on the results presented in Chapter 3 Section 3.3. Just as before, we use the Voronoi tessellation method as the density estimator and the definition of low- and high-density environments given in Chapter 3 Section 3.3. These new samples are defined as follows:

1. In addition to the conditions given in Chapter 3 Section 2.2, we select all galaxies that are more massive than the stellar mass completeness limit of the samples defined in Chapter 3 Section 3.2 and Chapter 3 Table 3.1 (K_s <24 and $M > M_{comp}$).

2. In addition to the conditions given in Chapter 3 Section 2.2, we select all galaxies that are more massive than the stellar mass completeness limit of the highest redshift sample defined in Chapter 3 Section 3.2 and Chapter 3 Table 3.1 (K_s <24 and $\log(M/M_\odot) > 9.97$). This is similar to a volume-limited sample of galaxies.

Using these new samples, we re-estimate the density fields and reinvestigate the results in Chapter 3 Section 3.3. Figure 6.1 is similar to Figure 3.10, but it also shows the results

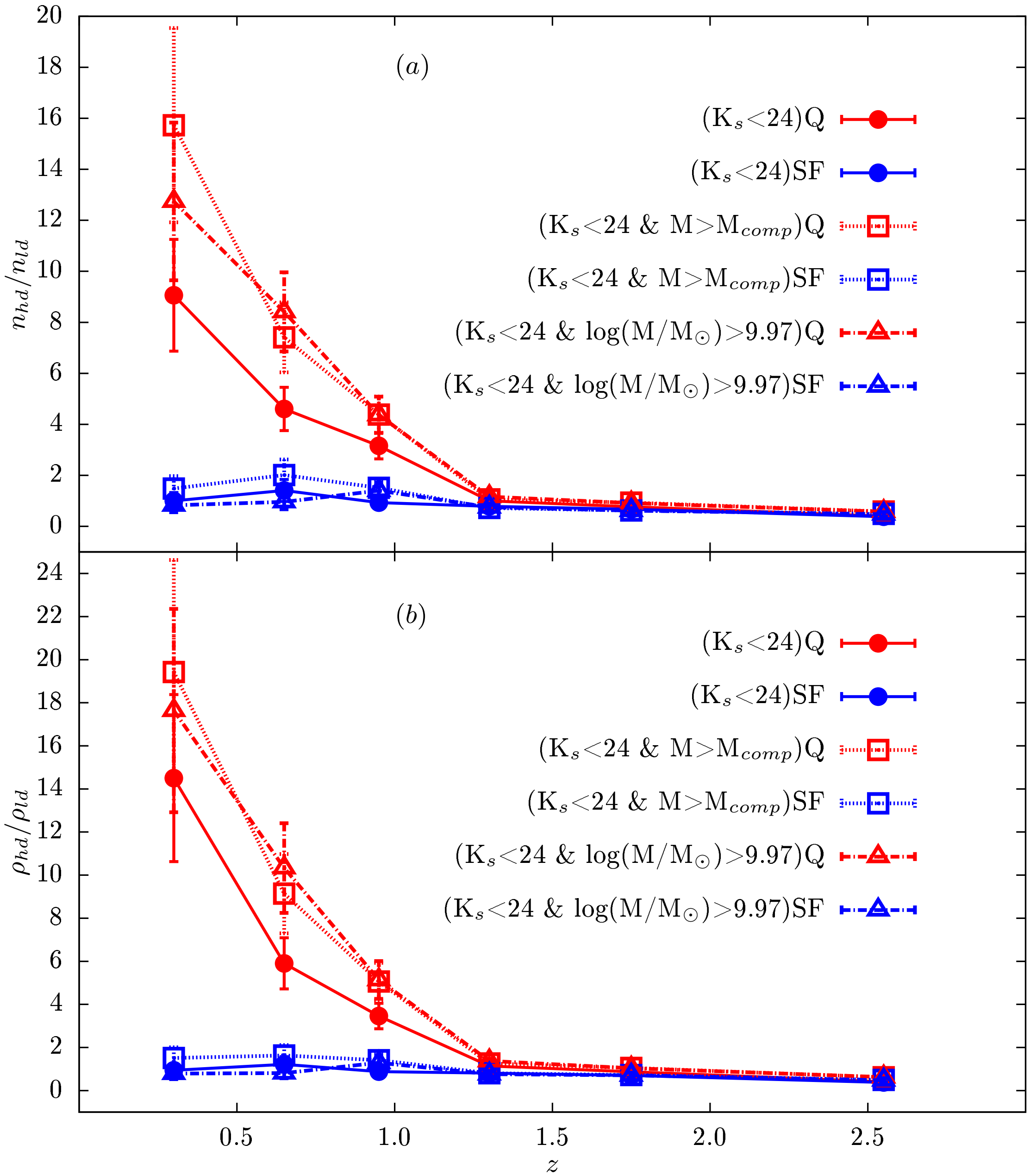

Figure 6.1: Similar to Figure 3.10 but the results are shown for the different samples used to estimate the density field of galaxies. Filled circles, empty squares, and empty triangles show the trends based on a flux-limited sample (K_s <24, same results in Figure 3.10), a sample of galaxies with (K_s <24 and M>M_{comp}), and a sample of galaxies with K_s <24 and log(M/$M_\odot$)>9.97 (which is similar to a volume-limited sample), respectively (see the appendix). We see the same trends obtained in Chapter 3 Section 3.3. Our results are not significantly influenced by the selection of the samples used to estimate the density field of galaxies.

based on the new samples used to estimate the density field. According to Figure 6.1, we are able to retrieve the main trends obtained in Chapter 3 Section 3.3 for quiescent (Q) and star-forming (SF) galaxies. However, we mention that for massive quiescent galaxies, the number and mass density trends become even more amplified at z <1 when we use the new samples for density estimation. This is expected because the new samples target more massive galaxies in order to estimate the density field, which tend to be more strongly clustered compared with less massive systems. We highlight that our results in Chapter 3 Section 3.3 are not significantly affected by the selection of the samples we used for density field estimation.